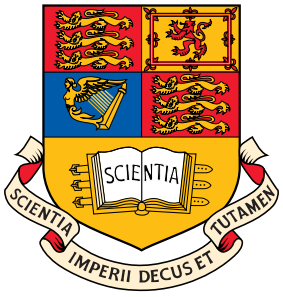
Understanding and modelling failure of laminated composites

by

Renaud Gutkin



Department of Aeronautics

South Kensington Campus

Imperial College London

London SW7 2AZ

U.K.

This thesis is submitted for the degree of Doctor of Philosophy of Imperial College London

2010

Abstract

In this thesis, experimental investigations together with analytical and numerical work on the understanding and modelling of failure in laminated composites are presented.

Failure of carbon fibre reinforced plastics is investigated using acoustic emission. Signals are collected for various test configurations which give rise to specific failure modes. The signals are then analysed using pattern recognition techniques and the fast Fourier transform. An identification of the failure modes with their acoustic signatures is proposed using the fast Fourier transform, which was found to be the most suitable technique.

The failure modes in longitudinal compression are then studied using microscopy techniques and finite element modelling. Experimental observations show that failure results from an interaction between shear-driven compressive failure and kink-band formation.

Micromechanical finite element analyses are used to explain the experimental observations. The interaction of shear-driven compressive failure and kinking captured by the model is used to explain the variation in characteristics typically measured in failure envelopes for combined longitudinal compression vs. in-plane shear.

Based on the experimental and the numerical results, a failure criterion for fibre kinking and splitting is developed and used to predict failure envelopes for combined longitudinal compression vs. in-plane shear. The model correlates well with the numerical predictions and experimental results.

The R-curve effect observed in mode I intralaminar matrix crack growth and its specimen-dependence are then investigated. Relationships between crack extension

and crack opening displacement are obtained for the Double Cantilever Beam (DCB) and Compact Tension (CT) specimens. Measured R-curves are used with the previous relationships to define a trilinear cohesive law. The cohesive law is implemented in finite element models and the load versus displacement curves predicted for the DCB and CT specimens show that the R-curve effect is numerically well captured.

Declaration

The work in this thesis is based on research carried out at Imperial College London. No part of this thesis has been submitted elsewhere for any other degree or qualification and it is all the authors own work unless referenced to the contrary in the text.

Contents

Abstract i

Declaration ii

Table of Contents iv

List of Figures xii

List of Tables xix

Acknowledgments xxi

Notation xxi

1 Introduction 1

2 Current state of the art on failure of laminated composites 4

2.1 Overview 4

2.2 The physics behind failure in laminated composites 4

2.2.1 Matrix dominated failure modes 6

2.2.2 Fibre dominated failure modes 11

2.3 Acoustic Emission 19

2.3.1 Principles 19

2.3.2 Damage detection in composite materials using Acoustic Emission 22

2.3.2.1 Conventional AE analysis 24

2.3.2.2 Pattern recognition and multivariable analysis 28

2.3.2.3 Modal acoustic emission 32
2.4 Modelling: current failure models and criteria 32
2.4.1 Failure criteria 33
2.4.1.1 Limit criteria 33
2.4.2 Polynomial criteria 34
2.4.2.1 Tsai-Hill quadratic failure criterion 34
2.4.2.2 Tsai-Wu quadratic failure criterion 35
2.4.3 Physically based criteria 35
2.4.3.1 Fibre failure 36
2.4.3.2 Matrix failure 46
2.4.4 Damage propagation 49
2.4.4.1 Phenomenological approaches 50
2.4.4.2 Energy based model 51
2.5 Discussion on the state of the art 53
2.5.1 Acoustic Emission 53
2.5.2 Longitudinal compressive failure 54
2.5.3 Failure models and criteria 55

3 On acoustic emission for failure investigation in CFRP 57
3.1 Introduction 57
3.2 Experiments 60
3.2.1 Introduction 60
3.2.2 Manufacture of the test specimens 60
3.2.3 Acoustic Emission equipment 63
3.2.4 Reported failure modes 63
3.3 Pattern Recognition Technique 66
3.3.1 AE parameters selections 66
3.3.2 Details of the algorithms used 67
3.3.2.1 k-means 67
3.3.2.2 Self Organising Map 68
3.3.2.3 Competitive Neural Network 69

3.3.3 Choice of algorithm . . . 69
3.3.4 Results of the clustering . . . 71
3.4 Results of the frequency analysis . . . 76
3.5 Discussion . . . 77
3.5.1 Pattern recognition technique . . . 77
3.5.2 Frequency based classification . . . 79
3.6 Conclusion . . . 81
3.7 Publications . . . 82

4 Experimental investigation on longitudinal compressive failure of notched CFRP laminates 83

4.1 Introduction . . . 83
4.2 Experimental procedure . . . 85
4.2.1 Test material and specimens geometry . . . 85
4.2.2 SEM test jig . . . 86
4.2.3 Polishing test jig . . . 86
4.3 Longitudinal compressive failure in unidirectional laminates . . . 87
4.3.1 In-situ observation with the SEM test jig . . . 87
4.3.1.1 Initiation and propagation . . . 88
4.3.1.2 Matrix microcracking . . . 88
4.3.1.3 Fibre failure . . . 90
4.3.2 In-situ observation with the polishing test jig . . . 92
4.4 Longitudinal compressive failure in cross-ply laminates . . . 94
4.4.1 In-plane observations . . . 94
4.4.2 Observations on the fracture planes . . . 94
4.4.2.1 Kink-band formation . . . 96
4.4.2.2 Shear driven fibre compressive failure . . . 96
4.5 Discussion . . . 96
4.5.1 Representativeness of the in-situ tests . . . 96
4.5.2 Microcracking . . . 98
4.5.3 Fibre failure at kink-band edge . . . 98

4.5.4 Kink-band propagation angle 99
4.5.5 Shear driven fibre compressive failure 99
4.5.6 Transition 100
4.5.7 Role of the 90° plies and delamination 100
4.6 Conclusions 101
4.7 Publications 101

5 Micro-mechanical modelling of longitudinal compressive failure for failure envelope generation 103

5.1 Introduction 103
5.2 Micromechanical FE model 106
5.2.1 Model setup 106
5.2.2 Model validation 109
5.3 Parametric failure envelope prediction 111
5.3.1 Effect of the matrix behaviour 111
5.3.2 Effect of the compressive strength of the fibres 112
5.3.3 Effect of initial fibre misalignment 113
5.3.4 Global model behaviour 115
5.4 Comparison to experiments 117
5.4.1 Experiments from Jelf and Fleck [22] 117
5.4.2 Experiments from the first World Wide Failure Exercise [37] . 118
5.5 Discussion 120
5.5.1 Shear-driven fibre compressive failure 120
5.5.2 Transition from shear-driven compressive failure to kink-band formation 120
5.5.3 Limit kinking/splitting 121
5.5.4 The trend of the failure envelope 121
5.5.5 Current analytical capabilities for failure envelope predictions 122
5.6 Conclusions 123
5.7 Publications 124

6 An analytical formulation to predict fibre kinking and splitting under combined longitudinal compression and inplane shear 125

6.1 Introduction . . . 125
6.2 Kink-band formation: experimental observations . . . 127
6.3 Model formulation . . . 129
6.3.1 Framework . . . 129
6.3.2 Equilibrium of the fibre . . . 131
6.3.3 Strain energy and dissipated fracture energy . . . 134
6.3.4 Energy balance . . . 134
6.3.5 Linear elastic shear response of the matrix . . . 135
6.4 Prediction of failure envelopes . . . 136
6.4.1 Numerical validation and parametric study . . . 136
6.4.2 Comparison with experimental results . . . 140
6.5 Discussion . . . 141
6.6 Conclusions . . . 143
6.7 Publications . . . 143

7 Modelling the R-curve effect and its specimen-dependence 145

7.1 Introduction . . . 145
7.2 Definition of the cohesive law from a measured R-curve . . . 148
7.2.1 Trilinear constitutive law . . . 148
7.2.2 Crack extension versus crack opening displacement relationship for the CT specimen . . . 151
7.2.3 Crack extension versus crack opening displacement relationship for the DCB specimen . . . 152
7.2.4 R-curves and load versus displacement curves . . . 154
7.3 Mode I intralaminar R-curve measurement . . . 155
7.3.1 Data reduction . . . 155
7.3.2 Specimen manufacture . . . 155
7.3.3 Test method and experimental setup . . . 156
7.3.4 Experimental results and analysis . . . 156

7.4 Numerical simulation of mode I intralaminar matrix failure 159
7.4.1 Finite Element models 159
7.4.2 Load displacement and R-curves predicted by the FE models . 161
7.4.3 Crack opening displacement 167
7.5 Discussion 169
7.6 Conclusion 171
7.7 Publications 171

8 Conclusions **172**
8.1 Damage identification using acoustic emission 172
8.2 Longitudinal compressive failure: Experiments 173
8.3 Longitudinal compressive failure: Micromechanical modelling 173
8.4 Longitudinal compression: Analytical modelling 174
8.5 Modelling the R-curve effect and its specimen-dependence 174

9 Future work **176**
9.1 Experimental 176
9.1.1 Damage identification using acoustic emission 176
9.1.2 Longitudinal compressive failure 177
9.2 Analytical 177
9.3 Numerical 178

Appendices **178**

A Damage identification using Acoustic Emission: Discrete Wavelet Transform **179**
A.1 Discrete Wavelet Transform 179
A.1.1 Level analysis 180
A.1.2 Results and discussion 182
A.2 Conclusion 182

B A failure criterion for shear-driven fibre compressive failure **186**
B.1 Introduction 186

B.2 Failure criterion . . . 187
B.3 Applications . . . 189
B.3.1 Failure envelope . . . 189
B.4 Discussion . . . 191
B.5 Conclusions . . . 191

C A micromechanical model for kink–band formation: Part I — experimental study and numerical modelling 192
C.1 Abstract . . . 192
C.2 Introduction . . . 193
C.3 Experimental study . . . 195
C.4 Numerical modelling . . . 196
C.5 Sequence of events . . . 204
C.6 Key features . . . 206
C.7 Conclusions . . . 207

D A micromechanical model for kink–band formation: Part II — analytical modelling 209
D.1 Abstract . . . 209
D.2 Introduction . . . 210
D.3 Development of the analytical micromechanical model . . . 213
D.3.1 Strategy . . . 213
D.3.2 Fibre geometry and loading . . . 214
D.3.3 2D equivalent model . . . 214
D.3.4 Equilibrium of the fibre . . . 215
D.3.5 Shear stresses acting on the fibres . . . 215
D.3.6 Governing differential equations . . . 217
D.3.7 Continuity and boundary conditions . . . 217
D.3.8 Composite compressive strength . . . 219
D.3.9 Axial stresses and fibre failure . . . 219
D.4 Results . . . 220
D.5 Discussion . . . 224

D.5.1 Qualitative analysis of fields 224
D.5.2 Agreement between analytical and FE results 225
D.5.3 Model outputs 226
D.5.4 Sensitivity study 226
D.6 Conclusions 228
D.A Analytical expressions for displacement and stress fields 229
D.A.1 Elastic domain 229
D.A.2 Peak load 230
D.A.3 Softening domain 230

Bibliography **231**

List of Figures

2.1 Typical laminate with global and local coordinate systems. 5
2.2 Matrix tensile failure with (a) a brittle matrix (x30) [2], (b) a ductile matrix [3]. 6
2.3 (a) Fibre bridging in a DCB specimen [4], (b) R-curve for mode I intralaminar fracture [5]. 7
2.4 Pure transverse compressive failure [6]. 8
2.5 Shear failure in FRP with (a) a brittle matrix [2], (b) a ductile matrix [3]. 9
2.6 Matrix microcracking in cross-ply laminate (a) in tension [17], (b) in compression. 11
2.7 Fibre failure in FRP with (a) a brittle matrix [2], (b) a ductile matrix [3]. 12
2.8 Fracture surface of CT specimens (a) 90 ° plies blocked: $[(90_2/0)_8/90]_s$ layup and (b) 0 ° plies blocked: $[(90/0_2)_8/90]_s$ layup; Corresponding R-curves for (c) 90 ° plies blocked and (d) 0 ° plies blocked [19]. . . . 13
2.9 Failure modes in longitudinal compression: (a) compressive shear failure [17], (b) splitting, (c) kink-band formation [17]. 14
2.10 Sequence of events in kink-band formation. 15
2.11 Sequence of kink-band formation from [30]. Label 1: Fibre failure; label 2: matrix crack; label 3: fibre/matrix splitting; label 4: kink-band edge. 16

2.12 (a) FE model used by Guynn et al. [32]; FE models for kink-bands analysis [31] (b) Array of fibre/matrix with uniform sinusoidal imperfection; (c) with sinusoidal imperfection at one edge and straight fibres at the opposite edge; (d) with centrally located sinusoidal imperfection. 17
2.13 AE waveform with some relevant parameters. 20
2.14 Acquisition, processing and classification of AE waveforms. 23
2.15 Failure modes classification using amplitude analysis: summary of the literature. 25
2.16 Failure modes classification using frequency analysis: summary of the literature. 26
2.17 Principle of wavelet decomposition. 27
2.18 Principal Component Analysis (PCA) principle. 30
2.19 Typical procedure for supervised pattern recognition. 31
2.20 Longitudinal tension versus in-plane shear failure envelopes for the criteria described in this section and experimental data from [37]. . . 37
2.21 Longitudinal compression versus in-plane shear failure envelopes for the criteria described in this section and experimental data from (a) Soden et al. [37], (b) Jelf and Fleck [22], (c) Mannigel [23] and (d) Yerramalli and Waas [38]. 39
2.22 Microbuckling theory: (a) Extensional mode, (b) Shear mode. 41
2.23 Models based on beam theory: (a) Fibre supported by matrix, (b) Smeared composite approach. 42
2.24 (a) Kinking theory under multi-axial stress state [74], LaRC fibre kinking criterion (b) 2D and (c) 3D [6, 67]. 43
2.25 Effect of a 3D formulation (adapted from [6]). 45
2.26 Definition of the tractions acting on the fracture plane. [67, 68] 47
2.27 Failure envelopes for matrix failure for various criteria for a carbon/epoxy composite (adapted from [6]) 49
2.28 Cohesive bilinear law. 53

3.1 Geometry (dimensions in mm) and sensor placement for the different specimen configurations. 62
3.2 Load versus displacement curve of a representative for each test. . . . 65
3.3 Post-tests C-Scans of typical specimens used in the T45, UDCT, CPCT and CPCC tests. 66
3.4 Performances of the k-means, the SOM combined with k-means and the CNN algorithms for the T90 test with 3 clusters and the T090 test with 6 clusters. 71
3.5 Clustering results for the T0, T90 and T45 tests using the combined SOM / k-means algorithm. 73
3.5 Clustering results for the T090, UDCT and CPCT tests using the combined SOM / k-means algorithm. 74
3.5 Clustering results for the CPCC, DCB and 4ENF tests using the combined SOM / k-means algorithm. 75
3.6 Frequency analysis for a representative sample of each test. 76
3.7 Summary of the classification using frequency content. 80

4.1 Typical kink-band geometry. 84
4.2 Specimen geometry (dimensions in mm). 86
4.3 (a) SEM test jig; (b) Polishing test jig. 87
4.4 Kink-band formation in unidirectional specimen. 89
4.5 Top edge of a kink-band. 90
4.6 Central part of a kink-band. 91
4.7 Bottom edge of a kink-band. 91
4.8 Fibre failure at kink-band edge. 92
4.9 Typical kink-band formation at the notch-tip of a UD specimen. . . . 93
4.10 Typical compressive fracture process in a cross-ply specimen. (a) Overall view of the fracture process; (b) Schematic of the failure process; (c) Definition of the three different failure patterns; (d) Close-up view of the transition region. 95
4.11 Fracture plane A-A on cross-ply specimen. 97

4.12 Effect of polishing. 98
4.13 Sequence of events at the transition. 100

5.1 Failure envelopes from the literature: (a) Michaeli et al. [102], (b) Soden et al. [37], (c) Jelf and Fleck [22], (d) Yerramalli and Waas [38]. 104
5.2 Trends predicted by: the maximum stress criterion; the Puck's criterion [68]; the Tsai-Wu criterion [65]; the LaRC05 criterion [30]. 105
5.3 Micromechanical FE model: geometry, boundary conditions and loading. 108
5.4 Shear stress versus shear strain curves. 108
5.5 Effect of the length of the model (L) on the predicted failure envelopes. 110
5.6 Effect of the volume fraction chosen for the FE model on the predicted failure envelopes. 111
5.7 Effect of the periodic boundary conditions on the predicted failure envelopes. 112
5.8 Effect of the constitutive response of the matrix on the predicted failure envelopes. 113
5.9 Effect of the fibre compressive strength (X_c^f) on the predicted failure envelopes. 114
5.10 Longitudinal compressive strength against misalignment: FE and LaRC05 fibre kinking predictions. 114
5.11 Stress-strain (σ_1 versus ε_1) curves, axial stress distribution along the fibres $\left(\sigma_1^f\right)$ and deformed shape for the baseline model for several values of τ_{12} (the deformed shapes and stress distributions are taken close to the peak stress, as shown by the circles) 116
5.12 Distance between the points of maximum axial stress w versus shear stress. 117
5.13 Experimental failure envelopes from (a) Jelf and Fleck [22] and (b) Soden et al. [37], together with the corresponding FE predictions. . . 119
5.14 Failure envelope construction. 122

6.1 (a) Kink-band propagation in a unidirectional single edge notch specimen under load; (b) Close-up view on the kink-band tip; (c) Close-up view on the top edge of a kink-band. 128
6.2 Undamaged and damaged state of the model. 131
6.3 Fibre equilibrium. 133
6.4 Shear responses for an IM7/8552 carbon-epoxy system. 137
6.5 Predictions for a linear and nonlinear shear response of the matrix, comparison between the present analytical model and FE results from Chapter 5. 139
6.6 Predictions for several values of: (a) the initial misalignment angle θ_0; (b) the shear strength of the resin S_L 140
6.7 Comparison with experimental results from (a) Jelf and Fleck [22] and (b) Soden et al. [37]. 141

7.1 DCB and CT specimen dimensions (in mm) 148
7.2 Simplified trilinear cohesive law. 150
7.3 Assumed crack profile for a CT specimen. 152
7.4 Assumed crack profile for a DCB specimen. 153
7.5 Load versus displacement curves and R-curves (a-b) for the DCB tests and (c-d) for the CT tests. 157
7.6 Trilinear cohesive law defined from DCB tests. 159
7.7 FE models of the DCB and CT specimens. 161
7.8 Load displacement curves for the DCB test; Experimental results with FE predictions for bilinear and trilinear cohesive laws and quasi-analytical predictions. 162
7.9 $G_R(\Delta a)$ for the DCB test. 163
7.10 FE and analytical $G_R(\delta)$ for the DCB test. 164
7.11 Load displacement curves for the CT test; Experimental results with FE predictions for bilinear and trilinear cohesive laws and quasi-analytical predictions. 165
7.12 $G_R(\Delta a)$ for the CT test. 166

7.13 FE and analytical $G_R(\delta)$ for the CT test. 167
7.14 Crack opening displacements extracted from the FE model for the DCB at the displacements indicated in Fig. 7.8. Each curve is superposed with a third order polynomial. 168
7.15 Crack opening displacements extracted from the FE model for the CT at the displacements indicated in Fig. 7.11. 169

A.1 (a) Wavelet decomposition of a typical AE signal; (b) Power spectrum of each decomposition level. 181
A.2 (Left) Wavelet levels and load versus displacement curves, (Right) Cumulative distribution of events per level for the T0, T90, T45 tests. 183
A.2 (Left) Wavelet levels and load versus displacement curves, (Right) Cumulative distribution of events per level for the T090, UDCT, CPCT tests. 184
A.2 (Left) Wavelet levels and load versus displacement curves, (Right) Cumulative distribution of events per level for the CPCC, DCB, 4ENF tests. 185

B.1 Orientaton of the fracture plane in a 3D space. 187
B.2 Traction components on the fracture plane. 188
B.3 Single Element for failure envelope generation (dimensions in mm). . 189
B.4 Failure envelope for combined longitudinal compression and in-plane shear. 190

C.1 Kink–band. 193
C.2 Specimen used in the experimental study and imposed displacements. All dimensions in mm. 196
C.3 Stages of fibre kinking (loaded). 196
C.4 Kink–band with matrix yielding and no fibre failure (unloaded). . . . 197
C.5 Detail of kink–band edge and fibre failure in compression (loaded) [123]. 197
C.6 Geometries, meshes and boundary conditions of the numerical models. 199
C.7 Non-linear elastic–plastic constitutive law for the matrix (CDM_f model). 200

C.8 Load vs. displacement curves from numerical models. 201
C.9 Fields from numerical analysis (curves for the central fibre and adjoining interface), at the points highlighted in figure C.8.b. 202
C.10 Fibre failure in compression (index `DAMAGEFC`) and damage propagation during kink–band formation. 203
C.11 Kink–band *propagation* in initially straight fibres. 203
C.12 Kink–band propagation: experimental and numerical results (same scale). 206

D.1 Kink–band. 210
D.2 Schematics of the fibre considered in the model: geometry and loads. 214
D.3 2D equivalent and matrix deformation. 216
D.4 Boundary and continuity conditions. 218
D.5 Results of the analytical model (compared to those of the *cohesive* model (detailed in *Part I* of this paper [105]), for a similar compressive load P). 222
D.6 Results of the analytical model (evolution of fields). 223
D.7 Sensitivity study for the initial imperfection. 227

List of Tables

2.1 Degradation of elastic properties from [65] 51

3.1 Type, layup and name of tests 61
3.2 Tensile specimens geometry 62
3.3 Clustering specification and performance for the SOM combined with k-means algorithm 72

4.1 Mechanical properties of T800/924 unidirectional lamina. 85

5.1 Input parameters used in the FE model 109

6.1 Geometrical and mechanical properties of the composites and resin. . 137

7.1 Parameters used for the definition of the cohesive law. 158
7.2 Material properties used for the FE models. 160

B.1 Mechanical properties used in the FE model. 190

C.1 Constituents elastic properties used in the numerical models (typical values for IM7/8551-7 from [124]). 200
C.2 Constituents strength properties used in the numerical models (typical values for IM7/8551-7 from [124]). 200
C.3 Constituents fracture toughness used in the numerical models (values based on [91]). 201
C.4 Geometrical and numerical composite parameters used in the numerical models. 201

D.1 Geometrical and composite parameters used in the analytical model. 221
D.2 Constituents mechanical properties used in the analytical model. . . . 221
D.3 Quantitative results from the analytical model at the peak load. . . . 221
D.4 Quantitative results from the analytical model at the onset of fibre failure. 222

Acknowledgments

The author would like to acknowledge the funding of this research from the Engineering and Physical Sciences Research Council and the Ministry of Defence under the project EP/E0Z3169/1 is gratefully acknowledged.

For their constant supervision, guidance and advice throughout the last three years, the author would like to thank both his supervisors, Dr. Silvestre Pinho and Dr. Paul Robinson.

The author would like to thank Professor P.T. Curtis of the Defence Science and Technology Laboratory (DSTL) for many helpful discussions.

The interest, involvement and participation of Ms. Soraia Pimenta, Mr. Christopher Green, Mr. William Francis, Mr. Surachai Vangrattanachai, Mr. Jean-Marie Dumont, Mr. Pascal Meysonnat, Mr. Tian Ye, Mr. Vij Dhayan and Ms. Anne-Mathilde Clairouin is acknowledged.

The author would also like to thank Mr.Gary Senior, Mr. Jon Cole and Mr Stephen Johnson for help with the manufacture of laminates, machining of specimens and manufacturing of the testing jigs; and Mr. Joseph Meggyesi for help with experimental testing.

Finally, the author would like to acknowledge his family, his girlfriend Anna and all his friends and colleagues for their constant support and inspiration.

Notation

Lower case Roman letters

a_o ..... initial crack length

a_o . initial length of the pre-crack (compact tension and compact compression tests)

$a\,(i)$ ..... average distance between the i^{th} vector and the other vectors in the same cluster

$b\,(i,k)$ ..... the average distance from the i^{th} vector to the other vectors in another cluster k

c_i ..... center of cluster i

c ..... winning neuron

d ..... damage variable

e ..... length of end-tab in tensile test specimen

f ..... failure index

f_{fcs} ..... failure index for the shear-driven fibre compressive failure mode

$f_{k/s}$ ..... failure index for the fibre kinking and splitting failure modes

f_i ..... frequency band $i = I, II, III, IV, V$

f_{CL}^{γ} . shear constitutive law of the matrix function of the shear strain in the matrix γ_m

f_{CL}^{θ} ..... shear constitutive law of the matrix function of fibre's rotation θ

h ..... thickness of the tabs in a tensile test specimen

h ..... ply thickness

$h_{cj}\,(k)$ neighbourhood function (Gaussian function centered on the winning neuron c)

j ..... j^{th} neuron

k ..... number of clusters in the k-means algorithm
$l \times p$ ..... dimension of the SOM
l_c ..... characteristic length used in FE smeared approach
l_{LPZ} ..... length of the Long Process Zone
l_{SPZ} ..... length of the Short Process Zone
n ..... number of the input vectors in pattern recognition algorithms
m ..... dimension number of the input vectors in pattern recognition algorithms
r .. ratio between the cohesive strength and the strength of a second failure process
s ..... silhouette value
t ..... thickness of a tensile test, DCB and CT specimen
t_m ..... thickness of the matrix layer in 2D kink-band models
w ..... width of a kink-band
$\mathbf{w}_i$ ..... weight vector assigned to the i^{th} neuron
x ..... geometric coordinate
$\mathbf{x}_i$ ..... i^{th} input vector
y ..... geometric coordinate
z ..... geometric coordinate

Upper case Roman letters

A_f ..... cross sectional area of a fibre
C ..... compliance
$\mathbf{C}^0$ ..... undamaged compliance tensor
$\mathbf{C}^d$ ..... damaged compliance tensor
C_i ..... i^{th} cluster
E ..... Young's modulus
E ..... damaged Young's modulus
E_0 ..... initial (undamaged) Young's modulus
E_i .... $i = 1, 2, 3$ longitudinal, transverse and through the thickness Young's moduli
E_f ..... Young's modulus of the fibres
E_m ..... Young's modulus of the matrix
$\mathbf{E}^0$ ..... initial (undamaged) elasticity tensor

$\mathbf{E}^{incl}$ ..... elasticity tensor of an inclusion

F ..... applied force on a DCB or CT specimen

F_{12} ..... biaxial coefficient in the Tsai-Wu criterion

G ..... shear modulus

G ..... complementary free energy

G_{12} ..... in-plane shear modulus

G_{ic} ..... $i = I, II, III$ toughness for mode I, II and III

G_c ..... toughness

G_{init} ..... initiation toughness

G_m ..... shear modulus of the matrix

G_m^{2D} ..... equivalent shear modulus for 2D models

G_{prop} ..... propagation toughness

G_R ..... R-curve

$\mathbf{I}$ ..... identity tensor

I_f ..... second moment of area of a fibre

K ..... penalty coefficient

L ..... length of the 2D micromechanical model

L ..... length of the tensile test specimen

P ..... axial load on a single fibre

S ..... shear load on a single fibre

S ..... shear strength of a composite

$\mathbf{S}$ ..... Eshelby's tensor

S_c ..... compressive shear strength of a composite

S_L ..... in-plane shear strength of a composite

S_m ..... shear strength of the matrix

S_T ..... transverse shear strength of a composite

S^f ..... compressive shear strength of a fibre

S^m ..... compressive shear strength of the matrix

U_A ..... strain energy in the undamaged state A

U_B ..... strain energy in the damaged state B

U_m ..... strain energy in the matrix

V ..... volume of the control volume

v_f ..... fibre volume fraction

W ..... width of the tensile test specimes

X_c ..... longitudinal compressive strength of a composite

X_c^f ..... compressive strength of a fibre

X_c^m ..... compressive strength of the matrix

X_t ..... longitudinal tensile strength of a composite

Y_c ..... transverse compressive strength of a composite

Y_t ..... transverse tensile strength of a composite

Lower case Greek letters

α ..... angle of the fibres in the kink-band

α ..... fracture angle under transverse compressive loading

α ..... coefficient of proportionality for the fracture toughness in chapter 6

α ..... learning rate

α ..... coefficient of best fit for the compliance in chapter 7

α_0 ..... fracture angle under pure transverse compressive loading

β ..... propagation angle of a kink-band

β .... measure of the actual normalised area of the microcracks formed between the fibres during fibre kinking

β ..... coefficient of best fit for the compliance in chapter 7

δ ..... crack opening displacement

δ_0 ..... elastic crack opening displacement

δ_f ..... end crack opening displacement

δ_i ..... intermediate crack opening displacement

ε ..... strain

η_i^j .. slope coefficient, $i = L, T$ (longitudinal or transverse) and $j = T, C$ (tension or compression)

γ_m ..... shear strain in the matrix

γ_Y ..... shear yield strain of the matrix

ϕ ..... orientation of the fracture during shear-driven fibre compressive failure

ϕ_f ..... fibre diameter

ϕ_f^{2D} ..... equivalent fibre diameter for 2D models

χ ..... coefficient of best fit for the compliance in chapter 7

λ .. non-dimensional parameter accounting for the specimen dependence of the end crack opening displacement in Chapter 7

ν ..... Poisson's ration

ν_{12} ..... major Poisson's ratio of a composite

ν_f ..... Poisson's ration of the fibre

ν_m ..... Poisson's ratio of the matrix

μ ..... coefficient of friction

θ ..... rotation of the fibres in the matrix due to the compressive loading

θ_0 ..... initial misalignment of the fibres

ψ ..... angle of the fracture plane during shear-driven fibre compressive failure

ρ .. crack density of the microcracks formed between the fibres during fibre kinking

σ ..... stress

σ_0 ..... cohesive strength

σ_N ..... normal traction on a fracture plane

σ_i ..... intermediate strength

σ_i .... $i = 1, 2, 3$ longitudinal, transverse and through the thickness normal stresses

σ_1^f ..... normal compressive stress at the circumference of the fibres

σ_{i^ψ} . $i = 1, 2, 3$ longitudinal, transverse and through the thickness normal stresses in a coordinate axis rotated to the angle ψ, used in appendix B

τ ..... shear stress

τ_{12} ..... in-plane shear stress

τ_m ..... shear stress in the matrix

τ_n ..... maximum shear traction on a fracture plane

τ_t ..... transverse shear traction on a fracture plane

τ_Y ..... shear yield strength

Upper case Greek letters

Δ ..... applied displacement in the DCB and CT tests

Δa . . . . . crack extension

Chapter 1

Introduction

During recent years, there has been a steady development towards using composite materials for high performance applications in the automotive, marine, aerospace and sport industries. A wider use remains limited by the high costs involved when designing with composites. Besides the cost of the material, an extensive experimental program is often necessary to characterise the material, obtain information on the structural response of a component and to validate a design. These experiments are often very expensive as they must be done for several types of loading, several sample configurations and as they also require specialist equipment and competences. Substantial cost savings could be achieved by replacing some of the physical tests by virtual tests. This type of approach is based on material models implemented in numerical codes (e.g. the finite element method) and would in principle allow the designers to assess their designs, and the effects of any relevant parameters, in a much faster and more controlled environment than by physical testing. However, current models often lack the reliability and robustness required in industrial design situations.

A key element to virtual testing tools is the failure theory they are built upon. An overview of the current failure theories available for composites and of their performances was given in the first world wide failure exercise [1], where 19 theories were applied to 15 different problems and compared to experimental results. While some aspects of failure in laminated composites are well captured by some theories,

for example the modelling of initiation for matrix or tensile fibre dominated failure modes, the exercise revealed some deficiencies for the load cases involving failure in longitudinal compression, damage accumulation and multi-axial loading.

The poor performances observed in the areas mentioned above can often be related to a lack of understanding of the physics behind failure in composites. Therefore, the objectives of the present work are to deepen this understanding and, building on this knowledge, develop analytical and numerical formulations to predict the behaviour of the composite up to failure.

In the second chapter of this thesis, the current state of the art on failure of laminated composites is reviewed and discussed. The review deals only with ply failure modes and focuses on three main areas. The first part of the review details experimental observations (and some micromechanical finite element analyses) on the different failure modes. This is closely related to the second part, in which several techniques to detect and monitor damage using acoustic emission are discussed. The third part of the review focuses on the current failure models and criteria.

Chapter 3 presents an investigation on failure of carbon fibre reinforced plastics using Acoustic Emission (AE). The objective of this work is to identify characteristic signal features associated with damage propagation for each failure mode, and investigate whether these features can be recognized in other specimens where more complex failure processes take place. The outcomes are a deeper understanding of the sequence failure takes place in different types of specimen and a classified AE database which can be used to recognise failure in other specimen configurations.

Experimental observations of failure in longitudinal compression are typically difficult to obtain. In Chapter 4, experiments to observe in-situ compressive failure by means of dedicated testing jigs are presented. The objective is to obtain information on the failure processes at the microscale and in a actual loading situation. This information can then be used as input for micromechanical models and as a basis to develop physically based criteria.

The effect of in-plane shear stress combined with longitudinal compression is studied in Chapter 5 with a Finite Element (FE) micromechanical model. The objectives are to explain some of the experimental observations from Chapter 4

and quantify the effect of the change in failure modes on the failure envelope. The outcomes are deformations and stress states of the constituents during failure, which can be used in the development of an analytical formulation, and failure envelopes for the case of longitudinal compression combined with in-plane shear, to which predictions from a failure criterion can be compared.

Using the insights gained from the previous chapters, an analytical formulation to predict the strength during fibre kinking and splitting under combined longitudinal compression and shear is presented in Chapter 6. The objective is to develop a simple, yet accurate, formulation based on simplifications and assumptions supported by physical observations. The outcome is a failure criterion which can be used in design situations.

Modelling the R-curve effect and its specimen dependence is studied in Chapter 7. The objective is to derive relationships to define a cohesive law from measured R-curves. The outcome is a cohesive law which account for toughening mechanisms and which can be used in numerical simulations of composite structures.

Finally conclusions and recommendations for future work are given in Chapters 8 and 9.

Chapter 2

Current state of the art on failure of laminated composites

2.1 Overview

The present chapter details the current state of the art on understanding and modelling failure in laminated composites. Experimental and numerical studies with focus on the mechanisms leading to failure are first presented and discussed. The different techniques to monitor and identify failure using acoustic emission are then detailed. Finally, the current failure models and criteria used to model failure in composites are reviewed.

2.2 The physics behind failure in laminated composites

This section describes and discusses the mechanisms leading to failure and damage accumulation, the origins of the toughening mechanisms found in composites and the interaction between different failure modes. The review and discussion are supported by experimental studies available in the literature and for the case of longitudinal compression, some Finite Element (FE) micromechanical analyses are also detailed.

A distinction is often made between failure in the ply—intralaminar or translam-

inar failure—and failure at their interfaces—interlaminar failure. Ply failures can be of several natures depending on the loading conditions—tension, compression, shear or combined—and are either matrix (intralaminar) or fibre (translaminar) dominated. Interlaminar failure, or delamination, of plies stacked together is often encountered in laminated composites; damage initiates and propagates at the interface between two plies in a opening (mode I), sliding (mode II) or tearing (mode III) mode and can lead to significant stiffness reduction in structures, even when no defect is visible. Interlaminar failure is however not in the scope of the present work.

A typical laminate is shown in Fig. 2.1, the global laminate coordinate system is noted (x, y, z) and the local ply coordinate system is noted $(1, 2, 3)$, with 1 the longitudinal direction, 2 the transverse direction and 3 the through the thickness direction.

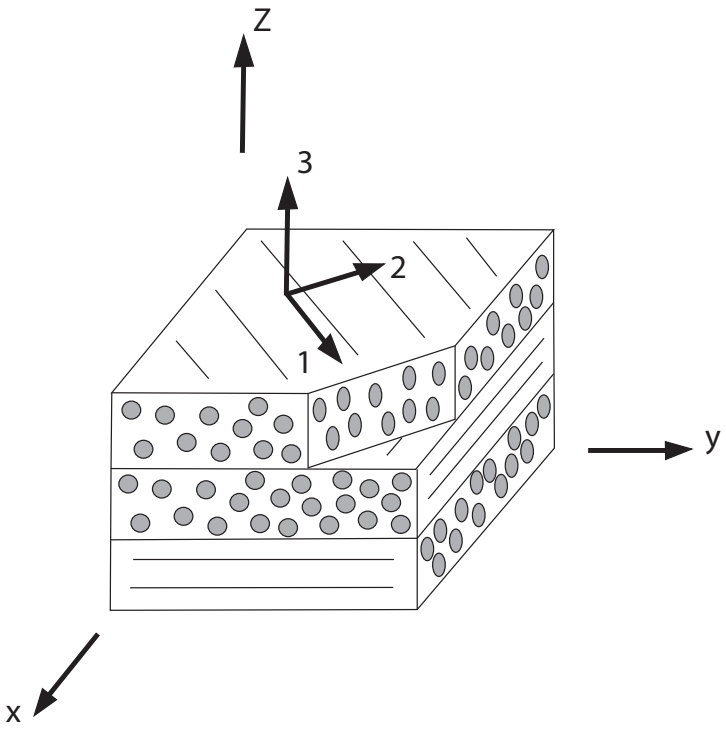


Figure 2.1: Typical laminate with global and local coordinate systems.

2.2.1 Matrix dominated failure modes

Failure is matrix dominated when it is driven by the failure mechanisms taking place in the matrix. They are mainly found when the ply stresses are in the transverse direction or in shear and are strongly influenced by the properties of the matrix.

Two main types of resin are used for the matrix: thermosetting (epoxy, polyester) or thermoplastic (polypropylene, nylon). From a fracture perspective, thermosetting resins have typically a more brittle behaviour than their thermoplastic counterparts. The brittleness of the matrix partially affects the brittleness of the composite, and can change the failure processes found in composites.

Under pure tensile transverse loading, or in combination with in-plane shear, microcracks form in the matrix and at the interface with the fibres. Failure results from the coalescence of some of these microcracks in a plane normal to the loading (2)-direction. This fracture plane is shown in Fig. 2.2a for a composite with a brittle matrix and in Fig. 2.2b with a more ductile matrix. In the brittle case, fracture is localised in a well defined fracture plane, while in Fig. 2.2b, the fracture plane is irregular with large areas where the matrix has been separated from the fibres and, where remaining, the matrix shows large plastic deformation.

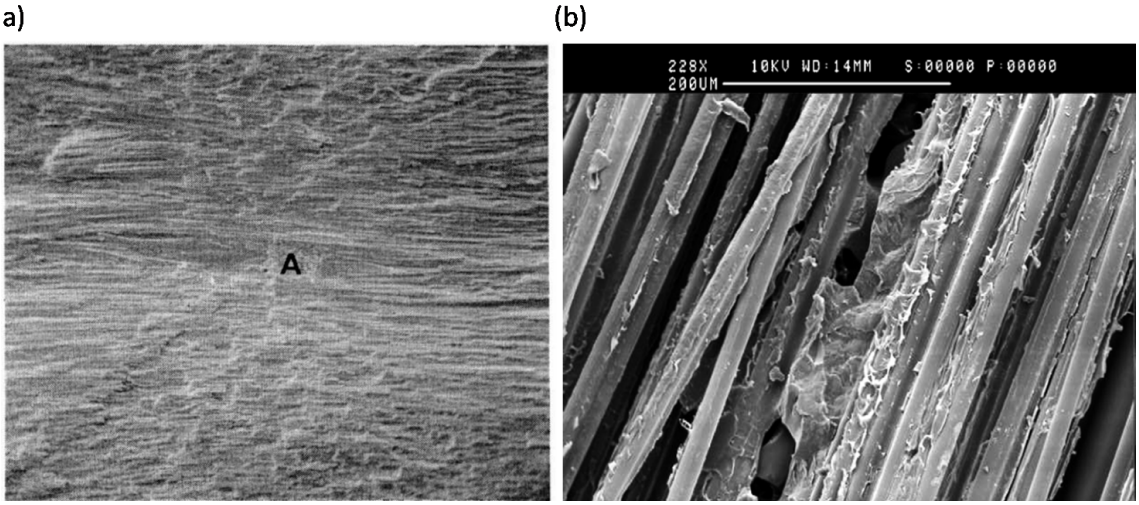


Figure 2.2: Matrix tensile failure with (a) a brittle matrix (x30) [2], (b) a ductile matrix [3].

In commenting Fig. 2.2a, Purslow [2] notes that the crack, which initiated from A, propagates in slightly different planes breaking fibres in tension or flexure. This mechanism of fibre bridging the crack faces is often at the origin of the rising resistance curve (R-curve) observed in composites—their resistance to fracture increases as the crack propagates. Such fibre bridging is shown in Fig. 2.3a [4], with the corresponding R-curves Fig. 2.3b, for intralaminar fracture in a DCB specimen. The R-curves plotted in Fig. 2.3 are obtained using DCBs with different heights of arms (H in the figure) and show that the R-curves are specimen dependent. In particular, the crack extension needed to reach a steady state (in this example ~ 2000 J/m^2), and which corresponds to the crack extension needed for the processes in the wake of the crack (here fibre bridging) to develop, increases as the bending stiffness of the specimens increases. Because R-curves are specimen dependent they cannot be used directly for material characterisation, and another measure of the material toughness is needed, this will be detailed later.

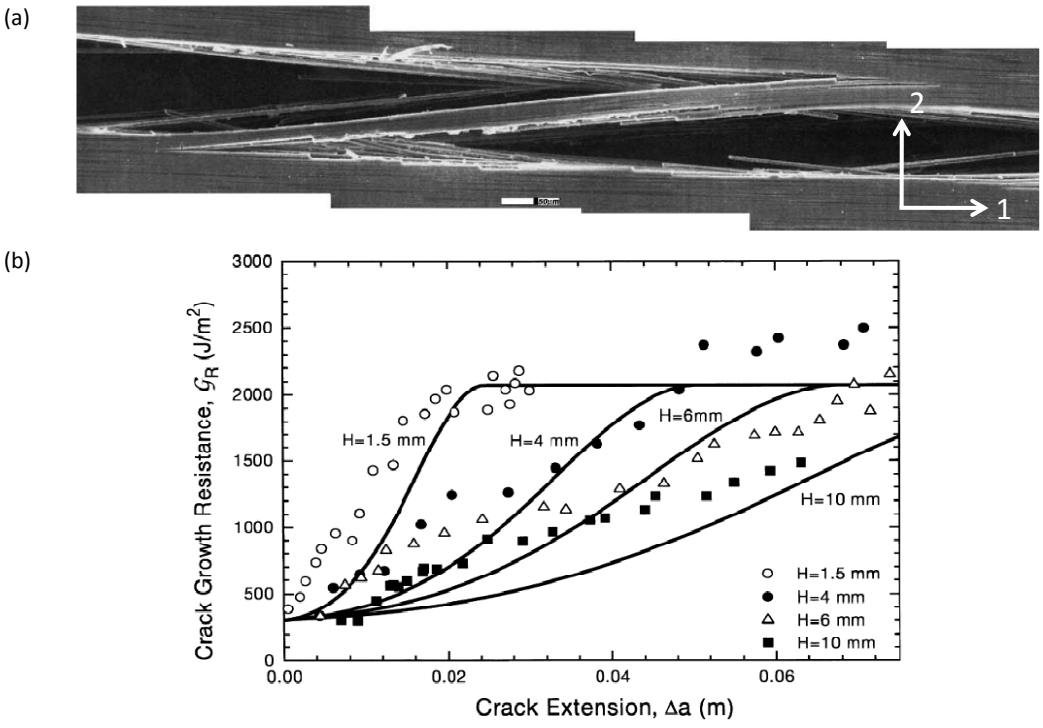


Figure 2.3: (a) Fibre bridging in a DCB specimen [4], (b) R-curve for mode I intralaminar fracture [5].

When the loading in the transverse direction is a combination of compression and in-plane shear, the magnitude of the compressive stresses has an effect on the orientation of the fracture angle. In cases of moderate compressive stresses, the fracture remains orthogonal to the transverse direction. However, when these stresses are increased, the fracture angle lies at an angle to the transverse direction; for a case of pure compression, the angle is $\alpha_0 \sim 53^\circ$ as shown in Fig. 2.4. It is often observed that for compressive stresses below half the transverse compressive strength, shear stresses greater than the shear strength can be carried by the material [6]; which witnesses the pressure dependency of composites in the transverse direction.

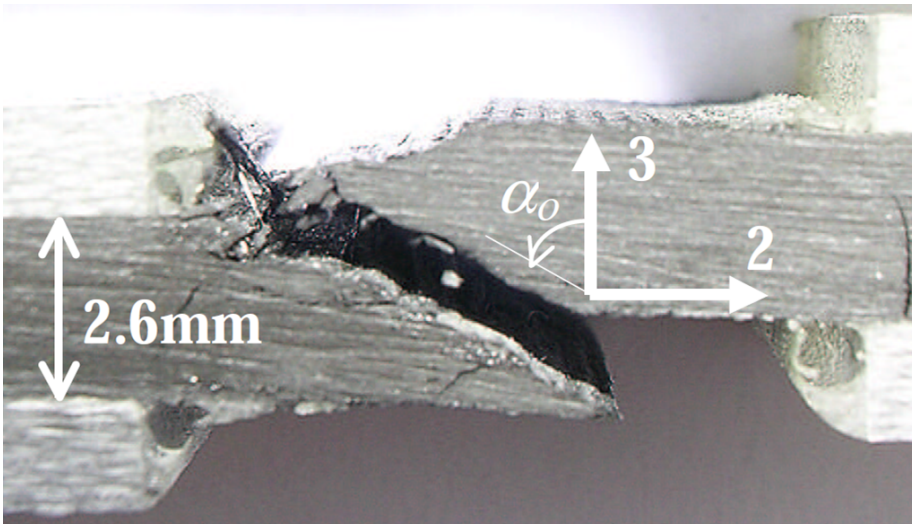


Figure 2.4: Pure transverse compressive failure [6].

Under pure shear loading, relatively few microscopic observations of the mechanisms leading to failure can be found in the literature, despite the fact that modelling correctly this failure mode is important, for example, to predict the response in longitudinal compression. One reason for this lack of studies is related to the difficulty of generating a state of pure shear in experimental samples, as witnesses the large number of standard methods available to determine the properties for in-plane shear

[7–10]. The shear response of a composite is typically nonlinear due to the presence of damage and to plastic or visco-plastic deformation of the matrix [11, 12].

A shear fracture in brittle matrix composites is shown in Fig. 2.5a. A typical feature of this type of failure are the shear cusps (B) which have formed in the matrix. The shear cusps are tensile cracks which initiate in a plane orientated at 45 ° to the loading direction [13]. Once initiated, they elongate, curve and eventually coalesce to form the pattern shown at B in Fig. 2.5a. In the ductile case, Fig.2.5b, the shear cusps are also seen but the amount of plastic deformation of the matrix is much more significant than in the brittle case.

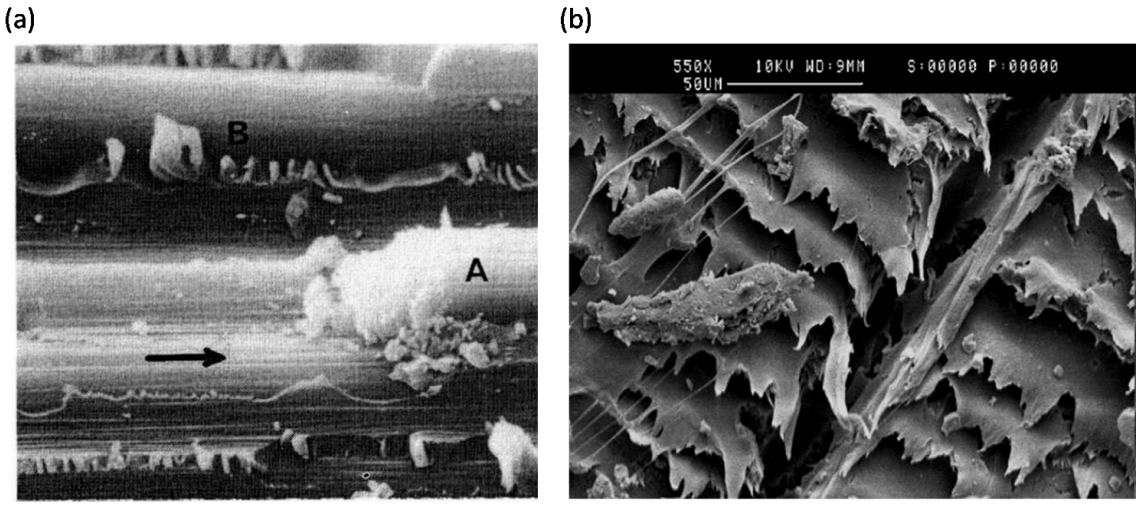


Figure 2.5: Shear failure in FRP with (a) a brittle matrix [2], (b) a ductile matrix [3].

The response of a ply embedded in a laminate is different to the response of an individual ply, as it is influenced by the neighbouring plies (which have different orientations). An increase in the transverse and shear strengths of plies in a laminate is typically reported in the literature [14–16]. In embedded plies, microcracks accumulation is observed, as shown in Fig. 2.6a for a cross-ply laminate in tension [2]. Regularly spaced transverse microcracks are seen in the 90 ° layers. The microcrack planes are perpendicular to the load and span the entire thickness of the layer. When the microcracks form, adjacent plies help to redistribute the load to

other, undamaged, regions of the layer which results into a higher strength of the embedded plies. Under increasing applied strain, the crack density increases (the spacing decreases) up to a saturation value, at which local delaminations form at the interface with the 0° plies, see drawing in Fig. 2.6a, and lead to failure of the laminate. The saturation value is dependent of the constraints imposed to the cracks being formed, e.g. the position of the ply in the laminate (inner or outer ply), the thickness of the layer, and the relative orientations of the neighbouring plies affect crack growth and determine the amount of additional strength [11].

Few experimental studies have detailed the behaviour of plies under transverse compression in a laminate. Damage formation is similar to the case of an individual ply: when low transverse compressive stresses are acting on the ply, failure occurs at an angle α to the loading direction. Fig.2.6b shows damage in a Compact Compression (CC) specimen with a cross-ply layup. At the edge of the laminate, matrix cracks are seen to lie at $\sim 50^\circ$ to the loading direction and these microcracks are thought to induce delamination with the 0° plies by a wedge effect, described in the drawing in Fig.2.6b (see also [12]). The delamination induces a loss of support of the fibres in the 0° plies resulting in kink-band formation.

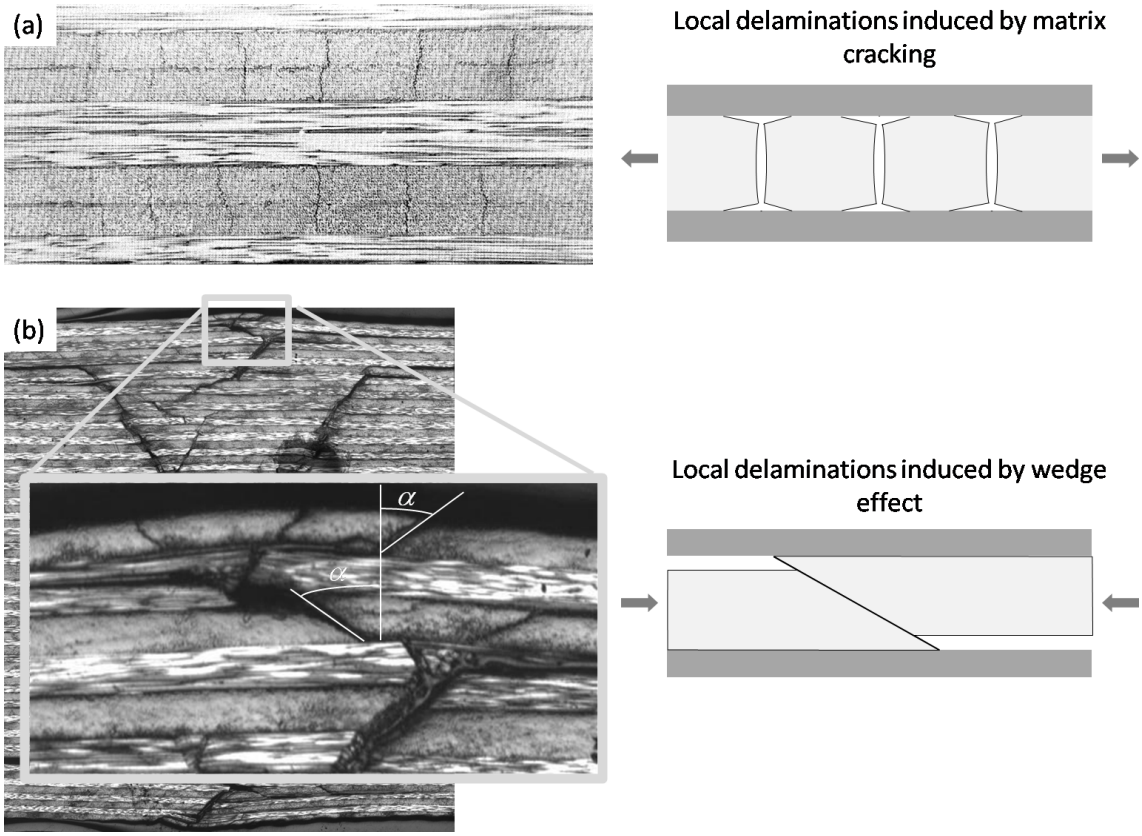


Figure 2.6: Matrix microcracking in cross-ply laminate (a) in tension [17], (b) in compression.

2.2.2 Fibre dominated failure modes

Longitudinal tension In longitudinal tension, matrix cracking and debonding of the fibre/matrix interface occur first. Final failure results from the fracture of the fibres and the strength of the ply depends strongly on the strength of the fibres. Nevertheless, the mechanical properties of the matrix can play a role on the failure processes found and on the energy dissipated. Fig. 2.7 shows the fracture surfaces of a composite failed in longitudinal tension, when the composites has (a) a brittle matrix and (b) a more ductile matrix. In Fig. 2.7a, the brittle nature of the resin is seen from the smooth aspect of the fracture surface and the river lines [13], in contrast to the large plastic deformation of the matrix in Fig. 2.7b. The yield behaviour of the matrix can have an impact on the tensile strength as it controls

the matrix-to-fibre strain transfer and reduces the stress concentration factor in the fibres at the vicinity of a fibre fracture [18]. From the micrographs in Figs 2.7a and b, it is interesting to note that in the brittle case, the crack has propagated through fibres and matrix in the same plane, while in the ductile case, the poor bond between fibre and matrix and the ductility of the matrix as resulted in significant fibre pull-out. The fracture of the interface and the friction generated during pull-out are important in dissipating energy and increase the fracture toughness of the material.

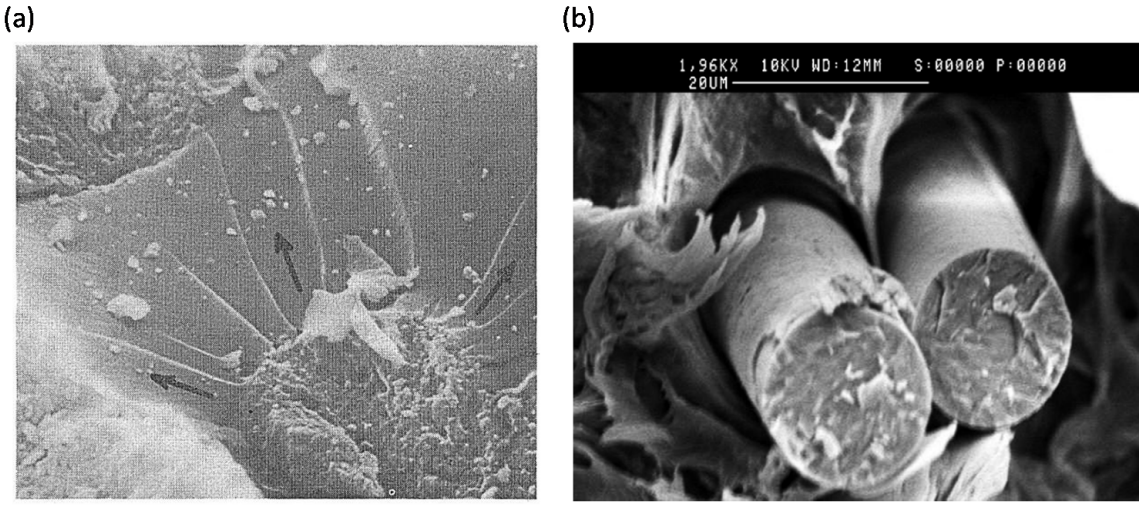


Figure 2.7: Fibre failure in FRP with (a) a brittle matrix [2], (b) a ductile matrix [3].

The increase in fracture toughness due to fibre pull-out has been reported in [19]. In this study the amount of pull-out is controlled by the layup of the laminates. Figs 2.8a and b show the fracture surfaces of a Compact Tension (CT) specimen with a $[(90_2/0)_8/90]_s$ layup (called 90° plies blocked) and a $[(90/0_2)_8/90]_s$ layup (called 0° plies blocked), respectively. When the 90° plies are blocked (a), little pull-out takes place in the 0° layers. On the contrary, the 0° blocked plies layup shows large bundles of fibre pull-out. The impact on the fracture toughness is shown in Figs 2.8c and (d). The R-curve of the specimens with 90° blocked plies is flat at $\sim$ 60kJ/m^2, while the specimens with the 0° blocked plies show a rising R-curve with a steady-state at $\sim$ 130 kJ/m^2.

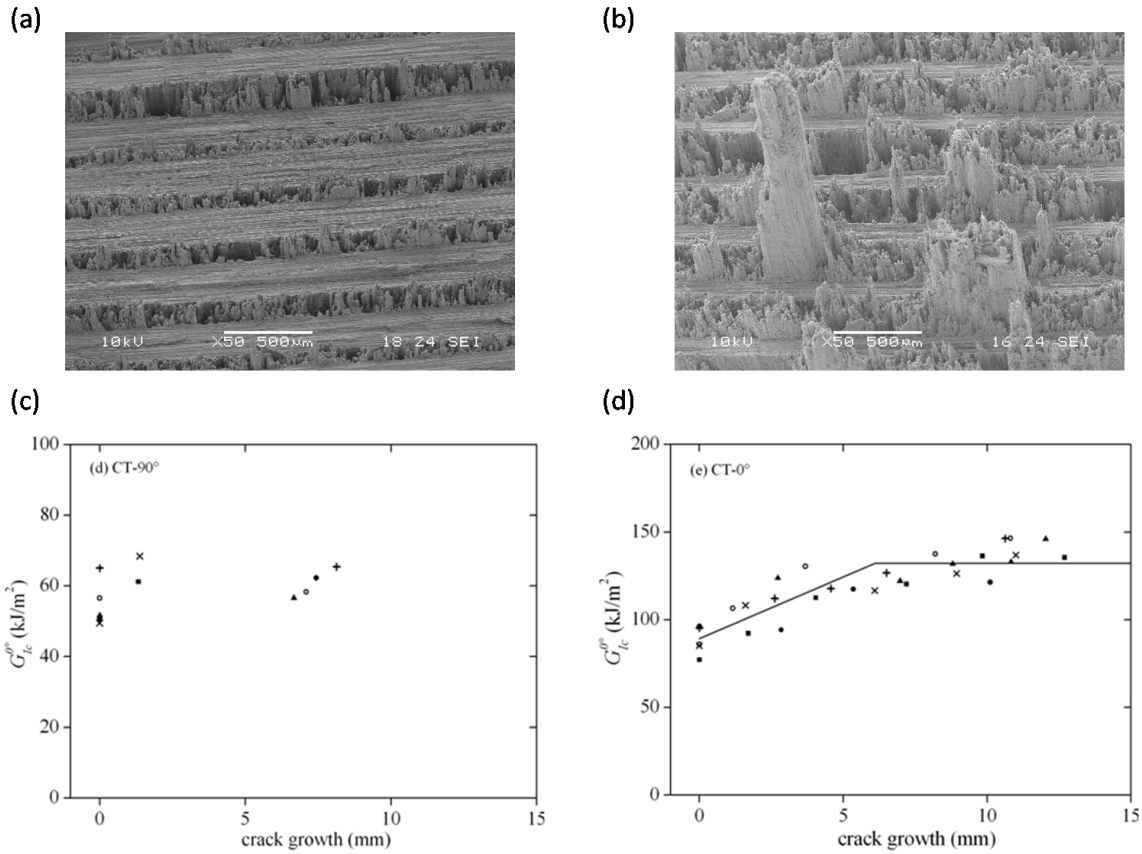


Figure 2.8: Fracture surface of CT specimens (a) 90° plies blocked: $[(90_2/0)_8/90]_s$ layup and (b) 0° plies blocked: $[(90/0_2)_8/90]_s$ layup; Corresponding R-curves for (c) 90° plies blocked and (d) 0° plies blocked [19].

Longitudinal compression In longitudinal compression, three main types of failure mechanisms are found, as shown in Fig. 2.9.

Compressive shear failure is characterised by a fracture plane oriented at 45° to the loading direction. In Fig. 2.9a and in the close-up view, a signicant amount of debris and abrasion is found on the fracture surfaces as the two crack faces slide on each other [17]. This type of failure has been observed by Ewins et al. [17] in composites with Courtaulds HM-S and HT-S (High Modulus and High Tensile strength, S is a surface treatment) carbon fibres and by Crasto and Kim [20] in AS4/PEEK and epoxy, however, because of the improved compressive strength of modern carbon fibres, compressive shear failure is not believed to occur in modern

composites as other failure modes would be triggered at lower stress level [21].

Large in-plane shear stresses, combined with the compressive loading, typically lead to splitting of the fibre/matrix interface [22, 23], Fig. 2.9b. The crack propagation along the fibre/matrix interface is very rapid. In structures where splitting occurs, the energy stored is rapidly released and can potentially lead to a catastrophic failure.

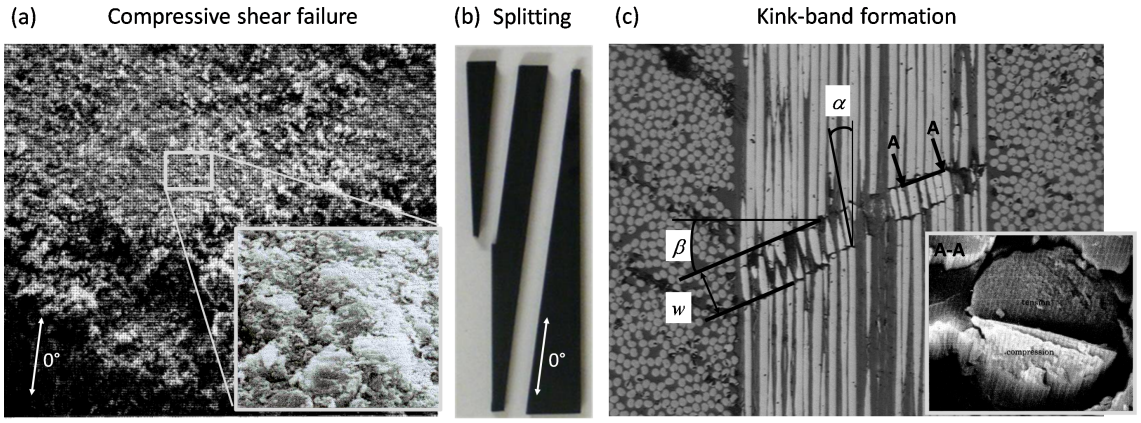


Figure 2.9: Failure modes in longitudinal compression: (a) compressive shear failure [17], (b) splitting, (c) kink-band formation [17].

A large part of the literature on longitudinal compressive failure is dedicated to kink-band formation [21, 24] as it is often recognised as the main failure mode in this loading configuration. Kink-band formation results from the rotation of initially misaligned fibres, which induces shearing of the matrix. When the shear stress in the matrix is large enough to cause failure or yielding, the fibres lose their support, resulting in further fibre rotation and failure localisation. Typical kink-band parameters such as the width w, the propagation angle β and the fibres rotation angle α (sometimes noted $\theta_0 + \theta$, with θ_0 being the initial misalignment and θ the additional rotation introduced by the compressive loading) are shown in Fig. 2.9c. Failure by kink-band formation is also found in many other engineering materials such as non-crimp fabric composites [25], wood [26], paper [27].

Obtaining experimental evidence on the failure mechanisms behind kink-band formation has proved challenging due to the unstable nature of failure and the

difficulty in observing specimens at the microscale while keeping them under load. Several studies have investigated the global / macroscopic sequence of events during kink-band initiation and propagation in single edge notched specimens ([28, 29]) or stack of paper [27]. The study by Moran et al. [28] is detailed here and a qualitative reproduction of the load versus displacement curve obtained in the experiment is given in Fig. 2.10. In the early stage of propagation, the angle β remains shallow ($\sim 10\,^\circ$), stage 2 in Fig. 2.10, and only reaches its final value of $20\,^\circ - 25\,^\circ$ after the fibres have undergone an unstable rotation to $40\,^\circ - 45\,^\circ$. Moran et al. [28] also pointed out that once the kink-band has propagated through the whole width of the specimen, stage 3 in Fig. 2.10, kink-band broadening occurs: the kink-band spreads in the fibre direction into the unkinked material, stage 4 in Fig. 2.10.

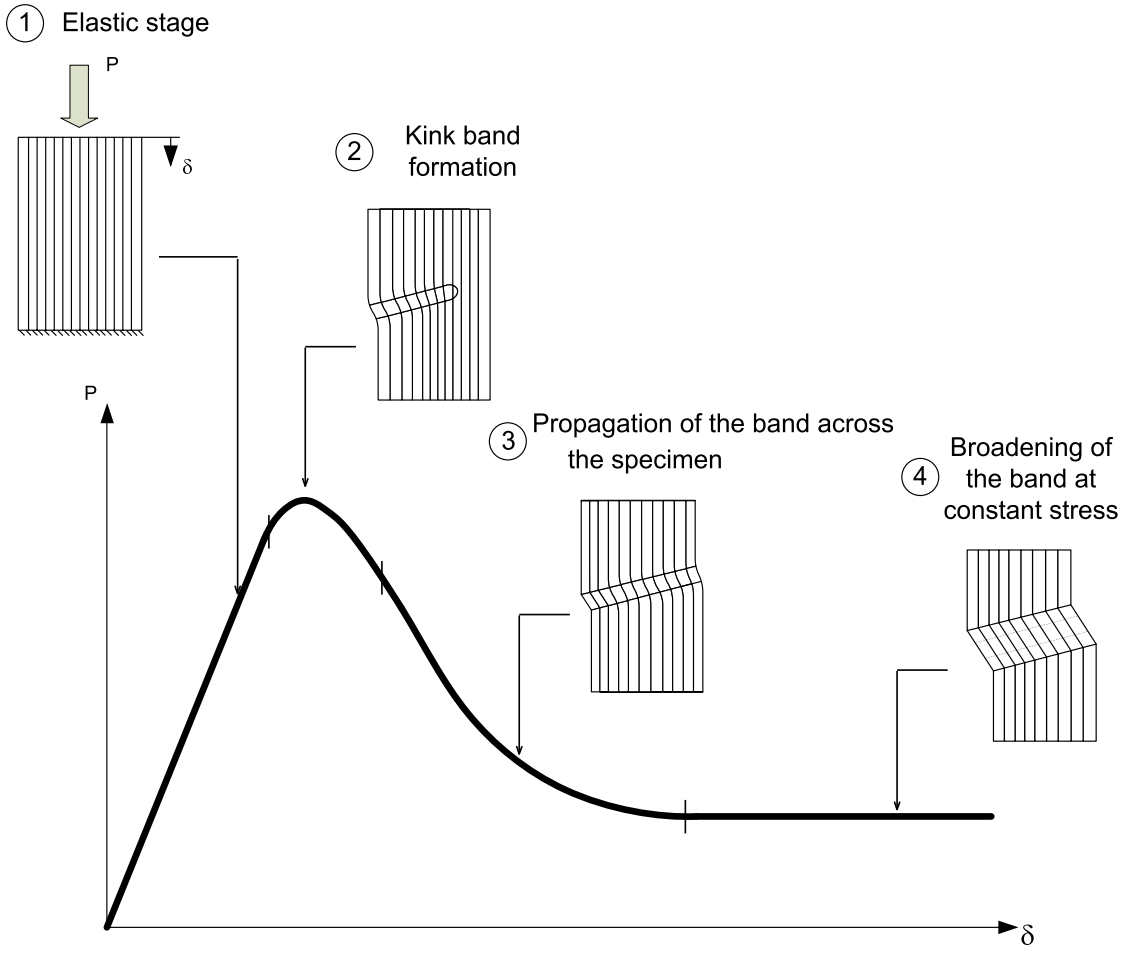


Figure 2.10: Sequence of events in kink-band formation.

Post-mortem observations made on compact compression cross-ply specimens have revealed the role of fibre / matrix splitting in kink-band formation [30]. In Fig. 2.11a and b, it can be seen that a matrix crack in the 90 ° layer (label 2) produces a loss of lateral support for the 0 ° layer. The first fibres next to the crack bend and induce matrix splitting (label 3), allowing the subsequent fibres to bend too. Fibre failures (label 1) appear first asymmetrically at two different places on opposite sides of the 0 ° layer, see Fig. 2.11a. As the occurrence of fibre failures propagate through the thickness of the 0 ° layer, the kink-band edges are defined (label 4), Fig. 2.11b, until the kink-band is fully formed, Fig. 2.11c.

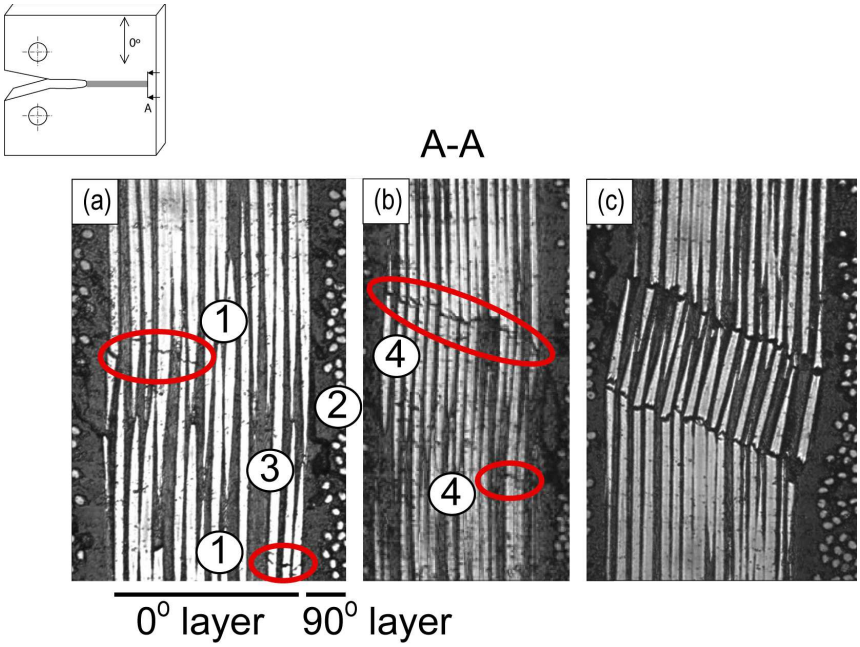


Figure 2.11: Sequence of kink-band formation from [30]. Label 1: Fibre failure; label 2: matrix crack; label 3: fibre/matrix splitting; label 4: kink-band edge.

Understanding longitudinal compressive failure is experimentally challenging due to the rapidity and often unstable nature of the mechanisms. Many micromechanical FE analyses have therefore been used to understand the role of each constituent and the significance of their material properties. FE analyses have focused on kink-band [31, 32] and have studied the role of the mechanical properties of the matrix, interface

and fibre as well as the role of the geometric imperfections (fibre misalignment: amplitude and distribution).

Using the unit cell model shown in Fig. 2.12a, Guynn et al. [32] showed that for a matrix with a linear elastic response, perfectly bonded to the fibres, kink-band do not form and the initially misaligned model deforms only linearly. With a nonlinear response of the matrix, kink-bands appear when the matrix starts yielding and the compressive strength depends on the yield strength of the matrix.

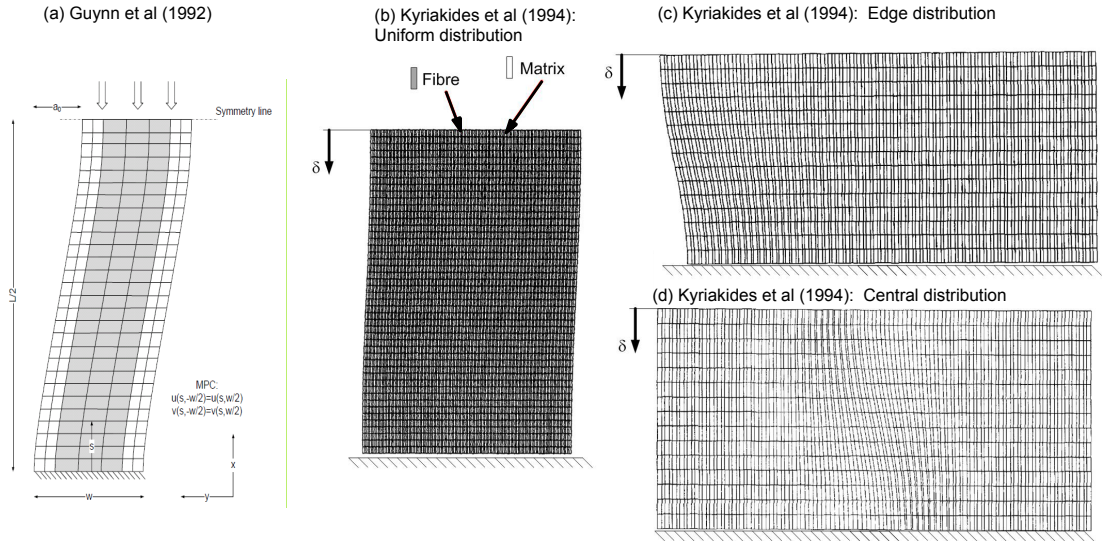


Figure 2.12: (a) FE model used by Guynn et al. [32]; FE models for kink-bands analysis [31] (b) Array of fibre/matrix with uniform sinusoidal imperfection; (c) with sinusoidal imperfection at one edge and straight fibres at the opposite edge; (d) with centrally located sinusoidal imperfection.

The role of the interface has also been investigated by Guynn et al. [32]. Centrally located split (zone of maximum shear stress) or two splits located at the edge of the model (line of symmetry) are inserted between fibre and matrix. Because these splits deprive completely the fibres from the support of the matrix, a compressive strength reduction up to 60% is reported for a centrally located split with a length of 10% of the length of the whole model.

Fibre waviness, often introduced during the manufacturing process, has been found to have a detrimental effect on the longitudinal compressive strength [21, 33, 34]. Based on microscopic observations of fibre waviness in representative samples, Kyriakides et al. [31] proposed the FE models shown in Fig. 2.12b-d, with an initial fibre imperfection in the form of a sinusoidal wave and different amplitude distributions. The fibres are linear elastic and the matrix has an elasto-plastic response. The load versus displacement curve of the models show nonlinearities at matrix yielding followed by a peak load when the kink-band is formed. This peak load is taken as the compressive strength.

Kyriakides et al. [31] find that the compressive strength is reduced by 40% when the amplitude is multiplied by three. Using the models in Figs 2.12c and d, it is found that the location of the misalignment: edge distribution (Fig. 2.12c) or central distribution (Fig. 2.12d) has only minor effects on the compressive strength. On the other hand, the proportion of misaligned fibres plays an important role with a 50% decrease in the compressive strength when the proportion of misaligned fibres is increased from 50% to 100%. It is also noted in [31] that the width w and kink-band angle β are only slightly affected by the location and magnitude of the imperfection.

Multi-axial testing Combining other stress components, e.g. hydrostatic pressure or in-plane shear, with the compressive stress has an effect on the failure modes triggered.

The effect of hydrostatic pressure has been studied by Oguni et al. [35] and Parry and Wronsky [36]. They found that for the specimens under atmospheric pressure, failure is by longitudinal splitting which, in some cases, prompt kink-band formation. Under hydrostatic pressure, only kink-bands and eventually complementary kink-bands are observed but longitudinal splitting is totally suppressed. They also note that when the failure mode shifts from splitting/kinking to pure kinking, the longitudinal compressive strength increases faster with the hydrostatic pressure.

Combined compression and shear loading experiments have been carried out by several research groups [22, 23, 37, 38] using torsion compression tubes. Significant scatter is typical in these tests and the trends reported for the failure envelopes differ

for each group. The general shape of the failure envelope is discussed later in the review, but in most cases it appears that in a first region, for low shear stresses, the longitudinal compressive strength is only slightly reduced, and in a second region, for larger shear stresses, the compressive strength decreases more rapidly. The limit between these two regions varies between the experiments and is difficult to relate to a specific failure mode as they are not always reported.

A change from kink-band formation to splitting is reported in Fleck et al. [22]: kinking occurred in all cases except for pure shear ($\sigma_1 = 0, \tau_{12} = S$). In Mannigel [23], kinking is found for compressive stresses $\sigma_1/X_c < -0.6$, a transition region where either splitting or kinking takes place is observed between $-0.6 < \sigma_1/X_c < -0.5$ and splitting occurs for $\sigma_1/X_c > -0.5$.

2.3 Acoustic Emission

To control and quantify the structural integrity of components, Non-Destructive Testing and Evaluation (NDT & E) equipments can be used. Traditional NDT methods are X-Ray, C-Scan, microscopy, ultrasound. However, none of these techniques can be used to monitor damage evolution on-line, i.e. in service or during a test. To this end, a method based on the stress waves emitted during damage initiation and propagation has been developed.

This technique, called Acoustic Emission (AE), has been used for metallic structures since the early 70's. Its development for composite materials is more recent and made more complex by the heterogeneity of the material. However, the range of application is already quite wide from the academic use to industrial applications such as pipe leak inspections, structural integrity test on full-scale aircraft or race cars.

2.3.1 Principles

During damage formation, part of the elastic energy is released and is dissipated by the creation of new crack surfaces, yielding at the crack tip and generation of elastic waves, which is the source of acoustic emission. The waves traveling within the

material induce displacements which are detected by piezoelectric sensors attached onto the surface of a specimen or structure.

A typical AE waveform is shown in Fig. 2.13 with the definition of some parameters commonly used in AE analysis:

- Peak Amplitude (A): Maximum amplitude in dB.
- Rise Time (RT): Time elapsed between the first threshold crossing and the peak amplitude (μs).
- Duration (D): Time elapsed between the first and last threshold crossing (μs).
- Ring Down Count (RDC): Number of threshold crossings.

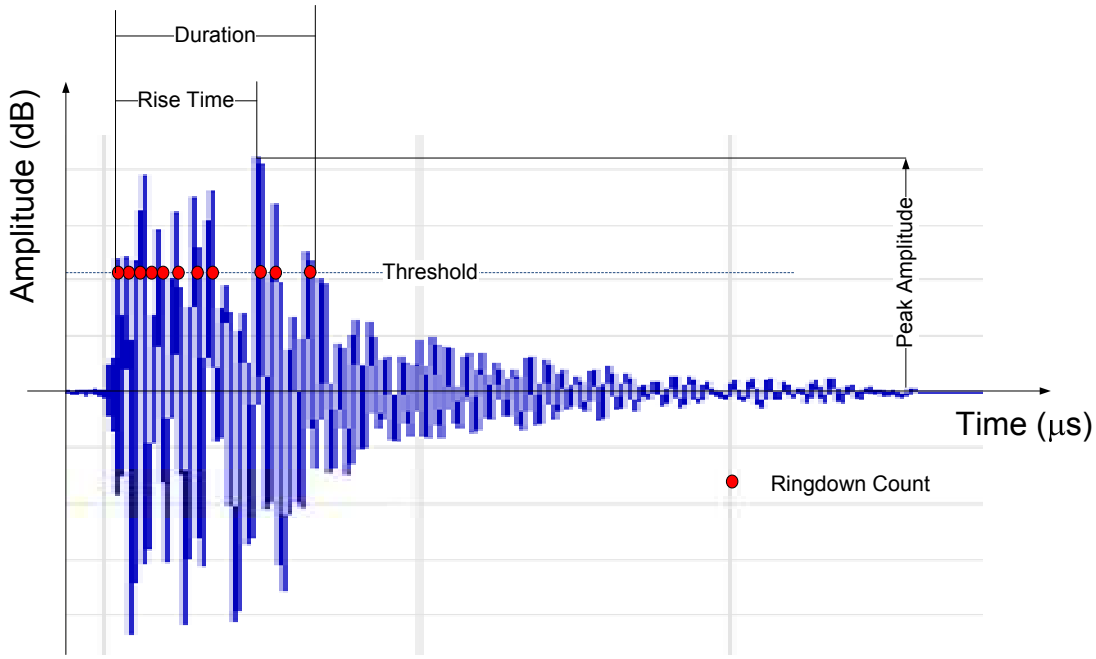


Figure 2.13: AE waveform with some relevant parameters.

Because damage detection using AE does not require external power sources, on the contrary to other NDT techniques as for example ultrasonic method where

waves have to be generated, AE is sometimes said to be a passive NDT method. AE is also non-invasive as it does not need a solution to enhance the signal (on the contrary to, for example, X-Ray). Because of these and because AE techniques are able to give an instantaneous knowledge of the location and intensity of damages occurring in a structure, AE is a very attractive candidate for application such as Structural Health Monitoring (SHM) (see [39]). Some of the factors preventing a wider use are related to the hardware—sensors—or the quality of the detection in noisy environment.

Two different types of sensors are commercially available: resonant and broadband sensors. The resonant sensors have an increased sensitivity in a narrow frequency band. They are mainly used in industrial applications where the frequency range of events to be detected is known beforehand. In this frequency range, resonant sensors offer a greater accuracy and reduce the background noise. The broadband sensors have a fairly constant response over a wide frequency range. They are preferred for research use, where the frequencies of the phenomenon under study are unknown.

Due to their narrowband operation, resonant sensors have been found to introduce signal distortion [40]: the sharpness of the high frequency peaks is damped and the low frequencies suffer amplitude attenuation. For the same reason, the broadband sensors are preferred for frequency studies.

Several types of noise can arise during a test: background noise, electromagnetic interference (EMI) and noise from the test machine grips. A threshold system is typically used during recording to suppress regular background noise. EMI can either be removed during post-processing as they have singular characteristics (same arrival time at each sensor, high frequency, no propagation effect, no plate wave characteristics [41]) or by using differential sensors (sensors equipped with two crystals) [42]. Finally, noises arising from the gripping part/interface are identified and removed from location plots.

2.3.2 Damage detection in composite materials using Acoustic Emission

Fig. 2.14 shows the typical chain of acquisition, processing and identification of damage mechanisms in composite materials. The wave emitted during damage formation travels through the material and can be affected by some distortions (e.g. attenuation, reverberation, etc.) and possibly interact with waves emitted from simultaneous damage formation. Once detected, the waveforms are stored then filtered and passed into processing modules. From the processing tools relevant parameters are extracted and passed to identification or classification tools, which eventually return an identification of the AE signatures with the damage processes.

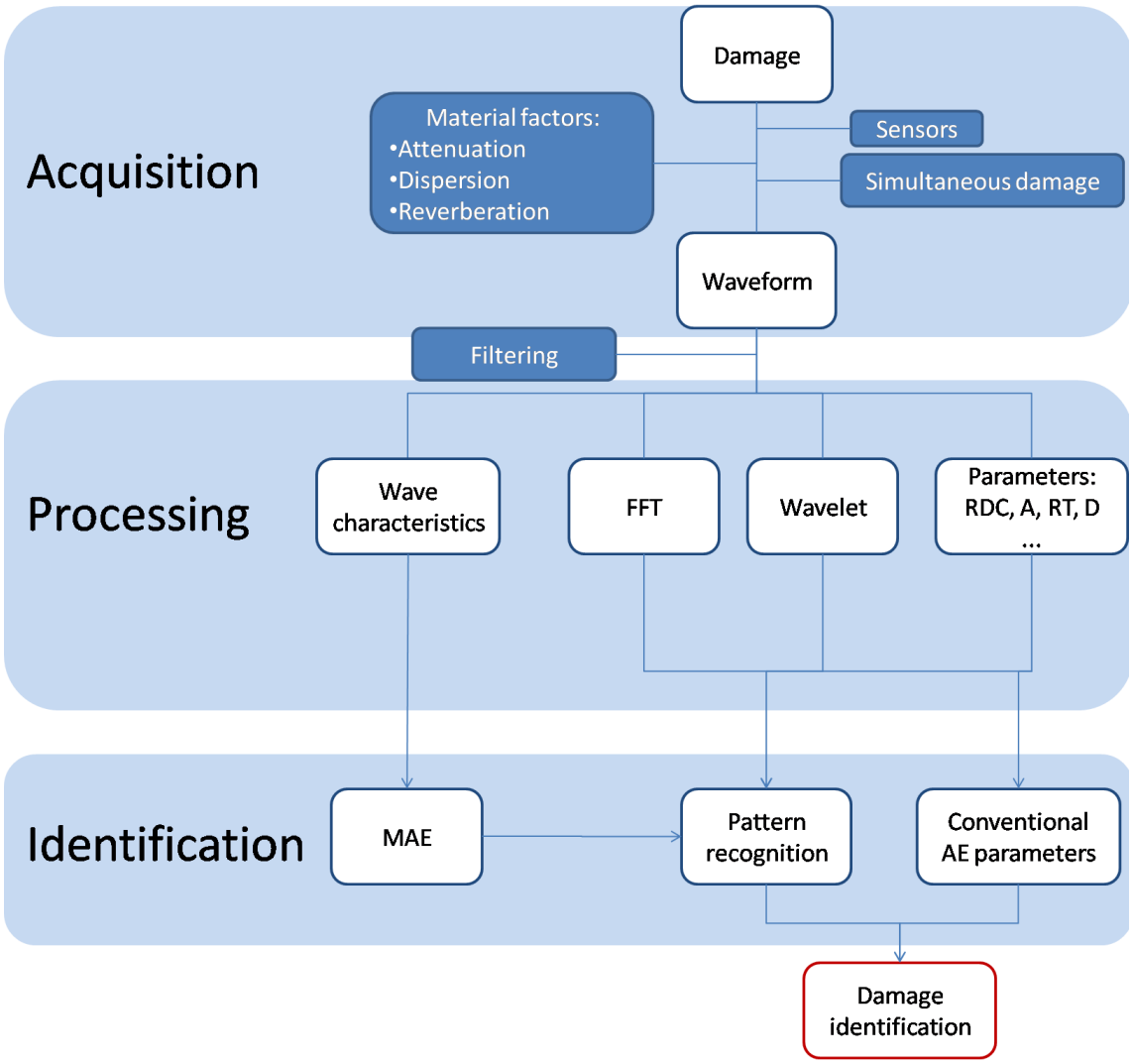


Figure 2.14: Acquisition, processing and classification of AE waveforms.

In the literature [43–45], AE databases are typically built from signals recorded during tensile tests of various ply orientations and lay-ups to give rise to specific failure modes. Three main techniques are used to characterise AE signals: (i) classification according to a single parameter, typically amplitude, frequency or wavelet level, and referred to as conventional AE analysis, (ii) classification according to several parameters using pattern recognition techniques and (iii) classification after examination of the extensional and flexural mode content, referred to as Modal Acoustic Emission (MAE).

2.3.2.1 Conventional AE analysis

A large body of literature can be found on amplitude based classification [44, 46–48], a summary is proposed in Fig. 2.15. A general trend is to associate low amplitude events with matrix cracking, intermediate amplitudes with delamination, debonding or fibre pull-out and high amplitudes with fibre failure. However, some studies reveal contradictory amplitude ranges for the failure modes observed. Longitudinal matrix microcracking is characterised by high amplitude signals and fibre fracture corresponds to low amplitude events in [43] while high amplitude signals are associated with fibre failure and low amplitude signals correspond to transverse/longitudinal matrix cracking and delamination according to [44]. Ni and Iwamoto [49] show that the amplitude of AE signals is greatly affected by sensor distance, and conclude that the peak frequency of AE signals—which is not affected by sensor distance—is a more reliable characteristic.

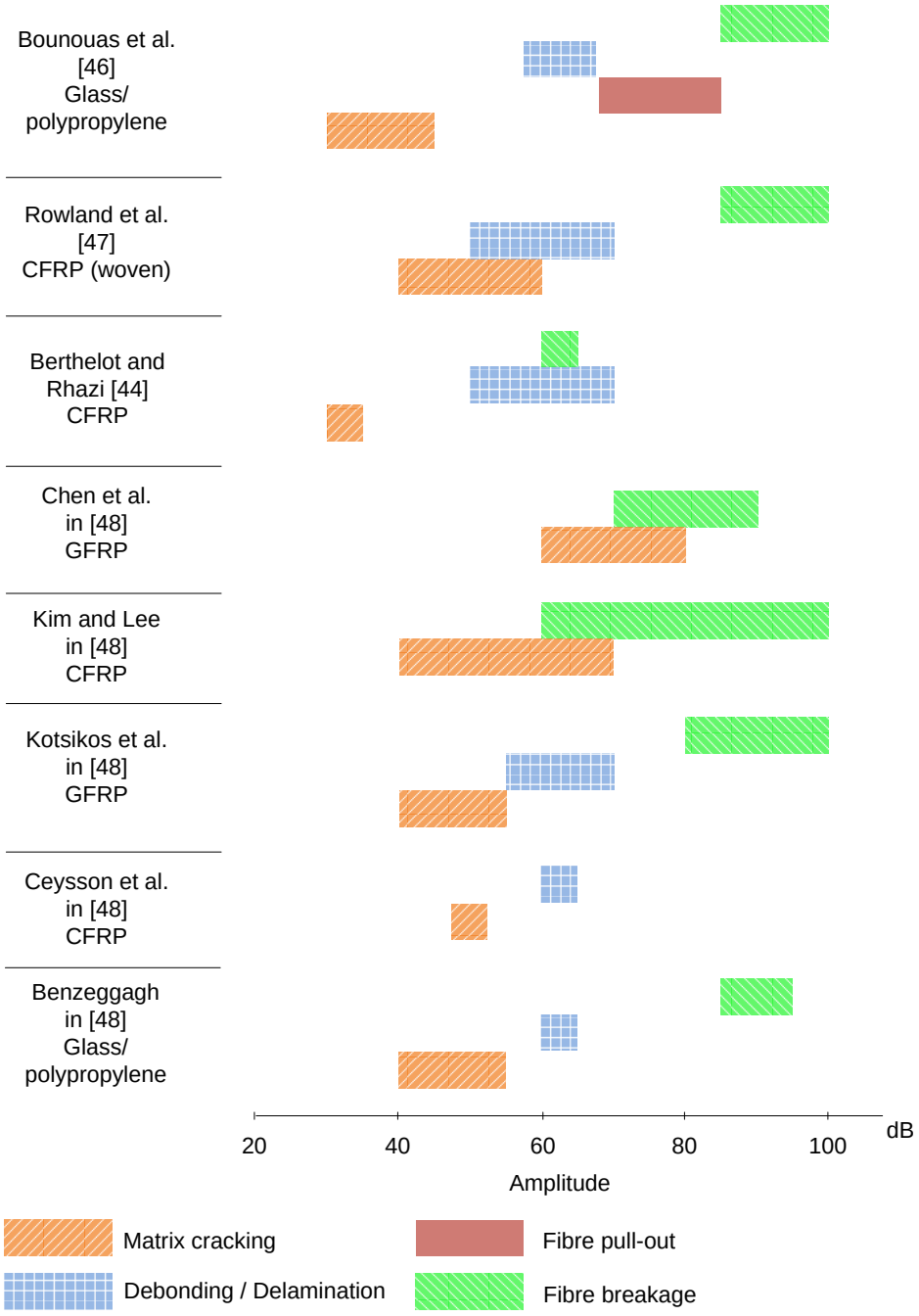


Figure 2.15: Failure modes classification using amplitude analysis: summary of the literature.

Frequency analyses rely on decomposing AE signals into their power spectra via the Fourier or fast Fourier transform (FFT), e.g. using Eq. (2.1). The power spectrum represents a unique signature of the signals, but often only the peak frequency

is used for classification. A summary of the classifications reported in the literature [3, 50] is given in Fig. 2.16.

$$\text{Fourier coefficients: } c_k = \sum_{n=0}^{N-1} f(n) e^{-ik\omega_0 n}. \tag{2.1}$$

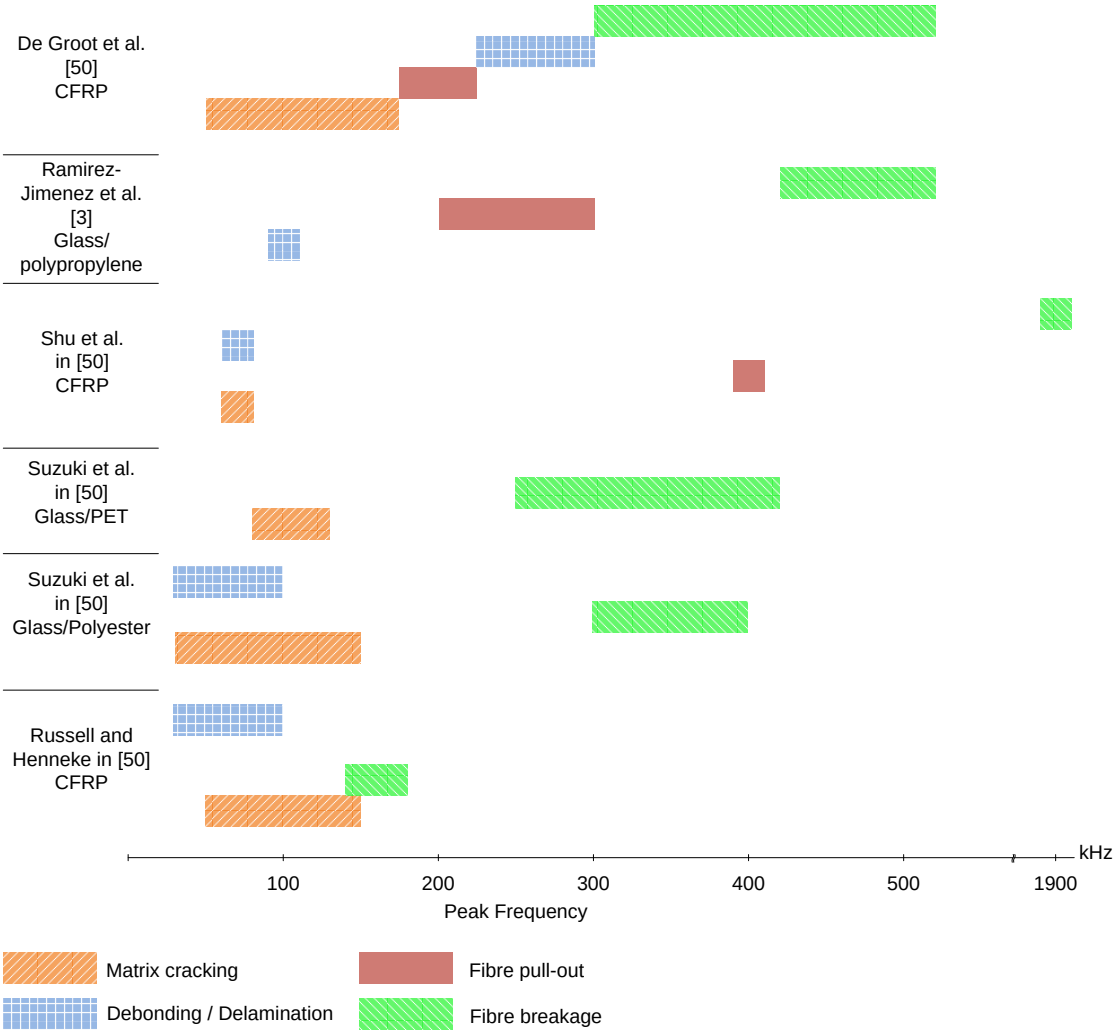


Figure 2.16: Failure modes classification using frequency analysis: summary of the literature.

A general trend is to associate low frequency events with matrix cracking, high frequency events with fibre failure and signals for delamination correspond to either low or intermediate frequency range.

However, AE signals are non-stationary and non-periodic and the selection of the time window (k in Eq. (2.1)) can be ambiguous. For this reason, the Wavelet Transform (WT) has been applied for the study of AE signals [51]. The Discrete Wavelet Transform (DWT) is a signal processing method in which a signal is decomposed into shifted and scaled versions of an original wavelet [52]. During one level of decomposition, the original signal passes through high- and low-pass filters so that approximation and detail coefficients are extracted from each filter, respectively and as seen in Fig. 2.17. The approximations correspond to the high scale, low frequency components of the signal while the details correspond to the low scale, high frequency components.

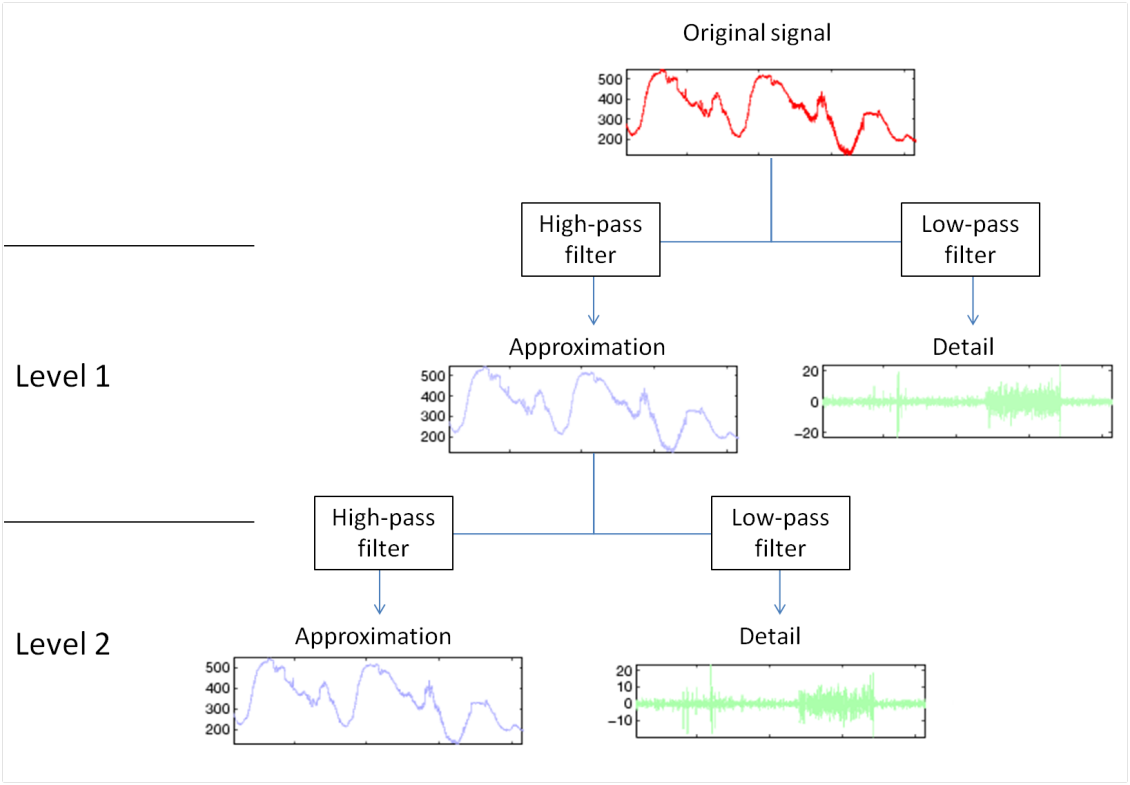


Figure 2.17: Principle of wavelet decomposition.

Using the DWT, AE signals are classified based on the energy contained in each level [51, 53]. The classification based on energy content give noisy result graphs where patterns are difficult to extract. More recently, the DWT has been used in

the framework of pattern recognition [54] and has shown encouraging results, as discussed in the next paragraph.

2.3.2.2 Pattern recognition and multivariable analysis

Pattern recognition techniques rely on the classification of several parameters (rise times, amplitudes etc.) into clusters forming patterns and identification of these clusters with failure processes. These techniques are either supervised or unsupervised. In the supervised case, the algorithm associates input signals to a given class or cluster after having seen a number of training labeled examples. On the contrary, unsupervised techniques seek for patterns in the data structure without having been presented with a training set.

Unsupervised pattern recognition Several types of algorithms can be used for unsupervised pattern recognition: k-means, fuzzy C-means, Self Organising Map (SOM) and Competitive Neural Network (CNN). These algorithms are described in the following paragraphs and the concept of Principal Component Analysis (PCA), which aims at reducing the dimension of the input vectors, is also introduced (technical details about the algorithms are reported to Chapter 3).

k-means The k-means algorithm is a clustering method aiming at partitioning n input vectors into k clusters. Each input vector is allocated to the cluster with the nearest mean. If one considers a set of n input vectors $(x_1, x_2, ..., x_n)$, the k-means algorithm partitions the n input vectors into k clusters $(C_1, C_2, ..., C_k)$ so as to minimize the within-cluster sum of squares

$$\sum_{i=1}^{k} \sum_{x_j \in C_i} \|x_j - c_i\|^2 , \tag{2.2}$$

where c_i is the center of the cluster C_i. The k-means algorithm is a robust and efficient method for data clustering but its accuracy is dependent on the initial starting conditions. To mitigate this, a global k-means algorithm—with multiple restarts–can be used [52].

fuzzy C-means Fuzzy C-means and k-means algorithm are very similar, with the exception that in the fuzzy C-means each vector has a degree of belonging to clusters, while in the k-means each point belong to only one cluster. The degree of belonging is typically calculated as the inverse of the distance to the cluster center, so that a point at the boundary of a cluster is in the cluster to a lesser degree than a point at the center of cluster [52].

CNN Competitive Neural Networks (CNN) are unsupervised artificial neural networks where the most similar neuron to an input vector is modified so that it becomes even more similar to the input [52].

SOM The Self Organising Map (SOM) [55] is an artificial neural network where neighbouring neurons compete and develop through mutual interaction to recognise patterns in a given set of data. In one way, the SOM can be seen as a competitive neural network, since the most similar neuron to an input vector is modified so that it becomes even more similar. However, it also exhibits cooperative learning as not only the most similar neuron is modified, but its neighbours on the map are also moved towards the input vector.

Besides its pattern recognition feature, the SOM is also a vector projection method as each neuron has two positions: one in the input space, where the neurons have the same dimensions as the input vectors, and another position in the output space, typically the 2D space of the map [56].

PCA The PCA is a method to reduce the dimension of the input (parameters) vector to a smaller number, according to the maximum variance of the input. This reduces the number of correlated variables into a smaller number of uncorrelated variables. An example is shown in Fig. 2.18 where the two dimensional input vector is reduced to one dimension. This method is often used before pattern recognition algorithm as it improves the computational efficiency.

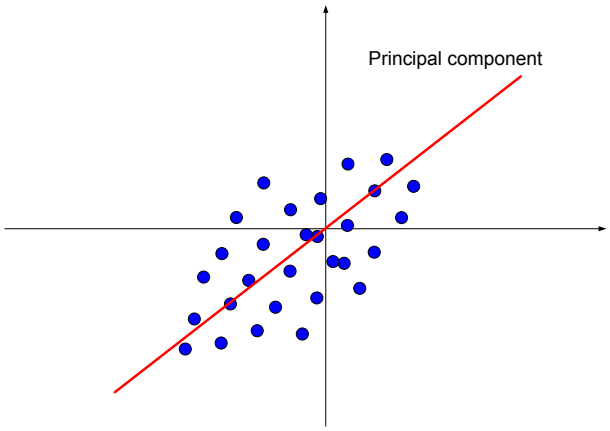


Figure 2.18: Principal Component Analysis (PCA) principle.

A combination of the Kohonen's SOM and the k-means algorithm has been used in [57, 58]. The Kohonen's SOM is used to reduce the dimension of the input vectors (similarly to a PCA). For example in [58], 4243 signals are recorded from a test on a cross-ply laminate in tension and each signal is characterised by 14 parameters, the size of the problem is then 4243×14. The SOM receives the 4243×14 matrix as an input and outputs a 45×29 map, which corresponds to 1305 neurons, and the size is reduced to 1305×2. The map obtained is then clustered using the k-means algorithm. This approach is usually computationally more effective and the results are comparable to those obtained from using directly the data (without reducing the dimension of the input vectors) [59].

Following a similar approach, Marec et al. [54] used PCA before clustering the principal components with the fuzzy C-means approach. Parameters extracted by wavelet transform have also been used and the results compared to an analysis using conventional parameters. Their findings indicate that reducing the dimension of the input space (using the PCA) before clustering improved the results. The parameters extracted using the wavelet decomposition have also proved to be more relevant.

Supervised pattern recognition

k-NN The k-Nearest Neighbours (k-NN) algorithm is a supervised pattern recognition technique where new signals are compared to a number k of neighbouring signals (already sorted) and assigned to the cluster in which most of its neighbours are. This method is schematically represented in Fig. 2.19.

Supervised pattern recognition techniques often follow manual or unsupervised classification as shown in Fig. 2.19. A combination of the k-means and k-NN algorithm has been used in Godin et al. [45] to study failure in pure resin and glass-epoxy. Two failure mechanisms have been identified: matrix cracking and interfacial decohesion. The results have been compared to a technique using only the unsupervised SOM algorithm and a good agreement have been found between the two.

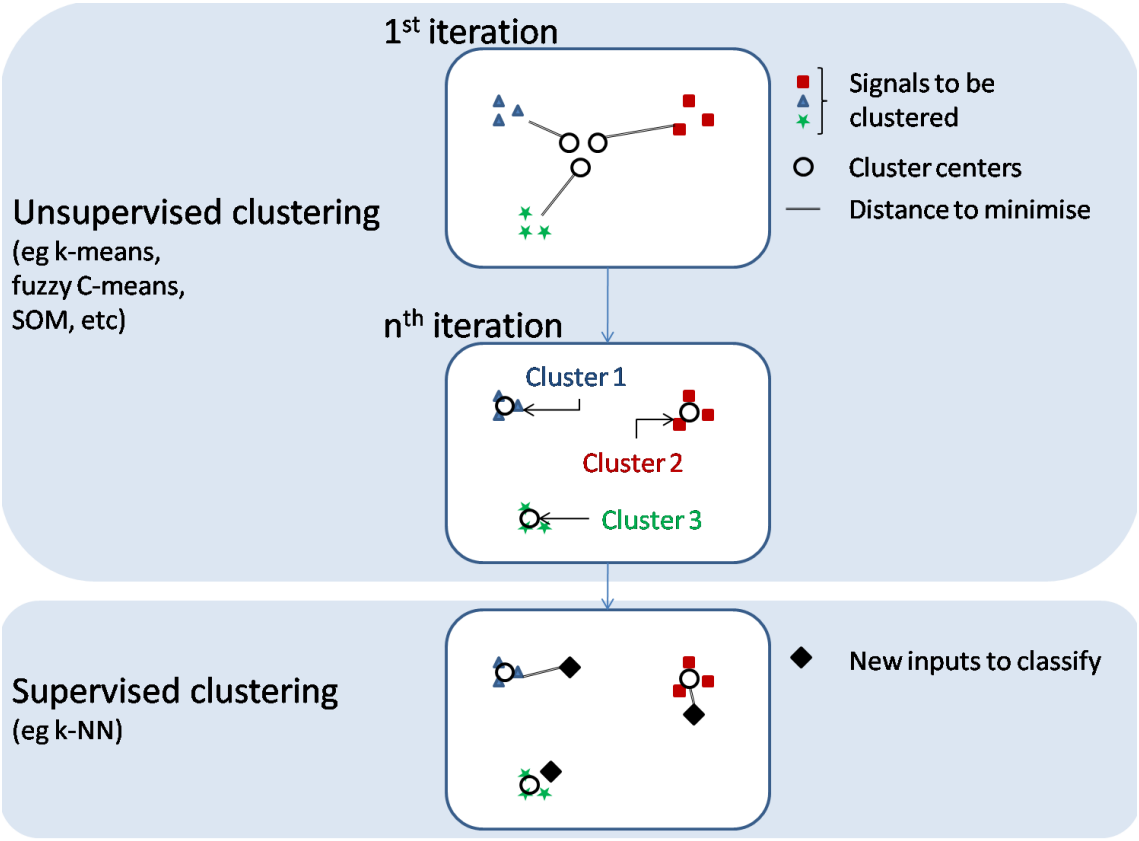


Figure 2.19: Typical procedure for supervised pattern recognition.

An interesting use of the PCA combined with the k-NN algorithm is presented

in [60]. The whole waveforms, recorded during uniaxial tests on glass-epoxy laminates with different lay-ups, are used as an input to the PCA (the waveforms are discretized in 140 points), and clusters are identified in the two first principal components. New signals are classified using the k-NN algorithm. The classification of several types of matrix cracking and local delamination is achieved and shows good agreement with a manual classification.

2.3.2.3 Modal acoustic emission

The identification of failure mechanisms can be based on the study of the wave modes contained in the AE waveforms: extensional or flexural mode content. Each mode shows specific characteristics—the extensional mode is symmetric and non-dispersive, while the flexural mode is antisymmetric and dispersive—which can be identified by looking at the waveforms. Gorman [40] and later on Surgeon and Wevers [41] suggested a discrimination process based on this decomposition and on the characteristics of the two modes.

Identification of matrix and fibre failure, in carbon epoxy cross-ply ($[0, 90_3]_S$ and $[0_2, 90_2]_S$) laminates loaded in tension, has been reported in Surgeon and Wevers [41]. Fibre failure is characterised by a high flexural content and matrix failure by a high extensional content. This method was also used by Johnson and Gudmundson [61] to locate matrix cracking through the thickness of a cross-ply GFRP: a crack in the central layer generates an extensional wave, while a crack in the outer layers generate a flexural wave.

2.4 Modelling: current failure models and criteria

This section describes several analytical and numerical modelling approaches for failure in laminated composites. The term failure models includes both failure criteria—which identify failure initiation—and treatment of the post-failure initiation behaviour (propagation).

2.4.1 Failure criteria

Composites have often been dealt with as "black metal", and some of the first failure theories developed for composites have been inspired by those existing in metals. Limit criteria (maximum stress, strain), polynomial criteria (Tsai-Wu, Tsai-Hill) are good examples of this. It is not until the 70's-80's that failure criteria taking into account the specificities of composites have been developed, and are referred to as physically based criteria [62].

2.4.1.1 Limit criteria

The maximum stress criterion The maximum stress criterion relies on the knowledge of the uniaxial strength of a UD ply. Failure initiation is predicted when one of the following condition is verified

$$\frac{\sigma_1}{X_t} = 1 \text{ for } \sigma_1 > 0 \text{ and } \frac{|\sigma_1|}{X_c} = 1 \text{ for } \sigma_1 < 0, \tag{2.3}$$

$$\frac{\sigma_2}{Y_t} = 1 \text{ for } \sigma_2 > 0 \text{ and } \frac{|\sigma_2|}{Y_c} = 1 \text{ for } \sigma_2 < 0, \tag{2.4}$$

$$\frac{|\tau_{12}|}{S} = 1, \tag{2.5}$$

where σ_1, σ_2 and τ_{12} are the ply normal and shear stress components, X_t, X_c are the longitudinal strengths in tension and compression, Y_t, Y_c are the transverse strengths in tension and compression and S the in-plane shear strength.

The wide application of this criterion derives from its simplicity. Evaluation in complex structures, with different ply orientations, only required stress analysis to find the components in the natural coordinate system, and a ply by ply comparison, which can be readily achieved by numerical methods. A major drawback is the lack of interaction between the stress components which is typically observed in the experiments.

The maximum strain criterion The maximum strain criterion is very similar to the maximum stress criterion as it relies only on the knowledge of the uniaxial

strain to failure of a UD ply. Failure initiation is predicted when one of the following condition is verified

$$\frac{\varepsilon_1}{\varepsilon_{1t}^u} = 1 \text{ for } \varepsilon_1 > 0 \text{ and } \frac{|\varepsilon_1|}{\varepsilon_{1c}^u} = 1 \text{ for } \varepsilon_1 < 0, \tag{2.6}$$

$$\frac{\varepsilon_2}{\varepsilon_{2t}^u} = 1 \text{ for } \varepsilon_2 > 0 \text{ and } \frac{|\varepsilon_2|}{\varepsilon_{2c}^u} = 1 \text{ for } \varepsilon_2 < 0, \tag{2.7}$$

$$\frac{|\gamma_{12}|}{\gamma_{12}^u} = 1, \tag{2.8}$$

where ε_1, ε_2 and γ_{12} are the ply normal and shear strain components, ε_{1t}^u, ε_{1c}^u are the longitudinal strains at failure in tension and compression, ε_{2t}^u, ε_{2c}^u are the transverse strains at failure in tension and compression and γ_{12}^u the in-plane shear strain at failure.

2.4.2 Polynomial criteria

Polynomial criteria used for composites have been adapted from the ones used for metals and have been modified to describe the anisotropic behaviour of composites.

2.4.2.1 Tsai-Hill quadratic failure criterion

For instance, the Tsai-Hill criterion is a direct adaptation of the classic von Mises yield criterion ([63, 64]). The first modification have been made by Hill so that the criterion could apply to ductile, anisotropic materials. Tsai adapted it further to orthotropic materials and such as the different behaviours in tension and compression are taken into account [64]. For a case of plane stress the criterion reads

$$\frac{\sigma_1^2}{X^2} - \frac{\sigma_1\sigma_2}{X^2} + \frac{\sigma_2^2}{Y^2} + \frac{\tau_{12}^2}{S^2} = 1, \tag{2.9}$$

with

$$X = X_t \text{ for } \sigma_1 > 0 \text{ and } X = -X_c \text{ for } \sigma_1 < 0, \tag{2.10}$$

$$Y = Y_t \text{ for } \sigma_2 > 0 \text{ and } Y = -Y_c \text{ for } \sigma_2 < 0, \tag{2.11}$$

and so that the material properties needed are only measured from standard uniaxial tests.

2.4.2.2 Tsai-Wu quadratic failure criterion

A more general form of the Tsai-Hill criterion has been proposed by Tsai and Wu [65]

$$\frac{\sigma_1^2}{X_t X_c} + \frac{\sigma_2^2}{Y_t Y_c} + \frac{\tau_{12}^2}{S^2} + 2F_{12}\sigma_1\sigma_2 + \frac{\sigma_1}{X_t} - \frac{\sigma_1}{X_c} + \frac{\sigma_2}{Y_t} - \frac{\sigma_2}{Y_c} = 1. \tag{2.12}$$

Because of the term F_{12}, the Tsai-Wu criterion requires biaxial test data, which are difficult to obtain.

A variant of the Tsai-Hill criterion proposed by Yamada and Sun [66] is given in Eq. (2.13). In this formulation, it is assumed that failure of a laminate is effective when it occurs in the fibre direction, and the transverse stiffness and stress are neglected.

$$\left(\frac{\sigma_1}{X}\right)^2 + \left(\frac{\tau_{12}}{S^{is}}\right)^2 = 1. \tag{2.13}$$

S^{is}, the in-situ shear strength, is introduced to reflect the higher strength of an embedded ply observed experimentally and mentioned in the first part of the review.

2.4.3 Physically based criteria

Criteria are physically based when each failure mode is described by a specific equation. For example, in Hashin and Rotem [62], who proposed the first physically based criteria, a criterion is assigned for each of the four failure modes considered: fibre tension, fibre compression, matrix tension and matrix compression. While limit and polynomial criteria can already account for the directionality of failure, physically based criteria also consider its nature. However, the term physically based does not always mean that the criterion for a given failure mode is developed on physical considerations, and often a combination of limit, polynomial, empirical and truly physically based criteria are used in this framework.

2.4.3.1 Fibre failure

Tension Fibre failure in tension is often described by the maximum stress criterion [62, 67, 68]

$$\frac{\sigma_1}{X_t} = 1. \tag{2.14}$$

In longitudinal tension, the matrix has an effect on the toughening mechanisms, see first section of the review, but is not believed to affect failure initiation. Another motivation for the choice of Eq. (2.14) comes from experimental observations as shown in Fig. 2.20. Only the experimental data points lying between 1250 MPa $\leq \sigma_1 \leq$ 1600 MPa correspond to fibre failure, and the longitudinal tensile strength of these samples do not appear to be affected by the shear stresses.

A criterion with a quadratic interaction between tensile longitudinal stress and in-plane shear is proposed in [69] (as cited in [70])

$$\left(\frac{\sigma_1}{X_t}\right)^2 + \left(\frac{\tau_{12}}{S}\right)^2 = 1 \text{ for } \sigma_1 \geq 0. \tag{2.15}$$

The criterion in Eq. (2.15) is similar to the Tsai-Hill criterion (Eq. (2.9)) and to the Yamada and Sun criterion (Eq. (2.13)) for this load case.

In the fibre failure dominated region 1250 MPa $\leq \sigma_1 \leq$ 1600 MPa, the maximum stress criterion appears to perform best as the strength is not affected by shear stresses. The other criteria predict a decrease in strength at lower shear levels than the ones measured, resulting in more conservative failure envelopes.

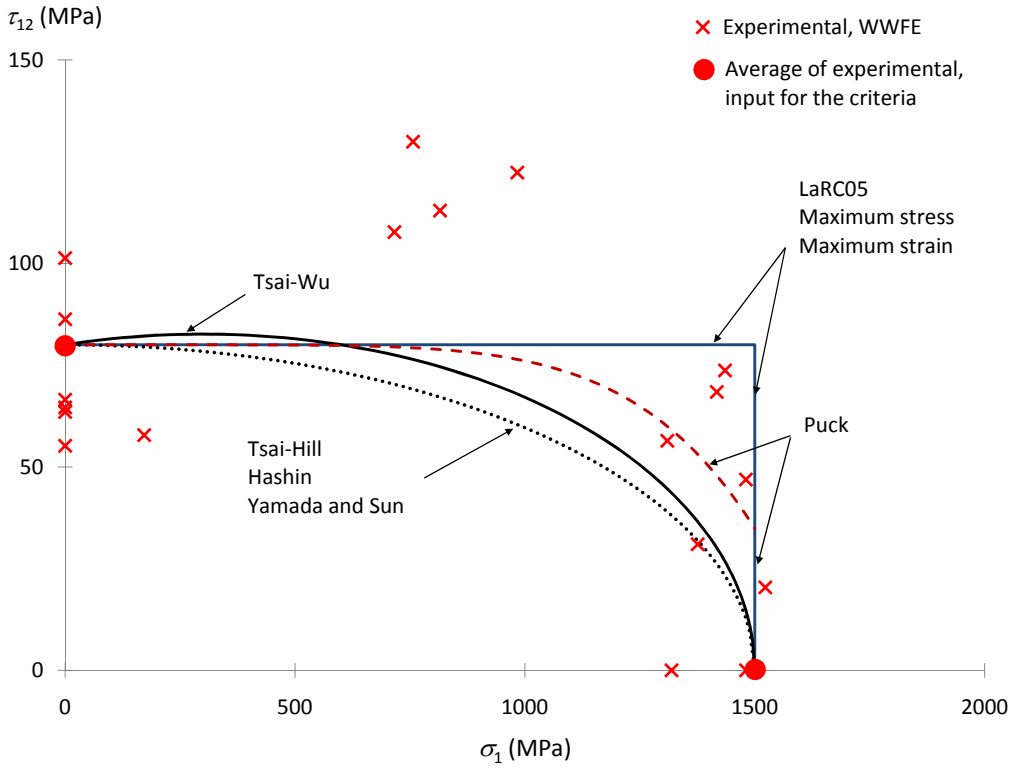


Figure 2.20: Longitudinal tension versus in-plane shear failure envelopes for the criteria described in this section and experimental data from [37].

Compression Fig. 2.21 shows the failure envelopes for combined longitudinal compression and in-plane shear measured experimentally by four research groups: (a) Soden et al. [37], (b) Jelf and Fleck [22], (c) Mannigel [23] and (d) Yerramalli and Waas [38]; and the failure envelopes predicted by the failure criteria described in the review. The experimental results show a large amount scatter, in fact, so much that in Fig. 2.21d, despite the very different envelopes predicted by the criteria, all the predictions are within the range of the experimental data. The scatter in longitudinal compression is expected as the failure mechanisms are sensitive to any material variability [71]. Besides the scatter, the general trend of the failure envelopes is very different from one research group to another and is probably the result of the dissimilar test methods or material layups used. It is interesting to note that the failure criteria also predict very different trends and for example a quadratic

interaction criteria (e.g. Tsai-Hill) fits well the experiments in Fig. 2.21a but not in Fig. 2.21b, while the LaRC05 criterion fits well the experimental data in Fig. 2.21b but not in Fig. 2.21a.

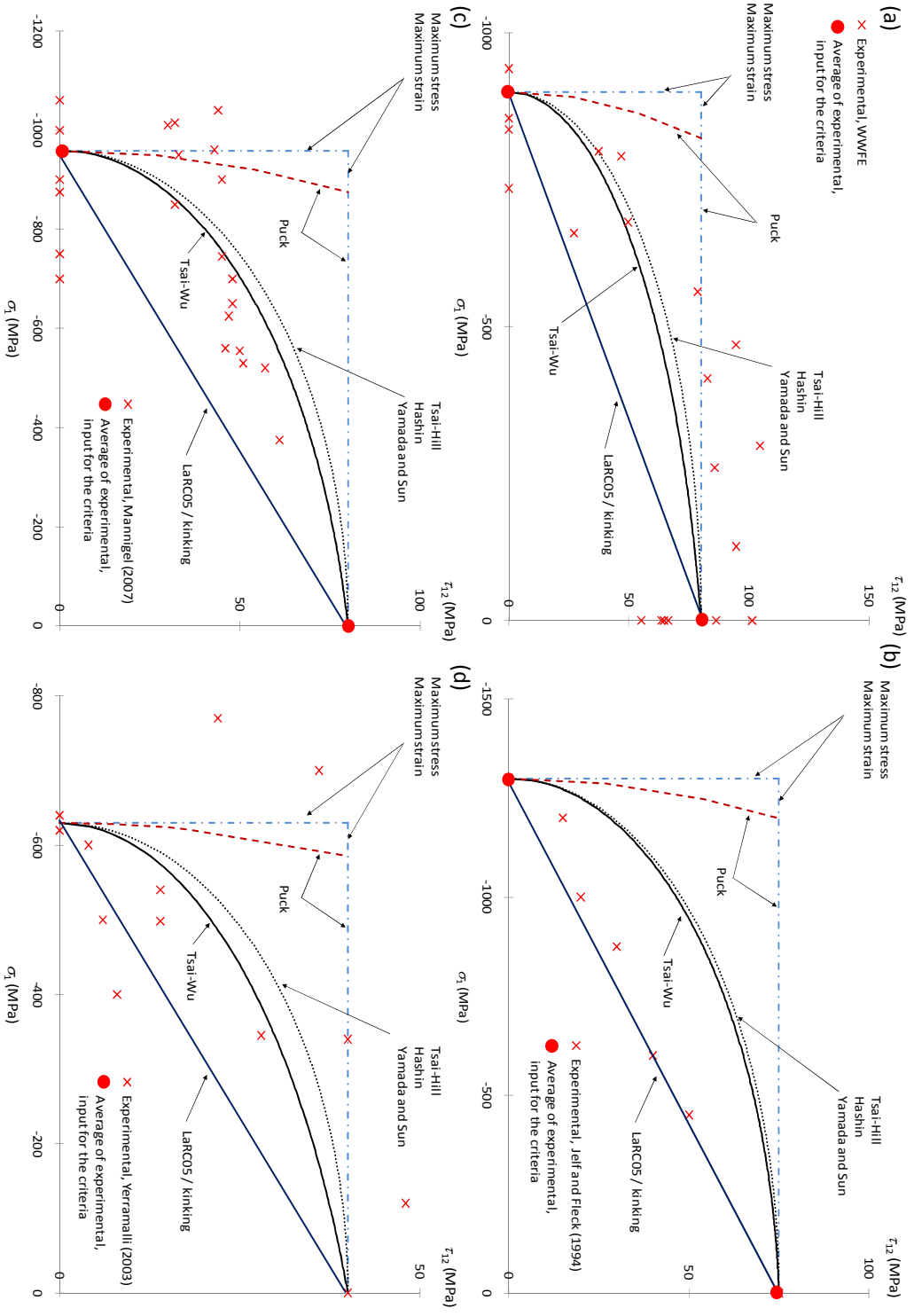


Figure 2.21: Longitudinal compression versus in-plane shear failure envelopes for the criteria described in this section and experimental data from (a) Soden et al. [37], (b) Jelf and Fleck [22], (c) Mannigel [23] and (d) Yerramalli and Waas [38].

Because of the clear lack of agreement between theory and experiments, the modelling of longitudinal compressive failure is emphasised in the review. Models based on a physical formulation to predict the pure longitudinal compressive strength are first reviewed, then models used for multi-axial stress states are detailed.

Pure longitudinal compressive strength In pure longitudinal compression, two of the three failure modes described in Section 2.2.2 are typically found, namely compressive shear failure and kink-band formation.

Compressive shear failure takes place in a fracture plane oriented at 45 ° to the loading direction, Fig. 2.9a, and both fibre and matrix fail at this orientation. Therefore, Ewins and Ham [72] proposed that the compressive strength of the composite should be related to the compressive shear strength of the fibre S^f and the compressive shear strength of the matrix S^m by the expression

$$X_c = 2\left(v_f S^f + (1 - v_f)\, S^m\right), \tag{2.16}$$

where v_f is the fibre volume fraction.

Many models and formulations to predict the compressive strength associated with kink-band formation can be found in the literature [24, 73–75]. Only the main approaches are discussed here: microbuckling [73] and fibre kinking [33, 74, 76].

Microbuckling. The microbuckling theory is based on a micromechanical approach in which the fibres are supported by an elastic foundation provided by the matrix. The compressive strength corresponds to the buckling load and depends on the buckling mode: extensional mode, Fig. 2.22a, or shear mode, Fig. 2.22b. The compressive strengths for the two modes are given in Eqs (2.17) and (2.18) where E_f and E_m are the Young's modulus for the fibres and the matrix respectively and G_m is the shear modulus of the matrix.

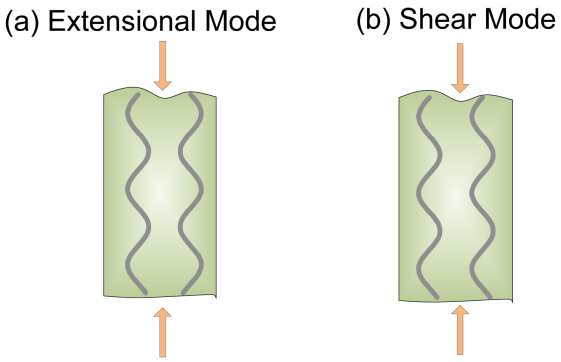


Figure 2.22: Microbuckling theory: (a) Extensional mode, (b) Shear mode.

$$X_c = 2v_f \left[\frac{v_f E_m E_f}{3(1-v_f)}\right]^{1/3} \quad \text{for the extensional mode,} \tag{2.17}$$

$$X_c = \frac{G_m}{(1-v_f)} \quad \text{for the shear mode.} \tag{2.18}$$

For typical fibre volume fraction, $v_\mathrm{f} \sim 0.6$, the shear mode is triggered at lower stress levels than the extensional mode [73]. However, the strength predicted by Eq. (2.18) is typically 3 to 4 times higher than the one experimentally measured. Modifications to include plastic behaviour of the matrix and initial fibre misalignment are found in later studies but still overpredict the strength (see [24, 77]).

Kinking theory. Kinking theory is based on the assumption that there is a region of misaligned fibres in the composite. Under a compressive load, the fibres rotate further and failure is predicted when the failure stress of the matrix is reached. On the contrary to microbuckling, failure is caused by matrix failure rather than fibre instability. Argon [33] developed the first kinking model in which the compressive strength derives from an energy balance between the energy spent by the plastic flow inside the band (shearing of the matrix), the change in elastic energy outside the band, the bending of the fibres and the work done to rotate the fibres. Assuming small rotation of the fibres and neglecting their bending contribution, the compressive strength reads

$$X_c = \frac{\tau_\mathrm{Y}}{\theta_0}, \tag{2.19}$$

where τ_Y is the shear strength of the matrix and θ_0 the initial misalignment of the fibres. This model has been later extended to account for the rotation of the fibres by Budiansky [76],

$$X_c = \frac{\tau_Y}{\theta_0 + \gamma_Y}, \tag{2.20}$$

where γ_Y is the shear yield strain of the matrix.

Micromechanical models. Several models have been proposed to study kink-band formation from micromechanical analyses and relying on assumptions similar to the ones used in kinking theory. The equilibrium of an initially misaligned fibre (Fig. 2.23a) or smeared composite (Fig. 2.23b) is studied under the action of a compressive load and with shear stresses transmitted onto the fibre by a matrix with a nonlinear constitutive response [75, 77, 78]. The framework of these models is one length scale below the one involved in kinking theory, which means that more information can be included but also obtained. For example, estimate of the kink-band width, angle of rotation of the fibres can be obtained and related to the load versus displacement response of the models [75]. However, the degree of complexity is often higher than that in kinking theory, and extending their applicability to multi-axial loading is difficult.

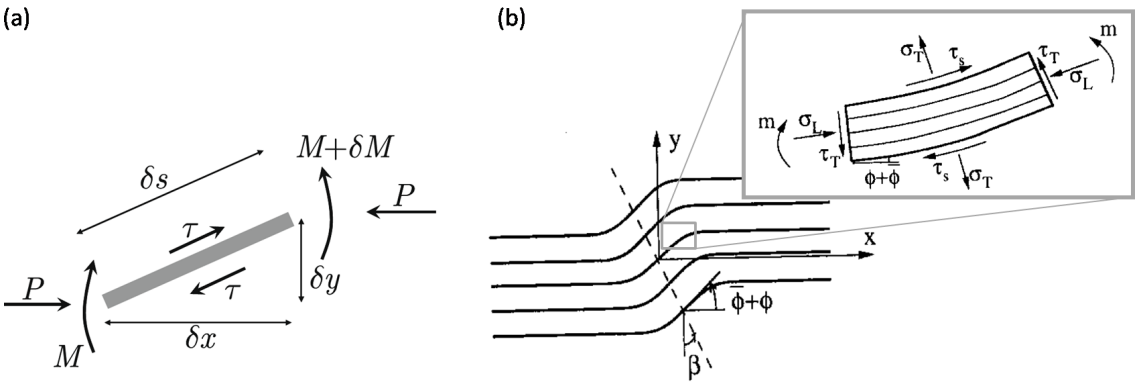


Figure 2.23: Models based on beam theory: (a) Fibre supported by matrix, (b) Smeared composite approach.

Multi-axial stress state in longitudinal compression The models detailed above are good examples of how the physics behind kink-band formation can be

included into an analytical framework in the case of pure compression. But in practical applications, the models need to be extended to account for other stress components.

The scope of the derivations by Budiansky [76], Eq. (2.20), has been extended and formalised by Fleck and Budiansky [74] to account for a multi-axial stress state. As seen in Fig. 2.24, the composite is treated as a continuum (region 1) and the kink-band as an inclined band (region 2) where the material properties have been rotated. Stresses (tractions) and displacements are computed in the coordinate system associated with the kink-band and their continuities are verified at the boundary with the outer region. The compressive strength is evaluated at matrix yielding. Several constitutive responses of the matrix have been used: elastic perfectly plastic, elasto-plastic, deformation theory, time dependent behaviour (see [21] for a review).

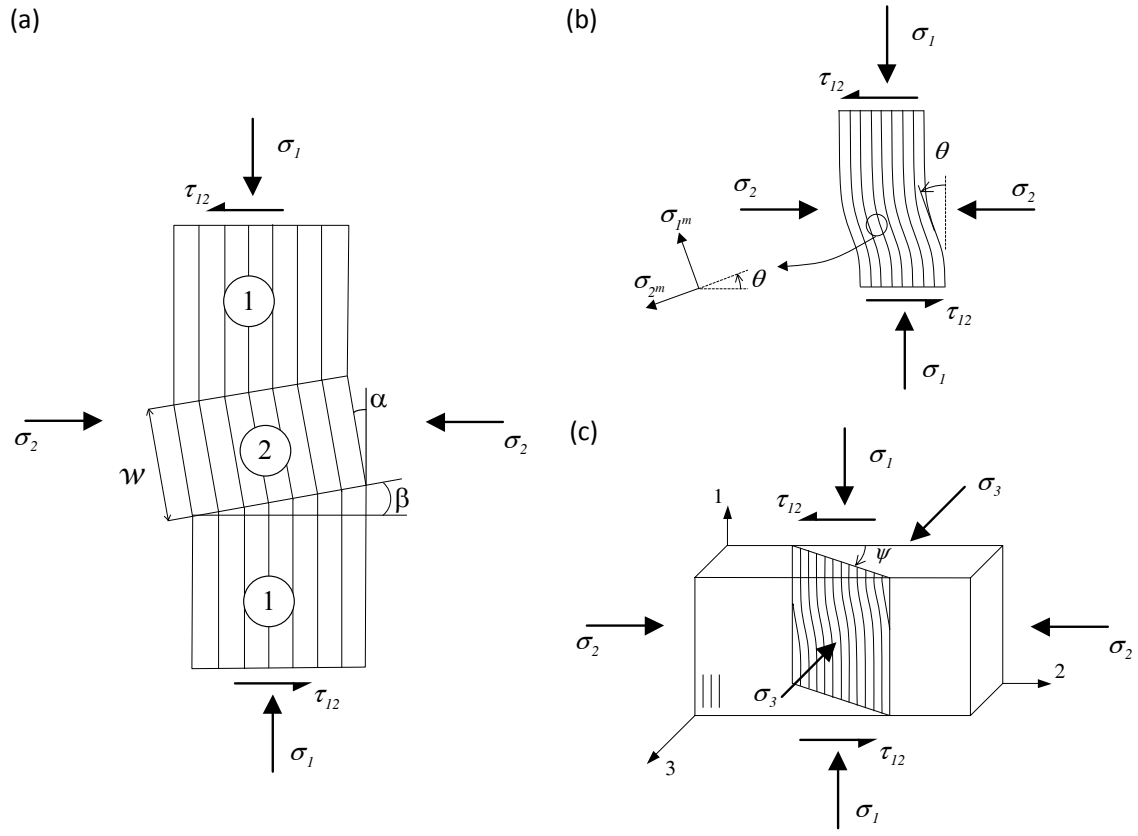


Figure 2.24: (a) Kinking theory under multi-axial stress state [74], LaRC fibre kinking criterion (b) 2D and (c) 3D [6, 67].

A relationship between the kink-band angle (β) and the fibre angle (α) is also found from this model, by writing that the conservation of volume within the kink-band is satisfied

$$\alpha = 2\beta. \tag{2.21}$$

Dávila et al. [79] have proposed a criterion for fibre kinking based on Argon's approach and the LaRC03 matrix failure criterion (detailed below). As shown in Fig. 2.24b, the applied stress on a unidirectional composite with a region of misaligned fibres is rotated in the misaligned frame (noted with the superscript m). The resolved stresses ($\sigma_1^m, \sigma_2^m, \tau_{12}^m$) are then used to calculate the LaRC03 matrix failure criterion and test for failure. The initial fibre misalignment angle is deduced from a case of pure compression.

This procedure has been developed further by Pinho et al. [6] to account for a nonlinear constitutive response of the composite in shear. The fibre kinking criterion is extended to 3D, as shown in Fig. 2.24c. A variable ψ is added to account for the orientation of the kink-band plane through the thickness. The angle ψ is found by assuming that the direction b^ψcorresponds to the maximum principal stress, *i.e.* the shear stress $\tau_{b^\psi c^\psi} = 0$. The failure criterion is applied as in the 2D case but now in the plane (b^ψ, c^ψ).

Other criteria, which are not based on the physics of compressive failure, have also been used for predictions in longitudinal compressive dominated load cases; for example the maximum stress criterion is used in [62, 69] and a modified version of the maximum strain criterion in [68]

$$\frac{\varepsilon_1}{\varepsilon_{1c}} = 1 - (10\gamma_{12})^2 . \tag{2.22}$$

The factor 10 in the right hand side term of Eq. (2.22) is empirical.

These criteria are plotted in Fig. 2.21 with some of the polynomial and limit criteria presented earlier. As mentioned, the experimental scatter and the different trends seen in the experiments make it difficult to compare with analytical formulations. For instance, in Fig. 2.21a the polynomials criteria appear to fit best the experimental data, while in Fig. 2.21b they are unconservative and the LaRC05

and kinking criteria appear best suited. The limit and Puck's criteria are for all the experiments unconservative.

Most of the failure criteria assume a plane stress formulation, on the grounds that composite plies are thin. However, if a thick layer of plies with the same orientation is considered, the failure mode might change and affect the prediction. This can for instance be the case in compression where the thickness of the layer and the stress state might lead to either in-plane or through the thickness kink-band formation. In Fig. 2.25a, the predictions from the LaRC04 fibre kinking criterion [6] when forcing in-plane kink-band formation give more conservative predictions in the compression-tension quadrant and less conservative predictions in the compression-compression quadrant than forcing through the thickness kink-band formation, Fig. 2.25b. In a case where none of the conditions is enforced, Fig. 2.25c, and for the same layer or ply thickness, the change in stress state induce shifts from in-plane to through the thickness kink-band formation.

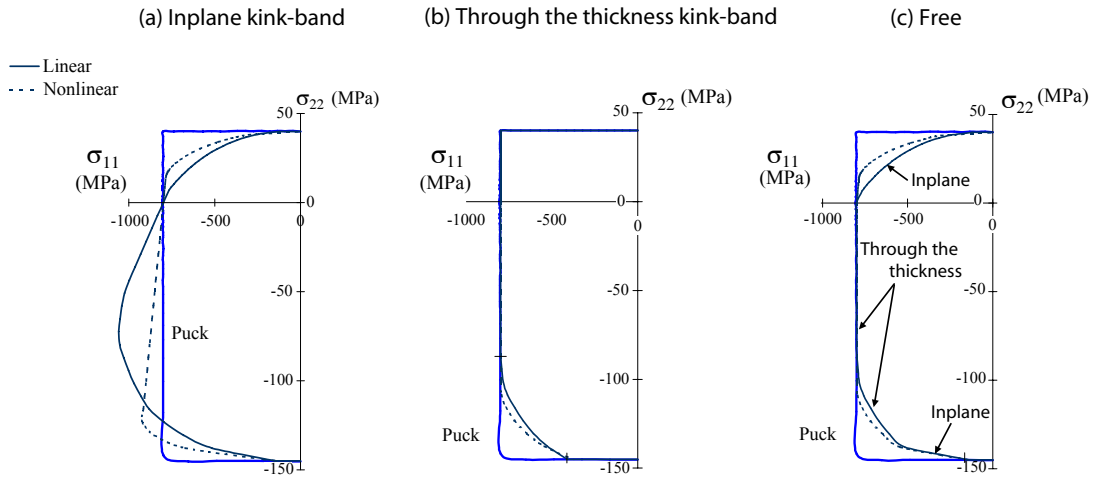


Figure 2.25: Effect of a 3D formulation (adapted from [6]).

A 3D formulation is important to capture the right failure mechanisms and to accurately predict the strength. Besides compression, 3D stress states are also important when the material is subjected to hydrostatic pressure, which typically

lead to a significant enhancement of the strength [30]. The effect of the nonlinear response of the composite is also shown in Fig. 2.25, and in this case appears to mainly affect the predictions when kink-bands form in-plane.

2.4.3.2 Matrix failure

Tension Experimental evidence on combined stress state in matrix dominated failure modes is relatively well documented [37]. Based on experimental data, Hashin and Rotem [62] proposed a quadratic criterion to capture the interaction between transverse tensile and in-plane shear stresses.

$$\left(\frac{\sigma_2}{Y_{\mathrm{t}}}\right)^2 + \left(\frac{\tau_{12}}{S}\right)^2 = 1. \tag{2.23}$$

The orientation of the fracture plane in tensile or compressive failure of the matrix depends on the stress state. Puck proposed a 3D criterion [12, 68] which considers the interaction of the tractions on the fracture plane, see Fig. 2.26. In tension, the criterion reads

$$\sqrt{\left[\left(\frac{1}{Y_T} - C_1\right)\sigma_N\right]^2 + \left(\frac{\tau_T}{S_T}\right)^2 + \left(\frac{\tau_L}{S_L}\right)^2} + C_1\sigma_N = 1 \text{ for } \sigma_N \geq 0. \tag{2.24}$$

The constant $C_1 = \frac{1}{\tau_L^2+\tau_T^2}\left(\frac{\eta_T^{(T)}}{S_T}\tau_T^2 + \frac{\eta_L^{(T)}}{S_L}\tau_L^2\right)$ is important as it introduces the longitudinal and transverse slope parameters

$$\eta_L^{(T)} = \frac{d\tau_{12}}{d\sigma_2}\,|_{\sigma_2=0^+}\ ,\ \eta_L^{(C)} = \frac{d\tau_{12}}{d\sigma_2}\,|_{\sigma_2=0^-}\ , \tag{2.25}$$

$$\eta_T^{(T)} = \frac{d\tau_{23}}{d\sigma_2}\,|_{\sigma_2=0^+}\ ,\ \eta_T^{(C)} = \frac{d\tau_{23}}{d\sigma_2}\,|_{\sigma_2=0^-}\ , \tag{2.26}$$

which control the apparent loss or gain in shear strength in the presence of transverse stresses, see Fig. 2.27. These slopes are evaluated from biaxial test results, which are often difficult to perform with good accuracy.

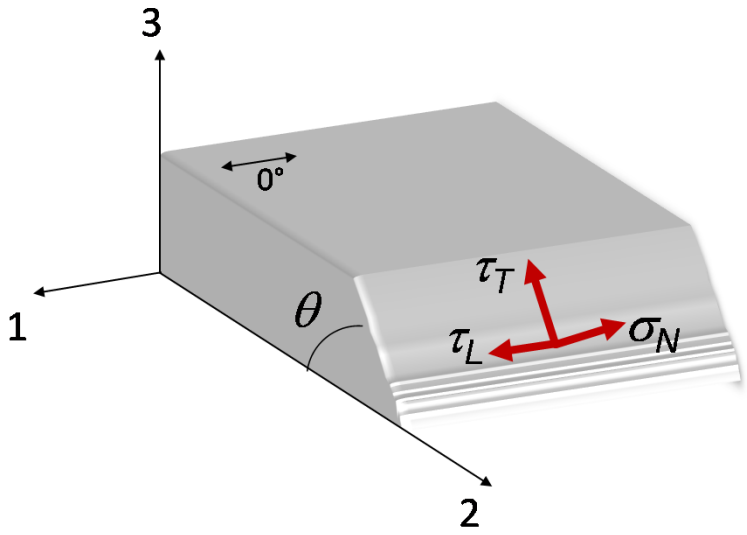


Figure 2.26: Definition of the tractions acting on the fracture plane. [67, 68]

A different approach has been proposed by Dávila et al. [80]; it relies on a mixed mode criterion expressed in terms of energy release rates, related to a criterion proposed by Hahn [81]. The different components—mode I and mode II/III—of the energy release rate and fracture toughness of a slit crack in a ply are calculated for different ply location in a laminate (embedded or outer) and different ply geometries (thin or thick plies). This analysis aims at capturing in-situ effects—increased strength of a ply embedded in a laminate— as detailed in the first section of the review. The criterion reads for a linear elastic response in shear

$$(1-g)\frac{\sigma_{22}}{Y_T^{is}} + g\left(\frac{\sigma_{22}}{Y_T^{is}}\right)^2 + \left(\frac{\tau_{12}}{S_L^{is}}\right)^2 + \left(\frac{\tau_{23}}{S_T^{is}}\right)^2 = 1, \tag{2.27}$$

where g is the ratio between mode I and mode II toughness. The exponent is in Eq. (2.27) stands for in-situ, and for example, the transverse tensile in-situ strength reads

$$Y_T^{is} = 1.12\sqrt{2}Y_T \text{ for a thick embedded ply, and} \tag{2.28}$$

$$Y_T^{is} = \sqrt{\frac{8G_{Ic}}{\pi h \Lambda}} \text{ for a thin embedded ply,} \tag{2.29}$$

where h is the ply thickness and Λ a constant depending on the Poisson's ratio,

transverse and longitudinal moduli. In Eqs (2.29) and (2.28), the in-situ strength for a thick ply depends on the unidirectional strength of the ply while the in-situ strength for a thin ply depends on the toughness; in that latter case, the thinner the ply, the higher the strength, which corresponds well with experimental observations [82].

Compression Fracture in transverse compression can give different orientations of the fracture plane ([68] and as discussed in the first part of the review). For pure transverse compression, specimens fail in shear with a fracture plane inclined at an angle of $53^o \pm 2^o$ [67] to the loading direction, which is higher than the $45\,^\circ$ expected from a shear failure. This can be explained by the existence of a friction stress, associated with the compressive stress, acting on the potential fracture surfaces. Therefore, and although the shear stress is maximum at an angle of $45\,^\circ$, the friction stress which opposes fracture is lower for larger values of the fracture plane angle. The Mohr-Coulomb criterion has been proposed to account for the brittleness of the material and for the internal friction [68]

$$\left(\frac{\tau_T}{S_T - \eta_T^{(C)}\sigma_N}\right)^2 + \left(\frac{\tau_L}{S_L - \eta_L^{(C)}\sigma_N}\right)^2 = 1. \tag{2.30}$$

The slope coefficients η_L and η_T defined in Eqs (2.25) and (2.26) play here the role of a coefficient of friction. For general loading conditions, the angle of the fracture plane is found iteratively by maximising Eq. (2.30).

Another criterion for transverse failure in compression developed by Hashin [69] (as cited in [70]), and often implemented in commercial FE package [83] is

$$\left(\frac{\sigma_2}{2S_{\mathrm{T}}}\right)^2 + \left[\left(\frac{Y_{\mathrm{c}}}{2S_{\mathrm{T}}}\right)^2 - 1\right]\frac{\sigma_2}{Y_{\mathrm{C}}} + \left(\frac{\sigma_{12}}{S_{\mathrm{L}}}\right)^2 = 1. \tag{2.31}$$

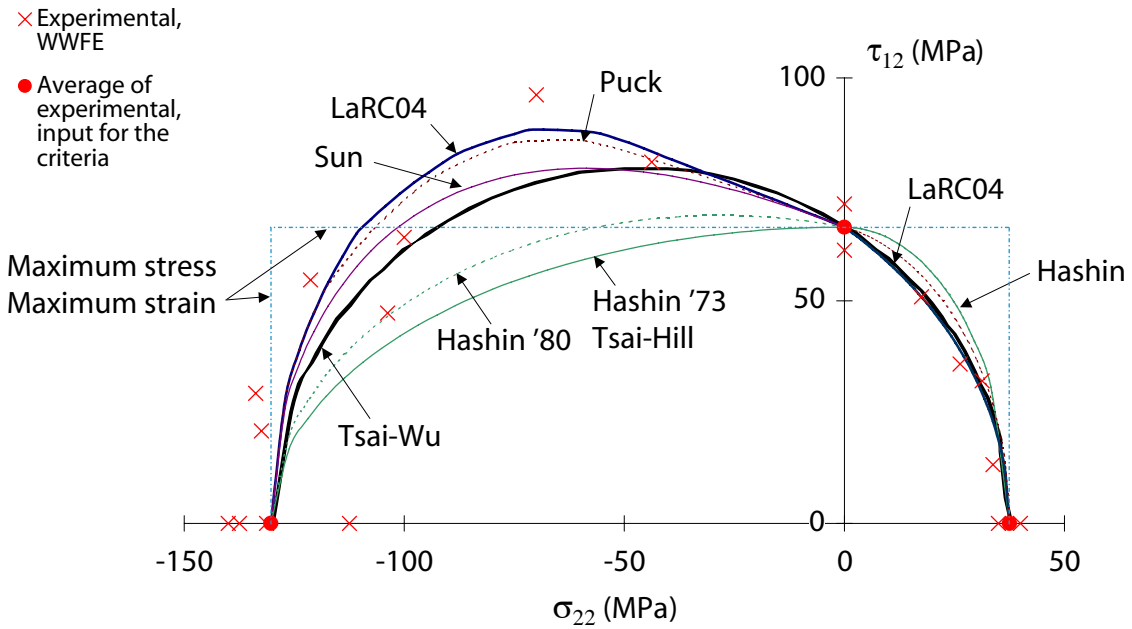


Figure 2.27: Failure envelopes for matrix failure for various criteria for a carbon/epoxy composite (adapted from [6])

A comparison between of the criteria discussed above is shown in Fig. 2.27. For $\sigma_2 > 0$, the criteria show sensibly the same trends. In compression, $\sigma_2 < 0$, the two criteria by Hashin and Rotem and Hashin do not capture the experimental trend for moderate compressive stress. The LaRC04 and Puck's criteria give very close results and are slightly less conservative than the Sun criterion. These three criteria agree well with the experiments.

2.4.4 Damage propagation

Damage growth in composite structures can result in significant loss of stiffness, which needs to be assessed in design. Damage models for composites have been developed in the context of Continuum Damage Mechanics (CDM), where the effect of damage is modelled by a loss of stiffness controlled by a damage variable d

$$E \to E_0 \left(1 - d\right), \tag{2.32}$$

where E is the current damaged modulus and E_0 the initial undamaged modulus. CDM models are often used with the failure indices (f) presented in the preceding section: while $f < 1$, failure has not initiated and $d = 0$, when $f = 1$, damage starts growing until total failure for $d = 1$. A key parameter is therefore the damage evolution law ($d = f(\sigma)$ or $f(\varepsilon)$), which can be determined from phenomenological or energy-based conservations.

This approach can be generalised to anisotropic materials, and different damage variables, corresponding to different failure modes, can be introduced. CDM is well suited for implementation into FE codes as the effect of damage is directly expressed in the stiffness matrix, however, such FE implementations often suffer from a mesh dependency, which can affect the response predicted.

An alternative to Eq. (2.32) is sometimes used [84]; it consists in translating the effect of damage on the stiffness (or compliance) tensor based on micromechanical considerations. The microcracks are idealised as inclusions on the fracture plane and are characterised by an elasticity tensor $\mathbf{E}^{incl}$. This tensor depends on the tractions acting on the fracture plane: for $\sigma_N > 0$, $\mathbf{E}^{incl} \equiv 0$ and for $\sigma_N < 0$, $\mathbf{E}^{incl} \equiv \mathbf{E}^0$ (where $\mathbf{E}^0$ is the initial elasticity tensor) and only the shear components are changed to account for shear stiffness recovery due to frictional forces ($G = \mu\sigma_N$).

The damaged compliance tensor is determined from a model based on mean field theory

$$\mathbf{C}^{\mathrm{d}} = \left\{ \mathbf{I} - d\left[(\mathbf{E}^{\mathrm{incl}} - \mathbf{E}^0) : (\mathbf{S} - d(\mathbf{S} - \mathbf{I})) + \mathbf{E}^0 \right]^{-1} \left[\mathbf{E}^{\mathrm{incl}} - \mathbf{E}^0 \right] \right\} : \mathbf{C}^0, \qquad (2.33)$$

where $\mathbf{I}$ is the fourth order identity tensor and $\mathbf{S}$ is the Eshelby tensor.

2.4.4.1 Phenomenological approaches

Ply discount. The ply discount method is a discrete version of the approach described by Eq. (2.32), since the damage variable is either 0 or 1. A typical example of this method is shown in Table 2.1; when a failure index, corresponding to the failure modes listed in the table, reaches one the relevant elastic properties are reduced to zero, following the scheme shown in the table.

Material state	Elastic properties			
No failure	E_1	E_2	ν_{12}	G_{12}
Matrix failure	E_1	0	0	G_{12}
Fibre failure (tension)	0	E_2	ν_{12}	G_{12}
Fibre/matrix shear	E_1	E_2	0	0
Shear failure	E_1	E_2	ν_{12}	0
Matrix failure + fibre/matrix shear	E_1	0	0	0
Matrix failure + shear damage	E_1	0	0	0
Fibre/matrix shear + shear damage	E_1	E_2	0	0
All failure modes	0	0	0	0

Table 2.1: Degradation of elastic properties from [65]

For a given failure mode, the constants reduced to zero in Table 2.1 are chosen based on micromechnical considerations, however, the amount by which they are reduced is purely empirical (simplest choice).

Meso-scale phenomenological approach. In [12, 68, 84], the damage evolution law is determined from the stiffness reduction measured experimentally on samples (meso-scale) with specific lay-ups. For example, in [68], stiffness reductions are considered for the transverse tension and in-plane shear: the damage evolution for transverse tension is found from the stiffness reduction measured in a $[0, 90]$ laminate, and for in-plane shear from a standard shear test.

In [84] the damage evolution laws found using this method are used with the micromechanical approach detailed in Eq. (2.33).

2.4.4.2 Energy based model

Energy based models assure that the effective stress and strain tensors are defined so that the right amount of energy is dissipated by damage formation. For an isotropic material (neglecting the shear contribution), the complementary free energy density can be written

$$G = \frac{\sigma^2}{2\,(1-d)\,E}. \tag{2.34}$$

Neglecting temperature and moisture effects, positive dissipation of mechanical

energy implies that the strain reads

$$\varepsilon = \frac{\partial G}{\partial \sigma} = C : \sigma, \tag{2.35}$$

and the compliance tensor reads then

$$C = \frac{\partial^2 G}{\partial \sigma^2} = \frac{1}{(1-d)\,E}, \tag{2.36}$$

which is equivalent to Eq. (2.32), but is now related to G, which during damage growth is the fracture energy G_c. A damage evolution is, however, still needed. As with the phenomenological approaches presented above, the damage evolution law can be back-calculated from experimental data [85] or simplified laws can be assumed.

The crack band or cohesive zone model [86] is sometimes used to relate the tractions and displacements on the fracture plane. After initiation, the stresses are reduced according to a softening law as seen in Fig. 2.28, and so that the area under the curve corresponds to the fracture energy. The shape of the softening law can be chosen to capture different processes happening at different stages of crack growth. For instance, Dávila [87] proposed a trilinear law to capture the rising R-curve observed during translaminar crack growth. The first part of the softening law corresponds to the development of a short process zone at the crack tip and the second part to the development of a long process zone in the wake of the crack (development of fibre bridging). The cohesive law therefore represents a measure of the material toughness instead of, for example, the R-curve which is specimen dependent [5].

Even though, continuum damage models are formulated in terms of stress-strain relationships, the direct implementation of the cohesive laws would lead to strain localisation: the fracture energy would be proportional to the volume of the failed element rather than to the fracture area. Therefore, the cohesive laws are formulated in terms of displacement, and a characteristic length function of the element size is

introduced [86, 88].

$$\varepsilon = \delta / l_c$$

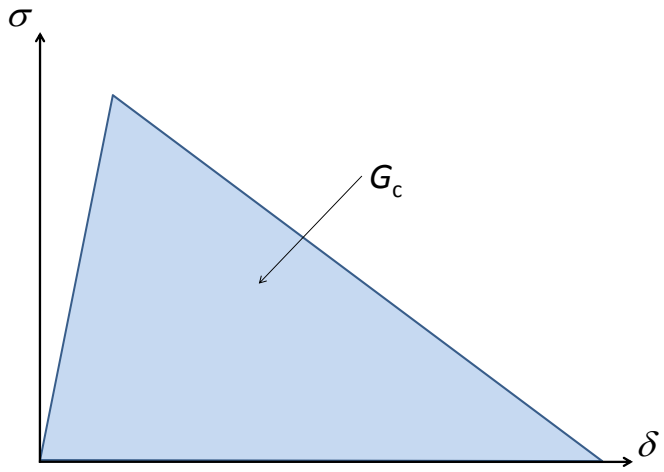


Figure 2.28: Cohesive bilinear law.

2.5 Discussion on the state of the art

2.5.1 Acoustic Emission

Acoustic Emission is an interesting tool for damage detection in composite materials. Its use for qualitative studies has already proved efficient. On the quantitative side a consensus needs still to be found.

The conventional analyses have been extensively used but are too sensitive to material properties and setup configurations.

Modal acoustic emission is accurate in discriminating failure mechanisms but its implementation for systematic studies is quite difficult.

The methods based on pattern recognition have shown interesting capabilities. The results presented above show that correct classification can be achieved even with the simplest of these techniques (k-means and k-NN).

AE studies often show good results in test configurations where there is damage accumulation before failure, i.e. cross-ply specimen. However, AE signals are collected from tensile tests where there is little, or no, damage growth. Therefore, Chapter 3 presents a study on AE where a more relevant AE database is built by recording signals in test coupons with stable or quasi-stable damage growth, e.g. intralaminar or interlaminar toughness test specimens.

2.5.2 Longitudinal compressive failure

Experimentally, many studies have been undertaken to observe kink-band formation; however, only the macroscopic behaviour of kink-band is understood. Studies at a the microscopic scale have shown to be the most relevant for modeling, but their results remain too limited to reach sound conclusions. Furthermore, the post-mortem observations aspect of these studies limits their validity.

In Chapter 4, in-situ observation of longitudinal compressive failure makes it possible to better understand:

- the mechanisms leading to kink-band initiation: fibre failure, matrix failure, interface failure.
- the interaction between the different constituents.
- the effect of adjacent plies, in a multi-axial laminate, on the damage propagation.

Numerical models have shown that matrix nonlinearity, interface strength and fibre waviness play an important role on kink-band formation and can considerably affect the compressive strength. Matrix and interface failure appear to have a similar effect on the response of the composite, nevertheless, the mechanisms leading to failure are different in both cases: (i) diffuse accumulation of microcracks (accounted for by matrix yielding in the FE analyses presented here), in the case of matrix failure; (ii) discrete crack running along the fibres, in the case of interface failure.

Numerical micromechanical FE models have proved to be an interesting tool to understand kink-band formation. However, these models are limited by the lack of

experimental evidence, needed as inputs. Based on the experimental observations from Chapter 4, new micromechanical FE models are presented in Chapter 5 and Appendix C and are used to:

- Quantify the role of the matrix and the fibre/matrix interface.
- Understand the evolution of kink-band parameters during propagation.
- Understand in a controlled environment the effect of multi-axial stresses.

2.5.3 Failure models and criteria

Amongst the different failure criteria, limit and polynomial criteria are the simplest and performed well during the first world wide failure exercise [1]. However, because they do not include information on failure modes, they often fail to predict realistic failure envelope trends. Furthermore, post failure initiation models are often based on physical considerations, i.e. the properties reduced depend on the failure mode activated, and are therefore, hardly compatible with non-physically based failure criteria.

Some physically based criteria achieved a good ranking during the first world wide failure exercise [1] and predictions of failure initiation in fibre tensile or matrix dominated failure compare well with available experimental data. However, the predictions for longitudinal compressive dominated failure are very different, and as accurate experimental data for this load case are difficult to collect, the performances of the criteria cannot be evaluated fully. Nevertheless, the large number of approaches available to model longitudinal compressive failure also reflects a lack of evidence on the failure mechanisms involved. Based on the work in Chapter 4 and 5, a failure criterion for fibre kinking and splitting under combined longitudinal compression and shear is presented. This criterion is based on the fracture mechanics of matrix microcracks in the kink-band and has a simple form, which can be used in design situations.

Modelling the post failure initiation behaviour of composites is very important due to their quasi-brittle nature. Damage evolution laws found by phenomenological

approaches can lead to inconsistent energy absorbtion and can be dependent of the type of specimens and lay-ups used to measure them.

Continuum damage mechanics is a good framework where physically based models can be integrated easily and which is suitable for FE implementation (even though mesh dependency problems need to be alleviated). Furthermore, using cohesive laws, toughening mechanisms can be accounted for. So far, the shape of the cohesive laws for the different failure modes has received little attention, even though, it was shown that appropriate softening laws result in more accurate predictions [87]. Therefore, in Chapter 6 a simplified tri-linear cohesive law is presented to account for R-curve effects. Mathematical relationships are also derived so that the cohesive law can be defined from standard tests simply and without being dependent on the specimen used for the tests.

Chapter 3

On acoustic emission for failure investigation in CFRP

3.1 Introduction

In metallic structures, Acoustic Emission (AE) techniques are often used as a structural health-monitoring system to detect and monitor the size and location of growing defects. In transport applications, the current trend is to replace metallic components with higher performance composite counterparts. AE techniques therefore need to be adapted to account for more intricate wave propagation features [89], caused by the orthotropic nature of composite materials, and to enable identification of a larger variety of failure modes.

AE studies typically rely on signals recorded during tensile tests of various ply orientations and lay-ups to give rise to specific failure modes [43–45, 50]. Three main techniques are used to characterise AE signals: (i) classification according to a single parameter (typically amplitude, frequency or wavelet level), (ii) classification according to several parameters using pattern recognition techniques and (iii) classification according to the extensional and flexural mode content.

A large body of literature can be found on amplitude-based classification. Valentin et al. [43] and Berthelot and Rhazi [44] have studied amplitude distribution of AE signals collected from various tests on unidirectional and cross-ply carbon/epoxy

composites. Both studies reveal contradictory amplitude ranges for the failure modes observed. Longitudinal matrix microcracking is characterised by high amplitude signals, and fibre fracture by low amplitude signals in [43], but this is in marked contrast to [44], which reports that high amplitude signals are associated with fibre failure and low amplitude signals with transverse/longitudinal matrix cracking and delamination.

Ni and Iwamoto [90] show that the amplitude of AE signals is greatly affected by sensor distance, and conclude that the peak frequency of AE signals, which is not affected by sensor distance, is a more reliable characteristic.

Classifications of failure modes based on the frequency content of AE signals have also been investigated and a summary is given in Fig. 2.16. Studies typically report fibre failure in the high frequency range and fibre pull-out in the intermediate frequency range. Matrix cracking is identified to the low frequency range, while delaminations have a frequency range between fibre pull-out and fibre fracture in [50].

The Discrete Wavelet Transform (DWT) has been used in [51, 53] to identify AE signals based on the energy contained in each level of decomposition and the frequency range of this level. From AE signals recorded during tensile tests on cross-ply notched laminates, three failure modes are identified with wavelet levels centered at: 300 kHz for fibre failure; 250 kHz for fiber–matrix debonding and 110 kHz for matrix cracking [51].

Pattern recognition techniques rely on the classification of several parameters (rise times, amplitudes etc.) into clusters forming patterns. These techniques are either supervised or unsupervised. In the supervised case, the algorithm associates input signals to a given class or cluster established from training examples with known failure modes. On the contrary, unsupervised techniques group signals having similar characteristics (forming patterns) in the data structure without having been presented with a training set (more details on these algorithms are given in Section 3.3.2). Godin et al. [45] use both supervised and unsupervised techniques for signal clustering of unidirectional glass/polyester composites. The supervised procedure consists of two parts: (i) the signals recorded during tests, in which spe-

cific failure modes are triggered, are clustered using the k-means algorithm, and labelled based on the knowledge of the damage mechanisms and (ii) input data, which are not labelled, are then classified using the k-Nearest Neighbours (k-NN) approach (this method classifies input signals based on the k closest training examples). When using the unsupervised technique, a Kohonen's Self Organising Map (SOM) is first built. Distinct zones are formed on the SOM, which are then visually identified and defined as clusters. Godin et al. [45] found that the supervised k-NN classifier and the unsupervised Kohonen's map compare well. More recently Godin et al. [57] and de Oliveira and Marques [58] used the Kohonen's SOM to group similar signals before clustering those groups with the k-means algorithm. This approach is usually computationally more effective and the results are comparable to those obtained when the k-means algorithm is applied directly on the data [59]. Following a similar approach, Marec et al. [54] used Principal Component Analysis (PCA)—to reduce the number of correlated variables into a smaller number of uncorrelated variables—before clustering the principal components using the fuzzy C-means approach. Parameters extracted by wavelet transform were also used and the results compared to an analysis using conventional parameters. Their findings indicate that reducing the dimension of the input space (using the PCA) before clustering improved the results. It was also shown that more relevant parameters could be extracted using wavelet decomposition.

Finally, signals can be classified according to their extensional or flexural mode. Each mode shows specific characteristics which can be identified by looking at the waveforms: the extensional mode is symmetric and non-dispersive, while the the flexural mode is antisymmetric and dispersive. This technique, called Modal Acoustic Emission, was used by Surgeon and Wevers [41] and proved to be efficient in terms of classification, but the individual examination of each waveform can be impractical.

The objective of the present work is to identify characteristic signal features associated with damage propagation for each failure mode, and then investigate whether these features can be recognized in other specimens where more complex failure processes take place. AE signals collected from a range of standard ten-

sile tests of various ply orientations and signals collected from interlaminar and intralaminar toughness tests are analysed. First, the performance of three unsupervised pattern recognition techniques — k-means, SOM combined with k-means and Competitive Neural Network (CNN) — are evaluated and the AE signals are post-processed using the most effective algorithm. Secondly, the frequency content of the signals recorded in each test is analysed.

3.2 Experiments

3.2.1 Introduction

Two different types of test are performed: standard tensile tests and tests for intra- and interlaminar toughness measurements. The tensile tests are well established procedures and give rise to specific failure modes. However, failure is often catastrophic making it impossible to record information on damage propagation. In contrast, the Compact Tension (CT) and Compact Compression (CC) tests, which are used to measure translaminar tensile and compressive toughnesses [91] (respectively) as well as the DCB [92] and 4-ENF, which are used to measure interlaminar mode I (opening mode) and mode II (sliding mode) toughnesses, allow for stable crack growth (or stick-slip crack growth in the case of the CT specimens with a cross-ply lay-up) and acoustic emissions to be recorded continuously. In most of these tests, some R-curve effects are observed [91], which means that failure processes change after initiation. Table 3.1 summarises the type of tests, the lay-ups used and abbreviated names used in the rest of the chapter.

3.2.2 Manufacture of the test specimens

The specimens were made of a high-performance unidirectional carbon/epoxy prepreg (IM7 / 8552), with a nominal ply thickness of 0.25 mm. The tensile and DCB specimens were manufactured according to ASTM standards [9, 92, 93]. All laminates were cured in an autoclave following the manufacturer cure schedule. The cured panels were inspected for defects using ultrasonic scanning (C-Scan). The

Table 3.1: Type, layup and name of tests

Type of test	Layup	Name	Number of specimens
Tensile Test	$(0\,^\circ)_8$	T0	3
	$(90\,^\circ)_{16}$	T90	5
	$(\pm 45)_{8S}$	T45	6
	$(90\,^\circ, 0\,^\circ)_{8S}$	T090	5
Compact Tension	$(90\,^\circ)_{16}$	UDCT	9
	$(90\,^\circ, 0\,^\circ)_{8S}$	CPCT	12
Compact Compression	$(90\,^\circ, 0\,^\circ)_{8S}$	CPCC	8
DCB	$(0\,^\circ)_{12}$	DCB	5
4-ENF	$(0\,^\circ)_{12}$	4ENF	4

tensile specimens were end-tabbed using glass-epoxy laminate of 1.5 mm thickness. For the Compact Tension (CT) and Compact Compression (CC) specimens, the geometry is taken from [91]. The geometries and sensor locations for each specimen are given in Fig. 3.1 and the dimensions for the various tensile specimens given in Table 3.2.

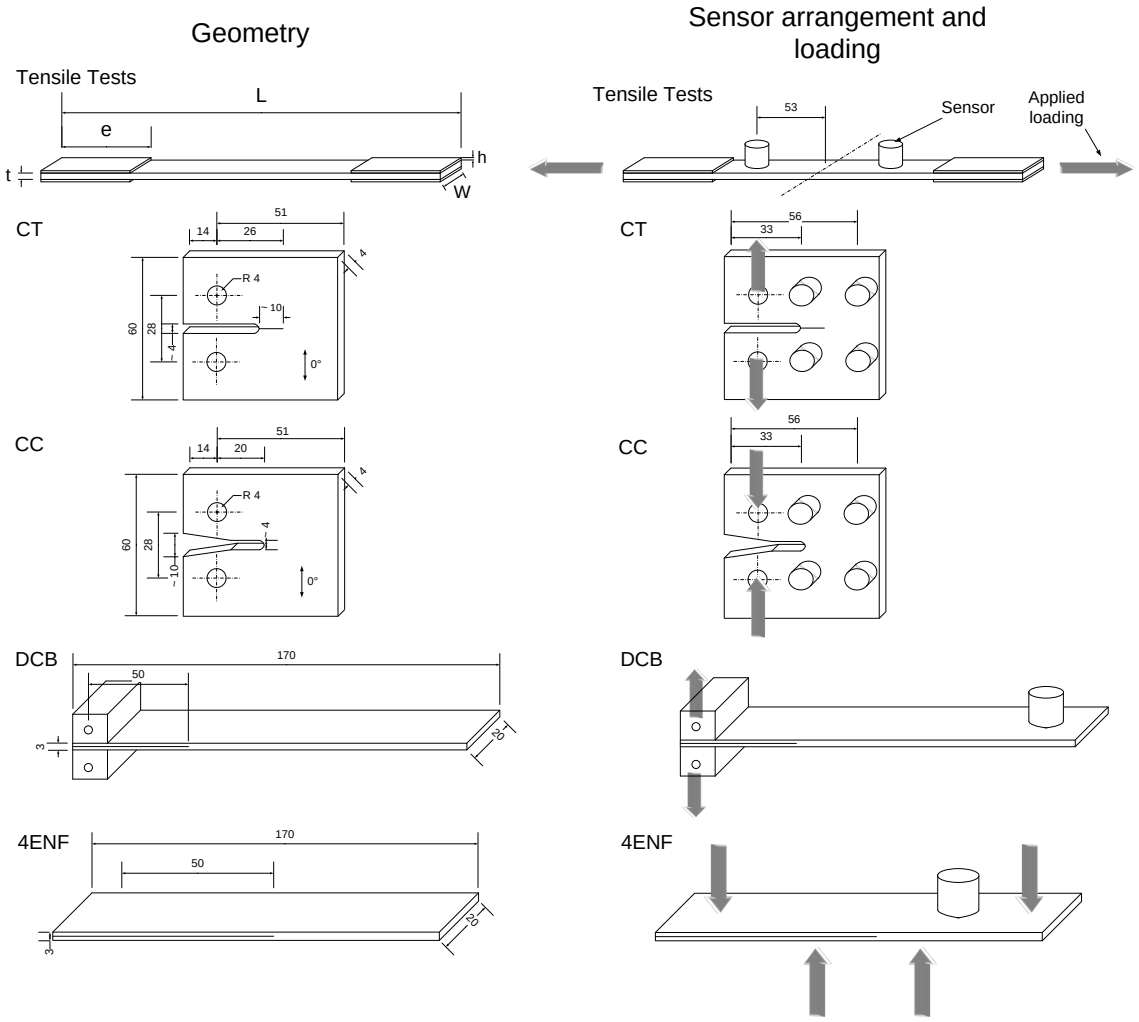


Figure 3.1: Geometry (dimensions in mm) and sensor placement for the different specimen configurations.

Table 3.2: Tensile specimens geometry

Specimen type	L (mm)	W (mm)	t (mm)	e (mm)	h (mm)
T90	175	25	4	25	1.5
T0	250	15	2	56	1.5
T45	250	25	4	50	1.5
T090	250	15	4	50	1.5

3.2.3 Acoustic Emission equipment

An AE suite manufactured by Physical Acoustic Corporation [94] is used. The sensors used are broadband (WD) sensors with a operating frequency range of 100 kHz to 1000 kHz kHz and the signals were pre-amplified with a pre-amplification level of 20 dB. The sensors are positioned as shown in Fig. 3.1, with silicon grease used as a coupling agent and secured with small clamps. The acquisition parameters for the material are calibrated using the pencil lead break test: a pencil break is broken on the surface of the specimen and the acquisition parameters are adjusted so that the signal is well defined (complete signal recorded but not the reflections) and well localised.

3.2.4 Reported failure modes

A representative stress versus strain curve of the T0 tests is shown in Fig. 3.2. The response is linear up to failure, with only a slight discontinuity at an applied strain of 0.71%. Matrix microcracking starts at low stress levels and do not affect the response. Towards the end of the test, fibre / matrix debonding takes place as well as fibre failure.

In the T90 tests, the principal failure mode is matrix microcracking, for which the onset is visible on the stress versus strain curve in Fig. 3.2. Some of these microcracks coalesce into a macroscopic crack leading to final separation of the specimen. Some fibres bridge the macrocrack, which induce fibre / matrix splitting, and eventually fibre failure at final separation.

For the shear tests T45, Fig. 3.2, matrix microcracks form in between the fibres; these microcracks coalesce to split the fibre / matrix interface. Towards the end of the test, some delaminations are created between the $+45^\circ$ and -45° plies. Some signs of splitting and the delamination can be seen on the C-Scan presented in Fig. 3.3.

The response recorded during a T090 test is shown in Fig. 3.2. A knee is observed early in the test ($\sim 0.12\%$) which corresponds to onset of matrix cracking in the 90° plies. The response remains then linear up to a strain of $\sim 0.93\%$ where

some nonlinearities appear before final failure. The sequence of events leading to failure for the T090 tests is difficut to observe in carbon-epoxy specimens, but is well documented for glass-epoxy [58] where the onset of transverse microcracking can be visually detected. During loading, transverse microcracks in the 90 ° layers are first to develop. Their density increases up to a saturation point where edge delaminations appear. Longitudinal cracking takes then place in the 0 ° plies, and eventually, fibre failures occur towards the end of the test.

The UDCT specimens are pre-cracked using a 0.1 mm a razor blade so that a crack propagates along the fibres as the applied displacement increases; the onset of crack growth is indicated on the load versus displacement curve in Fig. 3.2. Matrix microcracking is the main type of damage observed in this test; however, fibre bridging takes place, which leads to increase fibre / matrix splitting. Because the length available for crack growth in CT specimens is relatively small, failure of the bridging fibres is not significant. The C-scan of a UDCT specimen after testing is shown in Fig. 3.3, it can be seen that failure is very localised and follows the initial pre-crack.

The load versus displacement curve of a representative CPCT test is shown in Fig. 3.2, and the stick-slip crack growth is observed. The failure processes in the CPCT are as follows: the crack propagates first in the 90 ° layers before spreading into the 0 ° plies where fibre fracture occurs. An R-curve effect is observed in these tests and is related to fibre pull-out. These features are consistent with those observed in [91] except that in [91], no significant delamination is observed, while in the present study large delaminated zones and some longitudinal splitting on either side of the crack path can be seen in the C-Scan (Fig. 3.3).

The main failure modes observed for the CPCC are: matrix microcracking (initiating at the onset of nonlinearity in Fig. 3.2), fibre kinking (which itself is a combination of matrix microcracking and fibre failure) and delamination. These features have also been identified in [91], and more recently, it was found in [95] that shear-driven compressive failure of the fibres can also occur. In addition to these identified failure modes, contact and friction on the fracture surfaces can also contribute to the generation of AE signals.

The DCB and 4ENF tests are typical tests for interlaminar toughness characterisation in mode I and mode II, respectively. Both specimens are manufactured with a pre-crack from which a crack grows (onset marked in Fig. 3.2) in the predetermined mode. Mild fibre bridging occurs during the tests, which leads to some fibre / matrix splitting and fibre failure.

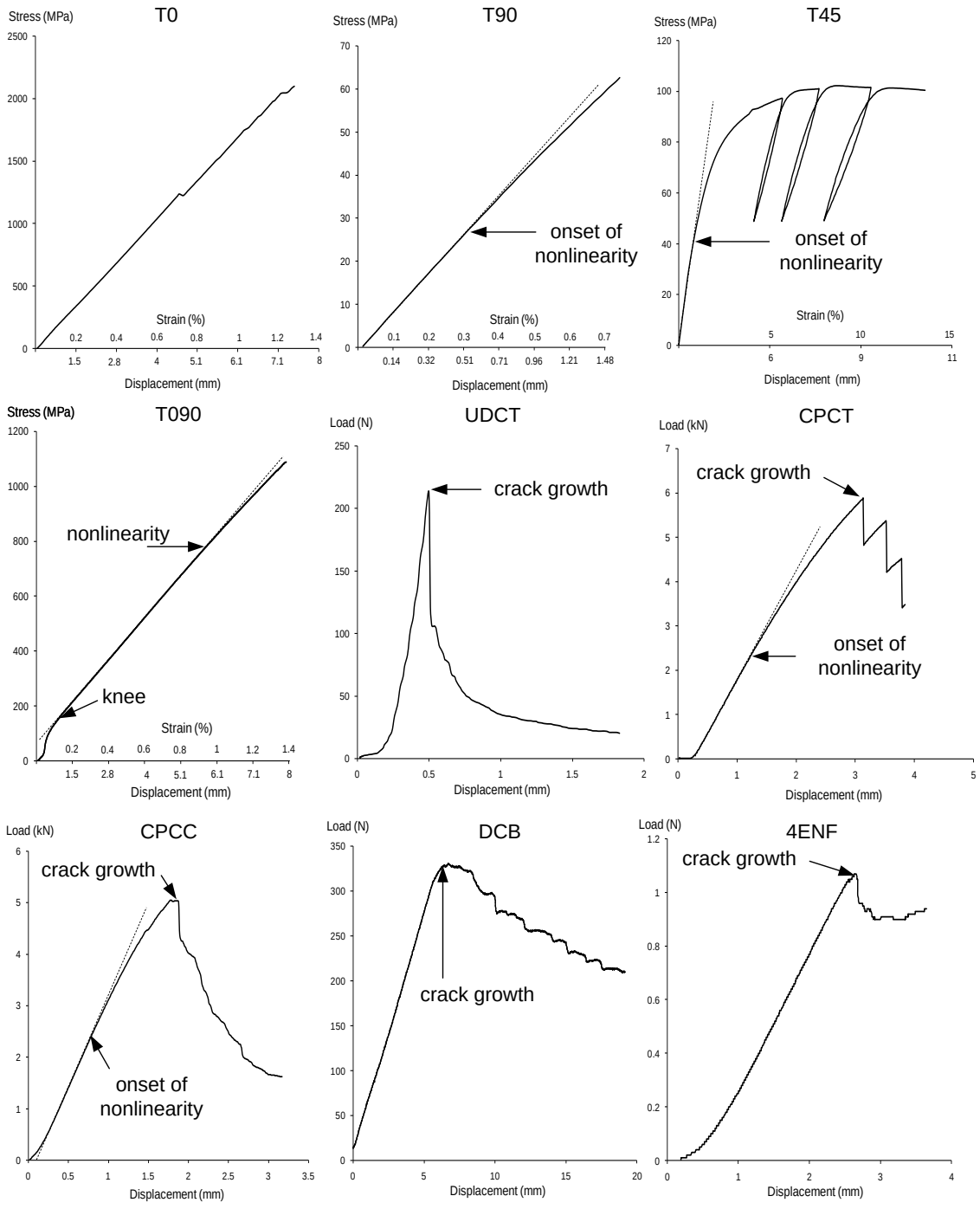


Figure 3.2: Load versus displacement curve of a representative for each test.

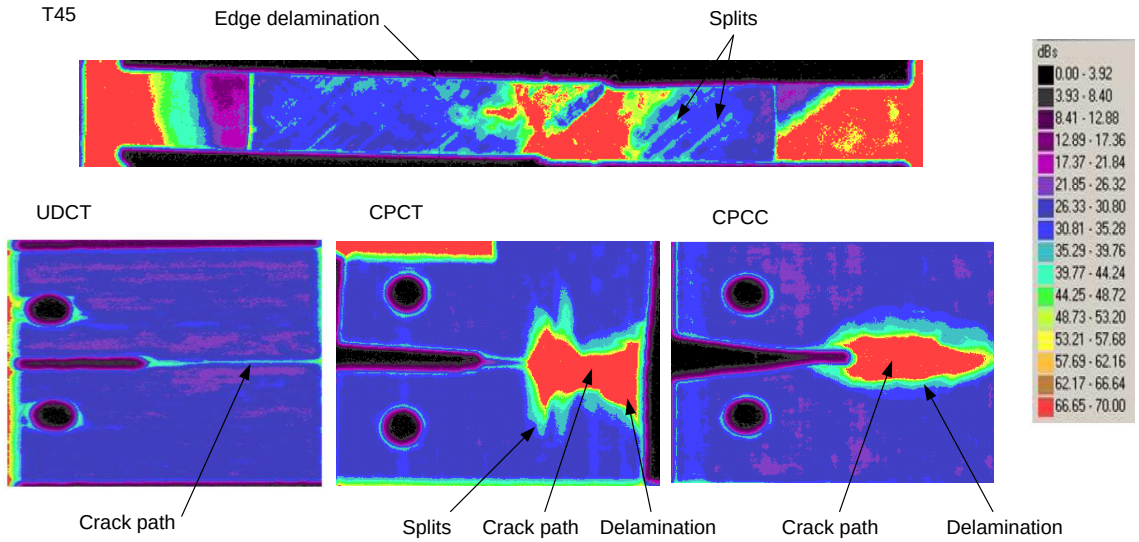


Figure 3.3: Post-tests C-Scans of typical specimens used in the T45, UDCT, CPCT and CPCC tests.

3.3 Pattern Recognition Technique

From the review of the literature presented in Section 3.1, it is unclear which parameters are representative enough of the AE signals to be used as a classifier. Therefore, a multi-parameters analysis of AE signals using pattern recognition techniques is presented first to identify one or several parameters showing common trends and which can be used for a classification of failure mechanisms.

3.3.1 AE parameters selections

Ideally, as many parameters extracted from the recorded AE signals as possible should be used as input vectors to the pattern recognition algorithms. As this would be too time consuming, only five representative parameters are selected: peak amplitude, peak frequency, energy, rise time (time elapsed from the first threshold crossing to the peak amplitude) and duration (time elapsed from the first to the last threshold crossing). During the clustering process, each parameter is non-dimensionalised

so that it falls in the range $[0; 1]$. All the AE parameters chosen here are random variables and each of them is described by normal distributions. These two conditions are necessary to apply unsupervised pattern recognition techniques, as detailed in [96]. It is also assumed that once activated, all the damage mechanisms are continuously active during loading and each damage mechanism is characterised by a single cluster (this latter assumption is discussed further in Section 3.5.1.

3.3.2 Details of the algorithms used

3.3.2.1 k-means

The k-means algorithm is a clustering method aiming at partitioning n input vectors into k clusters. Each input vector is allocated to the cluster with the nearest mean. To cluster a set of n input vectors $(\mathbf{x}_1, \mathbf{x}_2, ..., \mathbf{x}_n)$ into k clusters $(C_1, C_2, ..., C_k)$, the algorithm is [52]:

1. Randomly initialise the clusters center $\mathbf{c}_i$.
2. Compute the distance of each input vector to the clusters center and assign the input vectors to their nearest cluster center, all at once.
3. Recalculate the location of the clusters center, so that Eq. 3.1 is minimised

$$\sum_{i=1}^{k} \sum_{x_j \in C_i} \|\mathbf{x}_j - \mathbf{c}_i\|^2 . \tag{3.1}$$

4. Repeat steps 2 and 3 until the centers location do not change.

There are two phases in this algorithm. In a first phase, the calculations in steps 2 and 3 are done for each input vector and each centre, respectively, all at once (batch updates). In the second phase, the reassignment in step 2 is done individually and only if it reduces the sum in Eq. 3.1. The centres are updated after each reassignment (online updates). The k-means algorithm is a robust and efficient method for data clustering but its accuracy is dependent on the initial starting conditions. To mitigate this, the global k-means algorithm—with multiple restarts—implemented in MATLAB [52] is used in this study. The number k is chosen for

each test within a range $k \in [2; 10]$ and so that it maximises the silhouette value defined as

$$s = \frac{1}{n} \sum_{i=1}^{n} \frac{[\min (b(i,k) - a(i))]}{\max [a(i), \min (b(i,k))]}, \tag{3.2}$$

where $b(i,k)$ is the average distance from the i^{th} vector to the other vectors in another cluster k and $a(i)$ is the average distance between the i^{th} vector and the other vectors in the same cluster. A silhouette value greater than 0.6 generally assures that the clustering is of sufficient quality [52].

3.3.2.2 Self Organising Map

The Self Organising Map (SOM) [55] is an artificial neural network where neighbouring neurons compete and develop through mutual interaction to recognise patterns in a given set of data. A SOM consists of neurons organised on a regular low-dimensional grid (here a 2D map of dimension $l \times p$ is considered). The training of the map with n input vectors $(\mathbf{x}_1, \mathbf{x}_2, ..., \mathbf{x}_n)$ of dimension m is as follows:

1. Determine the number of neurons based on the length of the input data, and determine l and p (see [56] for details).

2. An m-dimensional weight vector $\mathbf{w}_j$ is assigned to each neuron j. The initialisation of the weight vectors is done following a procedure described in [56].

3. An input vector $\mathbf{x}$ is selected, and its distance to each neuron j is calculated. The nearest neuron to the input, called winning neuron c, is identified as

$$\|\mathbf{x} - \mathbf{w}_c\| = \min_j \|\mathbf{x} - \mathbf{w}_j\|, \tag{3.3}$$

   where $\|\bullet\|$ is the Euclidian distance.

4. The weight of the winning neuron, and of its neighbours, is updated as

$$w_j(k+1) = w_j(k) + \alpha(k) h_{cj}(k) [\mathbf{x} - \mathbf{w}_j(k)], \tag{3.4}$$

where k is the learning iteration, $\alpha(k)$ is the learning rate (which starts at a value of 0.5 and is decreased by a factor of 0.01 at each increament) and $h_{cj}(k)$ is a neighbourhood function (here a Gaussian function centered on the winning neuron c).

5. Repeat steps 3 and 4 for all the n input vectors.

In one way, the SOM can be seen as a competitive neural network, since the most similar neuron to an input vector is modified so that it becomes even more similar. However, it also exhibits cooperative learning as not only the most similar neuron is modified, but also its neighbours on the map are moved towards the input vector.

Besides its pattern recognition feature, the SOM is also a vector projection method as each neuron has two positions: one in the input space, where the neurons have the same dimensions as the input vectors, and another position in the output space, typically the 2D space of the map [56].

In the present chapter, a similar procedure to the one used in [57, 58] is followed: the SOM is first built before being clustered using the k-means algorithm. The SOM algorithm implemented in the freeware SOM toolbox [56] is used.

3.3.2.3 Competitive Neural Network

Competitive Neural Networks (CNN) are unsupervised artificial neural networks. Their algorithms are similar to the SOM, with the exceptions that only the winning neuron is updated, and updating only takes place in the input space as there is no projection on low-dimensional space.

The CNN algorithm as implemented in the neural network toolbox of MATLAB [52] is used here.

3.3.3 Choice of algorithm

The three algorithms introduced above are all unsupervised data clustering algorithms and present some similarities. For instance, it has been shown that for small map size and upon the condition that the neighbourhood radius decreases to zero, the SOM and k-means algorithms yield comparable results [97]. The SOM and CNN

also show similarities as both use the Kohonen learning rule (Eq. 3.4). The purpose of this section is to evaluate the performance of each algorithm both in terms of quality and computational effort on two of the tests presented above. The T90 test results are used since they contain a small number of signals, therefore leading to a low number of clusters. In contrast, the T090 test has a large number of hits and since several failure modes are involved, the number of clusters should be larger.

The index of validity used is the silhouette index defined in Eq. 3.2. Fig. 3.4 shows the performance of each algorithm for the T90 and T090 tests (with 3 clusters for the T90 test and 6 clusters for the T090). For the two tests given in Fig. 3.4, the CNN shows low performance in terms of quality but also in terms of computational effort; for the T090 test where the input file has approximately 4000 hits, the CNN has a CPU time approximately 10 times higher than the SOM. The SOM combined with the k-means algorithm has a slightly lower performance than the k-means algorithm for the T90 test but slightly better performances for the more complex T090 test. It also has a better computational efficiency and is, therefore, only considered for the rest of the study.

In addition to its performance, the SOM combined with k-means algorithm is a good choice as the k-means clustering is done on the neurons of the map, whose coordinates are uncorrelated, therefore ensuring that the results are not affected by an eventual correlation of the AE parameters selected.

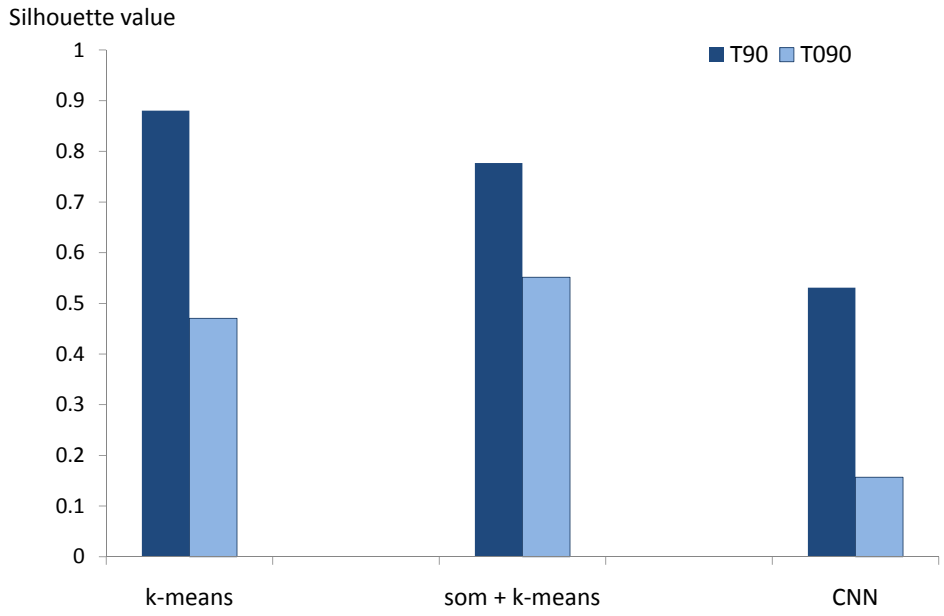


Figure 3.4: Performances of the k-means, the SOM combined with k-means and the CNN algorithms for the T90 test with 3 clusters and the T090 test with 6 clusters.

3.3.4 Results of the clustering

The quality of the clustering, shown in Table 3.3, is good or reasonable for 5 of the tests, acceptable ($0.6 < s < 0.7$) for two of them (CPCC and DCB) and very low ($s < 0.6$) for the T0 and T090.

Fig. 3.5 presents the clustering results for the different tests. Four of the five input parameters (amplitude, peak frequency, duration, energy) are plotted against the applied displacement and the color code indicates the classification. The features observed on the load versus displacement curves, Fig. 3.2, are reported on the graphs.

Table 3.3: Clustering specification and performance for the SOM combined with k-means algorithm

Test	Map size	Number of cluster	Mean silhouette value
T0	30 x 30	4	0.5795
T45	26 x 6	2	0.8144
T90	10 x 10	3	0.7854
T090	19 x 11	6	0.5910
UDCT	10 x 10	4	0.7157
CPCT	20 x 20	4	0.7325
CPCC	30 x 30	5	0.6841
DCB	30 x 9	3	0.6144
4ENF	28 x 11	3	0.9364

For most of the tests, each frequency band corresponds to a cluster. In cases where the optimum number of clusters is greater than the number of frequency bands (e.g. the T090, UDCT and to some extent the T0 and CPCC tests), events are classified according to their amplitude, energy duration and rise time ranges.

For the T45 test, there are less clusters than frequency bands and the classification does not follow patterns in the amplitude, duration or energy plots (the clusters overlap in these graphs). However, it appears that the events in cluster 2 are generated during the loading / reloading cycles.

In the DCB test, only one frequency band is observed on the peak frequency plot but the optimal number of cluster is $k = 3$. Clusters 1, 2 and 3 corresponds to the low, intermediate and high (respectively) amplitude, duration, energy events.

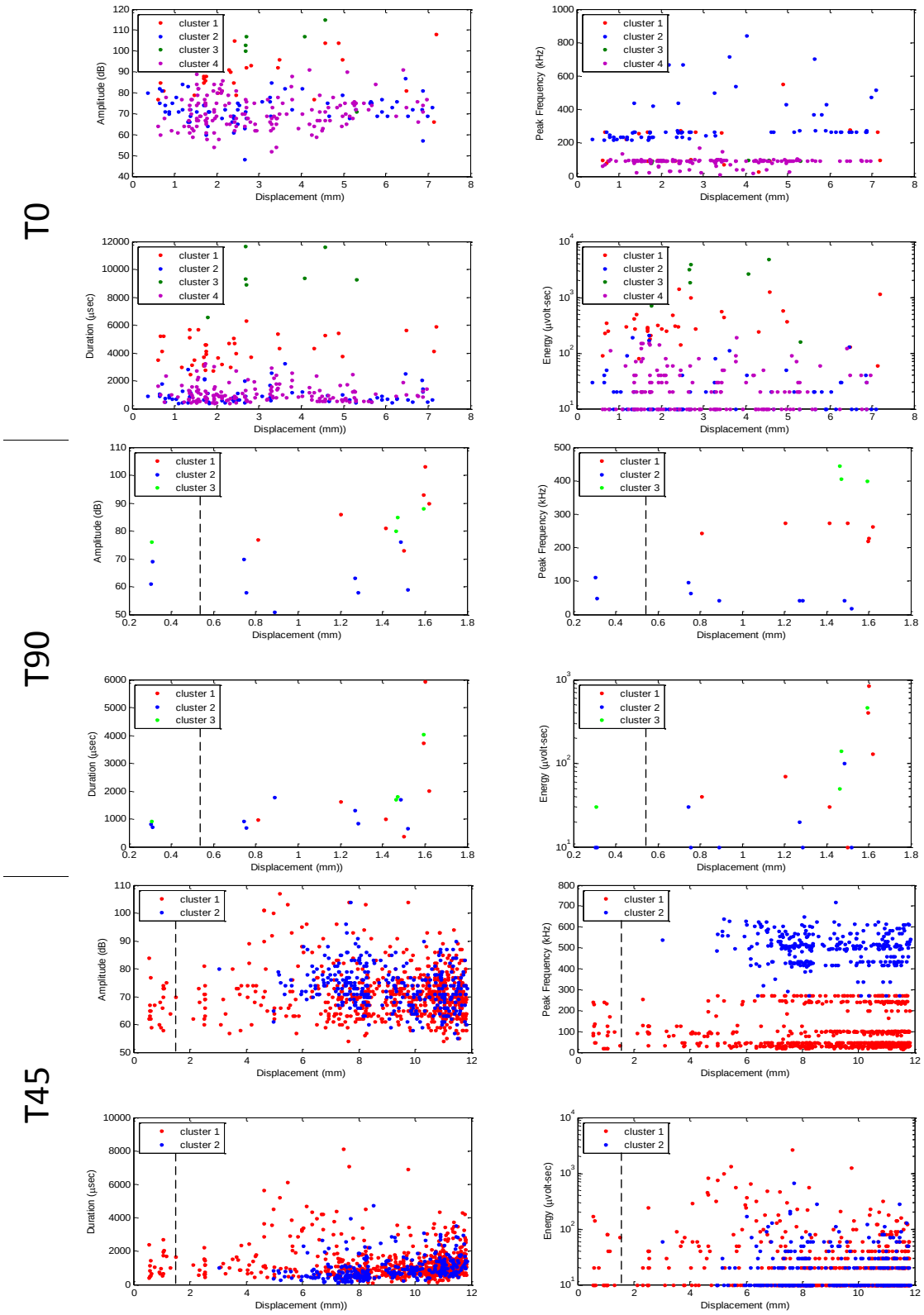


Figure 3.5: Clustering results for the T0, T90 and T45 tests using the combined SOM / k-means algorithm.

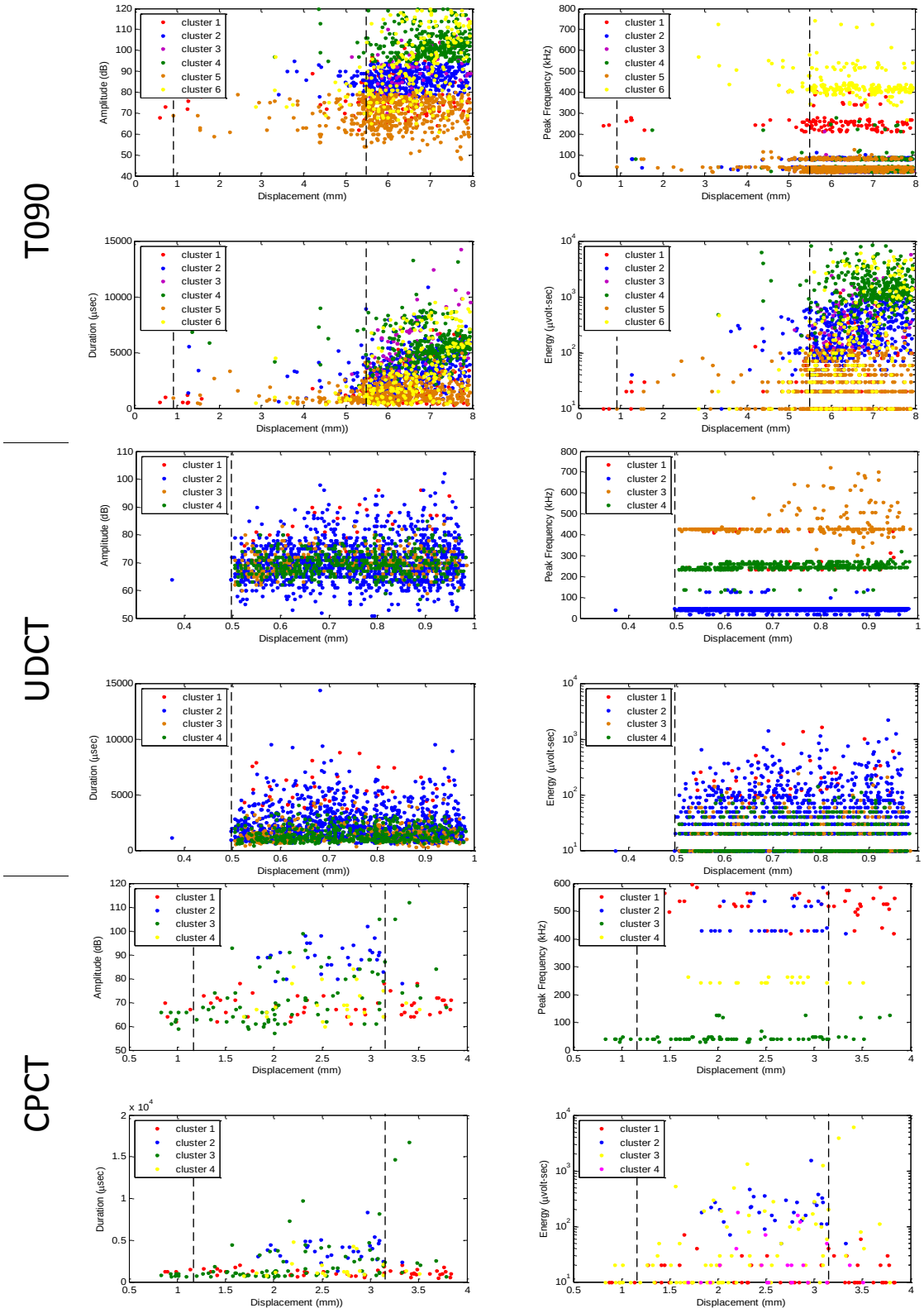


Figure 3.5 (cont.): Clustering results for the T090, UDCT and CPCT tests using the combined SOM / k-means algorithm.

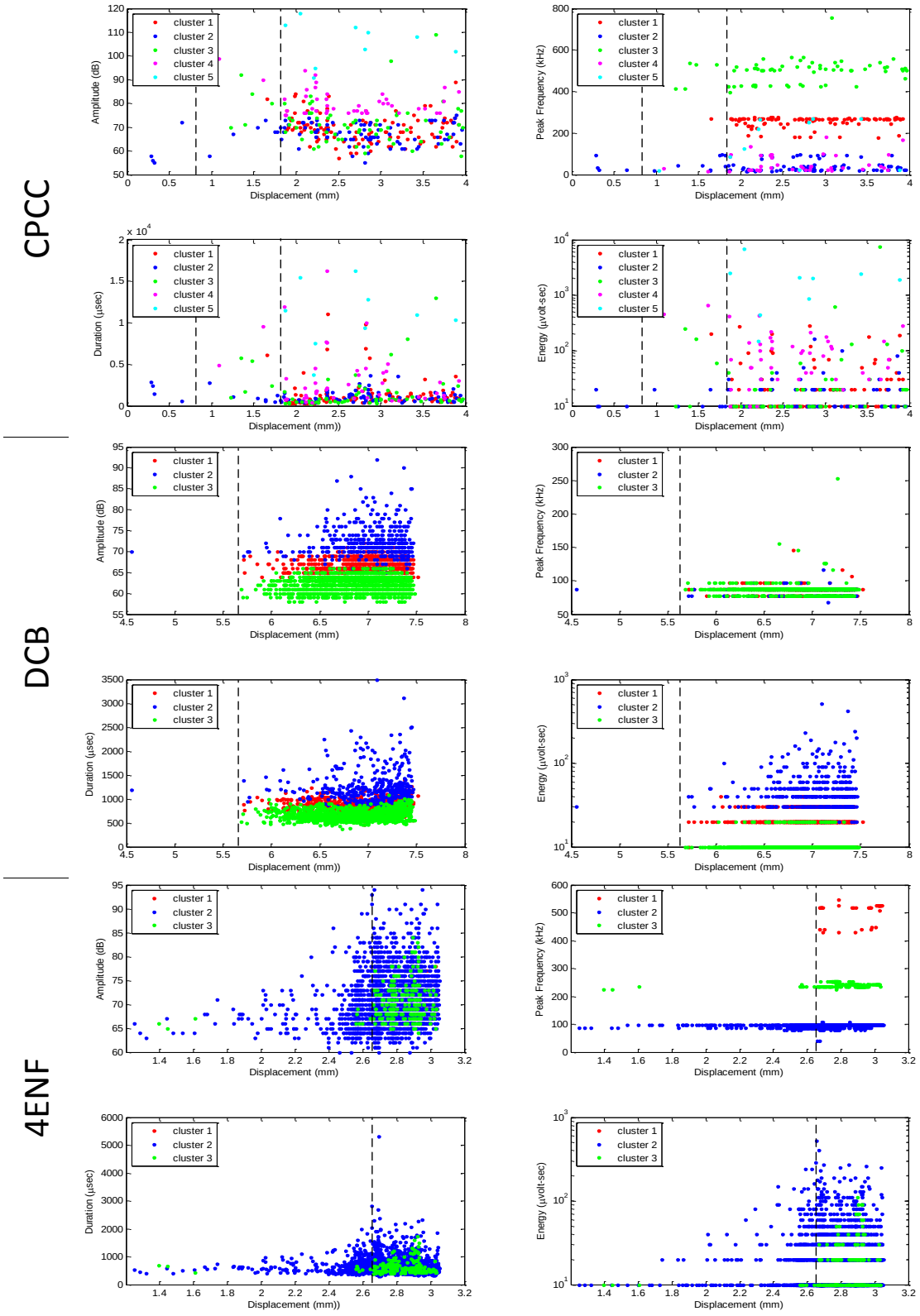


Figure 3.5 (cont.): Clustering results for the CPCC, DCB and 4ENF tests using the combined SOM / k-means algorithm.

3.4 Results of the frequency analysis

The pattern recognition analysis has revealed that consistent patterns, observable in each test, existed in the peak frequency distributions. In this section the peak frequency plot of each test is analysed and the definition of frequency bands is related to specific features of the tests, in view to be used for a classification of the failure mechanisms. For each test, frequency bands are visually defined in Fig. 3.6: (i) f_I between 0 and 50 kHz; (ii) f_{II} between 50 and 150 kHz; (iii) f_{III} between 200 and 300 kHz; (iv) f_{IV} between 400 and 500 kHz and (v) f_V between 500 and 600 kHz. The features observed on the load versus displacement curves, Fig. 3.2, are reported on the graphs.

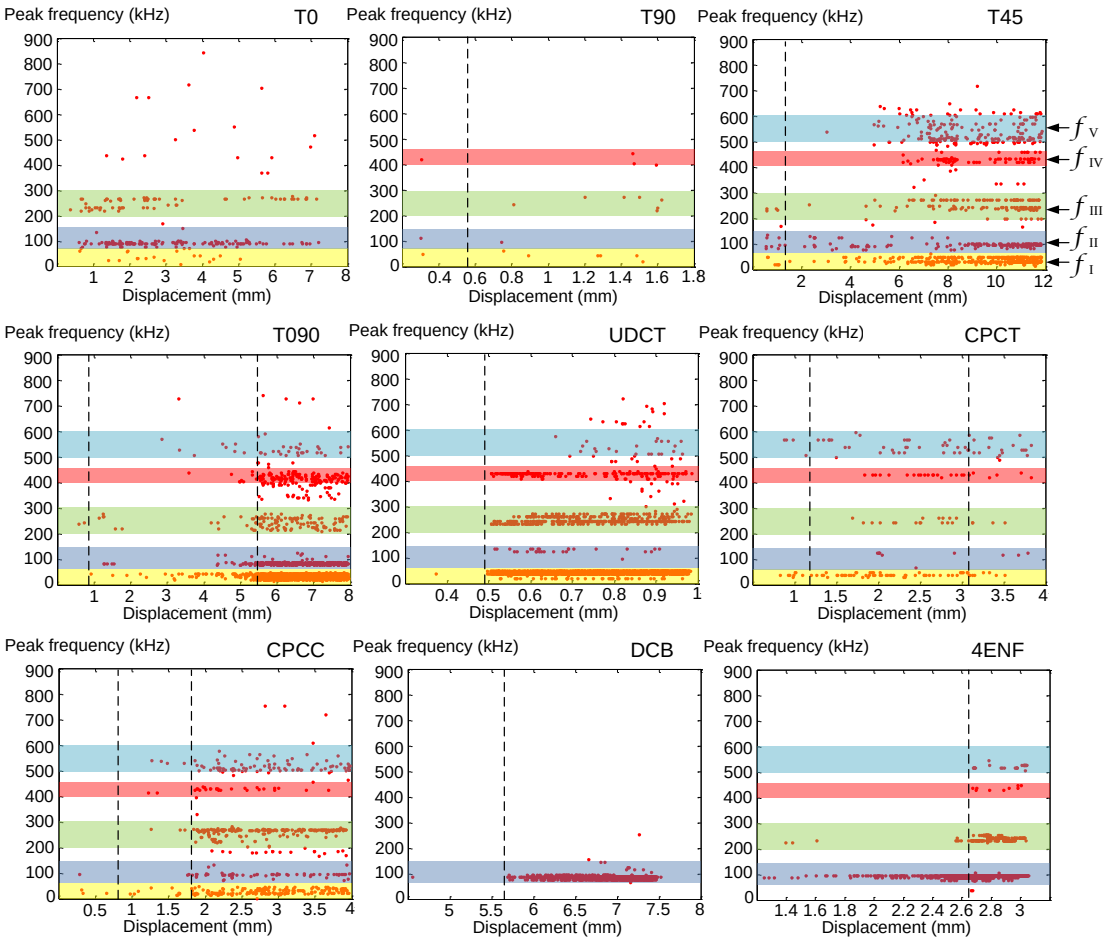


Figure 3.6: Frequency analysis for a representative sample of each test.

Events in the frequency band f_I are generated in most of the tests, except for the DCB and 4ENF, and begins early in the tests (or at the onset of crack growth in the UDCT). Relatively few events belong to this band in the T0 test, and they vanish towards the end of the test.

The frequency band f_{II} is visible in all the tests. It is the only band in the DCB test and begins at onset of crack growth in both the DCB and 4ENF. Few events belong to it in the T90 and CPCT tests.

f_{III} is common to all the tests, apart from the DCB test. The moment of the test at which the events in this band are generated varies from one test to another: close to the knee in the T0 test, at the onset of crack growth in the UDCT, just before the peak load in the CPCC and in the last stages of the other tests.

Events in f_{IV} are not found in the T0 and DCB tests, and they often start with events in f_{III} and f_V.

Events in the frequency band f_V are generated simultaneously with events in f_{III} and f_{IV} in the T090 and 4ENF tests, but occur later in the UDCT. This band is also present in the T45 test and begin just before the peak load in the CPCC test.

Other events above 300 kHz are found in the T0 test; they appear to be quite sparse and to occur at any time during the test. Some signals generated in the frequency range above 600 kHz are also observed in the T45 and UDCT tests, but not in the other tests.

3.5 Discussion

3.5.1 Pattern recognition technique

The clustering of the T45 test does not follow patterns in any of the five AE parameters used, instead cluster 2 corresponds to events emitted during the unloading/reloading cycles. The mechanisms taking place during these cycles, and responsible for the acoustic emissions, are not known, but they could have come from friction on the surfaces of the microcracks created during the previous loading [84].

The signals emitted between the displacement 0 mm and 2.8 mm in the 4ENF

could also come from friction, in this case generated by the rollers of the test setup, or background noise. As indicated in Fig. 3.1 only one sensor is used for the 4ENF test and signals coming from the setup could not be screened out.

In the CPCT, some events in f_V are generated very early in the test (before the onset of nonlinearity). The examination of their waveforms did not reveal any anomaly, i.e. the signals are not noise or reflections. From the clustering Fig. 3.5, it can been that some events change clusters when crack growth starts: from cluster 2 (high amplitude, duration and energy) to cluster 1 (low amplitude, duration and energy). To determine the origin of these signals further investigation is needed, and they should not be included in a classification.

The pattern recognition study shows that clusters are defined by the patterns found in the peak frequency distributions. In the case of the DCB, there is only one frequency band and a single cluster should then have been defined. This is however impossible as the minimum number of clusters allowed is 2 and explains the low silhouette value for this test. A pattern recognition analysis of this test is not needed as the single frequency band corresponds to the single damage mechanism: delamination.

The low silhouette values found in some of the other tests result from the presence of sub-clusters, since the silhouette value is more adapted to find a first partition choice [98]. The sub-clusters are clearly seen on the T090 test, where clusters 1, 5 and 6 in Fig. 6 are the main clusters formed by the patterns on the peak frequency distribution, while clusters 2, 3 and 4 are sub-clusters of cluster 5. These sub-clusters are attributed to slight variations of a same failure mode, for example, several types of matrix cracking (transverse, longitudinal and initiation), having each a specific acoustic signature, are reported for tensile tests on crossply laminates [58]. Giving a reliable classification of these sub-clusters would require a very detailed fractographic analysis and would be far too detailed for practical applications, in which the classification presented here is meant to be used.

3.5.2 Frequency based classification

The pattern recognition study revealed that clusters are defined by the patterns found in the peak frequency distributions. The classification presented in this section is therefore based on the peak frequency distributions, and the frequency bands defined above (Fig. 3.6), which are identified to the failure mechanisms observed during the tests and reported in Section 3.2.4.

The first band f_I is present in most of the tests apart form the DCB. The band begins early in the tests and its number of events increases at characteristic points of the response: knee in the T090, onset of nonlinearity (in e.g. the CPCT and CPCC tests) or onset of crack growth (UDCT). For these reasons, f_I is most likely associated with matrix microcracking.

Frequency band f_{II} is common to all the tests, but is the only band in the DCB and the predominant one in the 4ENF. f_{II} is then associated with delamination growth. This classification, however, rises a problem with the T0 and UDCT tests, which do not show signs of delamination (see C-Scan in Fig. 3.3 for the UDCT specimen) and yet have a large number of events in f_{II}. This classification is hence mitigated by noting that the main failure mechanism involved during delamination is matrix cracking, and f_I and f_{II} could be combined under the label matrix cracking.

A common failure mode to all the tests is fibre / matrix debonding (in the DCB and 4ENF, debonding results from fibre bridging and is only mild). This failure mode is associated with f_{III} as this band is present in all the tests with exception of the DCB. Additional arguments for this classification are that many events are emitted in f_{III} towards the end of the 4ENF test, which is consistent with the development of late fibre bridging.

In the frequency plots Fig. 3.6, it is seen that the bands f_{III}, f_{IV} and f_V often start close to each other. This type of behaviour is consistent with the sequence of events found in fibre bridging: (i) fibre and matrix split (or debond), (ii) the fibre breaks and (iii) the fibre is pulled out. f_{III} has been assigned to fibre/matrix debonding, hence, f_{IV} and f_V could correspond to fibre failure and fibre pull-out. The two are distinguished from the frequency plot of the UDCT; the band f_{IV}

starts earlier and is associated with fibre failure, and f_V is then associated with fibre pull-out.

Even though some events in the f_{IV} and f_V bands in the T45 test might correspond to fibre pull-out, they are not included in the present classification as it was noted above that these signals could come from friction generated by the microcracks faces during unloading.

Furthermore, fibre failure (band f_{IV}) and fibre pull-out (f_V) are not found in the T0 tests. A possible explanation for this is that these failure mechanisms should occur close to final failure, but because a large amount of energy is released at final failure, the whole specimen vibrates and can make it impossible for the AE suite to record signals emitted at this instant.

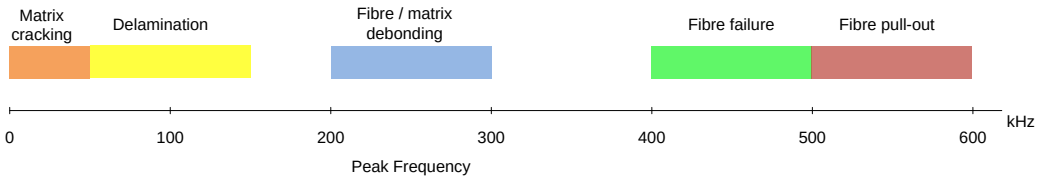


Figure 3.7: Summary of the classification using frequency content.

The CPCC specimen is a good example to verify the classification proposed above (and summarised in Fig. 3.7) as all the failure mechanisms are involved: matrix microcracking, fibre kinking (which itself is a combination of matrix microcracking and fibre failure), shear driven compressive failure and delamination have been previously observed, and contact and friction on the fracture surfaces may also generate AE signals. In the frequency plot presented in Fig. 3.6, events in the band f_I, corresponding to matrix microcracking, appears first in the test. The events in the bands f_{III}, f_{IV}, f_V begin just before the peak load and could correspond to kink-band initiation (band f_{III} and f_V) and formation of the kink-band edges or compressive shear failure of the fibre (band f_{IV}). The band f_{II} corresponding to delamination is also observed.

The classification proposed here and summarised in Fig. 3.7 can be compared to those found in deGroot et al. [50] and in Ramirez-Jimenez et al. [3], see Fig. 2.16. Matrix cracking (f_I) corresponds to a lower part of the frequency range than in [50], but this was mitigated as f_I and f_{II} can be combined, in which case the agreement is better. The classification for fibre / matrix debonding (f_{III}) is in good agreement with [50] but slightly higher than the one reported in [3]. The frequency range for fibre failure (f_{IV}) also matches the ones reported in [3, 50]. However, a strong discrepancy is found for fibre pull-out (f_V), between 500 kHz and 600 kHz in the present study, centered at 200 kHz in [50] and between 200 kHz and 300 kHz in [3]. Fibre pull-out is identified in [50] using a tensile 10 ° test, therefore pull-out is the result of an accumulation of shear microcracks in the matrix. In the present study, fibre pull-out refers to the actual drawing of the fibres (or fibre bundles) which occurs after fracture of the interface and of the fibres. In [3], pull-out is identified from a tensile 0 ° test; the frequency band 200 kHz and 300 kHz can also be observed in the T0 presented here (Fig. 3.6) but this band appears mainly in the first part of the test while fibre pull-out is expected towards the end. As mentioned earlier, it is believed that fibre pull-out has not been recorded in the T0 due to the large amount of energy released at the end of the test.

3.6 Conclusion

AE signals were collected from an extensive test program consisting of standard tensile tests with various layups and orientations and tests for intra- and interlaminar fracture toughness characterisation. The advantage of these toughness tests, over the tensile tests, is that damage evolves in a reasonably controlled and stable way. Furthermore, collecting AE signals from such tests appears more appropriate as in most structures, failure initiate from geometrical discontinuities, such as holes or notches.

Amongst the three pattern recognition algorithms used, the SOM combined with k-means clustering was found to give the best clustering quality and low computational efforts. When applied to the whole series of tests, the clustering followed

patterns found in the peak frequencies distribution. The detailed study of the frequency content of each test performed in this chapter can be summarised by the classification shown in Fig. 3.7. Even though some failure modes are clearly identified, e.g. matrix cracking, fibre / matrix splitting and delamination, some others such as fibre pullout or fibre fracture need further study. In particular, some frequency bands above 600 kHz in the T45 test require more attention.

In summary, characterisation of failure modes in carbon/epoxy systems using the frequency content of acoustic emissions appears to be a promising method investigated in the present study. Further work should aim at collecting signals from other types of configuration, ideally in which stable damage propagation can be achieved, to further confirm the proposed classification and to investigate the frequency ranges which remain unclear.

3.7 Publications

It is envisaged that the contents of this chapter will be submitted for journal publication in the near future.

Chapter 4

Experimental investigation on longitudinal compressive failure of notched CFRP laminates

4.1 Introduction

Carbon fibre composites are widely used, and increasingly so, for structural applications. At the design stage, an optimal use of composites requires a complete understanding of their properties and of their failure mechanisms.

A review of the literature [21, 24, 99, 100] shows that longitudinal compressive failure of carbon / epoxy systems is typically associated with kink-band formation—matrix shear instability in a region of misaligned fibres as shown in Fig. 4.1. Typical kink-band parameters such as the width w, the propagation angle β and the fibres' rotation angle α (sometimes noted $\theta_0 + \theta$, with θ_0 being the initial misalignment and θ the additional rotation introduced by the compressive loading) are also shown in this Figure.

As detailed in Chapter 2, obtaining experimental evidence of the failure mechanisms has proved challenging due to the unstable nature of the failure process

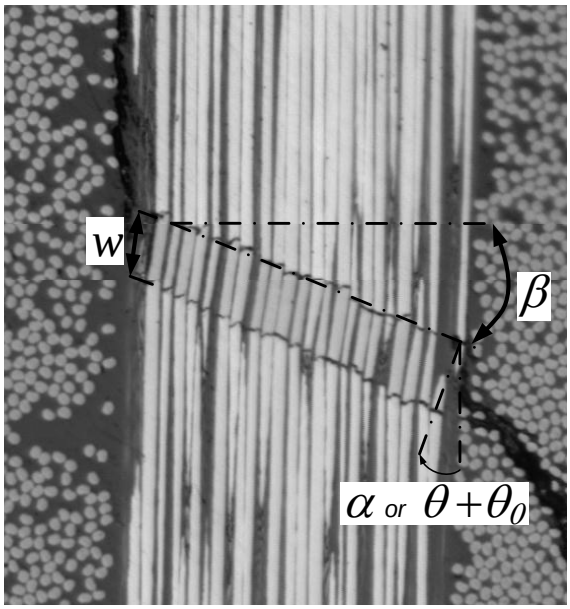


Figure 4.1: Typical kink-band geometry.

and the difficulty in observing specimens at the microscale while keeping them under load. Experimental investigations have mainly focused on kink-band formation ([28, 30, 101]), but other failure mechanisms have also been observed such as shear-driven fibre compressive failures ([17, 20]) or fibre / matrix splitting, in which a crack runs along the fibre / matrix interface across the whole specimen, when large in-plane shear stresses are combined with the longitudinal compression [22, 102].

In studies outlined above, the sequence of events leading to failure and the role of the different constituents can be inferred. However, the post-mortem nature of the observations means that fracture surfaces can be altered during unloading as well as during the process of preparing the specimens for microscopic examination. In studies where in-situ observations were attempted [28, 103], the low resolution of the recording system is insufficient to obtain information on microscopic events, which is necessary for instance for developing physically-based failure criteria.

The present work investigates the failure mechanisms found in longitudinal compression of single edge notch unidirectional and cross-ply specimens. Dedicated test jigs were developed to observe failure processes at the microscale and in-situ. Those observations are combined with post-mortem analysis to investigate the sequence of events leading to failure and the reasons for the occurrence of different types of

failure modes.

In the next chapter, an FE micromechanical model is used to investigate numerically the failure mechanisms found in longitudinal compression and to relate the findings to the experimental investigation presented here.

4.2 Experimental procedure

4.2.1 Test material and specimens geometry

The specimens were made of high-performance carbon-epoxy system (Hexcel T800 / 924), provided as unidirectional pre-preg with nominal cured ply thickness of 0.125 mm and a fibre volume fraction of 63%. Other mechanical properties are given in Table 4.1. Two types of layup are used: unidirectional (UD) $[0\,^\circ]_{40}$ and cross-ply $[90\,^\circ{}_2, 0\,^\circ{}_8, [90\,^\circ, 0\,^\circ]_5]_S$ laminates. In the second layup, the two outer $90\,^\circ$ plies aim at contraining out of plane movements of the kink-bands in the $0\,^\circ$ layer, which is itself chosen thick (8 plies) to promote inplane kinking. The material was manufactured using standard methods for pre-preg laminates and a representative sample of specimens was inspected by C-scan after manufacturing to assess their quality.

Table 4.1: Mechanical properties of T800/924 unidirectional lamina.

Modulus (GPa)		
Longitudinal	Transverse	Shear
165	45.9	4.5
Strength (MPa)		
Longitudinal Tension	Longitudinal Compression	Shear
2136.9	1295.7	93.9

Fig. 4.2 shows the geometry used for the specimens. The initial part of the notch was manufactured using a band saw (radius of ~ 2 mm), then a finer slit was made with a model saw (radius of ~ 0.2 mm) and finally the tip was sharpened with a razor blade (radius of ~ 0.1 mm).

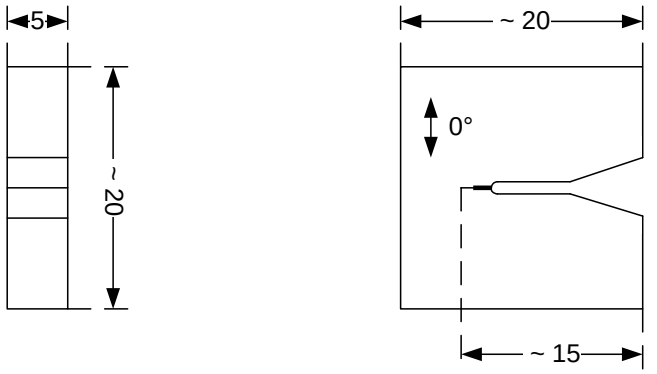


Figure 4.2: Specimen geometry (dimensions in mm).

4.2.2 SEM test jig

The Scanning Electron Microscope (SEM) test jig shown in Fig. 4.3a was used to apply a compressive load to the unidirectional specimens. The test jig was designed so that stable in-plane kink-band propagation could be achieved and so that the specimens could be observed under load within an SEM chamber.

The testing procedure was as follows: (i) each specimen was polished to obtain a good finish on the surface to be visible during the test; (ii) it was coated with gold and slid into the top and bottom pockets of the test jig; (iii) compression was applied until failure could be visually observed; (iv) the whole rig, with the specimen kept under compression, was placed into the SEM chamber for observation. The main advantage of this jig is that it allows for a loaded kink-band to be observed in the SEM, including any out-of-plane displacements, without having interfered with it in any way. The main disadvantage is that it only allows the observation of surface failure.

4.2.3 Polishing test jig

The polishing test jig shown in Fig. 4.3b was used to apply a compressive load to cross-ply and UD specimens. The test jig was designed so that once stable in-plane

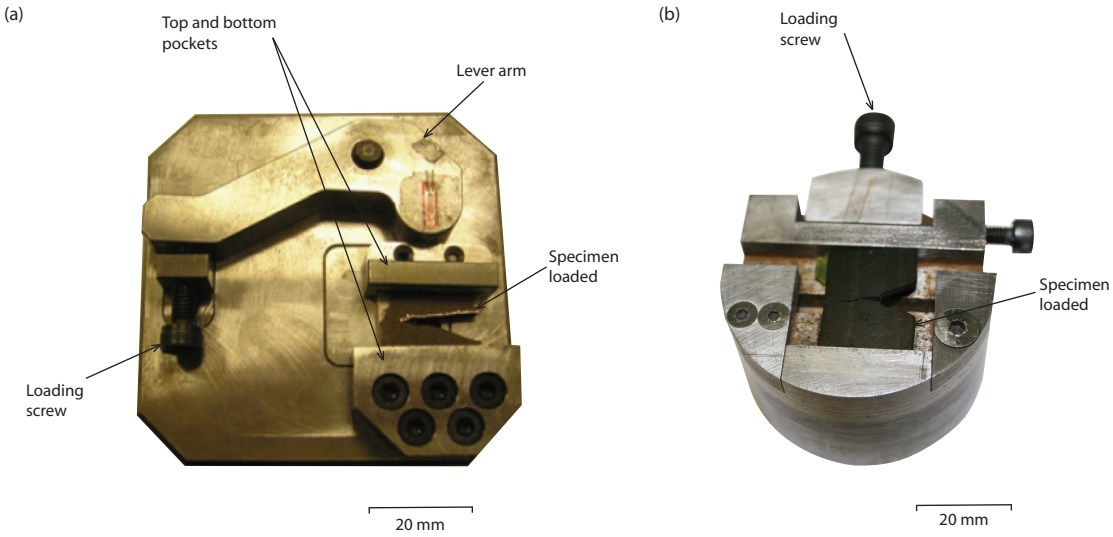


Figure 4.3: (a) SEM test jig; (b) Polishing test jig.

kink-band propagation in the 0° plies was achieved, the outer 90° plies in the cross-ply specimens could be polished off while keeping the specimens under load (i.e. the specimen is never unloaded, not even during polishing, until after the microscopic observation).

The testing procedure for the cross-ply specimens was as follows: (i) each specimen was set into the rig; (ii) compression was applied until failure was observable on the outer plies; (iii) the specimen was kept under load in the rig and the outer layers were polished to reveal the 0° plies; (iv) the failure characteristics in the 0° plies were observed under an optical microscope.

4.3 Longitudinal compressive failure in unidirectional laminates

4.3.1 In-situ observation with the SEM test jig

The micrographs presented in this section are obtained using the procedure detailed in Section 4.2.2, and show loaded specimens.

4.3.1.1 Initiation and propagation

Fig. 4.4a shows a low magnification image of the damage close to the notch tip. Fig. 4.4b presents a line drawing of the main features of the damage and shows the location of the higher magnification images presented in Figs 4.4c-g. The load is applied along the x direction, and the direction of propagation is indicated in Fig. 4.4b.

Ahead of the kink-band tip, Fig. 4.4c, the angle of propagation is shallow $\beta_1 \leq 5\,^\circ$ and the fibres have rotated to $\alpha \sim 18\,^\circ$, deforming in a pronounced sine-wave shape. Few fibres are broken and the kink-band edges are not fully defined. Some fibres appear to buckle out of the plane of the specimen.

In Figs. 4.4d-e, the bottom edge of the kink-band is fully defined with broken fibres. The formation of the top edge of the kink-band lags behind that of the bottom edge by approximately 30 fibre diameters. Fibre rotation has increased to an angle $\alpha \sim 30\,^\circ$ and the kink-band propagates at its final angle $\beta_2 \sim 20\,^\circ$.

The kink-band is fully formed in Fig. 4.4f and the fibres have rotated to $\alpha \sim 40\,^\circ$. It is observed in Fig. 4.4g that they do not rotate further. In this micrograph, a third edge has formed and the kink-band has a V-shape pointing out of the plane of the specimen.

4.3.1.2 Matrix microcracking

From all the micrographs of Fig. 4.4, matrix failure and fibre / matrix splitting can be observed. Figs. 4.5, 4.6 and 4.7 show close-up views of the top-edge, central part and bottom edge of a kink-band, respectively. The microcracks appear to be localised at the fibre/matrix interface as shown in Figs. 4.5 and 4.6 label 'm'. The morphology and accumulation process of those microcracks is similar to cusp formation as reported in Purslow [13]. This is in fact as expected since the stress state in the matrix is shear dominated in the local axes of the kink-band. The microcracks eventually coalesce to form a split as seen in Figs 4.5 and 4.7, label 'c'.

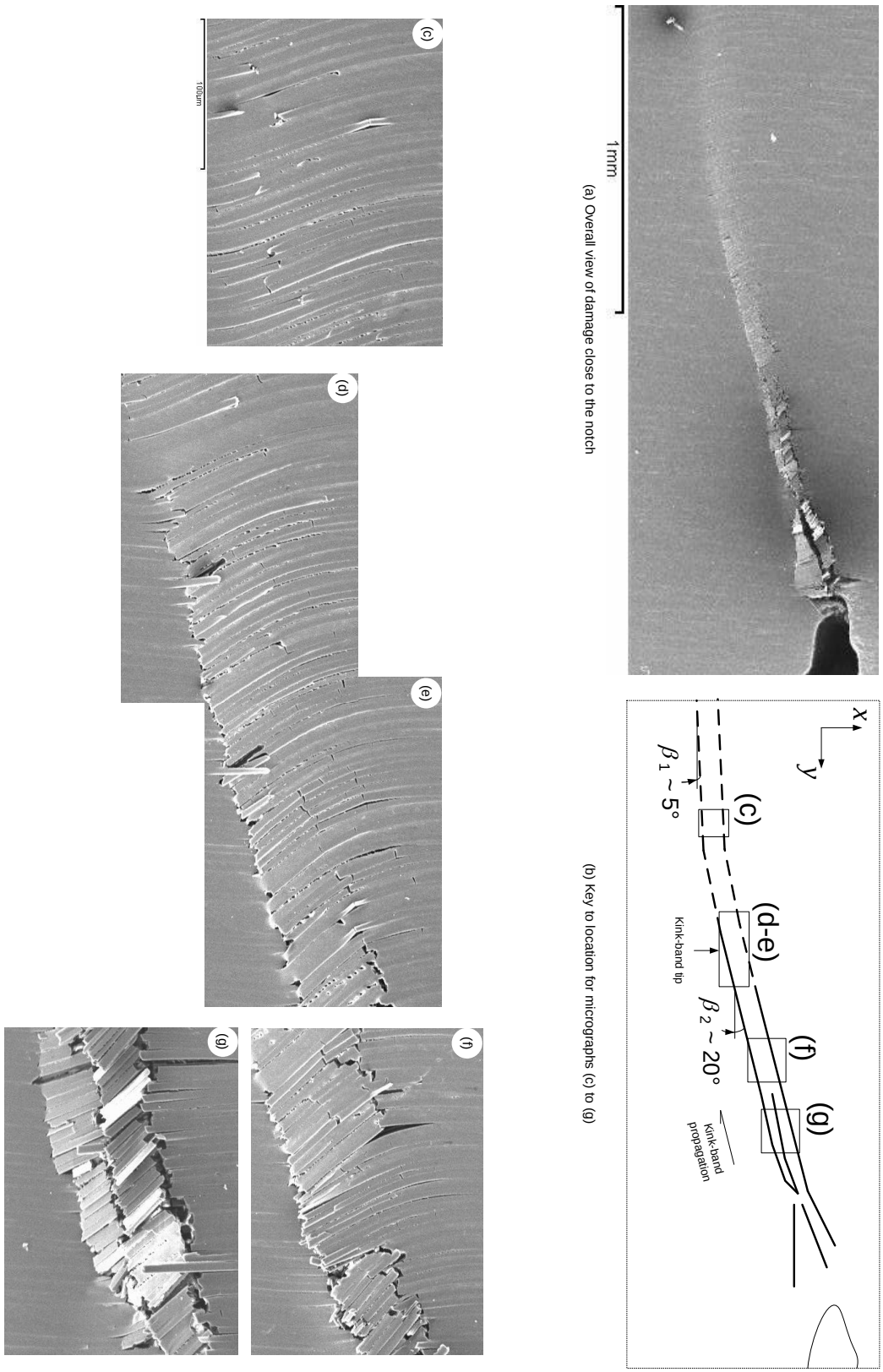


Figure 4.4: Kink-band formation in unidirectional specimen.

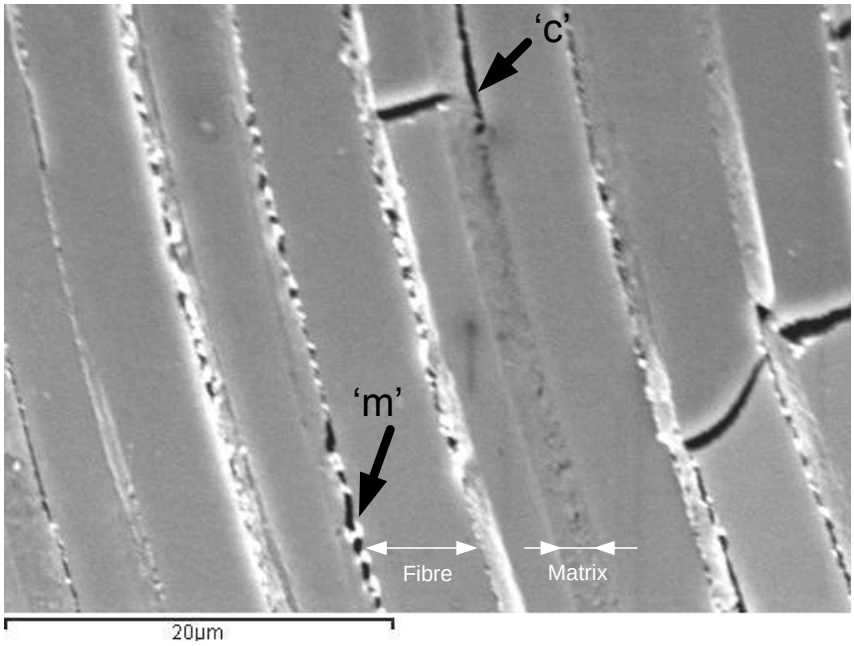


Figure 4.5: Top edge of a kink-band.

In many cases, the splits are open, which indicates that they were formed under tensile traction acting on their fracture plane.

4.3.1.3 Fibre failure

When the kink-band is fully formed its edges are defined by fibre failure; close-up views indicated by labels (1) and (2) in Fig. 4.7 are shown in Figs 4.8a and b, respectively. The fibre shown in Fig. 4.8a corresponds to a stage where the kink-band is not fully defined, and from the micrograph it can be seen that failure has started on one side of the fibre in the form of shear bands. On this side, compressive stresses are maximum, resulting from a combination of both bending and axial compressive stresses.

In Fig. 4.8b, failure on the side of maximum compressive stress has localised on a shear plane. The crack faces slide on each other on this plane, eventually leading

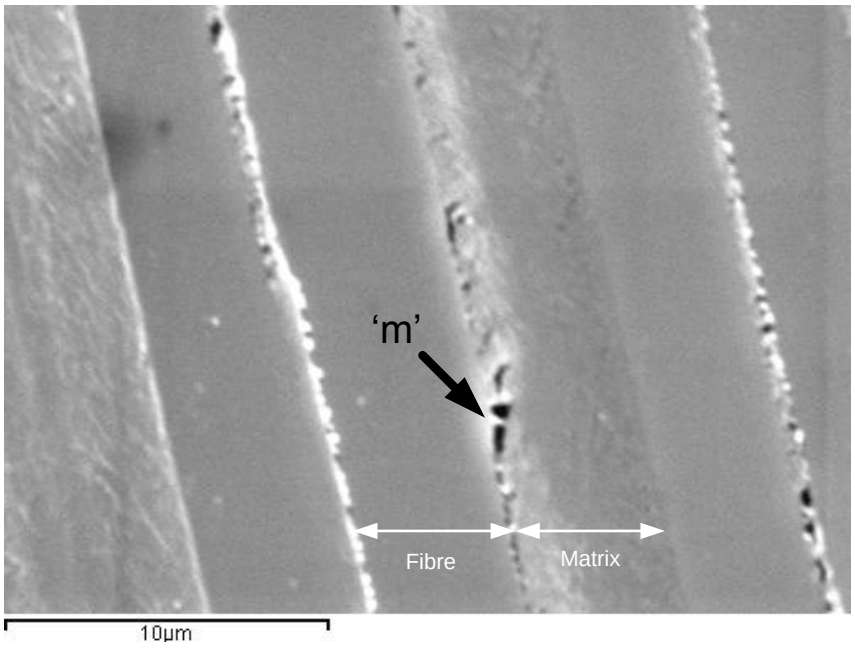


Figure 4.6: Central part of a kink-band.

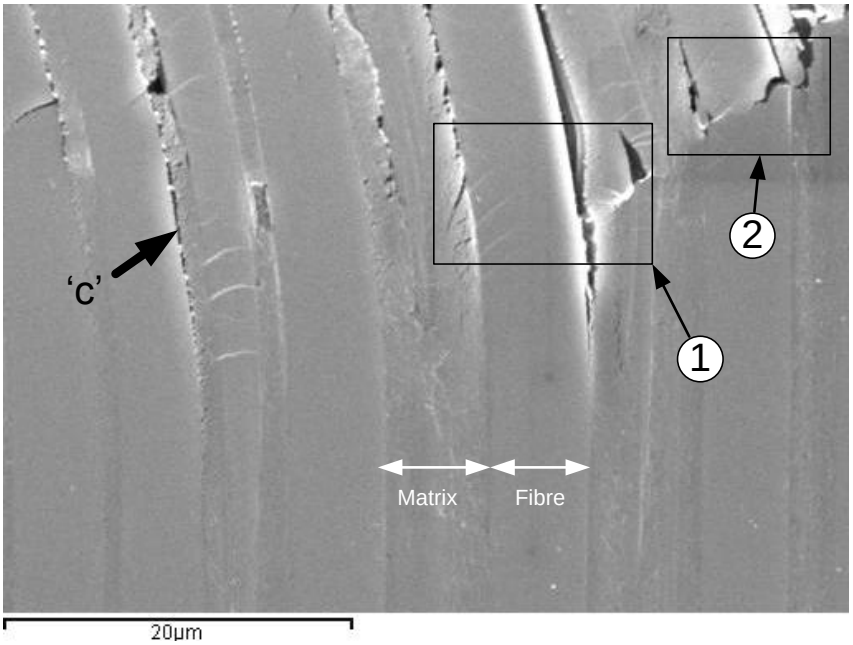


Figure 4.7: Bottom edge of a kink-band.

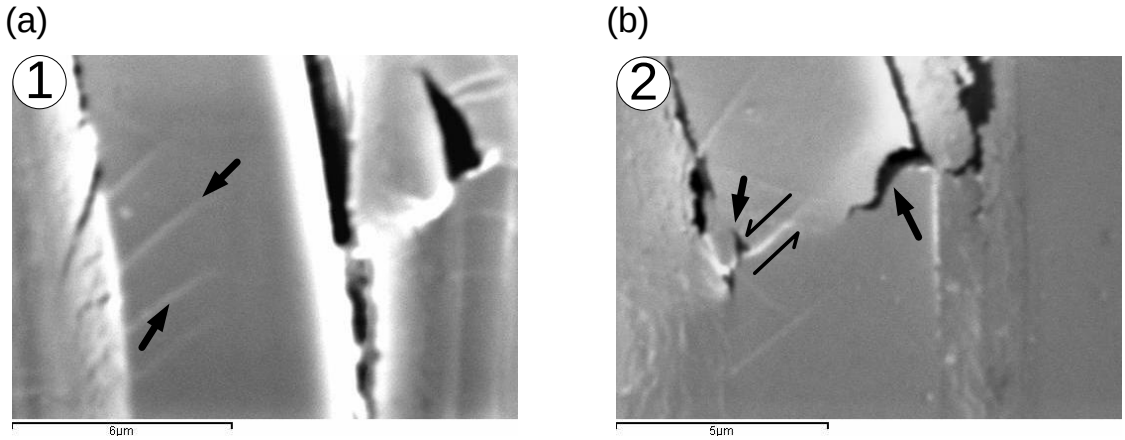


Figure 4.8: Fibre failure at kink-band edge.

to a wedge close to the fibre/matrix interface. Because of the stress redistribution, a crack is formed on the opposite side of the shear crack. This crack is open which indicates that it is driven in the presence of tensile stresses.

4.3.2 In-situ observation with the polishing test jig

Some unidirectional specimens were tested using the procedure detailed in Section 4.2.3. In these specimens, the exact sequence of events (shown in Fig. 4.9) was difficult to infer in a post mortem examination. Shear driven fibre compressive failure of the fibres initiates at the notch and propagates at an angle $\beta \sim 45\,^\circ$ (label (1) Fig. 4.9b), through approximately 20 fibres. Several failure processes take place at the crack tip (label (c) in Fig. 4.9b), which is also shown in the close-up view Fig. 4.9c and schematically represented in Fig. 4.9d. Fibres next to the crack tip are rotated over a length of 3 to 5 fibre diameters, label (2). The first fibre at the tip shows a shear failure at $\sim +45\,^\circ$, label (2), as well as a second lower crack at $\sim -31\,^\circ$, which continues to the next two fibres. At the shear crack tip, the fibre/matrix splits, label (3). It can be seen in Fig. 4.9b that an in-plane kink-band, label (4), and an out-of-plane kink-band, label (5), appear to be connected to the splits originating from the notch tip, label (6), and the shear crack tip, label (3) in Fig. 4.9d.

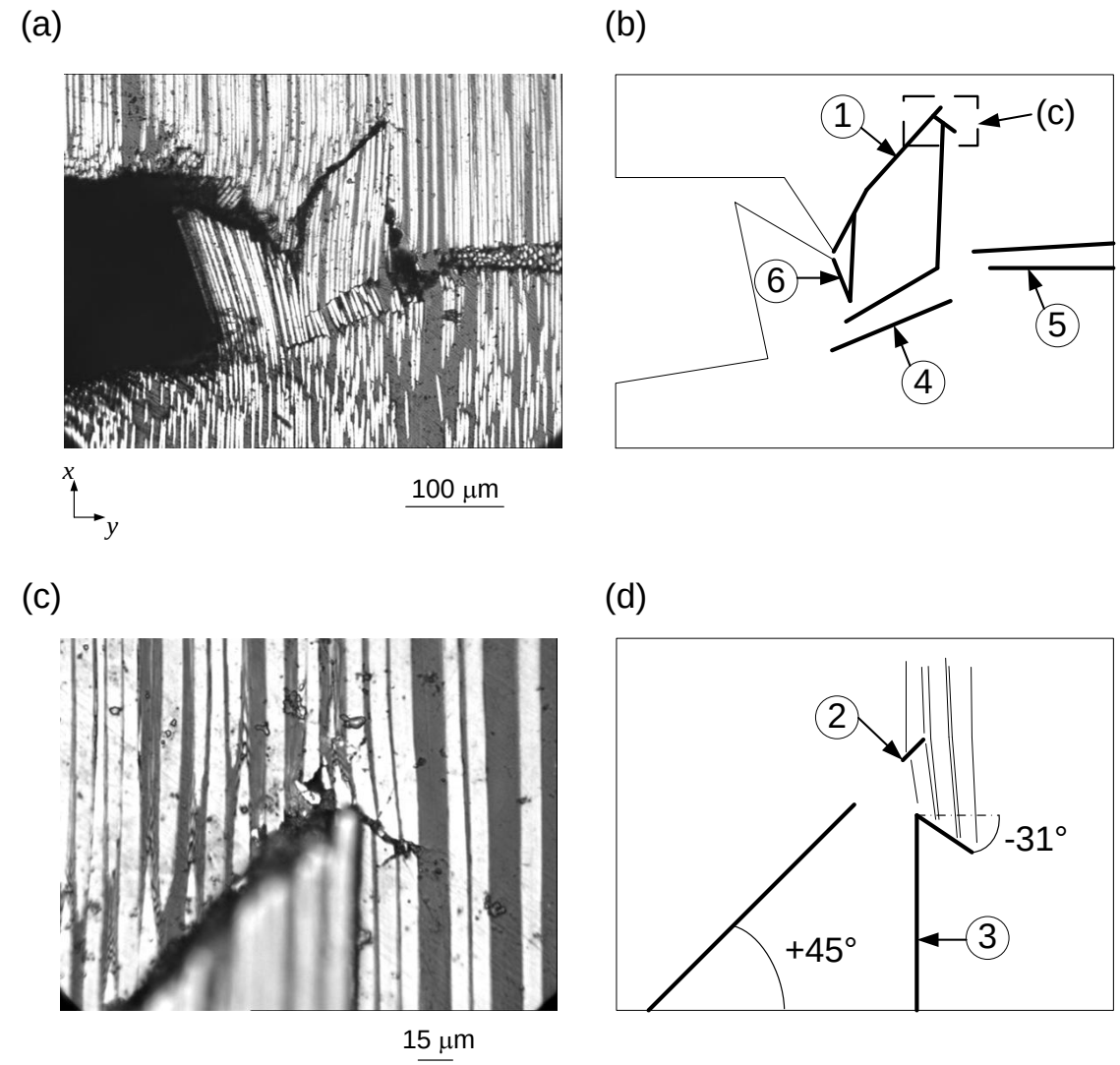


Figure 4.9: Typical kink-band formation at the notch-tip of a UD specimen.

The split, label (6), appears to originate from a wedging effect induced by the sliding of the crack faces on the shear fracture plane, label (1).

4.4 Longitudinal compressive failure in cross-ply laminates

4.4.1 In-plane observations

In cross-ply specimens, three regions showing different fracture patterns can be distinguished, see Figs 4.10a-c. Firstly, failure initiates at the notch tip in the form of shear driven fibre compressive failure and propagates at an angle $\beta \sim 45\,^{\circ}$. This is followed by a region of transition, defined by two edges of broken fibres inclined at an angle $\beta \sim 45\,^{\circ}$. A kink-band is finally formed and propagates in-plane at an angle $\beta \sim 25\,^{\circ}$. The kink-band tip is situated at approximately 2 mm from the transition, with the two edges being formed. Close to the transition, three edges can be observed on the kink-band, in a pattern similar to the one observed in Fig. 4.4g.

During the transition, fibres below the faces of the shear crack are slightly bent, Fig. 4.10d label (1). The upper edge of the failing band is defined by a sharp crack which appears to be the prolongation of the shear failure while the bottom edge appears to be defined by the failure in bending of the fibres, label (2).

4.4.2 Observations on the fracture planes

A specimen in which failure had propagated across the whole width was open so that the fracture planes could be observed with an SEM. Observations are made along the A-A cut shown in Fig. 4.10b. Fig. 4.11a shows the actual fracture plane and Fig. 4.11b a line drawing of the main features of the damage. The load was applied along the x axis and the three regions identified in the $x - y$ plane in Fig. 4.10c are also reported.

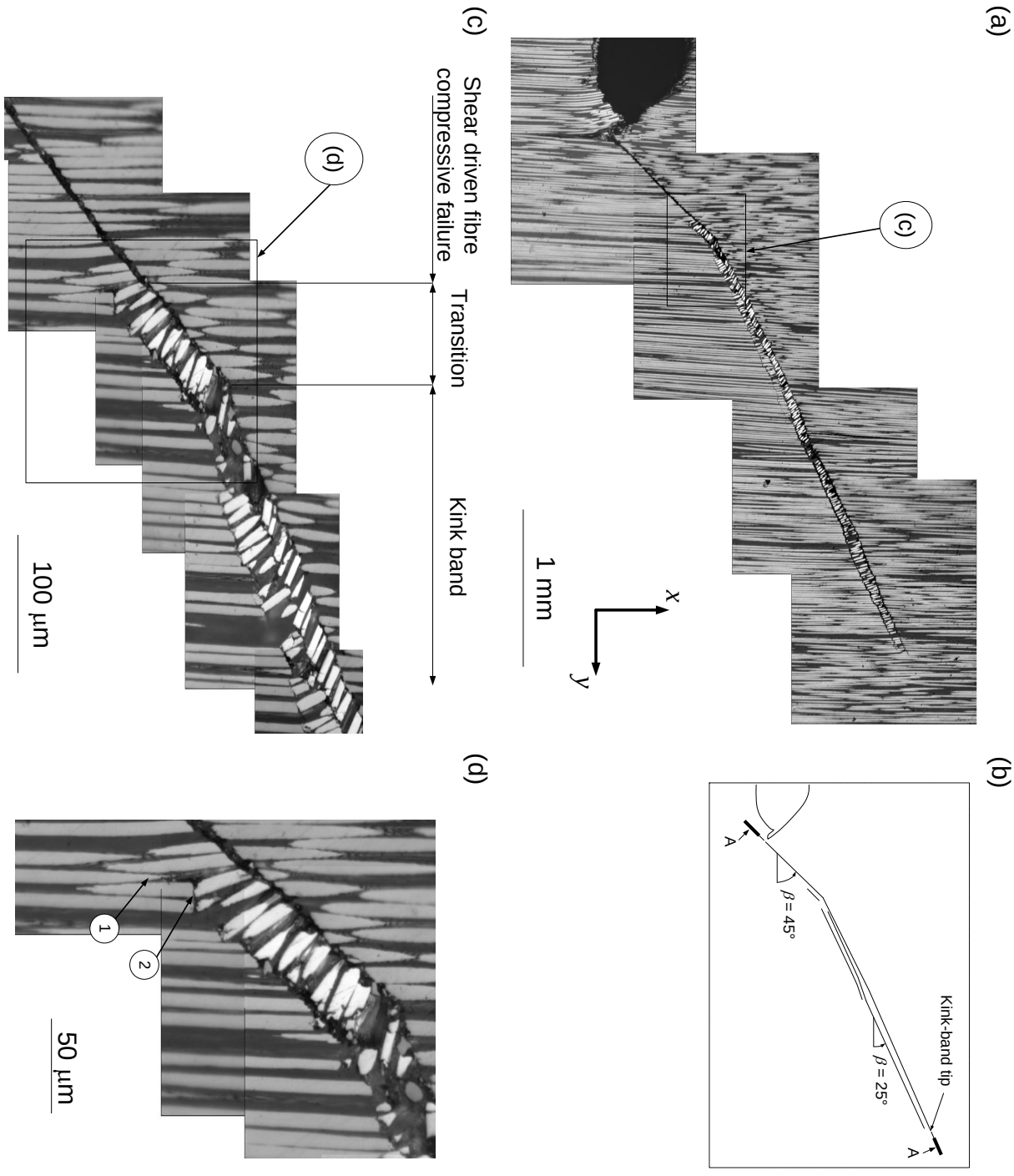


Figure 4.10: Typical compressive fracture process in a cross-ply specimen. (a) Overall view of the fracture process; (b) Schematic of the failure process; (c) Definition of the three different failure patterns; (d) Close-up view of the transition region.

4.4.2.1 Kink-band formation

In the region corresponding to kink-band propagation, step-like patterns can be observed in Figs 4.11a-c. These patterns correspond to the planes defining the boundary of the kink-band, i.e. they define the kink-band edges when intersecting with the $x - y$ plane, as already observed in [17]. In the close-up view, Fig. 4.11d, the segments of broken fibres can be identified.

Fig. 4.11e shows a fibre end on the kink-band plane. Fracture patterns indicate that the fibres fail in bending. The neutral axis defines two sides: (i) one where radial patterns, typical of tensile fracture ('T'), can be observed, (ii) the other side corresponding to compressive failure 'C'.

4.4.2.2 Shear driven fibre compressive failure

Observations of the shear failure on the fracture plane, Fig. 4.11f, show a significant amount of debris as the two faces of the shear crack rubbed on each other. Fibre ends show a smooth fracture surface, which witnesses for the significant abrasion taking place on this fracture plane.

4.5 Discussion

4.5.1 Representativeness of the in-situ tests

The procedure followed for the in-situ observations on the unidirectional specimens may introduce artefacts that are not representative of the core material behaviour. The specimens were polished so that the observations could be facilitated; however, such a practice modifies the geometry of the fibres close to the surface, as shown in Fig. 4.12. The fibres close to the surface have their cross section (and bending stiffness) reduced, which means their buckling load is reduced. Such out of plane buckling of the fibres can be seen in the top part of Fig. 4.4c.

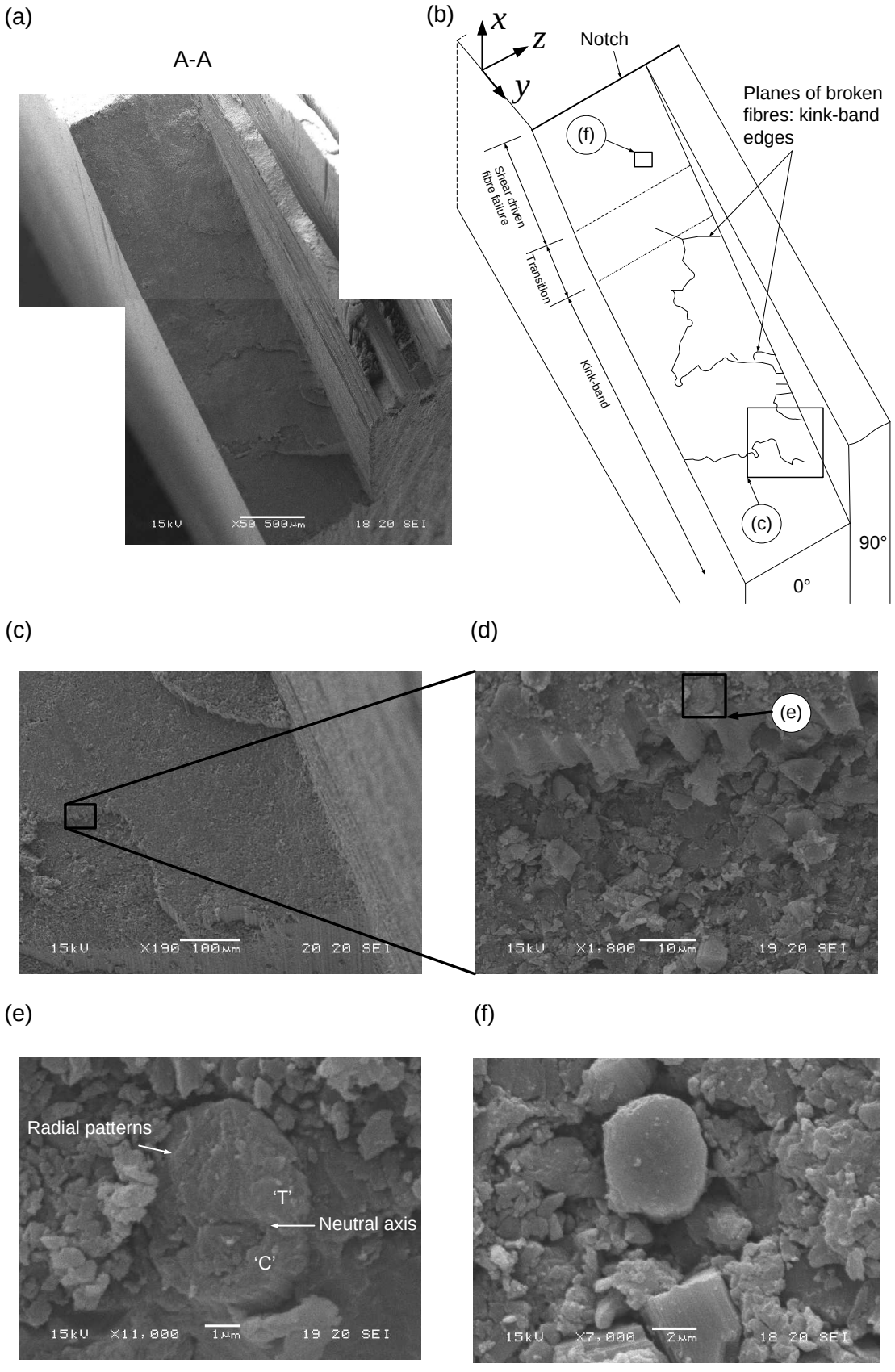


Figure 4.11: Fracture plane A-A on cross-ply specimen.

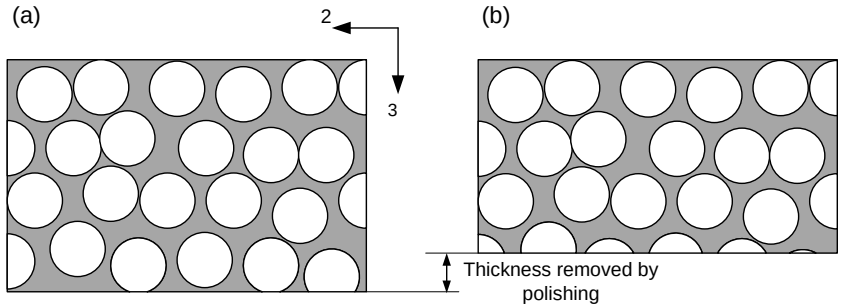


Figure 4.12: Effect of polishing.

A similar phenomenon is probably at the origin of the V-shape observed in Fig. 4.4g. Once the fibres have rotated to their final angle $\alpha \sim 45\,^\circ$ and have failed at the edges, compressive stress are still transmitted across the kink-band and the fibres probably snap in the 3 direction, as the outer layers are not supported. It should be noted that a similar pattern is observed in the inner $0\,^\circ$ layers of the cross-ply specimens as seen in Figs 4.10c and d. In that case, some local delamination around the kink-band tip may take place, such that fibre segments in the kink-band are not supported in the 3 direction by the adjacent $90\,^\circ$ plies.

4.5.2 Microcracking

The role of the matrix during kink-band formation is important as it supports the fibres and controls their rotation. As shown in Figs. 4.5, 4.6 and 4.7, matrix failure takes place in a region close to the fibre/matrix interface and shows patterns similar to the ones observed in shear, i.e. cusp formation as explained in [13]. The microcracks accumulate, coalesce and finally separate from the fibre.

An important outcome of such observations is that stress based criteria to predict kink-band initiation may not be representative of the physical failure process, but a criterion based on an energy balance might be more appropriate.

4.5.3 Fibre failure at kink-band edge

As before, observations made on fibre failure in Fig. 4.8 should be treated carefully as they are made on a free surface. The fibres at the kink-band edge are subjected to compressive stresses due to bending and the applied compressive load, which

triggers the formation of a shear band on the side of maximum compressive stress. As the shear crack propagates, the fibre hinges around the shear crack tip. The increased rotation means that tensile stresses are produced on the other side of the fibre and an opening crack is formed.

4.5.4 Kink-band propagation angle

The kink-band propagation angle β observed in the experiments on unidirectional specimens (Fig. 4.4) is relatively small at kink-band initiation, which would indicate that it does not need to be accounted for predicting fibre kinking strength, as long as no kink-band propagation has taken place at the maximum load. This point is confirmed in the numerical study presented in the next chapter and in Appendix C.

4.5.5 Shear driven fibre compressive failure

From both unidirectional and cross-ply specimens, it appears that failure initiates by compressive shear failure of the fibres at the notch tip. In this region, shear driven fibre compressive failure is promoted by the large compressive stresses with small rotation of the fibres. As the shear driven fibre compressive failure propagates, the faces of the shear crack slide on each other inducing bending of the fibres ahead of the crack tip (Fig. 4.13b), which promotes kink-band formation (Fig. 4.13c).

Similar observations were made by Crasto and Kim[20] in unidirectional AS4 - epoxy composites axially compressed in an un-notched mini-sandwich setup. They observed that shear driven fibre compressive failure of the fibres initiate at the edge of the specimen—where the in-plane shear stress τ_{xy} is zero because of the free edge—and, after some propagation, the failure mechanism changes to kink-band formation.

This similarity also suggests that the failure process should be fairly notch insensitive: in the present case, the notch is sharp (radius ~ 0.05 mm) while Crasto and Kim [20] describe identical sequence of events in un-notched unidirectional specimens.

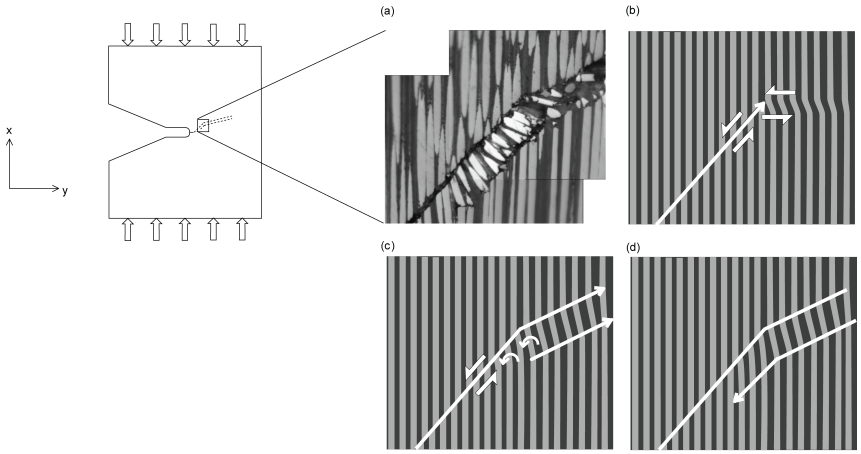


Figure 4.13: Sequence of events at the transition.

4.5.6 Transition

An explanation for the formation of the transition region, Figs 4.10c and 4.13a, is proposed here. The shear crack formed at the notch propagates first. As the crack faces slide on each other, fibres rotate ahead of the shear crack, Fig. 4.13b. Because of this rotation and of the longitudinal compression, a kink-band forms as shown in Fig. 4.13c. However, as the specimen is loaded further, the friction force created on the shear crack faces leads to a rotation of the fibres on the lower part of the crack, and eventually these fibres fail due to bending and axial compressive stresses, along a line parallel to the 45° shear crack, Fig. 4.13d.

4.5.7 Role of the 90° plies and delamination

Figs. 4.9 and 4.10 show similar failure processes; however, in the unidirectional case, the shear crack propagates over a shorter distance. It is reasonable to assume that the presence of the 90° plies can delay the splitting in the 0° plies as it constrains the rotation of the fibres and postpones the transition to kink-band formation.

Delamination between the 0° and 90° plies can reduce the support of the 90° plies, but obtaining experimental evidence of the role of delamination is challenging and should be looked at in more detail in the future.

4.6 Conclusions

In the present work, in-situ and post-mortem fractography has revealed that shear driven fibre compressive failure and kink-band formation could both occur in longitudinal compressive failure of carbon epoxy composites. Those two types of failure were found in unidirectional and cross-ply notched laminates. The typical sequence of events is: initiation of the shear driven fibre compressive failure at the notch tip—promoted by large compressive stresses and small fibres rotation; sliding of the crack faces induces bending of the fibres ahead of the crack tip and promote kink-band formation.

The 90° plies in the cross-ply specimen were found to inhibit splitting and to constrain fibre rotation and so result in postponing the transition to kink-band formation.

The role of matrix microcracking during kink-band formation was also highlighted. Microcracks form in-between fibres; the cusp-like shape indicate shear failure of the matrix. It was shown that the edges of the kink-band were defined by bending failure of the fibres first on the side of maximum compressive stress. Because of the stress redistribution, a crack initiates on the other side. The opening of this crack indicates it is driven by tensile stresses.

4.7 Publications

The work presented in this chapter resulted in the following publications:

On the transition from shear-driven fibre compressive failure to fibre kinking in notched CFRP laminates under longitudinal compression. R. Gutkin, S.T. Pinho, P. Robinson and P. T. Curtis. Composites Science and Technology, 2010, 70, 1223-1231.

In collaboration with Ms. Soraia Pimenta, during her MSc Project, kink-band formation was experimentally investigated using other test setups. The findings from this study are presented in Appendix C and published in:

A micromechanical model for kink-band formation: Part I—Experimental study

and numerical modelling. S. Pimenta, R. Gutkin, S.T. Pinho and P. Robinson. Composites Science and Technology, 2009, 69, 948-955.

Chapter 5

Micro-mechanical modelling of longitudinal compressive failure for failure envelope generation

5.1 Introduction

Longitudinal compressive loading plays an important role in predicting the damage tolerance of structural components using Fibre Reinforced Plastics (FRP). For typical carbon/epoxy UD tape systems, the longitudinal compressive strength is about half the tensile strength, which constitutes a limiting factor in design. This gap can increase when multi-axial loadings are considered, in particular the longitudinal compressive strength is significantly reduced when in-plane shear stresses act in combination of the compressive stress. Currently, deducing a universal trend for the failure envelope from either experimental results or analytical models is a challenging task.

Experimental determination of the failure envelope for a case of combined in-plane shear / longitudinal compression is a complex, time consuming and material consuming process. Different types of setups (e.g. cruciform test setup or torsion / compression of tubes, see [104] for a review) can be used to obtain the failure envelope. However, obtaining the required stress state is challenging because of free

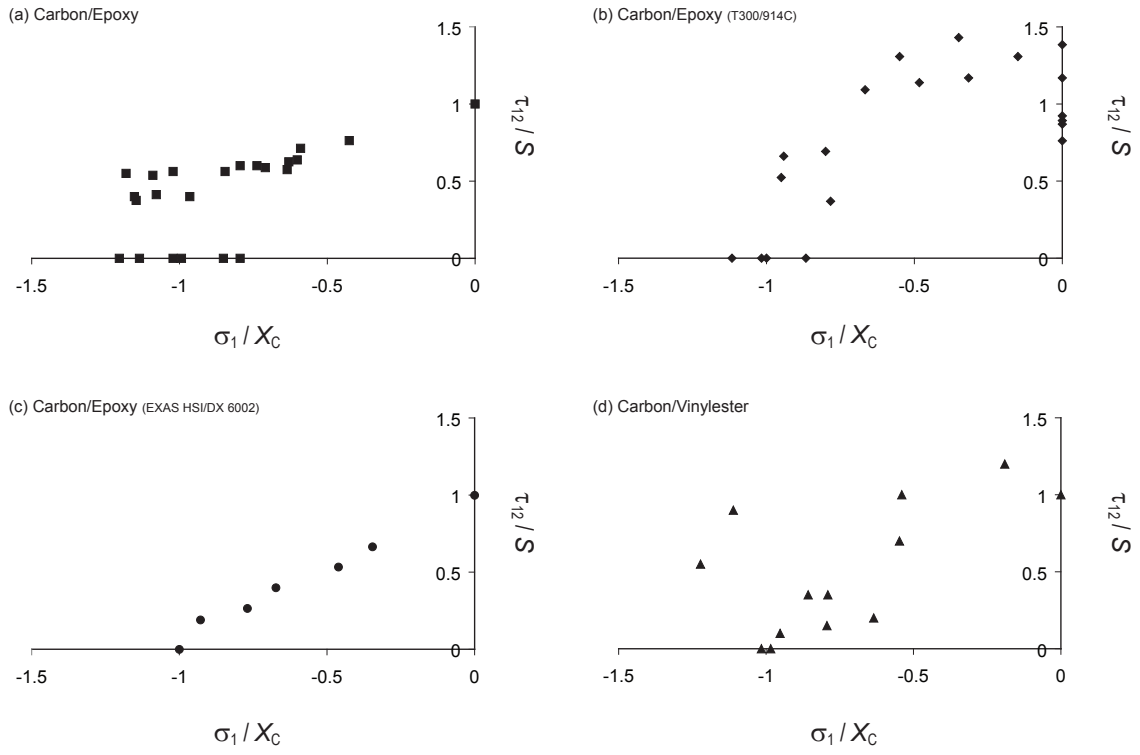


Figure 5.1: Failure envelopes from the literature: (a) Michaeli et al. [102], (b) Soden et al. [37], (c) Jelf and Fleck [22], (d) Yerramalli and Waas [38].

edge effects or changes in geometry. Several tests must be done for each point of the failure envelope as strength results in longitudinal compression are particularly sensitive to material defects and imperfections of the testing setup, resulting in large scatter.

Fig. 5.1 shows a reproduction of four failure envelopes, determined experimentally by torsion/compression of tubes, found in the literature [22, 37, 38, 102]. The values are non-dimensionalised by the shear and longitudinal compressive strengths (S and X_c respectively) of each material. The results from all studies show significant scatter, and the trends followed by the failure envelope differ from one study to the other.

The same disparity is found when the trends predicted by several failure criteria, available in the literature [30, 65, 68], are compared, as shown in Fig. 5.2. The failure

envelopes predicted by the maximum stress and Puck's [68] criteria are defined by two curves: the first one is a line parallel (or nearly) to the τ_{12}-axis (the compressive strength is not, or slightly, affected by the shear stress), the second curve is a line parallel to the σ_1-axis (constant shear strength). The Tsai-Wu [65] criterion defines, as expected, an elliptical failure envelope. Finally, the LaRC05 fibre kinking criterion [30] defines either a linear failure envelope, when the composite is assumed to behave linearly in shear, or is slightly concave, when the nonlinear behaviour of the composite in shear is accounted for.

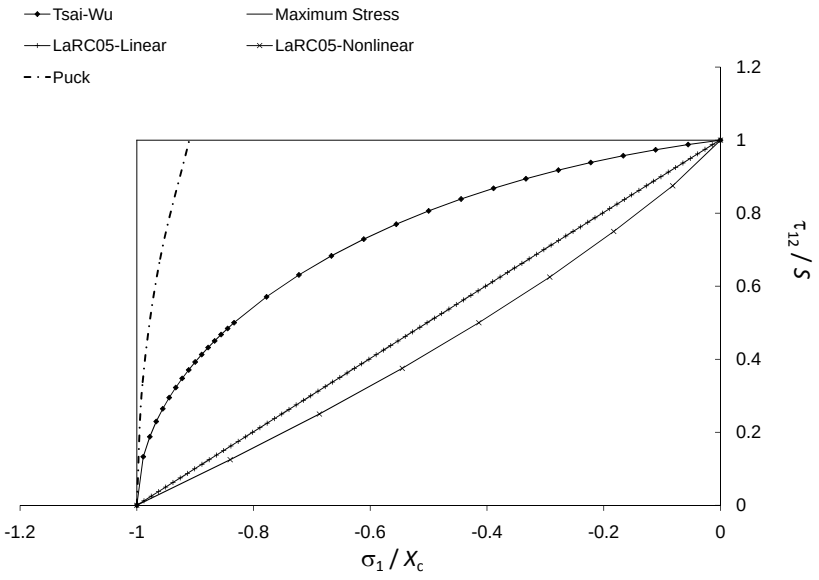


Figure 5.2: Trends predicted by: the maximum stress criterion; the Puck's criterion [68]; the Tsai-Wu criterion [65]; the LaRC05 criterion [30].

To determine the failure envelopes, an alternative to experimental or analytical work is the use of Finite Element (FE) analysis. FE analysis offers the advantage to identify parametric trends which are difficult to infer in the experimental results due to the observed scatter.

Micromechanical FE models have been used by Kyriakides et al. [31], Pimenta et al. [105] and Guynn et al. [32] to understand the mechanisms underlying kink-band formation and as a basis to develop analytical models for the prediction of

the longitudinal compressive strength as well as the kink-band parameters. In [31] and [105] several layers of fibres and matrix—the matrix is typically modeled with an elasto-plastic behaviour—initially misaligned are compressed until a kink-band forms. In Guynn et al. [32], the model is reduced to a unit cell of a layer of matrix sandwiched between two half-fibres and periodic boundary conditions are applied.

Those models assume that failure in longitudinal compression is due to kink-band formation. However, and as shown in the previous chapter, shear driven fibre compressive failure can also be found. This was also demonstrated by Ewins and Ham [72] who proposed that the longitudinal compressive strength can be derived using Eq. (2.16).

In the present work, a micromechanical FE model of a composite unit cell is detailed. Predictions of failure envelopes under combined in-plane shear / longitudinal compression are presented and the different failure mechanisms found at different stress states are discussed. A comparison with some of the experimental results shown in Fig. 5.1 is also given. In particular, the model is used to explain the different trends typically observed in the experiments. The failure mechanisms highlighted here correlate with the experimental observations of the previous chapter.

5.2 Micromechanical FE model

5.2.1 Model setup

The geometry, boundary conditions and loads applied on the FE model used in the present work are shown in Fig. 5.3. The model represents a unit-cell of the composite, with a layer of matrix sandwiched between two half fibres. The choice of the present unit cell has three important implications: (i) the initial misalignment of the fibres in the composite is uniformly distributed; (ii) the choice of the length L could affect the predictions; and (iii) up to initiation, the fibres deform in-phase. Regarding (i), the effect of various fibre distributions on kink-band formation has been studied by Kyriakides et al. [31] and it was found that the distribution affects

the value of the strength but does not change the formation process. The second (ii) implication results in a need to parametrically verify the influence of L, which is done below. For the third implication, from Fig. 4.4c in Chapter 4, it can be seen that the fibres at the kink-band tip, i.e. at initiation, deforms in-phase at a very small angle β to the y-axis. Below, it is verified that neglecting β does not change the predictions by comparing the results from the unit cell model to a model containing 100 fibres.

The periodic boundary conditions are applied on each side of the fibre as follows

$$\forall x \in [0, L] : \begin{cases} u(x, y = d) = u(x, y = 0) \\ v(x, y = d) = v(x, y = 0) - U \end{cases}, \tag{5.1}$$

where d and L are the height and length of the model. The constant U accounts for the transverse expansion caused by the compressive load.

Shearing forces are applied at $x = 0$ and $x = L$. A compressive displacement is applied at $x = L$, while the displacements in the 1-direction are restricted at $x = 0$. For the compression step, the Riks algorithm is used such that potential snap-back or snap-through can be captured.

Plane stress (CPS4R) elements, with a 1 mm thickness, are used. The material properties for the baseline model correspond to those of the IM7/8552 system, which are reported in Table 5.1. The baseline model is used in the parametric study and unless stated otherwise. For this baseline model, a nonlinear elasto-plastic behaviour is used for the matrix. The nonlinear shear curve for the matrix is back-calculated from the nonlinear shear curve of an IM7/8551-7 composite (given in [30]) and as shown in Fig. 5.4. When the effect of the constitutive response of the matrix on the failure envelope is investigated, an elastic perfectly-plastic model is used with the properties shown in Table 5.1. A fracture energy-based damage model implemented in ABAQUS [83] is used for the fibres, with only fibre tensile and compressive modes activated. The maximum stress criterion is used to predict failure onset and the toughness of the fibres is taken as in [106].

To define the failure envelopes, the longitudinal compressive strength is defined

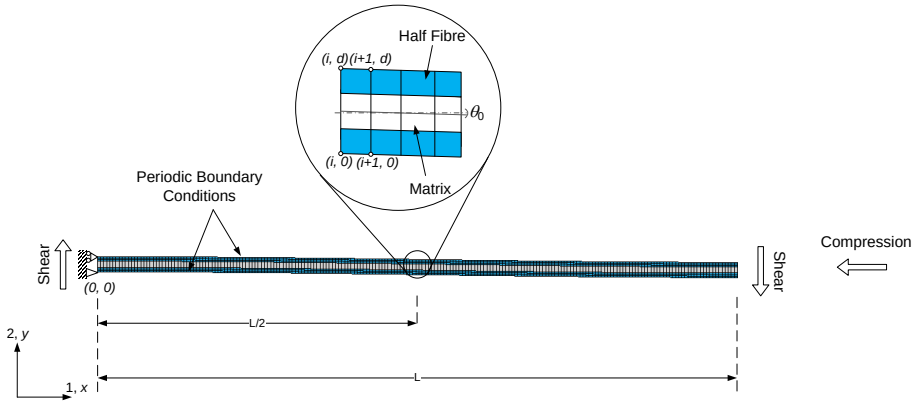


Figure 5.3: Micromechanical FE model: geometry, boundary conditions and loading.

as the peak load reached during the compression step.

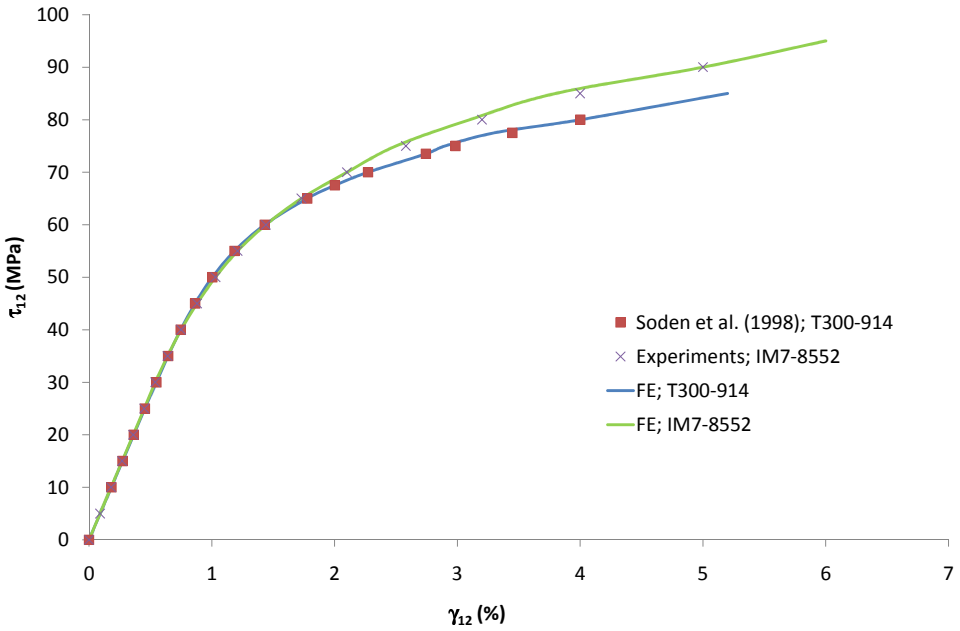


Figure 5.4: Shear stress versus shear strain curves.

Table 5.1: Input parameters used in the FE model

Table	IM7-8552	T300-914	EXAS HSI - DX 6002
Fibre diameter ϕ_f (μm)	7	7	7
Fibre Young's modulus E_f (GPa)	276	231	276
Fibre Poisson's ration ν_f	0.3	0.3	0.3
Fibre compressive strength X_c^f (MPa)	3200	1330	2140
Fibre compressive toughness G_{Ic}^{fc} (J/m^2)	7	7	7
Initial misalignment θ_0	0°	$0.5^\circ/1.5^\circ$	4°
Matrix shear modulus G_m (GPa)	1.4	1.5	1.5
Matrix yield stress τ_Y (MPa)	80/90/100	95/125	75

5.2.2 Model validation

To ensure that the geometrical representation and boundary conditions defined for the FE simulation do not influence the model predictions, the effects of the model length, the fibre volume fraction and the periodic boundary conditions are investigated.

The length L of the model needs to be big enough to allow kink-band formation—typical kink-band widths are in the range 10 to 30 fibre diameters—and as short as possible to be computationally efficient. Ultimately, the failure envelope should be independent of L. Fig. 5.5 shows predictions for $L = 100\ \mu$m $= 14$ fibre diameters, $L = 500\,\mu$m $= 71$ fibre diameters and $L = 10,000\,\mu$m $= 14,320$ fibre diameters. It can be seen that the predictions converge to the same failure envelope for $L \geq 500\,\mu$m. For the shortest model, geometric hardening of the model occurs for large shear stresses and induce an asymptotical behaviour of the failure envelope when $\sigma_1 \to 0$. For the rest of the investigation, the model with $L = 500\,\mu$m is used as this is a converged length.

For convenience in the discussion of the results, the failure envelope is divided in two regions, as shown in Fig. 5.5: region *I*, where the compressive strength is just slightly affected by the shear stress and region *II*, where the decrease in compressive strength with the shear stress is more significant.

Because the present FE model represents a 2D slice of a 3D composite, the fibre

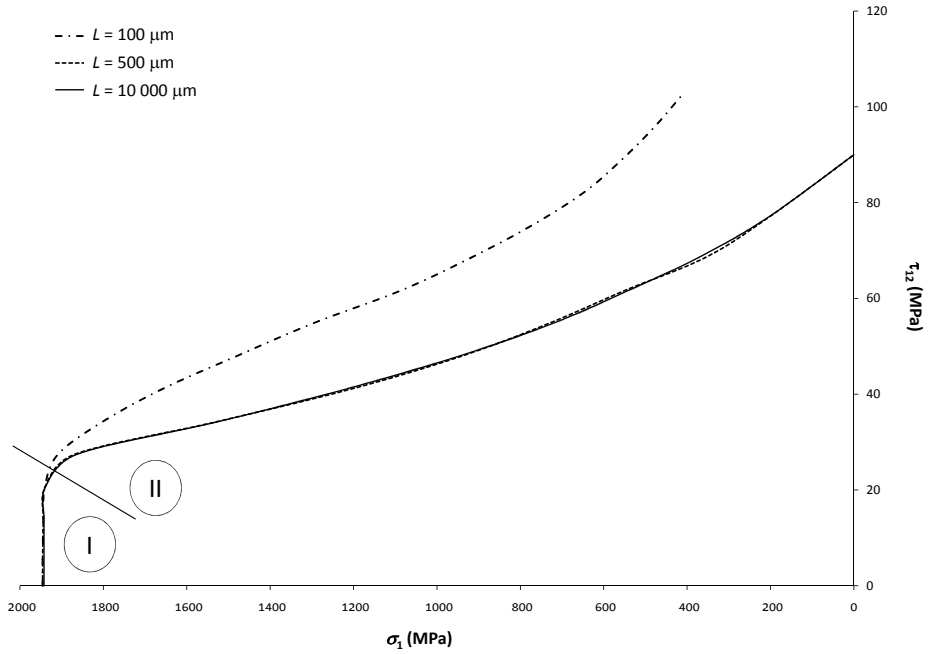


Figure 5.5: Effect of the length of the model (L) on the predicted failure envelopes.

volume fraction of the model can be chosen so that: (i) the fibre volume fraction of the 2D model equals the actual fibre volume fraction, $v_f^{2D} = v_f$; (ii) it represents an hexagonal fibre arrangement $v_f^{2D} = \sqrt{\frac{2\sqrt{3}}{\pi} v_f}$ or (iii) the bending stiffness of the fibre layer equals the bending stiffness of an actual fibre, $v_f^{2D} = v_f$ and $\phi_f^{2D} = \left[\frac{12}{64}\pi\phi_f^4\right]^{1/3}$, where ϕ_f is the fibre diameter.

As shown in Fig. 5.6, the model with assumptions (i) and (iii) yield the same predictions while the model with the hexagonal arrangement (ii) gives less conservative predictions in region *II*. Nevertheless, in all three cases the trend of the failure envelope remains unchanged, with regions *I* and *II* being well defined. For the rest of the study, assumption (i) is kept as it enhances the effect of the matrix behaviour in region *II* (due to the larger thickness of the matrix layer) and does not significantly affect the predictions in region *I*.

Typical kink-band propagate at an angle $\beta \sim 20\,^\circ$ perpendicular to the fibre direction as shown in the previous chapter. Using periodic boundary conditions means that this angle β is indirectly set to $0\,^\circ$. To evaluate what effect the periodic

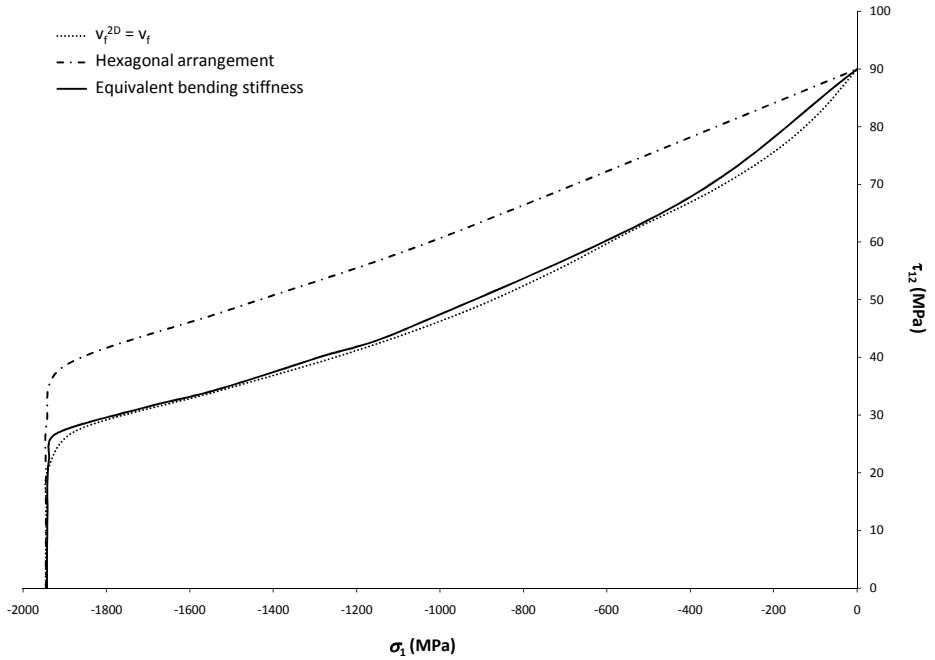


Figure 5.6: Effect of the volume fraction chosen for the FE model on the predicted failure envelopes.

boundary conditions have on the failure envelope predictions, the model used in [105], and shown in Fig. 5.7, is adapted here for biaxial loading and used with 100 fibres. The results in Fig. 5.7 show that both models yield the same predictions. Therefore, periodic boundary conditions can be used to reduce the computational size of the model.

5.3 Parametric failure envelope prediction

5.3.1 Effect of the matrix behaviour

In region *II* of the failure envelope, the type of behaviour chosen to represent the matrix plays an important role. Fig. 5.8 shows the failure envelopes predicted when: (i) the matrix has a nonlinear elasto-plastic constitutive response, (ii) the matrix has an elastic perfectly-plastic response.

The shape of the envelope in region *II* is modified from a linear to a concave curve when the matrix behaviour is changed from (ii) to (i). As shown in Fig.

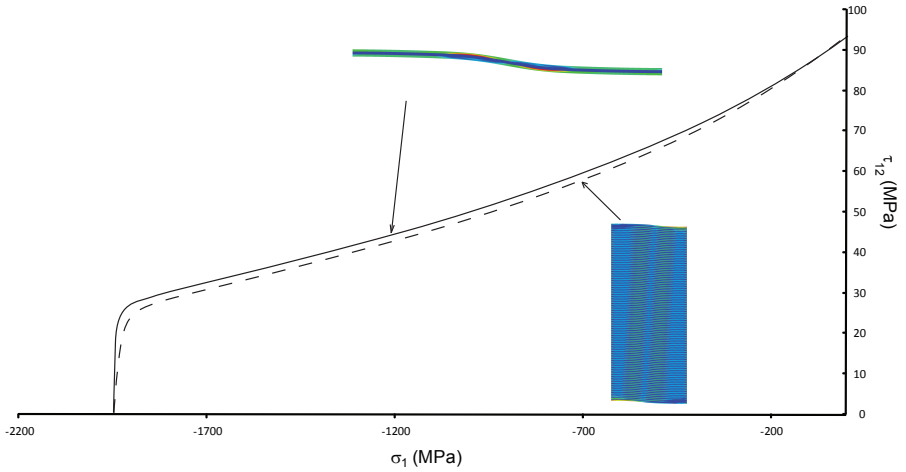


Figure 5.7: Effect of the periodic boundary conditions on the predicted failure envelopes.

5.8, modifying the yield strength has an effect on the shear stress at the transition between region *I* and *II* and changing the shape of the shear stress-strain curve has an effect on the concavity of the curve.

The shear strength of the resin (and of the composite) also affects the predictions. To see clearly this effect, the failure envelopes given in Fig. 5.8 are predicted using an elastic perfectly-plastic behaviour of the matrix and shear strengths of 90 and 100 MPa. The slope of the lines defining region *II* are not modified when the shear strength is changed; they move parallel to each other.

5.3.2 Effect of the compressive strength of the fibres

Failure envelopes for two values of the fibre compressive strength ($X_c^f = 3200$ MPa and $X_c^f = 6400$ MPa) are shown in Fig. 5.9. The case $X_c^f = 6400\,\text{MPa}$ is the limit case where region *I* vanishes completely. A decrease in the strength of the fibre results in a similar decrease in the compressive strength of the composites in region

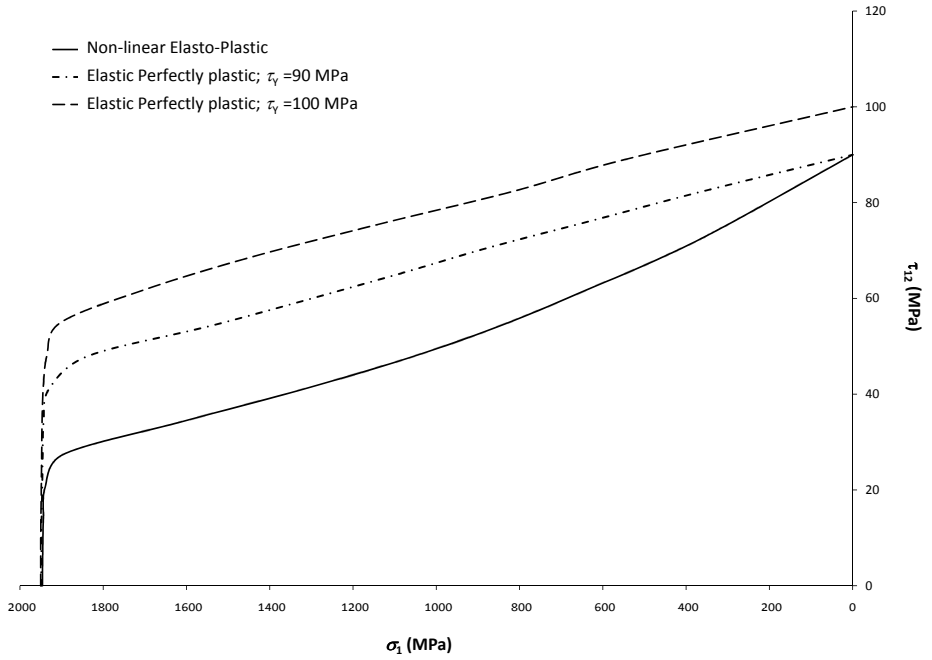


Figure 5.8: Effect of the constitutive response of the matrix on the predicted failure envelopes.

I. For $\tau_{12} = 0$, the rule of mixture applies and the longitudinal compressive strength of the composites follows Eq 2.16 (and replacing $2S^f$ by X_c^f).

Region *II* of the failure envelope is unchanged.

5.3.3 Effect of initial fibre misalignment

The effect of an initial fibre misalignment in the model (θ_0) is investigated. As seen in Fig. 5.9, the initial misalignment controls region *II* of the failure envelope. As a consequence, region *I* of the failure envelope is reduced when θ_0 increases, and eventually vanishes (in this case for $\theta_0 \geq 1\,^\circ$).

Fig. 5.10 shows the pure longitudinal compressive strength as a function of the misalignment angle for the FE model and the LaRC05 fibre kinking criterion [67]. The two predictions agree well when the misalignment is large enough for the failure envelope to be only defined by region *II* but the LaRC05 criterion overestimates the strength for low values of θ_0.

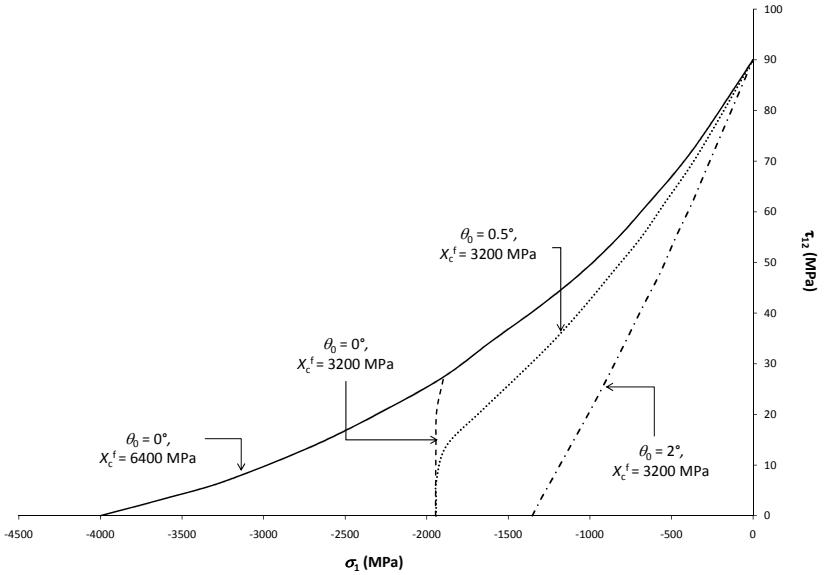


Figure 5.9: Effect of the fibre compressive strength (X_c^f) on the predicted failure envelopes.

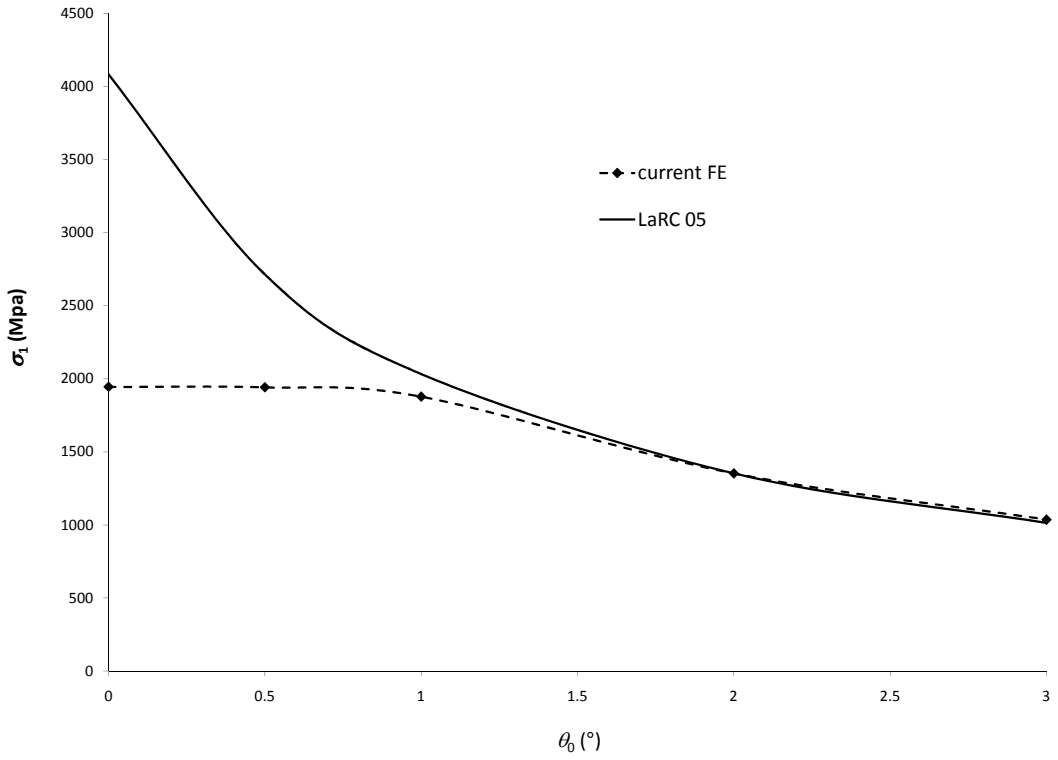


Figure 5.10: Longitudinal compressive strength against misalignment: FE and LaRC05 fibre kinking predictions.

5.3.4 Global model behaviour

Fig. 5.11 shows the stress-strain (σ_1 versus ε_1) curves, the axial stress distribution along the fibres (at the interface with the matrix), $\left(\sigma_1^f\right)$, and the deformed shape for the baseline model for several values of applied shear stress τ_{12} (the deformed shapes and stress distributions are taken close to the peak stress, as shown by the circles in Fig. 5.11).

For small values of τ_{12} in region *I*, shown in Fig. 5.11a, the model shows a perfectly linear behaviour until a drop in the applied stress corresponding to fibre failure. In Figs 5.11b-d, the model shows a linear behaviour for low values of τ_{12} and some nonlinearities before the peak stress for higher values of shear stresses. The model snap-backs after the peak stress and both the axial stress distribution and the deformed shape show some localisation corresponding to kink-band formation. In Fig. 5.11e, a kink-band is still forming but the model does not snap-back. Finally in Fig. 5.11f, the stress-strain curve does not have a peak stress, the deformed shape shows no sign of localisation and no kink-band is formed.

The distance between the two points of maximum difference in the axial stress distribution, called w and defined in Fig. 5.11, has been measured against the applied shear stress. The axial stress distributions $\left(\sigma_1^f\right)$, Fig. 5.11, for the model with a length $L = 500\mu$m show some edge effects close to the localisation, therefore, w has also been measured in a longer model with $L = 2000\mu$m, where the edge effects are away from the localisation. The longer model is used to produce the graph in Fig. 5.12 (w is non-dimensionalised by the fibre diameter ϕ_f) as both models give identical results, except for pure shear where there is no localisation and w tends to the length of the model. The curve is divided in two sections: (i) w is constant ($\sim 12\,\phi_f$) for $25\,\text{MPa} \leq \tau_{12} \leq 70\,\text{MPa}$; (ii) w increases with τ_{12} between $\tau_{12} = 70\,\text{MPa}$ and $\tau_{12} = 85\,\text{MPa}$. It is reasonable to assume that the transition at which the width increases defines the limit between kinking and splitting, and for this model lies between $70\,\text{MPa} \leq \tau_{12} \leq 80\,\text{MPa}$.

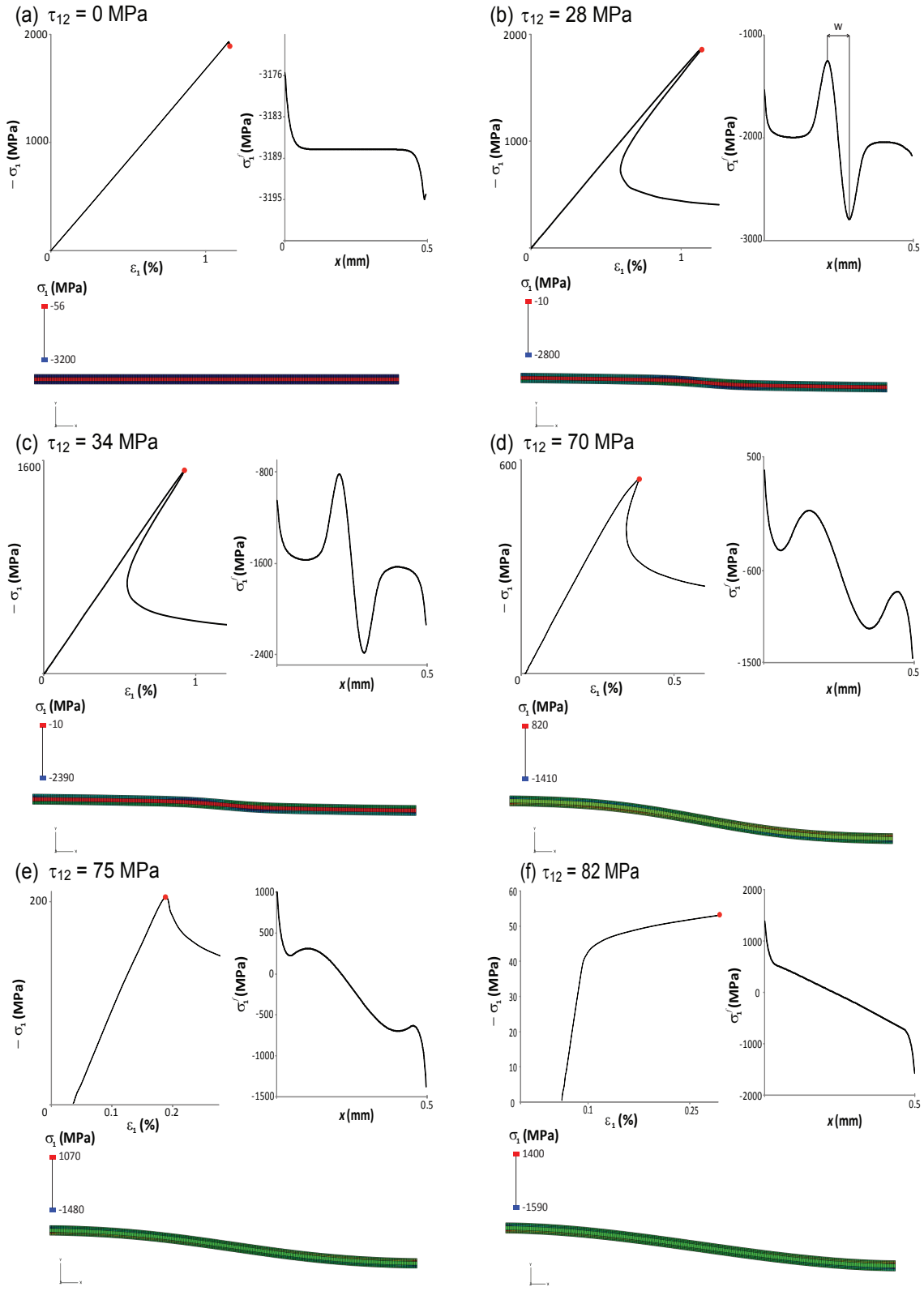


Figure 5.11: Stress-strain (σ_1 versus ε_1) curves, axial stress distribution along the fibres $\left(\sigma_1^f\right)$ and deformed shape for the baseline model for several values of τ_{12} (the deformed shapes and stress distributions are taken close to the peak stress, as shown by the circles)

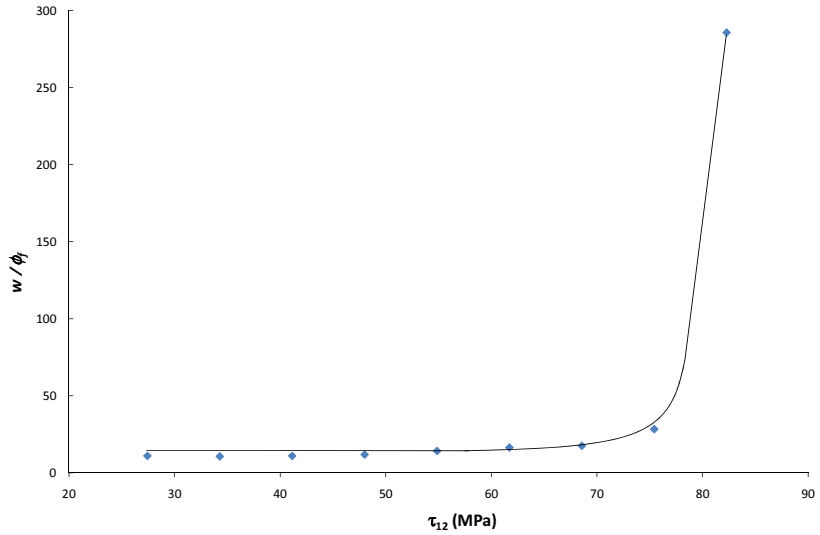


Figure 5.12: Distance between the points of maximum axial stress w versus shear stress.

5.4 Comparison to experiments

As mentioned in the introduction, experimental studies to determine the in-plane shear/longitudinal compression failure envelope typically show significant scatter and different trends. The parametric study has highlighted the main characteristics of the failure envelope and the effect of the key parameters, the correlation with experimental results found in the literature is now analysed.

The model is calibrated to reproduce the results reported in Jelf and Fleck [22] and Soden et al. [37]. The properties used are either those of the EXAS HDI-DX 6002 system [22], or of the T300-914 system [37] or approximated to the best of the authors' knowledge (a summary is given in Table 5.1 and in Fig 5.4).

5.4.1 Experiments from Jelf and Fleck [22]

The compressive strength of the fibres is 2140 MPa, so that the longitudinal compressive strength of the composite is reached and the initial misalignment angle of 4 °

is chosen to capture the slope of region *II* of the failure envelope. Fig. 5.13a shows the experimental failure envelope from [22] and the corresponding FE prediction.

The FE model predicts a small region *I*—fibre failure dominated—and a region *II*—matrix failure dominated—for the rest of the failure envelope.

The correlation with experimental results is good, but as the scatter of these experimental results is not reported, this good correlation refers only to the general trend. In Fig. 5.13a, theoretical predictions from the LaRC05 fibre kinking criterion [67] are also reported, for $\theta_0 = 3\,^\circ$—corresponding to the best fit—and $\theta_0 = 3.3\,^\circ$, for which both shear and longitudinal compressive strengths are reached. For $\theta_0 = 3\,^\circ$, FE predictions and the LaRC05 fibre kinking criterion agree well in region *II*, which can be expected since the compressive strength in kinking theory is determined by matrix failure. However, region *I* is not captured by the LaRC05 fibre kinking criterion and leads to an over-prediction of the longitudinal compressive strength. Shear and longitudinal compressive strengths are well predicted by kinking theory for $\theta_0 = 3.3\,^\circ$, but in turn, the failure envelope is slightly conservative in the range $0\,\text{MPa} \leq \tau_{12} \leq 40\,\text{MPa}$.

The misalignment in the FE model is set to $\theta_0 = 4\,^\circ$, which is slightly bigger than the one used for the LaRC05 model. For both the FE and LaRC05 models, the misalignment angle used is in fact an equivalent misalignment angle which aims to represent, in a single variable, several effects (e.g. actual misalignments, manufacturing-induced micro-cracks, etc). Furthermore, in the LaRC05 model the stresses and strains in the kink-band are homogenised which is not the case in the present FE model. Therefore, and since the models are significantly different, it is not trivial to deduce a relation between the two angles.

5.4.2 Experiments from the first World Wide Failure Exercise [37]

In Soden et al. [37], it is mentioned that the bi-axial results were obtained from different sets of tubes (two for torsion/compression and one for torsion/tension and

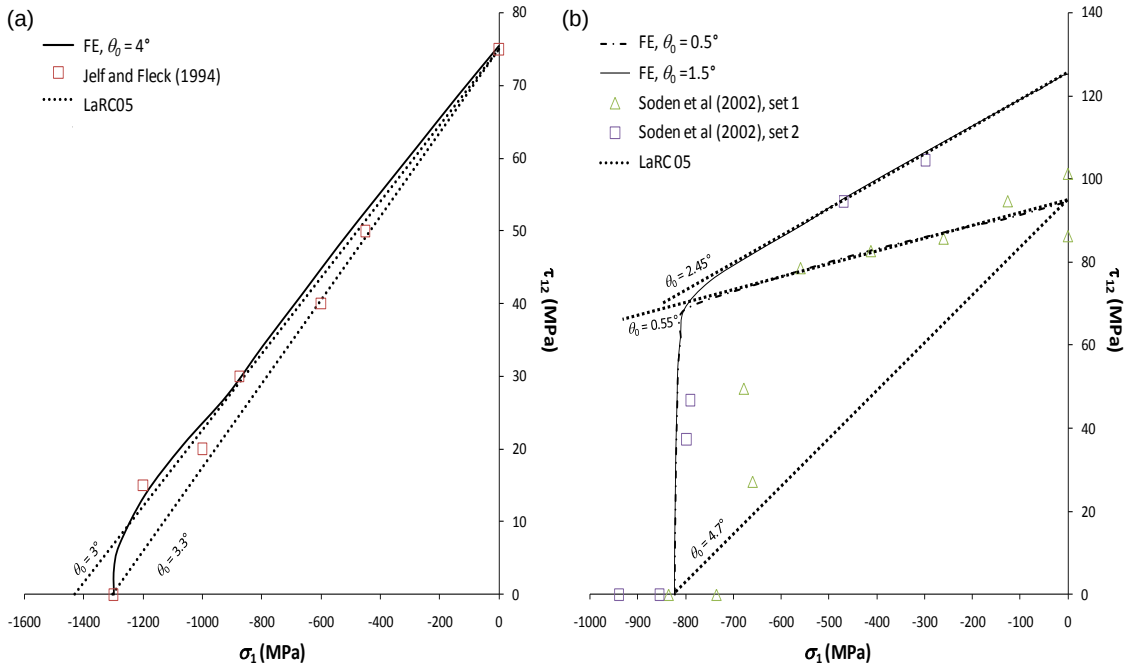


Figure 5.13: Experimental failure envelopes from (a) Jelf and Fleck [22] and (b) Soden et al. [37], together with the corresponding FE predictions.

pure torsion). Because results in compression are sensitive to material variability, experimental set-up and coupon manufacture, it appears reasonable to look at the sets 1 and 2 independently. Fig. 5.13b shows the experimental failure envelope from [37] and the corresponding FE predictions.

In Fig. 5.13b for set 1, the inputs of the FE model are changed according to Table 5.1 and so that the apparent shear strength of 95 MPa could be reached; an initial misalignment angle of $0.5\,^\circ$ is chosen to capture the slope of the linearly decreasing part of the failure envelope.

In region *II* of the failure envelope in Fig. 5.13b, the trend predicted by the FE model agrees well with the experimental results and with the LaRC05 criterion when used with an initial misalignment angle $\theta_0 = 0.55\,^\circ$. The agreement between experimental and FE results is also good in region *I*.

In Fig. 5.13b for set 2, the inputs of the FE model are given in Table 5.1 and so that the apparent higher shear strength of 125 MPa could be reached (an elastic perfectly-plastic model was used for the matrix); the compressive strength of the fibres is set to 1330 MPa, so that the longitudinal compressive strength of the

composite is reached and the initial misalignment angle of 1.5 ° is chosen to capture the slope of the linearly decreasing part of the failure envelope.

In region *II* of the failure envelope in Fig. 5.13b, the trend predicted by the FE model agrees well with the experimental results and with the LaRC05 criterion when used with an initial misalignment angle $\theta_0 = 2.45\,^\circ$. The agreement between experimental and FE results is also good in region *I*.

5.5 Discussion

5.5.1 Shear-driven fibre compressive failure

Fibre compressive failures define region I of the failure envelope, where the compressive strength is slightly affected by shear stresses so that the failure envelope runs nearly parallel to the τ_{12}-axis. The location of this region on the σ_1-axis is directly determined by the compressive strength of the fibres. Oya and Johnson [107] reported values of 1000 MPa and 1800 MPa for the compressive strength of T300 fibres, the differences arise when the recoil or direct test method (respectively) is used. In Fig. 5.13, a value of 1330 MPa is used, which in the range given by Oya and Johnson [107].

Furthermore, this failure mechanism corresponds to the experimental evidences given in [95].

5.5.2 Transition from shear-driven compressive failure to kink-band formation

Longitudinal compressive failure of single edge notch specimens was investigated in the previous chapter, and it was observed that failure initiates as shear-driven fibre compressive failure followed by kink-band formation. The transition between those two mechanisms was related to fibre rotation ahead of the shear crack, which in conjunction with the compressive load lead to the formation of a kink-band. A similar transition is observed in the failure envelopes presented here. In region *I*, the shear stresses are not large enough to induce the fibre rotation necessary to trigger a

kink-band and consequently failure is due to compressive shear failure of the fibres. In region *II*, however, the fibre rotation induced by the shear stresses is sufficient for kink-bands to form.

5.5.3 Limit kinking/splitting

As already mentioned, two regions—fibre dominated failure or matrix dominated failure—can be identified on the failure envelope. For pure shear, failure is matrix dominated without kink-band formation; for small amount of compression, splitting should take place. The transition between kinking and splitting is hard to identify as no specific change of trend on the failure envelope is observed. Some insight can be obtained by analysing the applied compressive stress-strain curves and the deformed shape of the model. From Fig. 5.12 it can be inferred that, for the IM7-8552 system, the transition between kinking and splitting occurred between $70\,\text{MPa} \leq \tau_{12} \leq 80\,\text{MPa}$. Experimental information on this limit are scarce in the literature; however, Jelf and Fleck [22] reported that all the samples with $\sigma_1 \leq -450$ MPa and $\tau_{12} \leq 50$ MPa in Fig. 5.13a failed by kink-band formation and only the sample corresponding to pure shear failed by splitting. This suggests that the limit kinking/splitting for their tests lies between $50\,\text{MPa} \leq \tau_{12} \leq 75\,\text{MPa}$ and is close to the current findings from the FE model.

5.5.4 The trend of the failure envelope

From the results obtained by the FE models and the comparison with experimental results, a more accurate picture of the actual shape of the failure envelope for a case of in-plane shear/longitudinal compression can be drawn.

The failure envelope is defined by two regions corresponding to two different failure mechanisms. The first region is defined by a curve (nearly) parallel to the τ_{12}-axis. In this region, the strength of the composite can be related to the compressive strength of the fibres. The second region corresponds to kinking (eventually splitting) and is defined by a curve starting at the shear strength on the τ_{12}-axis and going towards the negative σ_1-axis either in a linear way (linear behaviour of

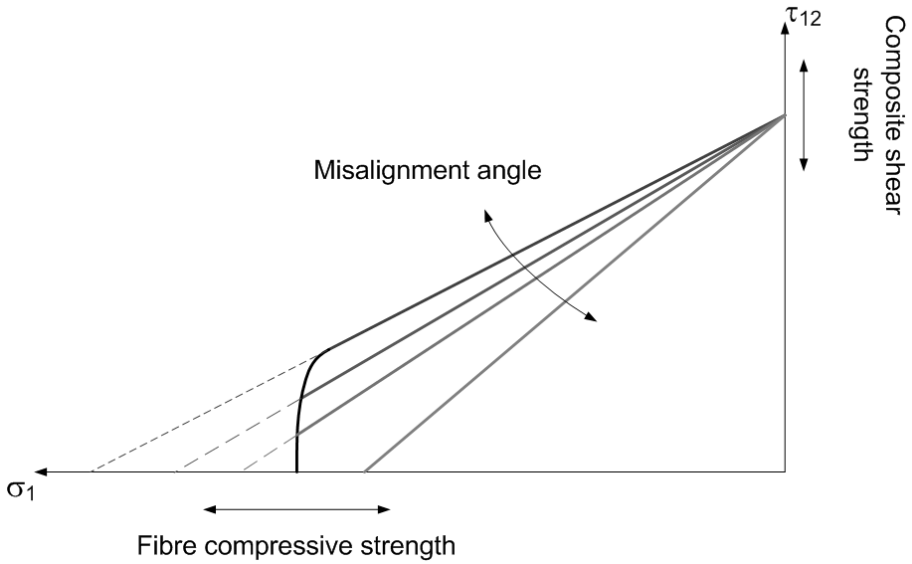


Figure 5.14: Failure envelope construction.

the composite in shear) or with a concave shape (nonlinear behaviour of the composite in shear). The rate at which the curve goes to $\tau_{12} = 0$ is dependent on the misalignment angle.

As shown schematically in Fig. 5.14 the whole failure envelope can be constructed from those two curves. As the misalignment in the composite (or the imperfection in the test setup) increases, the size of region I decreases and eventually vanishes. The presence of those two regions does not only depend on the misalignment but also on the compressive strength of the fibres, e.g. in a case of a large initial misalignment but low compressive strength of the fibres, the two regions might still be observable.

5.5.5 Current analytical capabilities for failure envelope predictions

The results obtained by the FE analysis presented here show that two failure mechanisms can be found in longitudinal compression, depending on the amount shear stress.

For the prediction of the fibre failure dominated region, region I, no failure criteria relating (σ_1, τ_{12}) and based on this failure mechanism could be found in the

literature. The hypothesis that, for pure longitudinal compressive failure, shear-driven fibre compressive failure could be encountered was made by Hahn et al. [99], Kozey [108], Effendi et al. [109]. In the FE model presented here, the maximum stress criterion was used and it is believed that the shape of the failure envelope in region *I* depends on the criterion chosen. However, and as the experimental results presented in the previous chapter show, the fibres fail along the planes of maximum shear stress, and a criterion similar to Tresca would probably be more appropriate.

When it comes to the matrix dominated region, region *II*, models based on kinking theory appear to be adequate to predict the failure envelope. In particular, the concave shape of the envelope for nonlinear shear behaviour of the composite is well captured (as compared to FE results).

5.6 Conclusions

Failure envelope predictions for a case of in-plane shear/longitudinal compression have been obtained using a micromechanical FE model.

It was found that the failure envelope is defined by two regions. A first region where the strength is related to the compressive failure of the fibres and a second region which can be related to kink-band formation and splitting.

The role of the material properties such as fibre compressive strength, matrix behaviour, and misalignment in the composite were detailed.

The FE model was calibrated to reproduce the results of two typical failure envelopes as found in the literature, and the difference between the two trends was explained.

When compared to the failure criteria available in the literature, models based on kinking theory (Jelf and Fleck [22] and LaRC05 [30]) are able to capture the linear trend seen in region *II*, when the behaviour of the composite in shear is linear, and the concave-shaped trend (LaRC05), when the nonlinear behaviour of the composite is accounted for.

5.7 Publications

The work presented in this chapter resulted in the following publications:

Micro-mechanical modelling of shear-driven fibre compressive failure and of fibre kinking for failure envelope generation in CFRP laminates. R. Gutkin, S.T. Pinho, P. Robinson and P. T. Curtis. Composites Science and Technology, 2010, 70, 1214-1222.

In collaboration with Ms. Soraia Pimenta, during her MSc Project, kink-band formation was numerically investigated using other micromechanical FE models. The findings from this study are presented in Appendix C and published in:

A micromechanical model for kink-band formation: Part I—Experimental study and numerical modelling. S. Pimenta, R. Gutkin, S.T. Pinho and P. Robinson. Composites Science and Technology, 2009, 69, 948-955.

Chapter 6

An analytical formulation to predict fibre kinking and splitting under combined longitudinal compression and inplane shear

6.1 Introduction

Accurate predictions for combined longitudinal compression and in-plane shear loadings are important for the design of Carbon Fibre Reinforced Polymers (CFRP) structures as the longitudinal compressive strength decreases significantly with in-plane shear stresses [22, 102]. In the present chapter, an analytical model to predict the strength associated with fibre kinking and splitting under compression and shear loading is derived. A key element of the formulation is the fracture mechanics approach adopted, following experimental observations presented in [95].

A large variety of models to predict the strength related to fibre kinking under pure longitudinal compressive loading can be found in the literature [21, 33, 67, 78, 110]. In an early model by Rosen [73], the strength is derived from a buckling analysis of a fibre supported by an elastic matrix—often referred as microbuckling—and given in Eq. (2.18). This type of model typically gives two to three times higher

strength than the one experimentally measured.

Some other approaches, still based on a micromechanical analysis, have studied the equilibrium of an initially misaligned fibre supported by an elasto-plastic matrix [21, 78, 110]. The longitudinal compressive strength reads for example in [110]

$$X_c = S_m \frac{G_m^{2D}.\phi_f + \frac{\pi^2}{L^2} E_f I_f}{S_m + \pi \frac{\overline{y_0}}{L} G_m^{2D}}.\frac{v_f^{2D}}{A_f}, \tag{6.1}$$

where S_m, G_m^{2D} are the shear strength and 2D equivalent shear modulus of the resin, and E_f, I_f, A_f and ϕ_f are the Young's modulus, second moment of area, cross sectional area and diameter of the fibre, respectively. L is the length of the fibre and $\overline{y_0}$ a measure of its initial imperfection. By introducing an initial misalignment and assuming that the strength is reached when the matrix fails or yields (concepts first introduced in a model by Argon [33]), these latter approaches typically give predictions in good agreement with experimental results. Some of them, and depending on the level of complexity included in the analysis, can predict the kink-band width, w, as well as the deflection of the fibres and stress fields during kink-band formation [110].

Under combined loading, the number of approaches based on the physics of kink-band formation is more limited. Budiansky and Fleck [74] developed a model where the kink-band is seen as a band with its edges lying at angles $\theta + \theta_0$ and β, see Fig. 4.1. $\theta + \theta_0$ corresponds to the angle of rotation of the fibres within the kink-band (θ_0 is the initial misalignment and θ the additional rotation introduced by the compressive loading) and β to the kink-band propagation angle. The edges of the kink-band are well defined, which means that the bending contribution of the fibres is neglected. The band has orthotropic material properties which are rotated in the misaligned coordinate system of the fibres (angle $\theta + \theta_0$). The stresses (tractions) and displacements are computed in the coordinate system associated with the kink-band and their continuities are verified at the boundary with the outer region. The longitudinal compressive strength is evaluated when yielding of the matrix in the band is reached. For a case of longitudinal compression and in-plane shear, the

applied stresses (σ_1, τ_{12}) are related by [74]

$$\sigma_1 = \frac{\tau - \tau_{12}}{\theta + \theta_0}, \tag{6.2}$$

where τ is the shear stress due to (σ_1, τ_{12}) in a coordinate system aligned with the rotated fibres.

Dávila et al. [80] proposed a criterion for fibre kinking based on Argon's approach and the LaRC matrix failure criterion. The stress applied on a unidirectional composite, containing a region of misaligned fibres, is rotated in that misaligned coordinate system. The resolved stresses are then used to evaluate the LaRC matrix failure criterion to test for failure. This approach was developed further in [67] to account for the nonlinear response of the composite in shear as well as to handle 3D loading situations.

In this chapter, some experimental observations, important to characterise the processes involved in kink-band formation, are first reviewed. The formulation of the analytical model is then presented, and a close-form failure criterion is derived for the case of a linear elastic matrix. Finally, the results of the model are compared to experimental data and numerical results available in the literature and discussed.

6.2 Kink-band formation: experimental observations

Kink-bands typically initiate in regions of large fibre misalignment [21] or in regions where fibre rotation has been introduced by other failure mechanisms (e.g. delamination of neighbouring plies [30], following a shear-driven fibre compressive failure [95]). Under compressive load, initially misaligned fibres rotate which leads to shear stresses in the matrix. As the matrix fails, the fibres lose their supports resulting in further fibre rotation. Fig. 6.1a shows a kink-band propagating in a unidirectional single edge notch specimen under load (see Chapter 4 for details). Ahead of the kink-band tip, marked in Fig. 6.1a and shown in the close-up view Fig. 6.1b, the deformation of the fibres in the kink-band and the extensive cracking of the matrix is

observed. The microcracks span the entire width of the kink-band, and the amount of microcracks increases as the kink-band propagates (from right to left) and fibre rotation increases. A close-up view of the top edge of a kink-band (Fig. 6.1c) shows the shape of the matrix microcracks, labelled 'm'. Some of these microcracks have coalesced to form a split, labelled 'c' in Fig. 6.1c. By resolving the applied longitudinal compressive stress in the misaligned coordinate system of the fibres, it can be shown that the stress field in the inter-fibre region is shear dominated. This stress state, together with the shape of the microcracks, indicates that these microcracks are shear cusps being formed. It can also be observed that many of the splits are open.

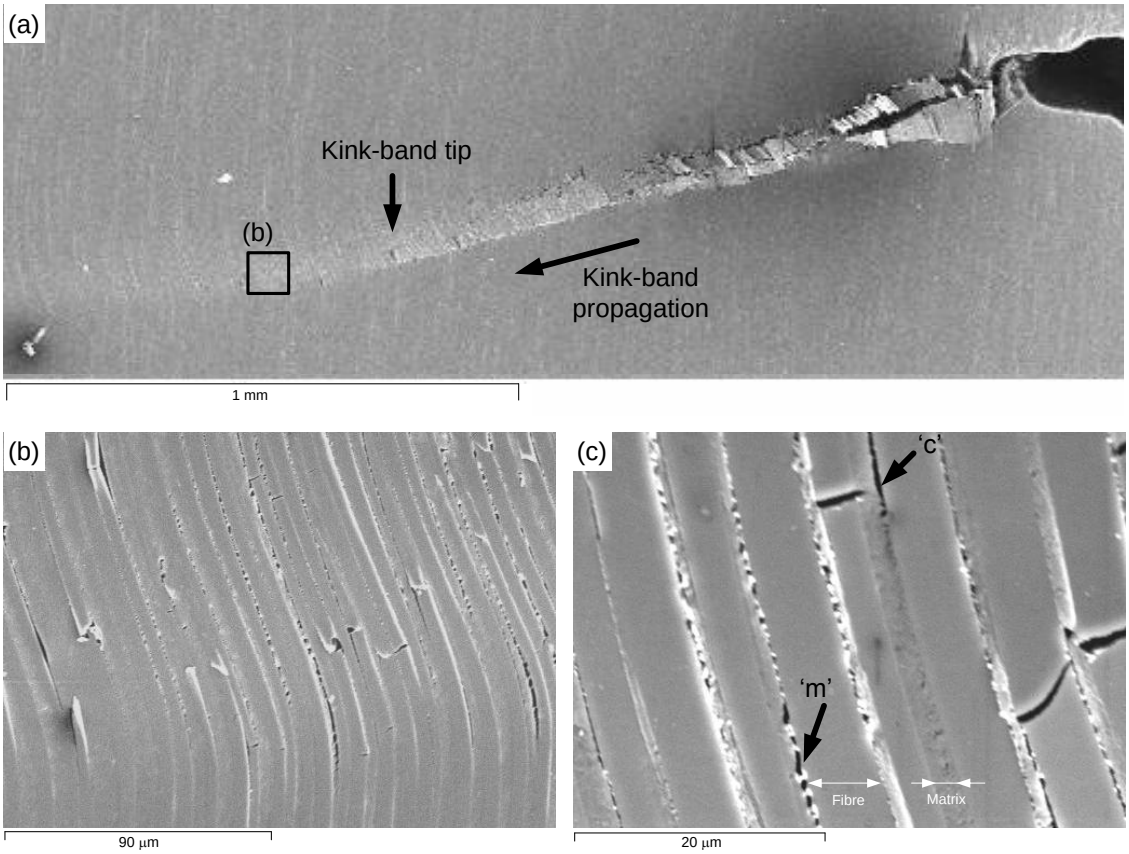


Figure 6.1: (a) Kink-band propagation in a unidirectional single edge notch specimen under load; (b) Close-up view on the kink-band tip; (c) Close-up view on the top edge of a kink-band.

Fibre splitting is less well documented, but it often takes place when a composite ply is subjected to large in-plane shear stress [22, 102]. It originates from matrix failure (eventually in a region of misaligned fibres) and the mechanisms are similar to those involved in kink-band formation, with the exception that failure does not localise in a band. Furthermore, experimental [22, 102] and numerical evidence (see Chapter 5) suggest that there is no change in the failure envelope when the failure mode changes from kinking to splitting. Based on these comments, a failure criterion applicable to kinking should also be applicable to splitting. Therefore, the model presented here is formulated in terms of kink-band formation but can also be applied to splitting.

6.3 Model formulation

6.3.1 Framework

The experimental observations show that kink-band initiation results from the formation of matrix microcracks and split in the inter-fibre region. Therefore, the present model is based on the hypothesis that: the strength associated with fibre kinking is reached when the strain energy released per unit area of crack generated between an undamaged state and a damaged state is equal to the energy required to create the cracks (fracture energy).

To calculate the strain energies and fracture energy, some simplifications and assumptions on the geometry, loading conditions and material response are made and listed below.

Simplifications:

S(i) The control volume chosen for the model is shown in Fig. 6.2 and corresponds to a representative element of material in the kink-band. A 2D representation of the composite is defined. The fibres are considered to be perfect cylinders of diameter ϕ_f and are arranged in a hexagonal pattern with a fibre volume fraction v_f. The model has a unit thickness (in the 3-direction), and is taken from one of the symmetry planes of the fibre arrangement such that the width

of the matrix layers between the fibres is [110]

$$t_m = \phi_f \left(\sqrt{\frac{\pi}{2\sqrt{3}v_f}} - 1 \right). \tag{6.3}$$

A fibre volume fraction for the 2D equivalent model can also be defined as

$$v_f^{2D} = \frac{\phi_f}{\phi_f + t_m}. \tag{6.4}$$

S(ii) Fibre bending is neglected and the fibres are considered to be incompressible. The ratio between the contribution made by fibre bending and matrix shearing to the compressive strength can be evaluated from Eq. 6.1, and for typical carbon-epoxy systems and L from [110] is

$$\frac{\frac{\pi^2}{L^2} E_f I_f}{G_m^{2D}.\phi_f} \sim 0.02\%. \tag{6.5}$$

S(iii) The deformation of the matrix due to the rotation of the kink-band to the propagation angle β is neglected, as it was experimentally observed in Chapter 4 that, at initiation, this angle is close to zero (this was also verified numerically in Chapter 5).

S(iv) The matrix transmits only shear stresses; for instance, the contribution of the matrix in compression is neglected as $E_m/E_f \ll 1$. The shear stresses are considered constant across the matrix layer, which is consistent with numerical findings in [110].

Assumptions:

A(i) When a nonlinear shear response of the matrix is considered, the nonlinearities are assumed to be induced by damage alone.

A(ii) Crack formation between the undamaged state (A) and damage state (B), Fig. 6.2, is assumed to occur at constant displacement and the kinetic energy is neglected.

A(iii) The microcracks have complex shapes and distribution, and their actual area is not observable in Fig. 6.1. Hence, it is assumed that the area of the microcracks created per unit of thickness, for a width w of kink-band, can be written:

$$\alpha w t_m, \tag{6.6}$$

where the coefficient α is an undetermined proportionality factor and has for dimension $[\text{mm}]^{-1}$.

A(iv) Matrix cracking is assumed to occur under a certain mixed mode critical energy release rate G_c.

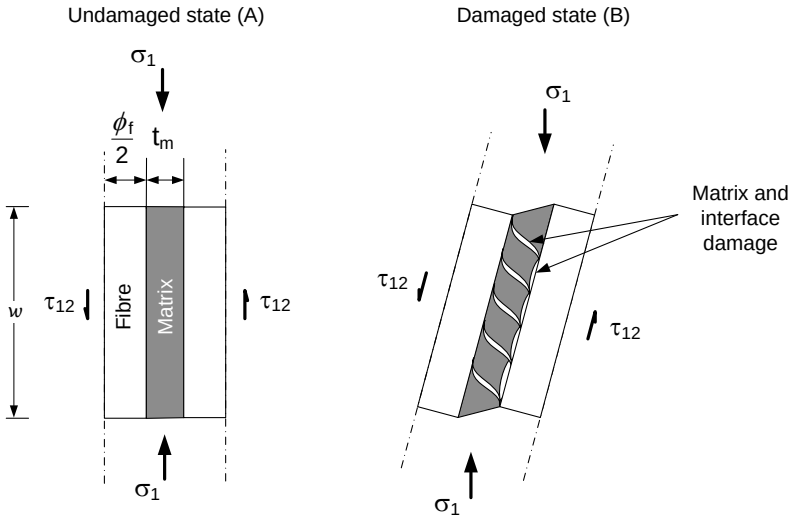


Figure 6.2: Undamaged and damaged state of the model.

6.3.2 Equilibrium of the fibre

To obtain the strain energy stored in the control volume, its equilibrium under combined compression and shear is first considered as shown in Fig. 6.3. A fibre of length w, initially misaligned at an angle θ_0, is subjected to an axial force P and a shear force S. Under the action of these two forces, the fibre rotates by an additional angle θ, such that at equilibrium, the fibre is at an angle $\theta_0 + \theta$. The axial

and shear forces acting on the fibre can be expressed in terms of the homogenised applied stresses (σ_1, τ_{12})

$$\sigma_1 \sim \frac{P}{\phi_f} v_f^{2D}, \tag{6.7}$$

$$\tau_{12} \sim \frac{S}{\phi_f}. \tag{6.8}$$

The fibre is supported by the matrix which transmits a shear traction τ_m onto the surface of the former; the shear constitutive law of the matrix is typically non-linear so that the shear strain can be related to the shear stress by a generic function f_{CL}^{γ} such that

$$\tau_m = f_{CL}^{\gamma}(\gamma_m). \tag{6.9}$$

Assuming that the rotation of the fibres θ remains small and that adjacent fibres deform in phase, as shown in Fig. 6.2, the shear strain in the matrix and the fibre rotation are related by [110, 112]

$$\gamma_m \sim \frac{\theta}{1 - v_f^{2D}}, \tag{6.10}$$

and the shear stress in the matrix is written

$$\tau_m = f_{CL}^{\gamma}\left(\frac{\theta}{1 - v_f^{2D}}\right) = f_{CL}^{\theta}(\theta). \tag{6.11}$$

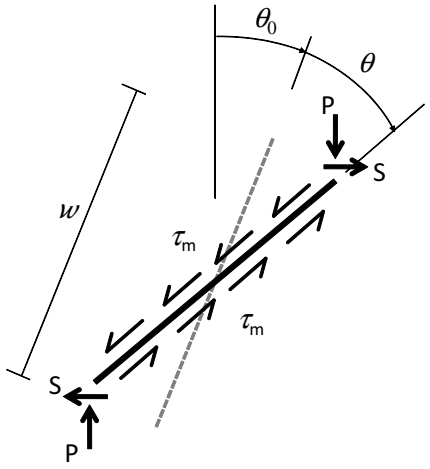


Figure 6.3: Fibre equilibrium.

From Fig. 6.3, the equilibrium of the fibre, assuming small angles, reads

$$P\theta w + P\theta_0 w - \tau_m \phi_f w + Sw = 0. \tag{6.12}$$

Replacing P and S by the expressions given in Eqs 6.7 and 6.8, and expressing τ_m as a function of θ with Eq. 6.11 (note that the matrix is initially in a stress free state), Eq. 6.12 reads

$$\sigma_1 \frac{(\theta + \theta_0)}{v_f^{2D}} + \tau_{12} = f_{CL}^{\theta}(\theta)\,. \tag{6.13}$$

For a given stress state (σ_1, τ_{12}), the rotation of the fibres θ is found by solving Eq. 6.13.

6.3.3 Strain energy and dissipated fracture energy

Using the simplifications S(ii) and S(iv), the strain energy of the model in the undamaged state A, see Fig. 6.2, reduces to the strain energy stored in the matrix

$$\begin{aligned} U_A = U_m &= \frac{1}{2}\int_{V_m} \tau_m \gamma_m dV \\ &= \frac{1}{2} t_m w \frac{\theta}{1 - v_f^{2D}} f_{CL}^{\theta}(\theta). \end{aligned} \tag{6.14}$$

In the damaged state B, the element is considered fully damaged (the matrix does not resist any stresses) and $U_B = 0$.

Under assumptions A(iii) and A(iv) and with Eq. 6.6, the fracture energy dissipated from the state A to state B is written as

$$\Delta G = \alpha w t_m G_c. \tag{6.15}$$

6.3.4 Energy balance

In a general case, and with assumption A(ii), the energy balance during crack formation reads

$$\Delta W - \Delta U = \Delta G, \tag{6.16}$$

where ΔW is the work of the external forces. At constant displacement, the work is zero and the energy balance becomes

$$-\Delta U = -\left(U_B - U_A\right) = U_m = \Delta G. \tag{6.17}$$

Replacing Eqs 6.14 and 6.15 in Eq. 6.17, it follows that

$$\frac{\theta f_{CL}^{\theta}(\theta)}{2\left(1 - v_f^{2D}\right)\alpha G_c} = 1. \tag{6.18}$$

Using Eq. 6.13 in Eq. 6.18, a failure criterion for fibre kinking and splitting

under combined compression and shear is obtained

$$f_{k/s} = \frac{\theta f_{CL}^{\theta}(\theta)}{2\left(1-v_f^{2D}\right)\alpha G_c} = 1 \text{ with } \sigma_1 \frac{(\theta+\theta_0)}{v_f^{2D}} + \tau_{12} = f_{CL}^{\theta}(\theta). \tag{6.19}$$

Eq. 6.19 does not involve the length scale w, so that the criterion does not only apply to a localised process, but to matrix failure in a region of misaligned fibres and can therefore be applied to splitting.

6.3.5 Linear elastic shear response of the matrix

In the case of a linear elastic matrix, the relationships in Eq. 6.19 can be simplified and the criterion $f_{k/s}$ written in close form. The shear stress in the matrix reads

$$\tau_m = G_m \gamma_m \text{ or } f_{CL}^{\gamma}(.) \rightarrow G_m, \tag{6.20}$$

where, as stated above, G_m is the shear modulus of the matrix, and with Eq. 6.10

$$\tau_m = G_m \frac{\theta}{\left(1-v_f^{2D}\right)} \text{ or } f_{CL}^{\theta}(.) \rightarrow \frac{G_m}{\left(1-v_f^{2D}\right)}. \tag{6.21}$$

The angle of rotation of the fibres is related to the applied stresses by using Eq. 6.13

$$\sigma_1 \frac{(\theta+\theta_0)}{v_f^{2D}} + \tau_{12} = \frac{G_m}{\left(1-v_f^{2D}\right)}\theta, \tag{6.22}$$

so that

$$\theta = \frac{\tau_{12} v_f^{2D} + \sigma_1 \theta_0}{\frac{G_m}{\left(1-v_f^{2D}\right)} v_f^{2D} - \sigma_1}. \tag{6.23}$$

From Eqs 6.18 and 6.23, the following expression is derived

$$\left(\frac{\tau_{12} v_f^{2D} + \sigma_1 \theta_0}{\frac{G_m}{\left(1-v_f^{2D}\right)} v_f^{2D} - \sigma_1}\right)^2 \frac{G_m}{\left(1-v_f^{2D}\right)} = 2\left(1-v_f^{2D}\right)\alpha G_c, \tag{6.24}$$

which is expanded in a second order equation in τ_{12}:

$$\tau_{12}^2 + \frac{2\sigma_1\theta_0}{v_f^{2D}}\tau_{12} + \left[\frac{(\sigma_1\theta_0)^2}{\left(v_f^{2D}\right)^2} - 2\left(\frac{1-v_f^{2D}}{v_f^{2D}}\right)^2 \alpha\frac{G_c}{G_m}\left(G_m\frac{v_f^{2D}}{\left(1-v_f^{2D}\right)} - \sigma_1\right)^2\right] = 0. \tag{6.25}$$

The positive root of Eq. 6.25 is

$$\tau_{12} = -\frac{\sigma_1\theta_0}{v_f^{2D}} + \left(\sqrt{2\left(\frac{1-v_f^{2D}}{v_f^{2D}}\right)^2 \alpha\frac{G_c}{G_m}}\right)\left(G_m\frac{v_f^{2D}}{\left(1-v_f^{2D}\right)} - \sigma_1\right), \tag{6.26}$$

which is rearranged as

$$\frac{\tau_{12}}{\sqrt{2\alpha G_c G_m}} + \frac{\sigma_1}{v_f^{2D}}\left(\frac{\left(1-v_f^{2D}\right)}{G_m} + \frac{\theta_0}{\sqrt{2\alpha G_c G_m}}\right) = 1. \tag{6.27}$$

Considering Eq. 6.27 for pure shear loading ($\sigma_1 = 0$) leads to

$$S_L = \sqrt{2\alpha G_c G_m}, \tag{6.28}$$

and Eq. 6.27 leads finally to a simple stress based criterion for fibre kinking and splitting

$$f_{k/s} = \frac{\tau_{12}}{S_L} + \frac{\sigma_1}{v_f^{2D}}\left(\frac{\left(1-v_f^{2D}\right)}{G_m} + \frac{\theta_0}{S_L}\right) = 1. \tag{6.29}$$

6.4 Prediction of failure envelopes

6.4.1 Numerical validation and parametric study

In this section, a sensitivity study on the parameters S_L and θ_0 used in the model is presented. The properties of an IM7/8552 carbon-epoxy system are used, and given in Table 6.1. Unless stated otherwise, a baseline model is used for the parametric study with S_L and θ_0 given in Table 6.1. In Eq. 6.19 f_{CL}^{θ} is taken as either the shear modulus or the nonlinear response of the composite. For the nonlinear case, the experimental shear response is approximated by a polynomial expression as seen in Fig. 6.4.

Table 6.1: Geometrical and mechanical properties of the composites and resin.

ϕ_f (μm)	v_f (%)	G_{12} (GPa)	S_L (MPa)	θ_0 ($^\circ$)
7	60	5.5	90	0

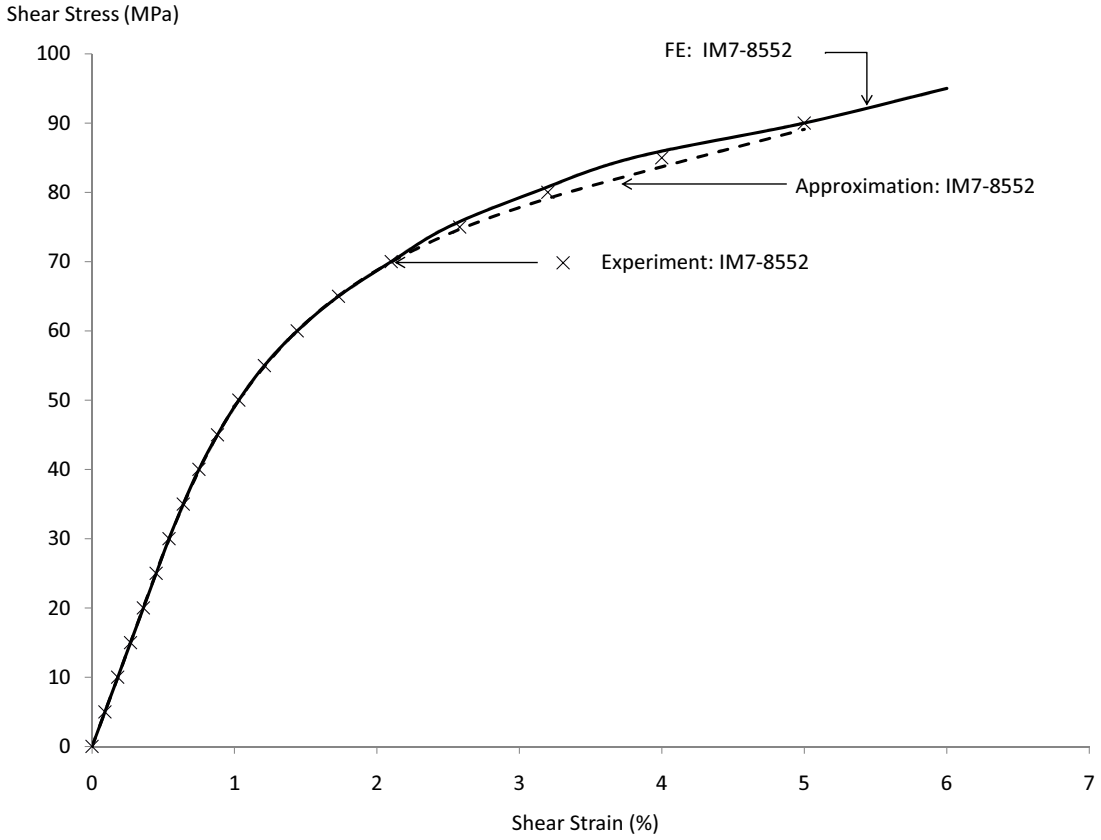


Figure 6.4: Shear responses for an IM7/8552 carbon-epoxy system.

The predictions of the present analytical model for a linear and nonlinear shear response of the matrix are compared with the results of a micromechanical finite element (FE) model presented in Chapter 5. The FE model represents a 2D unit cell of the composites (a matrix layer between two half fibres), with periodic boundary conditions applied to it, and subjected to combined longitudinal compression and in-plane shear. With this model, the effects of: the initial misalignment θ_0, the

response of the matrix (linear and nonlinear) and the compressive strength of the fibres X_c^f have been studied. Two failure envelopes predicted by the FE model are shown in Fig. 6.5 for a linear and a nonlinear response of the matrix (the response of the FE model in pure shear is shown in Fig. 6.4), a initial misalignment $\theta_0 = 0\,^\circ$ and $X_c^f = 3200$ MPa. The FE study revealed that two failure modes should be expected in combined longitudinal and in-plane shear: shear-driven fibre compressive failure and kink-band formation (or splitting for high shear stresses), as indicated in Fig. 6.5. In the present study, the focus is only on the region related to fibre kinking and splitting.

For the linear case, both FE and analytical predictions (Fig. 6.5) agree well with similar initial misalignment angles ($\theta_0 = 0\,^\circ$ in the FE and $\theta_0 = 0.3\,^\circ$ in the analytical model). For the nonlinear case, the initial misalignment angles are $\theta_0 = 0\,^\circ$ in the FE and $\theta_0 = 0.7\,^\circ$ in the analytical model; both models predict the same trend with the failure envelope changing to a concave shape.

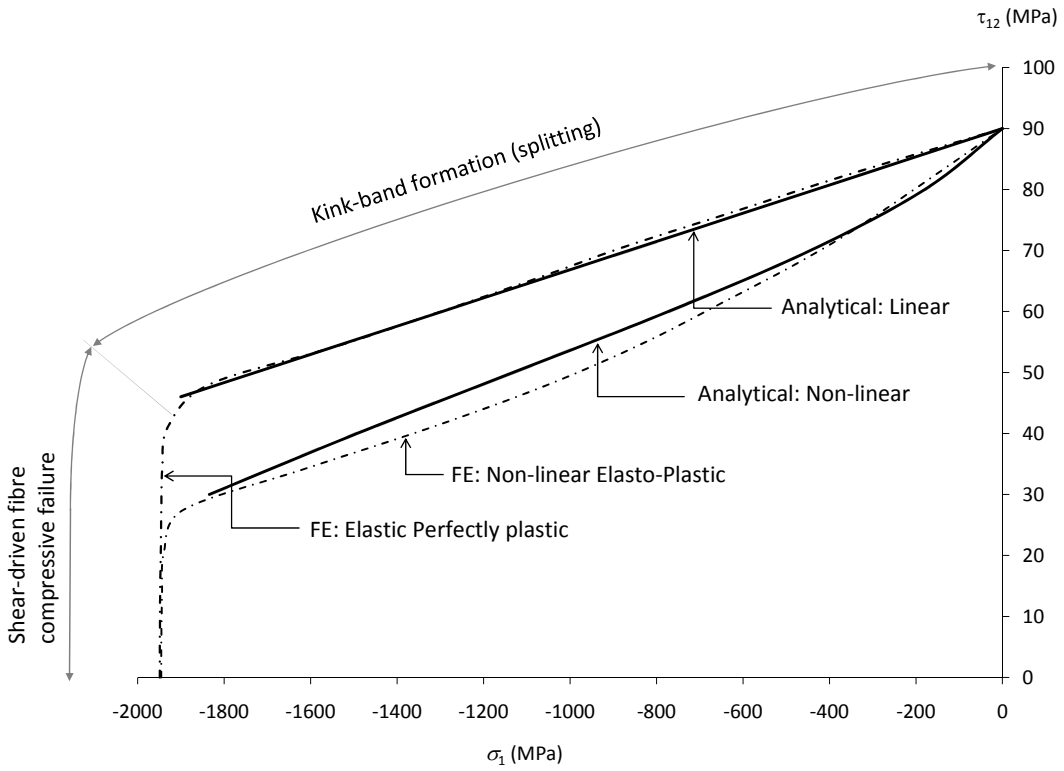


Figure 6.5: Predictions for a linear and nonlinear shear response of the matrix, comparison between the present analytical model and FE results from Chapter 5.

Fig. 6.6a shows the effect of the initial misalignment θ_0 on the predicted failure envelopes. The envelopes rotate around the point $(\sigma_1 = 0, \tau_{12} = S_L)$ and increasing θ_0 leads to a significant decrease of the domain defined by the failure envelope. This effect can also be seen in Eq. 6.29, where θ_0 controls the slope between σ_1 and τ_{12}.

On the contrary to the effect of θ_0 on the predictions, increasing S_L results in an increase of the domain defined by the failure envelope and does not affect the slope, as shown in Fig. 6.6b .

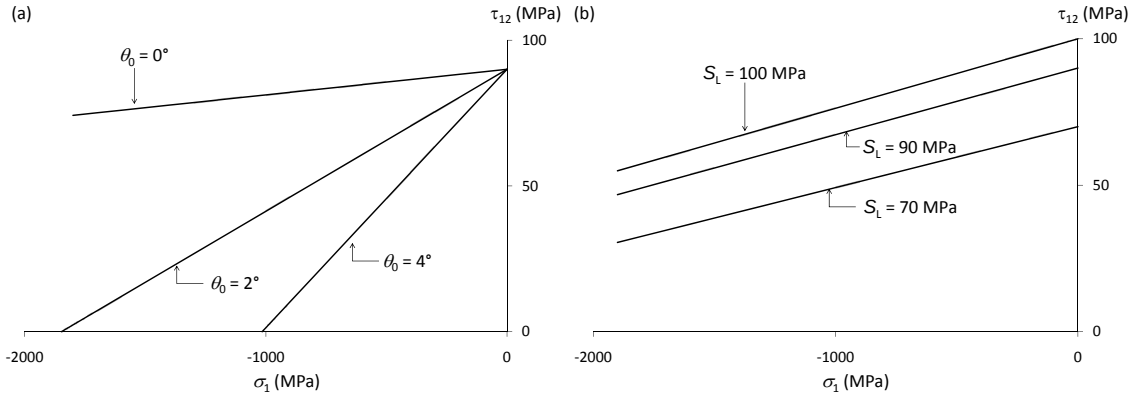


Figure 6.6: Predictions for several values of: (a) the initial misalignment angle θ_0; (b) the shear strength of the resin S_L

6.4.2 Comparison with experimental results

Measuring experimentally the failure envelope for a case of combined in-plane shear and longitudinal compression is a complex, time consuming and material consuming process. Strength results in longitudinal compression are particularly sensitive to material defects and imperfections of the testing setup, resulting in large scatter, and several tests must be done for each point of the failure envelope. Furthermore, experimental results often show different trends, which can be introduced by the type of setup used or by the presence of several failure modes (e.g. shear-driven compressive failure and kink-band [95]) depending on the amount of initial misalignment in the composites. Two examples of such failure envelopes for CFRP are given in Fig. 6.7. In Fig. 6.7a, the data are taken from Jelf and Fleck [22] and failure was reported to be due to kink-band formation (except for the sample with $\sigma_1 = 0$ MPa, which failed by splitting). The data shown in Fig. 6.7b are taken from Soden et al. [37]; the failure modes were not reported in the publication but it is apparent that by comparison with the two different domains in the failure envelopes predicted by FE (Fig. 6.5), only the specimens loaded with $\tau_{12} \gtrsim 60$ MPa failed by kink-band formation.

In Fig. 6.7a, all the experimental points lie between the failure envelopes predicted by the analytical model for $\theta_0 = 2.1^\circ$ and 2.5°. In Fig. 6.7b, the scatter

is larger and the experimental results come from two different sets, therefore two different S_L have been chosen and the difference in θ_0 is larger (1° and 2.6°). The experimental results, however, fall on or between the failure envelopes defined as explained above.

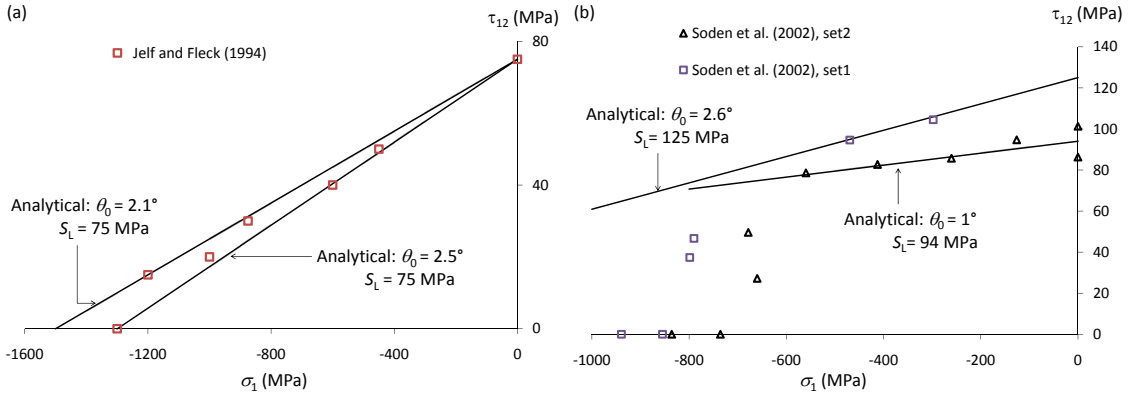


Figure 6.7: Comparison with experimental results from (a) Jelf and Fleck [22] and (b) Soden et al. [37].

6.5 Discussion

The failure envelopes predicted by the present model correlate well with the numerical findings in Chapter 5. The change from a linear to a concave shape of the failure envelope when the response of the matrix is changed from linear to nonlinear is well captured. The FE and analytical models are based on slightly different assumptions, for example, fibre bending is accounted for in the FE but not in the analytical model, which result in slightly different values of initial misalignment angles. In the nonlinear case, the differences in the predicted failure envelopes come from the two different approximations of the experimental response as shown in Fig. 6.4. The effects of varying the initial misalignment angle and the shear strength predicted by the analytical model are comparable to those observed in Chapter 5.

Eq. 6.19 gives a failure criterion for fibre kinking and splitting under combined compression and shear, which can be expressed in a simple and close-form for a

linear shear response, Eq. 6.29. The results this equation yields for some particular load combinations are now discussed.

For pure shear, $\sigma_1 = 0$, the shear strength is obtained as $S_L = \sqrt{2\alpha G_c G_m}$, which has a similar form to the in-situ shear strength for thin embedded plies (with linear shear response) defined in [11]

$$S_L^{is} = \sqrt{8 G_{IIc} G_{12}/\pi h}, \tag{6.30}$$

where G_{IIc} is the mode II fracture toughness and h the ply thickness. Recalling that α has for dimension $[\text{mm}]^{-1}$, it can be seen that both the equation for S_L and for S_L^{is} have the same form and involve similar terms, i.e. a fracture toughness, a shear modulus and a parameter related to the geometry. Therefore, S_L in Eq. 6.28 can be interpreted as the in-situ strength of a thin layer of matrix embedded between fibres.

Eq. 6.29 yields also an interesting result when S_L is large. In the limit when $S_L \to \infty$, Eq. 6.29 leads to $\sigma_1 = v_f^{2D} \frac{G_m}{\left(1-v_f^{2D}\right)}$. This result indicates that for a linear elastic matrix with an infinite strength, the compressive strength is not affected by in-plane shear stresses and corresponds to the microbuckling strength derived by Rosen [73] (Eq. 2.18) multiplied by a factor v_f^{2D}.

A similar result to the one from Budiansky and Fleck [74], Eq. 6.2, can also be retrieved by rewriting Eq. 6.23 as

$$\sigma_1 = \frac{\frac{G_m}{\left(1-v_f^{2D}\right)}\theta - \tau_{12}}{(\theta + \theta_0)} v_f^{2D}. \tag{6.31}$$

Here too, the result is multiplied by a factor v_f^{2D}. This factor is introduced by the different assumptions on the stress and strain state in the two models. In kinking theory, the kink-band is modeled as an homogeneous medium where the stresses and strains are homogenised, while in the micromechanical approach presented here, the shear stresses are the same in the fibres and matrix but the strains are different.

The parameter α, introduced in assumption A(iii), see Eqs 6.6 and 6.15, accounts for two characteristics of the microcracks: (i) a crack density ρ, and (ii) a measure

of their actual normalised area β, so that $\alpha = \rho\beta$. The exact values of ρ, β and the mixed-mode ratio do not need to be known, as from Eq. 6.28 they are implicitly defined through the shear strength of the composite. This observation means that only standard properties are needed to evaluated the criterion in Eq. 6.19 (or Eq. 6.29), and assures that the predictions are not affected by the details of the shape and distribution of the microcracks, but rather on the overall fracture toughness which can be evaluated indirectly through the shear strength.

6.6 Conclusions

An analytical model to predict the strength associated with fibre kinking and splitting under combined longitudinal compression and in-plane shear has been developed. The model is based on a fracture mechanics study of the microcracks and splits created between the fibres, and results in a failure criterion which can be readily used for failure predictions. The criterion requires only standard properties and the formulation ensures that the predictions are not affected by the details of the microcracking process. A sensitivity analysis has shown that the effect of important parameters such as the nonlinear response in shear of the resin and the effect of the initial misalignment in the composite are well captured. The predictions of the model have been found to be in good agreement with experimental data [22, 37] and numerical results presented in Chapter 5.

6.7 Publications

It is envisaged that the contents of this chapter will be submitted for journal publication in the near future.

In addition, in collaboration with Ms. Soraia Pimenta during her MSc Project, an analytical model to predict kink-band formation was developed. The model is based the equilibrium of an initially misaligned fibre supported by an elastic perfectly plastic matrix, and the strength is derived when the matrix yields. This model is a good contrast to the approach presented in this chapter and is detailled in Appendix

D and published in:

A micromechanical model for kink-band formation: Part II—Analytical modelling. S. Pimenta, R. Gutkin, S.T. Pinho and P. Robinson. Composites Science and Technology, 2009, 69, 956-964.

Chapter 7

Modelling the R-curve effect and its specimen-dependence

7.1 Introduction

Several types of materials, such as concrete and fibre-reinforced composites, often show rising resistance (R)-curves—their resistance to fracture increases as the crack propagates—which are important to model in order to predict accurately the response of such a material during damage propagation. This chapter is concerned with modelling the R-curve effect and its specimen-dependence displayed under large scale bridging conditions associated with longitudinal intralaminar fracture in unidirectional laminated composites.

Increasing R-curves can be attributed to toughening mechanisms acting in the wake of the crack; in laminated composites these could be fibre bridging and pull-out, cross-over fibre bridging or z-pins. The length over which these mechanisms act, called process or bridging zone, is often large compared to the characteristic dimensions of the specimen. For instance, in compact tension (CT) specimens, used to measure the fracture toughness of the tensile fibre failure mode in carbon / epoxy [91], the length of the process zone can be approximately 11 mm. When such large-scale bridging conditions prevail, it has been shown that the R-curve is not a material property but is dependent on the specimen geometry [113]. Similarly, the length of

the process zone is in general not constant during crack growth. The specimen-dependency of the R-curve has been experimentally demonstrated in [5] and [114] using a double cantilever beam (DCB) specimen loaded with pure moments, for which case the length of the process zone is constant during crack growth, to measure the R-curve associated with mode I intralaminar longitudinal crack growth. R-curves were measured for several values of the height of the DCB's arms and it was found that for a height of 1.5 mm the length of the process zone was in the region of 28 mm, while for a height of 4 mm, the process zone was approximately 56 mm long.

Under large-scale bridging conditions, it has been proposed in [113] and [5] to use the bridging law—which relates the traction in the bridging zone with the crack opening displacement— as a material property. Experimentally, the bridging law can be calculated from the knowledge of the R-curve (and therefore the critical energy release rate G_R) and the crack end-opening displacement (δ) as:

$$\sigma(\delta) = \frac{\partial G_R}{\partial \delta}. \tag{7.1}$$

Sørensen et al. [5] used the pure moment loaded DCB specimen to determine the bridging law associated with cross-over fibre bridging in mode I intralaminar crack growth. With this test configuration, crack growth is under pure mode I and the J-integral evaluated along the boundaries of the specimen is equal to the energy release rate (G) [113], which can be expressed as a function of the applied moments, material properties and geometry of the beams. In this case, the bridging law was found to be nonlinear and independent of the specimen geometry. This approach was recently extended to mixed-mode behaviour using the uneven bending moment DCB specimen [115].

In Finite Element (FE) analyses, simplified cohesive laws are often used (cohesive laws assume a finite stress field at the crack tip, while bridging laws assume a singularity at the crack tip; see [116] for a discussion of the two approaches). Bilinear cohesive laws (or linear softening laws) are for example often used to model interlaminar delamination. These laws are typically sufficient in the case of delamination as the fracture energy is dissipated by a single failure mechanism and the R-curves

are typically flat. However, in the case of intralaminar crack growth, energy dissipation due to matrix failure and cross-over fibre bridging need to be accounted for. A mixed-mode trilinear cohesive law has been proposed by Hansen et al. [117] to model delamination exhibiting fibre bridging. The parameters required to define the cohesive law are obtained from an R-curve $G_R(\delta)$ and Eq 7.1. Hansen et al. [117] show that because each energy dissipating mechanism is accounted for, and represented by a different slope in the softening law, the R-curve behaviour is well captured.

Recently, Dávila et al. [87] proposed a similar modelling strategy for translaminar crack growth (through the fibres). The parameters required to define the cohesive law were obtained from the R-curve measured with CT specimens [91]. In this case, the R-curve was measured as a function of the crack length and not the end-opening displacement. Therefore, the cohesive law cannot be evaluated using Eq 7.1. By building a trilinear law as the superposition of two bilinear laws, Dávila et al. [87] derived an expression for the R-curve as a function of the crack extension. This expression, related to the analysis of Foote et al. [118], assumes that the crack faces are straight over the softening region and requires the length of the process zone to be known (eg from the analysis of the R-curve $G_R(a)$).

In the present chapter, the R-curve effect and its specimen-dependence is investigated for intralaminar fracture of CFRP, using CT and DCB specimens as shown in Fig. 7.1. The mathematical relationships between crack extension and crack opening displacements for these two types of specimens are first derived and related to a simplified tri-linear cohesive law. The tri-linear cohesive model is calibrated with the experimental results from a DCB specimen, and used to reproduce the R-curves measured experimentally during the DCB and CT tests both analytically and using an FE implementation.

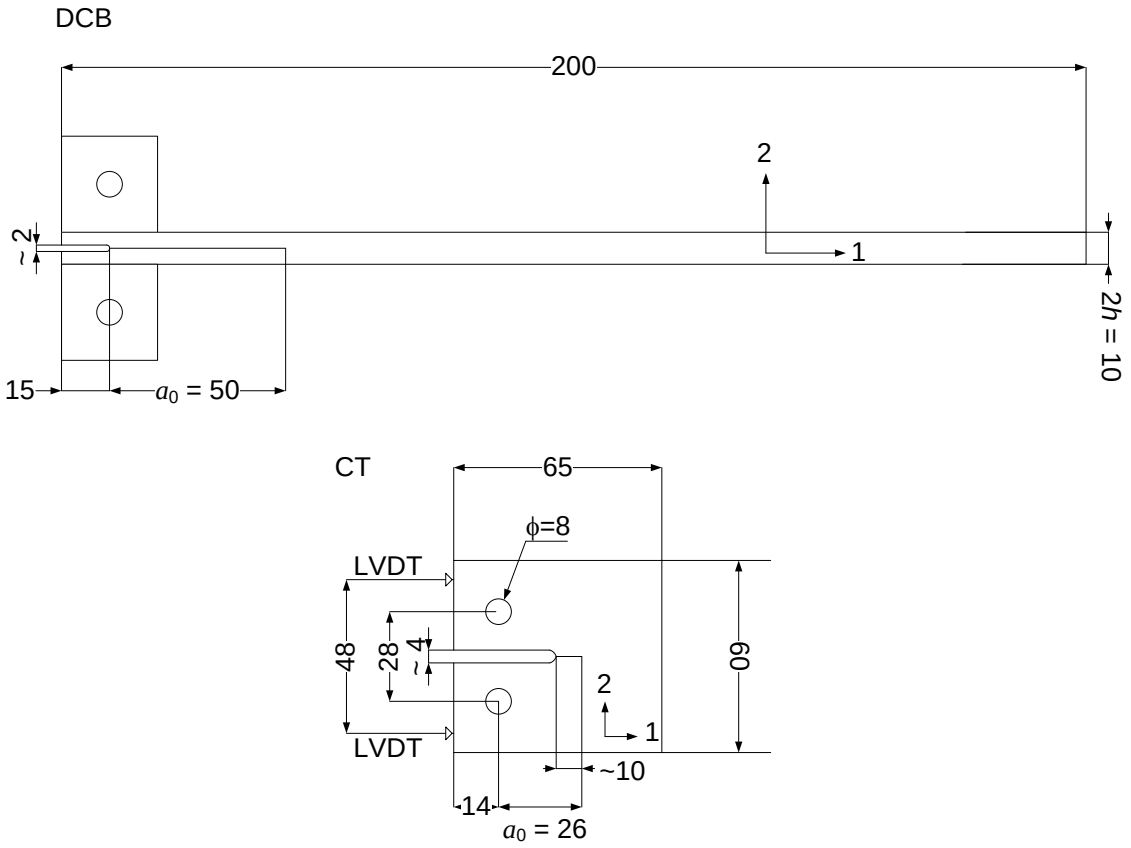


Figure 7.1: DCB and CT specimen dimensions (in mm)

7.2 Definition of the cohesive law from a measured R-curve

7.2.1 Trilinear constitutive law

In this section, a method to define a cohesive law from an R-curve ($G_R(a)$) is presented. The relationship between end-opening and crack extension is studied for two specimen types showing significantly different crack profiles. To derive this relationship, it is assumed that the opening profile in the long process zone (LPZ) is the same as in the arms of the specimen. Specifically for the CT specimen, the arms deform in shear, so that the crack profile is assumed to be linear also in the LPZ. For the DCB, the deformation is due to a linearly varying bending moment, so

that the crack profile is assumed to be a third order polynomial. The validity of this assumption relies on suitable CT and DCB specimen configurations (so that they deform under shear and bending respectively), and restricts the maximum dimension of the process zone (relative to the crack length) as well as the magnitude of the cohesive stresses in the LPZ. This assumption, for the specimens and material used in this study, will be tested by comparison with numerical data in Section 7.4.3.

The parameters of the cohesive law are defined in Fig. 7.2. In the present case, the cohesive strength σ_0 is equal to the transverse tensile strength of the composite, Y_t. In the linear elastic part, the stress and displacement are related through an elastic stiffness $K = E/l_c$, where E is the transverse modulus of the composite and l_c is a characteristic length associated with the thickness of the damage zone. For an ideal zero-thickness crack, K should be as high as possible. For a smeared FE implementation, l_c is related to the size of the element used, see [86, 88] for further details. In Fig. 7.2, δ_0 is the opening at failure initiation and is defined as

$$\delta_0 = \frac{\sigma_0}{K}. \tag{7.2}$$

The small scale failure process at the crack tip is called short process zone (SPZ), and is characterized by a crack tip toughness G_{init}. When the SPZ is fully developed, the corresponding crack opening displacement is called the intermediate separation δ_i (see Figs 7.2, 7.3 and 7.4). A strength ratio between the intermediate strength and the cohesive strength is defined as

$$r = \frac{\sigma_i}{\sigma_0}. \tag{7.3}$$

In Fig. 7.2, the toughness associated with fibre bridging is denoted $G_{prop} - G_{init}$, and the final separation δ_f.

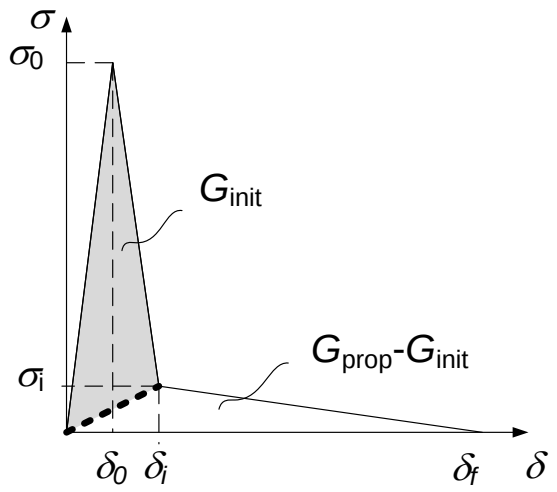


Figure 7.2: Simplified trilinear cohesive law.

From Fig. 7.2, the cohesive law can be written as

$$\sigma = \begin{cases} K\delta & \text{for } 0 \leq \delta \leq \delta_0 \\ \frac{\sigma_0}{\delta_i - \delta_0}\left[(r-1)\,\delta + (\delta_i - r\delta_0)\right] & \text{for } \delta_0 \leq \delta \leq \delta_i \\ \frac{r\sigma_0}{\delta_f - \delta_i}\left(\delta_f - \delta\right) & \text{for } \delta_i \leq \delta \leq \delta_f \end{cases} . \tag{7.4}$$

The energy dissipated by fibre bridging, corresponding to area $(G_{prop} - G_{init})$, reads

$$G_{prop} - G_{init} = \frac{\sigma_i \delta_f}{2}, \tag{7.5}$$

hence, from the definition in Eq 7.3

$$r = \frac{2\left(G_{prop} - G_{init}\right)}{\delta_f \sigma_0}. \tag{7.6}$$

In the same way, the energy dissipated in the SPZ, and corresponding to area G_{init}, reads

$$G_{init} = \frac{\sigma_0}{2}\left(\delta_i - r\delta_0\right). \tag{7.7}$$

Substituing r from Eq 7.6 into Eq 7.7, and solving for δ_i, leads to

$$\delta_i = \frac{2}{\sigma_0}\left[G_{init} + (G_{prop} - G_{init})\,\frac{\delta_0}{\delta_f}\right]. \tag{7.8}$$

On the right hand side of Eq 7.8, σ_0 is the relevant strength of the material, δ_0 is determined from Eq 7.2, and G_{init} and G_{prop} are measured from the R-curve. To obtain δ_f, a relationship between the crack extension and the crack opening needs to be established. This relationship depends on the type of specimen used and is derived now for the CT and DCB specimens.

7.2.2 Crack extension versus crack opening displacement relationship for the CT specimen

Under the aforementioned assumption that the CT specimen deforms in shear and hence the crack profile outside the SPZ is linear, the crack profile for the CT specimen can be schematically represented as in Fig. 7.3. From geometrical considerations, the crack end opening displacement at the initial crack tip (located by the length a_0) can be written

$$\delta = (\Delta - \delta_i)\,\frac{\Delta a}{a_0 + \Delta a} + \delta_i. \tag{7.9}$$

When the R-curve just reaches steady-state $G_R = G_{prop}$, and considering the crack tip to be at the trailing edge of the short process zone, the crack extension is equal to the length of the LPZ, $\Delta a = l_{LPZ}$, and $\delta = \delta_f$. Posing

$$\lambda = \frac{l_{LPZ}}{a_0 + l_{LPZ}}, \tag{7.10}$$

and using Eq 7.8 in Eq 7.9 leads to a second order equation in δ_f

$$\delta_f^2 - \left(\frac{2}{\sigma_0}G_{init}\,(1-\lambda) + \Delta\lambda\right)\delta_f - \frac{2\delta_0}{\sigma_0}\,(1-\lambda)\,(G_{prop} - G_{init}) = 0, \tag{7.11}$$

where the applied displacement Δ, is taken at the beginning of the steady-state: $\Delta = \Delta_{G_R = G_{prop}}$ and the physically relevelant solution for δ_f is the positive root of

Eq 7.11.

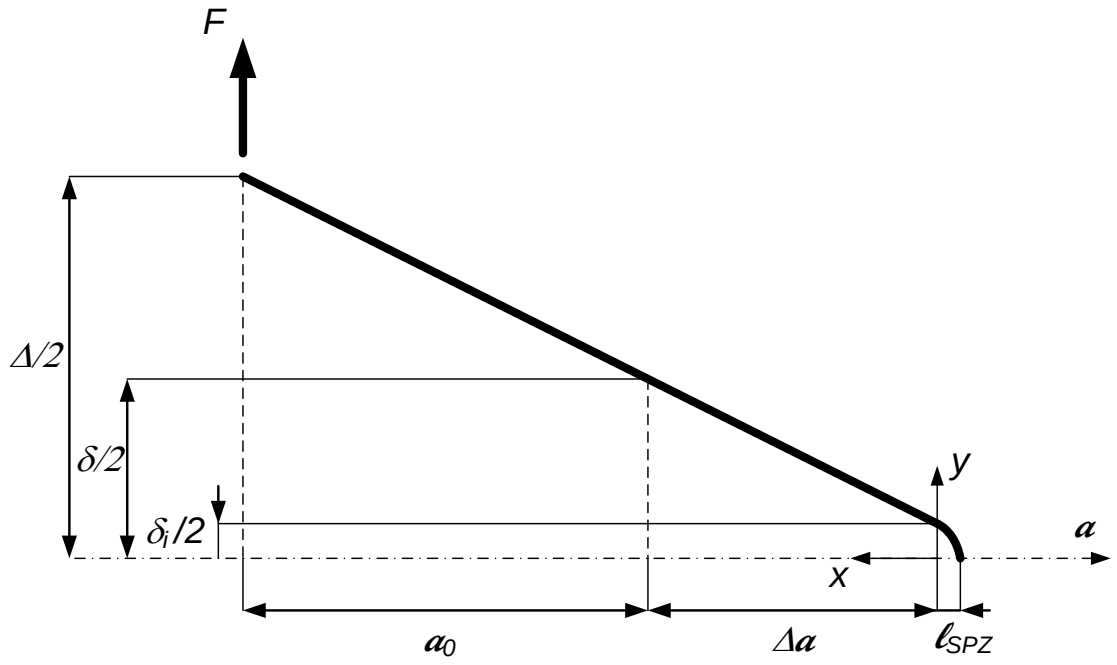


Figure 7.3: Assumed crack profile for a CT specimen.

7.2.3 Crack extension versus crack opening displacement relationship for the DCB specimen

For the DCB, the arms outside the short process zone are assumed to deform in pure bending, due to the applied load F, such that the crack profile can be schematically represented as in Fig. 7.4. The crack profile is assumed to follow a third order polynomial

$$y(x) = c_0 + c_1 x + c_2 x^2 + c_3 x^3. \tag{7.12}$$

At $x = 0$, $y(0) = \delta_i/2$ and the rotation at the end of the SPZ is neglected so that $y'(0) = 0$, hence, $c_0 = \delta_i/2$ and $c_1 = 0$. The two constants remaining are solved by noting that for $x = a_0 + \Delta a$, $y(a_0 + \Delta a) = \Delta/2$ and the moment is zero

$y''(a_0 + \Delta a) = 0$, which yield

$$c_2 = \frac{\Delta - \delta_i}{2(a_0 + \Delta a)^2} \text{ and } c_3 = -\frac{\Delta - \delta_i}{6(a_0 + \Delta a)^3}. \tag{7.13}$$

Therefore, for $x = \Delta a$

$$\delta = (\Delta - \delta_i)\frac{\Delta a^2(2\Delta a + 3a_0)}{(a_0 + \Delta a)^3} + \delta_i. \tag{7.14}$$

When the R-curve just reaches steady-state $G_R = G_{prop}$, the crack extension is equal to the length of the LPZ, $\Delta a = l_{LPZ}$, and $\delta = \delta_f$. Posing

$$\lambda = l_{LPZ}^2 \frac{(2l_{LPZ} + 3a_0)}{(a_0 + l_{LPZ})^3}, \tag{7.15}$$

and using Eq 7.8 in Eq 7.14 leads to a second order equation in δ_f identical to Eq 7.11 (but with λ given by Eq 7.15 instead of Eq 7.10).

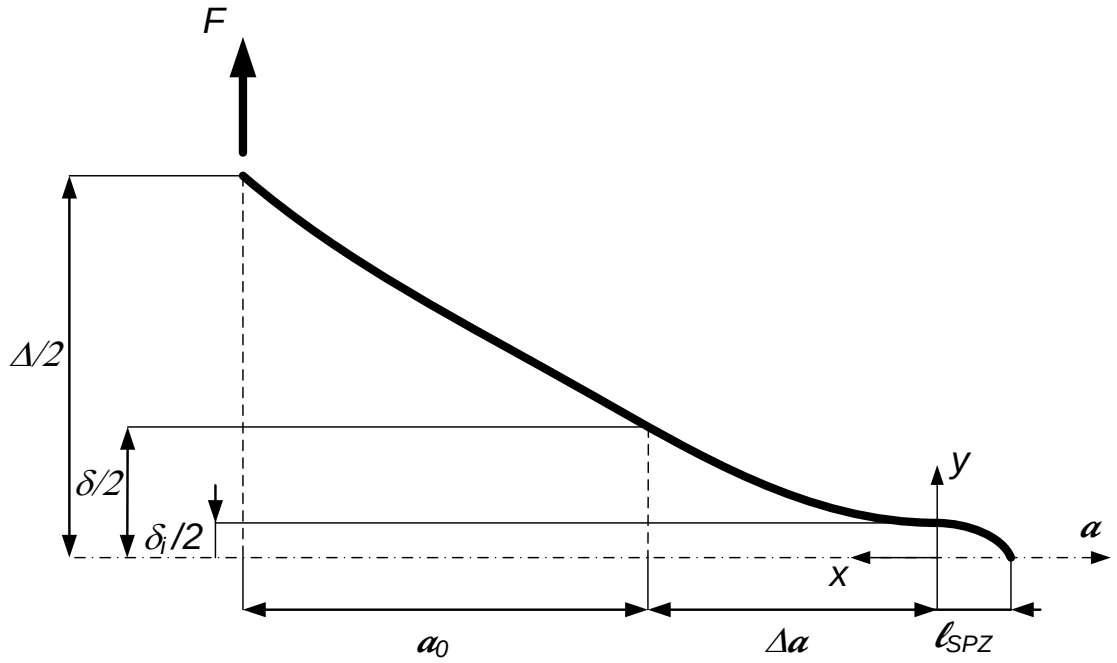


Figure 7.4: Assumed crack profile for a DCB specimen.

7.2.4 R-curves and load versus displacement curves

The R-curve as a function of the crack opening can be found by integrating Eq 7.1. The SPZ being quickly developed in both the CT and DCB specimens, only the R-curve during the development of the LPZ and in the steady-state is considered, so that integrating Eq 7.1 gives

$$G_R = \begin{cases} \int_0^{\delta} K\delta d\delta & \delta < \delta_i \\ G_{init} + r\sigma_0 \frac{\delta_i}{2} + \int_{\delta_i}^{\delta} \frac{r\sigma_0}{\delta_f - \delta_i} (\delta_f - \delta) \, \mathrm{d}\delta & \text{for } \delta_i \leq \delta \leq \delta_f \\ G_{prop} & \text{for } \delta > \delta_f \end{cases}, \tag{7.16}$$

which leads to

$$G_R = \begin{cases} K\delta^2/2 & \delta < \delta_i \\ G_{init} + r\sigma_0 \frac{\delta_i}{2} + \frac{r\sigma_0}{\delta_f - \delta_i} \left[\delta_f (\delta - \delta_i) - \frac{\delta^2 - \delta_i^2}{2} \right] & \text{for } \delta_i \leq \delta \leq \delta_f \\ G_{prop} & \text{for } \delta > \delta_f \end{cases}. \tag{7.17}$$

In Eq 7.17, it has been implicitly assumed that the J-integral is equal to the energy release rate which involves an approximation for the CT and DCB specimens under large scale bridging condition [113].

The crack end opening displacement δ in Eq 7.17 can be replaced by its expression as a function of the crack extension Δa given in Eq 7.9 for the CT specimen and Eq 7.14 for the DCB specimen.

The only remaining unknown is the applied displacement in Eq 7.9 or Eq 7.14 and which can be solved by writing the energy release rate for a linear elastic material as

$$G = \frac{F^2}{2t} \frac{\mathrm{d}C}{\mathrm{d}a} = \frac{\Delta^2}{2tC^2} \frac{\mathrm{d}C}{\mathrm{d}a}, \tag{7.18}$$

where $C = \Delta/F$ and $C = C^{DCB}(a)$ and $C = C^{CT}(a)$ are the compliance of the DCB and CT specimens, respectively, and t the thickness of the specimens. These compliances are found using the FE models presented later in Section 7.4, without the damage model and loaded with a unit load for several values of the crack length

a. The curve $C(a)$ is then fitted using a function of the form

$$C = (\alpha a + \beta)^{\chi}, \tag{7.19}$$

where α, β and χ were calculated to best fit the data.

Once Δ and C are known, the load versus displacement curve can also be predicted.

7.3 Mode I intralaminar R-curve measurement

7.3.1 Data reduction

The data reduction scheme is the same for both types of specimens (DCB and CT). The critical strain energy release rate can be calculated using the change in compliance, C, with crack length, a, in Eq 7.18. The compliance calibration method is used in this study, therefore, the elastic compliance of the specimen at each optically measured crack length is determined directly from the load displacement curve by unloading and reloading the specimens, see Figs 7.5 a and c. The experimental C vs. a data is then plotted and fit with a function of the form defined in Eq 7.19, where α, β and χ were calculated to best fit the experimental data. The critical strain energy release rate at each measured crack length is then obtained as

$$G_{Ic} = \frac{F_c^2}{2t}\alpha\chi\left(\alpha a + \beta\right)^{(\chi-1)}. \tag{7.20}$$

7.3.2 Specimen manufacture

The material system used in this study is an IM7/8552 unidirectional carbon/epoxy prepreg of 0.25 mm nominal ply thickness. Composite panels with a lay-up of $[0]_{20}$ were manufactured using the hand lay-up method and cured to the prepreg manufacturer's instructions. A wet saw was used to cut the rectangular plates to the geometries shown in Fig. 7.1; the 8 mm holes were made using a carbide tipped drill.

The precracks were machined using a razor saw up to a length of 50 mm for the DCB and 26 mm for the CT. The DCB specimens were opened to initiate a crack over a few millimeters at the tip of the precrack, this allowed for a sharp crack tip to be obtained. This process was not performed for the CT specimens due to the small crack growth range possible.

Prior to testing, a scale with a 1 mm increment was drawn on the specimens in order to optically measure crack growth and the individual specimen dimensions were measured and recorded.

7.3.3 Test method and experimental setup

Six specimens of each configuration were tested using an Instron machine with a 1 kN load cell; each specimen was loaded under displacement control at a rate of 0.5 mm/min. Measurements of load and crosshead displacement were recorded using a data logger. A CCD camera and monitor was used to view a magnified image of approximately 12 mm of the area of the specimen containing the crack-growth scale. This magnified image was used together with an event marker connected to the data logger to monitor crack growth.

7.3.4 Experimental results and analysis

A representative load versus displacement curve recorded during the DCB tests is shown in Fig. 7.5a. The response is quasi-brittle with a linear region followed by a long nonlinear one, where the load slowly increases with displacement. The latter corresponds to the propagation of the crack and subsequent development of the long process zone. Once the LPZ is fully developed, the load decreases as the applied displacement increases. The R-curves for the DCB specimen (Fig. 7.5b) show a linear increasing trend from an initiation value of $G_{init} = 0.256 \pm 0.034$ kJ/m^2 to a steady state value of $G_{prop} = 1.626 \pm 0.213$ kJ/m^2. The length of the LPZ is approximately $l_{LPZ} = 66$ mm.

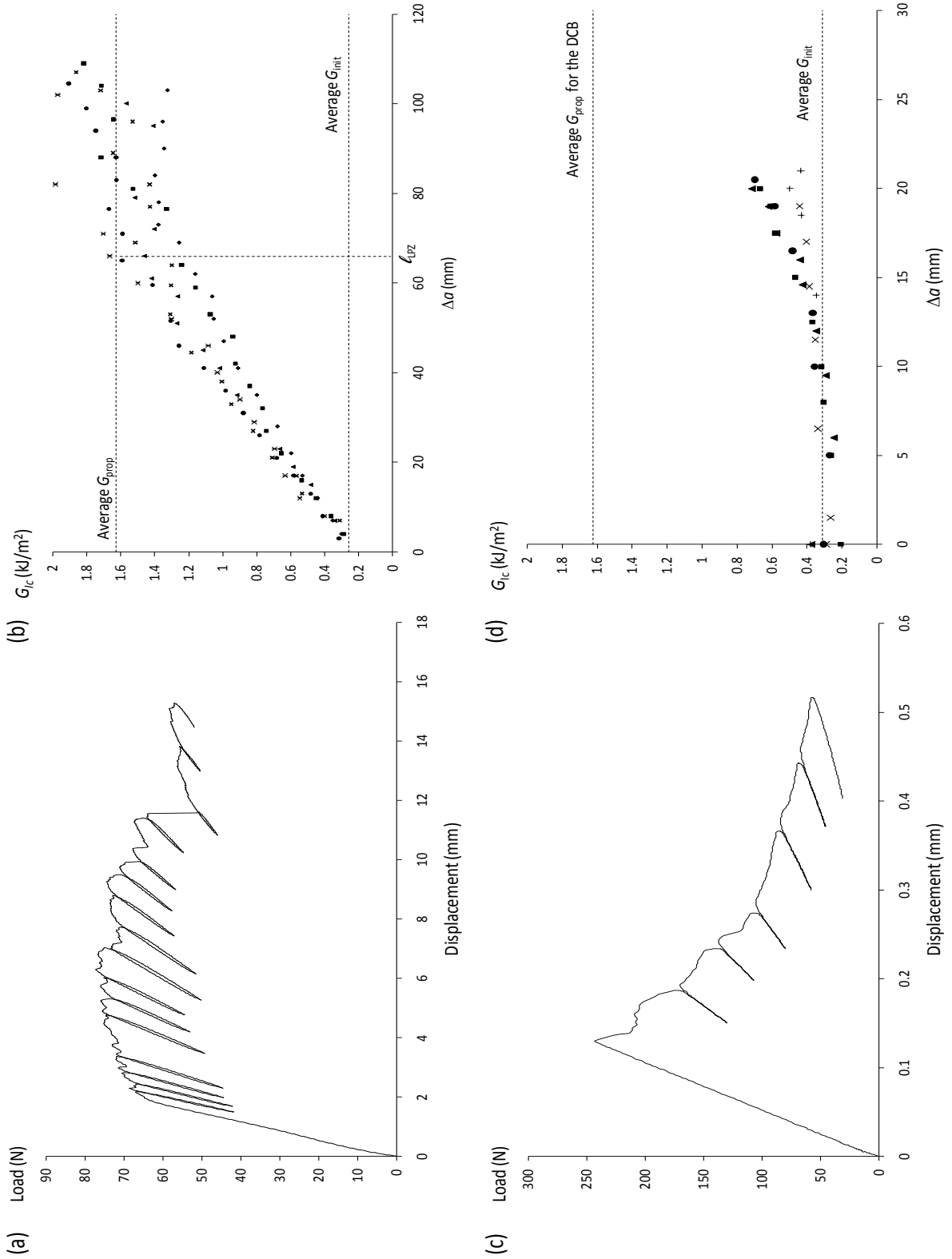


Figure 7.5: Load versus displacement curves and R-curves (a-b) for the DCB tests and (c-d) for the CT tests.

Table 7.1: Parameters used for the definition of the cohesive law.

Parameter	Value	Source
G_{init} (kJ/m^2)	0.256	R-curve DCB test
G_{prop} (kJ/m^2)	1.626	R-curve DCB test
l_{LPZ} (mm)	66	R-curve DCB test
$\Delta_{G_R=G_{prop}}$ (mm)	9.49	Load-displacement curve DCB test
E_{22} (MPa)	8600	Standard test
σ_0 (MPa)	62	Standard test
δ_0 (mm)	0.0014	Eq 7.2
K (MPa/mm)	44285	
r	0.01254	Eq 7.6
δ_f (mm)	3.5228	Eq 7.11
δ_i (mm)	0.00827	Eq 7.8

The load versus displacement curve for the CT specimen (Fig. 7.5c) indicates a brittle response with the linear elastic region immediately followed by a drop in load. After this load drop, crack propagation appears to be stable. The R-curves (Fig. 7.5d) have an initiation toughness of $G_{init} = 0.311 \pm 0.07$ kJ/m^2. The curves show a knee at approximately $\Delta a = 14.5$ mm, after which the toughness increases faster with crack growth. Because of the short width of the CT specimen, the LPZ does not fully develop and the R-curve only reaches $\sim 50\%$ of the propagation value found in the DCB test.

The parameters used to define the cohesive law are the average values of the DCB tests and are summarised in Table 7.1, and the corresponding cohesive law is plotted in Fig. 7.6.

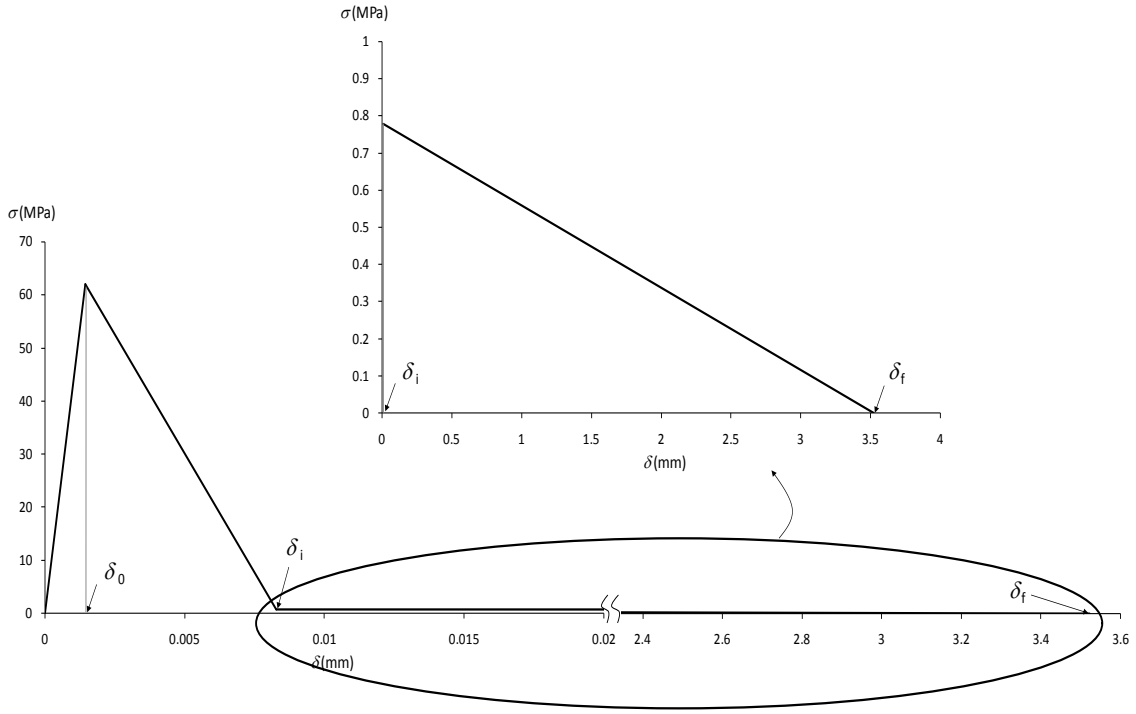


Figure 7.6: Trilinear cohesive law defined from DCB tests.

7.4 Numerical simulation of mode I intralaminar matrix failure

7.4.1 Finite Element models

The FE models used are shown in Fig. 7.7. The geometries are based on the dimensions of the test specimens in Fig. 7.1. 3D reduced integration (Abaqus [83] C3D8R) elements are used. The height of each DCB arm is divided into three elements such that the bending stresses can be well captured. A 2 mm-high band is defined after the precrack, see Fig. 7.7, which corresponds to the crack width observed in the experiments. In this band, the cohesive model defined in Section 7.2 is used. The properties used for the models are summarised in Table 7.2.

Table 7.2: Material properties used for the FE models.

E_1 (MPa)	E_2 (MPa)	ν_{12}	G_{12} (MPa)	Y_t (MPa)
176600	8600	0.34	4480	62

The models were run using Abaqus/Explicit [83]. A displacement in the 2-direction is applied to the nodes shown in Fig. 7.7 (nodes that correspond to the points of application of the load in the experiments). The displacements of these nodes are fixed in the 1-direction. The load is extracted on the nodes where the displacement is applied in both models. Crack lengths are measured at several values of the load, so that an R-curve can be calculated following the same data reduction scheme used in the experiments, and detailed in Section 7.3.1. For these measurements, the crack tip is defined as the node where stress and displacement are equal to (σ_i, δ_i) defined in Figs 7.2 and 7.6.

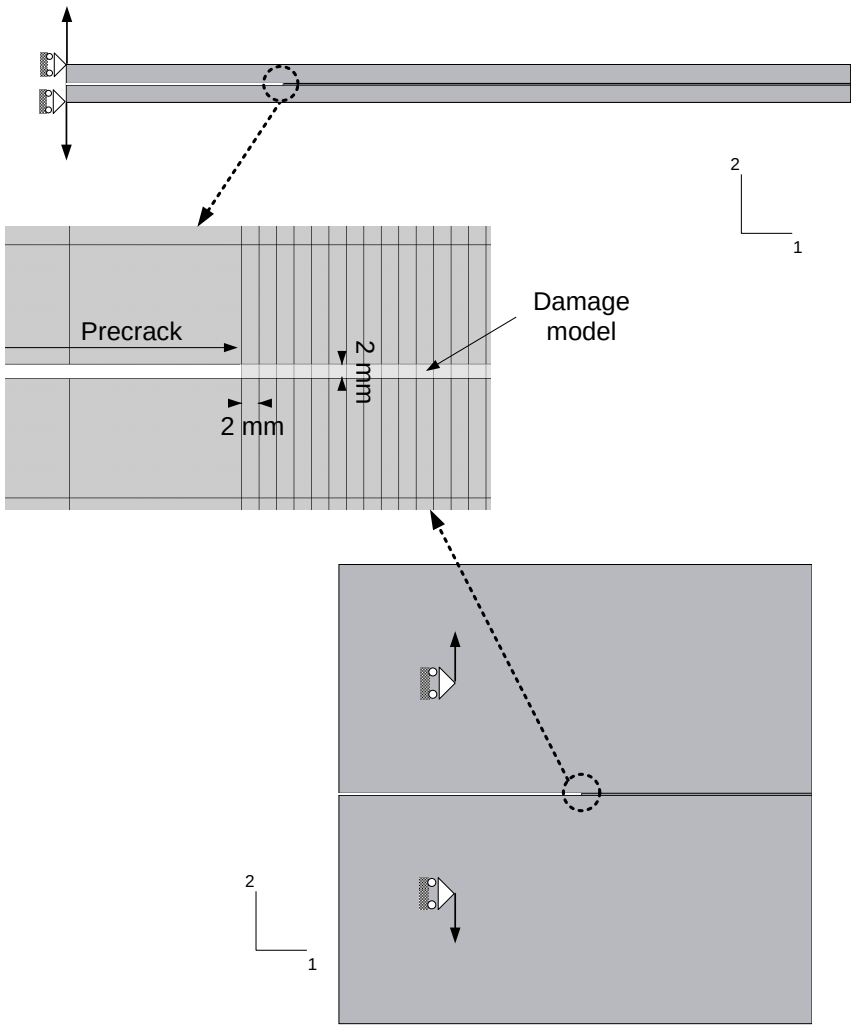


Figure 7.7: FE models of the DCB and CT specimens.

7.4.2 Load displacement and R-curves predicted by the FE models

Fig. 7.8 shows the load versus displacement curves predicted for the DCB specimen using: (i) a bilinear law with $G_c = G_{init}$, (ii) a bilinear law with $G_c = G_{prop}$ and (iii) the trilinear law as defined in Fig. 7.6 and the properties from Table 7.1. The

bilinear laws capture well either the onset of non-linearity or the softening region but not the transition between the two regions. However, the trilinear cohesive law is able to capture the experimental trend across the whole displacement range. The FE models show a stiffer response in the linear elastic part as the manual precrack is not included in these models. The load versus displacement curves predicted using the quasi-analytical expressions presented in Section 7.2.4 are also plotted in Fig. 7.8 and agree well with the FE results.

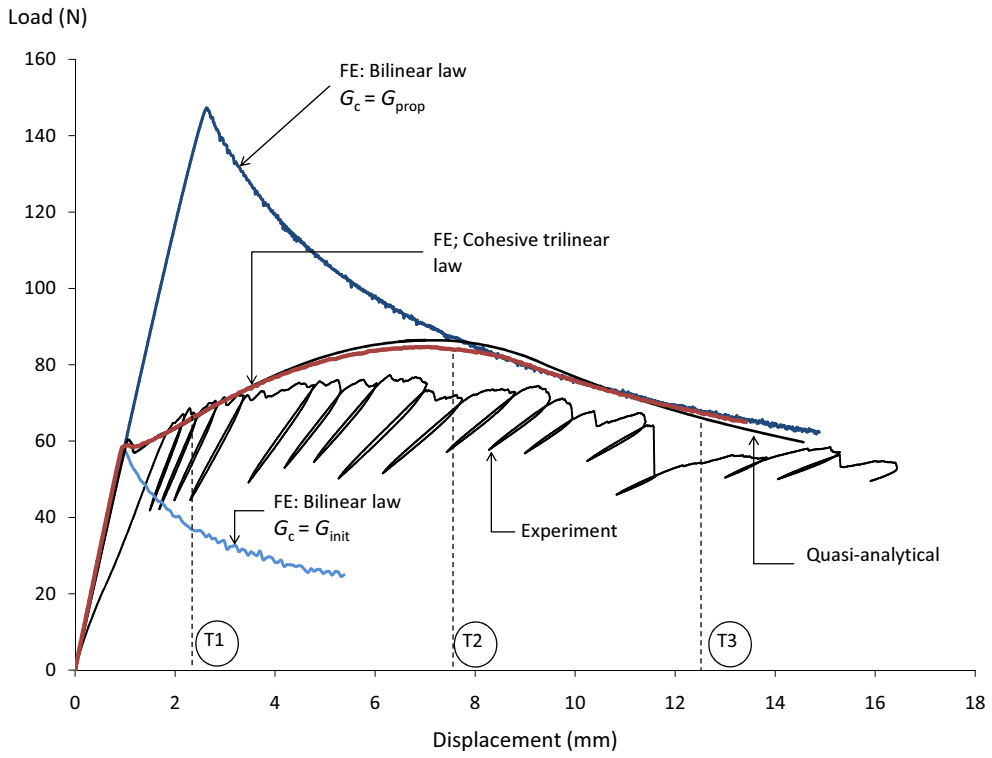


Figure 7.8: Load displacement curves for the DCB test; Experimental results with FE predictions for bilinear and trilinear cohesive laws and quasi-analytical predictions.

Fig. 7.9 shows the R-curve measured experimentally, $G_R(\Delta a)$, together with the FE and quasi-analytical predictions for the DCB specimen. The predicted R-curves show an S-shaped trend while the experiments appear to be more linear. Overall, the agreement in terms of initiation and propagation as well as for the length of the LPZ are good.

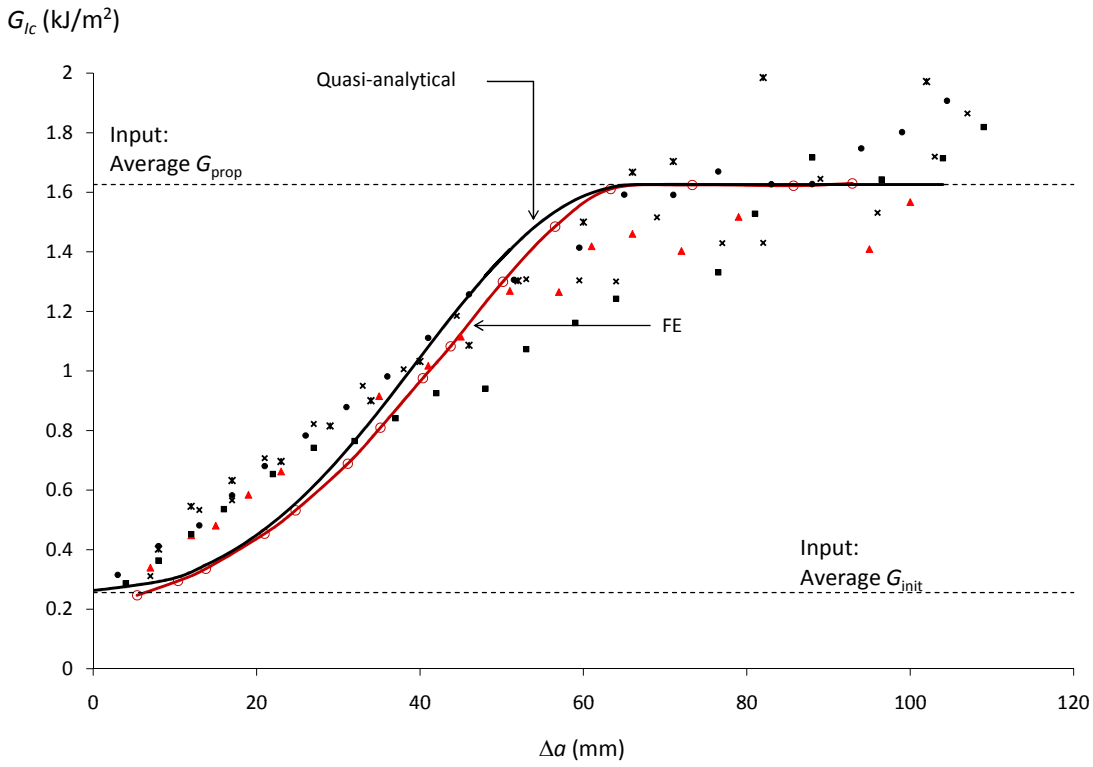


Figure 7.9: $G_R(\Delta a)$ for the DCB test.

Fig. 7.10 shows the R-curves as a function of the end-opening extracted from the FE model and calculated using Eq 7.17. The FE result lies slightly under the analytical prediction for $\delta_i \leq \delta \leq \delta_f$, but show a similar trend and matches exactly for $\delta \geq \delta_f$.

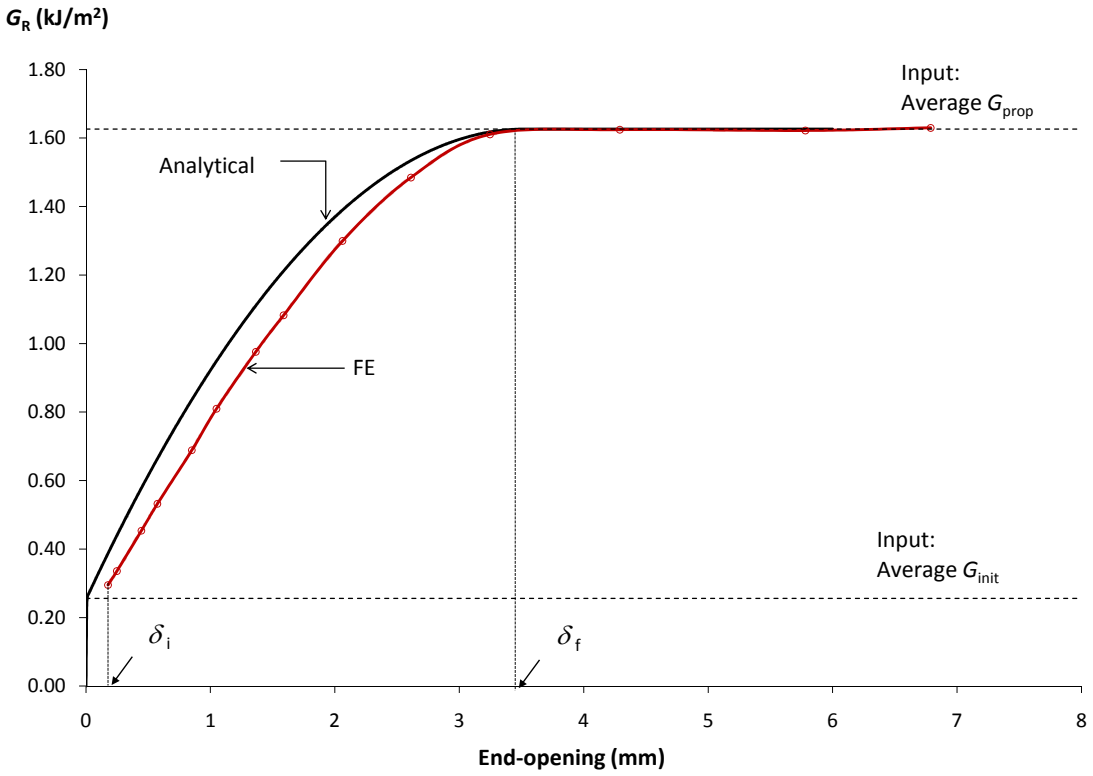


Figure 7.10: FE and analytical $G_R(\delta)$ for the DCB test.

Fig. 7.11 shows the load versus displacement curves predicted by the CT FE model using: (i) a bilinear law with $G_c = G_{init}$, (ii) a bilinear law with $G_c = G_{prop}$ and (iii) the trilinear law, defined from the DCB results, Fig. 7.6 and properties from Table 7.1. The bilinear law with the initiation value captures well the peak load but significantly underpredicts the load at the tail of the curve. When the propagation value of the toughness is used, the FE prediction tends towards the experimental result only at the tail of the curve. The trilinear cohesive law is able to capture both the initiation and tail of the load versus displacement curve. The load versus displacement curves predicted using the quasi-analytical expressions are also plotted and show a close agreement to the experimental and FE results.

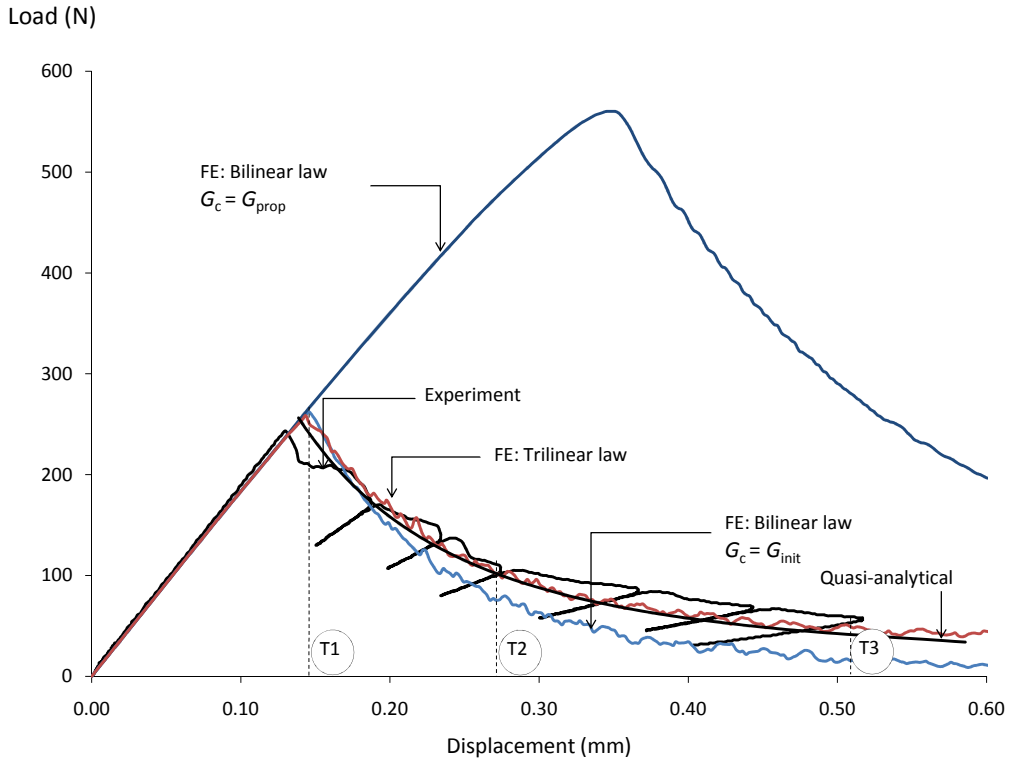


Figure 7.11: Load displacement curves for the CT test; Experimental results with FE predictions for bilinear and trilinear cohesive laws and quasi-analytical predictions.

Fig. 7.12 shows the R-curve measured experimentally as a function of the crack extension together with the FE and quasi-analytical prediction for the CT specimen. The R-curves have all the same trend up to a crack extension of 15 mm, where the experimental R-curves show a steeper rise and the predictions agreeing only with the bottom range of experimental data. It should be noted that the FE and quasi-analytical models have input properties from the DCB tests only, not from the CT tests.

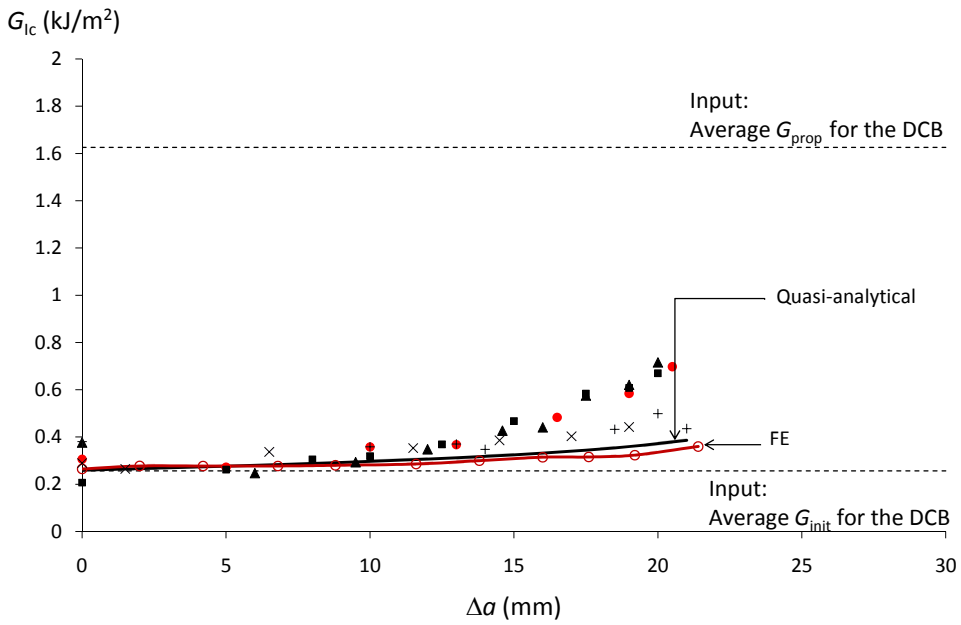


Figure 7.12: $G_R(\Delta a)$ for the CT test.

The R-curves as a function of the end-opening extracted from the FE model and calculated using Eq 7.17 are shown in Fig. 7.13. Analytical and FE predictions show the same linearly increasing trend, but the FE have slightly lower slope.

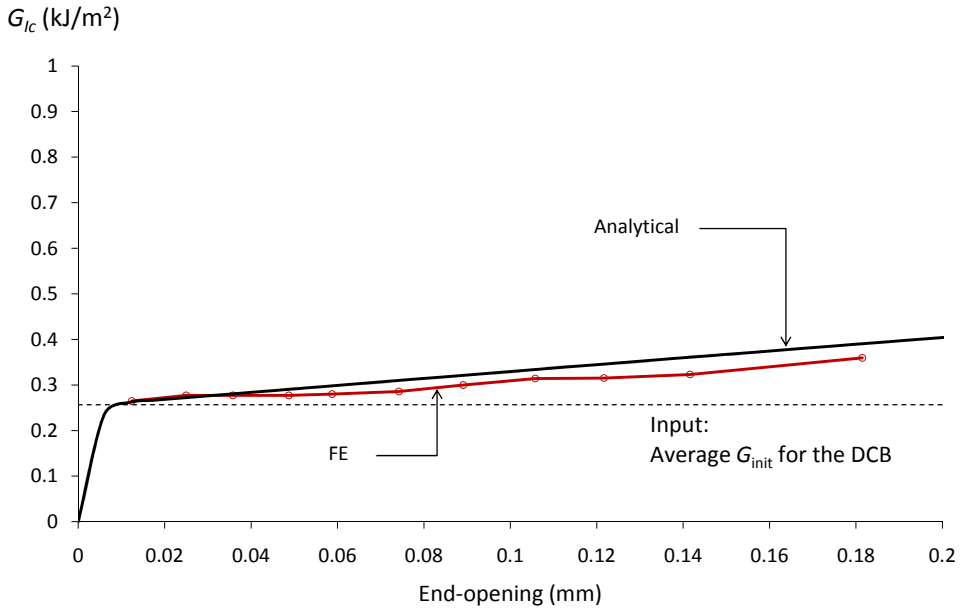


Figure 7.13: FE and analytical $G_R(\delta)$ for the CT test.

7.4.3 Crack opening displacement

The FE predicted opening displacements for the DCB specimen are plotted in Fig. 7.14 for three different applied displacements T_1, T_2 and T_3 indicated in Fig. 7.8. In Fig. 7.14, a third order polynomial is fitted to each profile, for displacements in the range $\delta_i \leq \delta \leq \Delta$ (in the LPZ). The actual curve and the polynomial fit match exactly, which implies that the crack opening displacements are of the form given in Eq 7.12, which validates the asumptions of the model presented in Section 7.2.3.

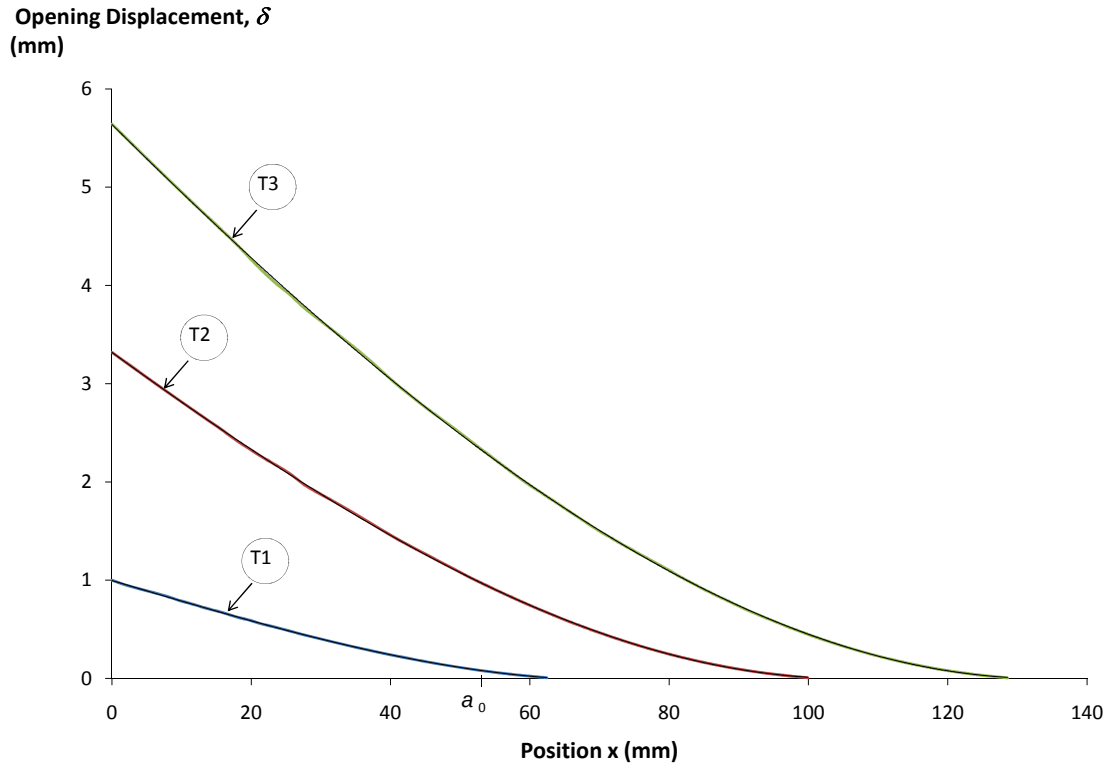


Figure 7.14: Crack opening displacements extracted from the FE model for the DCB at the displacements indicated in Fig. 7.8. Each curve is superposed with a third order polynomial.

The predicted opening displacements of the CT specimen are plotted in Fig. 7.15 for three different applied displacements T_1, T_2 and T_3 indicated in Fig. 7.11. In Fig. 7.15, a first order polynomial (linear profile) is fitted to each profile, for displacements in the range $\delta_i \leq \delta \leq \Delta$ (in the LPZ). The actual curve and the polynomial fit agree well for the curve labeled T3. Slight discrepancies occur close to δ_i for the curves labeled T1 and T2. The overall good agreement validates the assumptions of the model developed in Section 7.2.2.

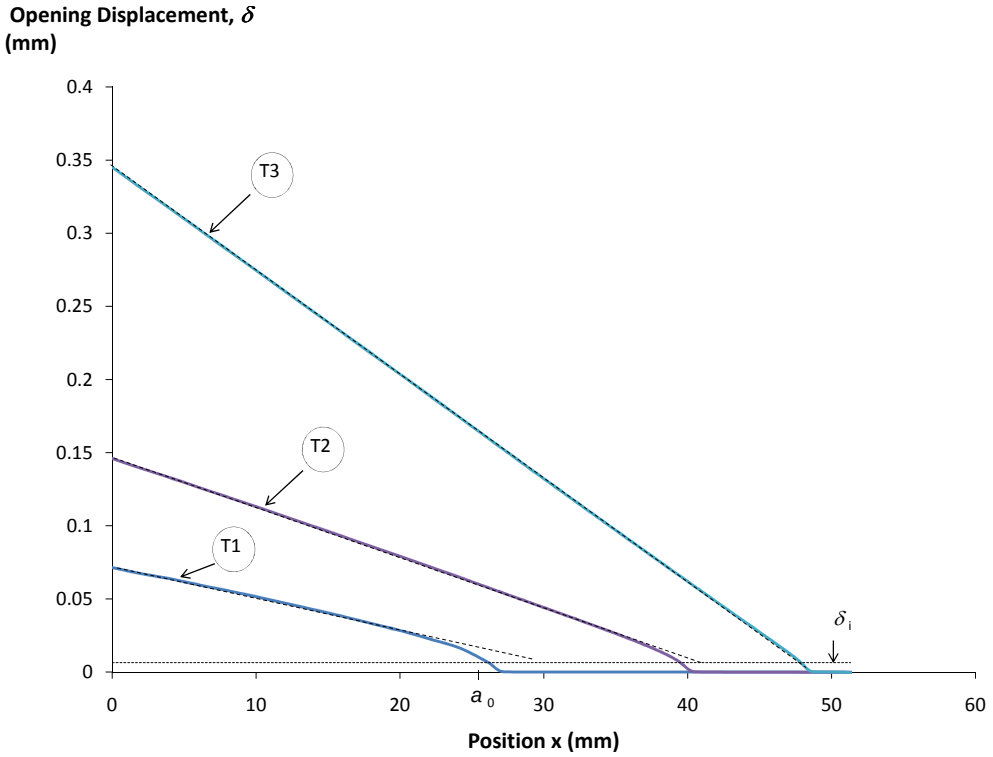


Figure 7.15: Crack opening displacements extracted from the FE model for the CT at the displacements indicated in Fig. 7.11.

7.5 Discussion

The relationships between crack extension and crack opening displacement derived in Eqs 7.10, 7.11 and 7.15 for the CT and DCB specimens rely on assumptions on the deformation of the specimen arms.

For the CT specimen, it is assumed that the bridging stresses in the long process zone (LPZ) do not affect the crack profile, and that the specimen deforms in shear, so that the crack profile is linear. The assumption is fulfilled for crack extension above 45 mm, Fig. 7.15, but for smaller crack extension, slight discrepancies can be seen close to δ_i. Nevertheless, these discrepancies remain small and Eq 7.9 holds for smaller crack lengths as well.

For the DCB specimen, it is assumed that the arms deform in pure bending, and

in the long process zone, the crack profile is not affected by the bridging stresses. The crack opening displacements extracted from the FE model fit exactly a third order polynomial in the range $\delta_i \leq \delta \leq \Delta$, Fig. 7.14, and therefore satisfy Eq 7.12. The assumption of pure bending would not hold in cases where h becomes very large with respect to the length of the precrack (a limiting case being the CT specimen) or when h becomes very small, as the deflection might be affected by the bridging stresses).

The load versus displacement and R-curve retrieved from the FE model of the DCB using the trilinear cohesive law derived from the DCB test results and Eqs 7.6, 7.8 and 7.11 are in good agreement with experimental results. Crack initiation, process zone development and steady state propagation are well captured by the model because the trilinear law allows for different scales and different energy mechanisms to be accounted for. This is not the case for the bilinear laws, Fig. 7.8, which are able to capture crack initiation or steady-state, when initiation or propagation values are chosen for the fracture toughness, respectively.

The quasi-analytical load versus displacement curve and R-curve show an excellent agreement with the FE results; the slight differences between the curves are due to the interpolation of the compliance using Eq 7.19.

The same cohesive law is used in an FE model of the CT specimen. Because the average toughness initiation value from the DCB tests is slightly higher than the initiation toughness of the CT test shown in Fig. 7.11, the peak load is slightly over-predicted. However, crack initiation and softening of the load versus displacement curve are well captured by the cohesive law model. The R-curves predicted by FE and quasi-analytically for the CT specimen falls in the experimental scatter but have a lower slope for $\Delta a > 14.5$ mm. This is also observed in the R-curves for the DCB, Fig. 7.9, where the predictions rise following an S-shape trend while the experiments show a more linear trend.

7.6 Conclusion

The mathematical relationships between crack extension and crack opening displacements for both CT and DCB specimens have been derived and related to a tri-linear cohesive law. These relationships are based on the assumptions that the arms of the CT specimen remain straight outside the short process zone; and the arms of the DCB deform in pure bending outside the short process zone. These assumptions have been verified numerically. Experimental tests for intralaminar fracture of CFRP have been carried out and analysed. The R-curve in the DCB tests has been found to rise from an initiation value of $G_{init} = 0.256 \pm 0.034$ kJ/m^2 to a steady state value of $G_{prop} = 1.626 \pm 0.213$ kJ/m^2. A rising R-curve has also been measured in the CT tests, but because of the short width of the specimens, the steady-state has not been reached. The tri-linear cohesive model has been implemented in FE. Using, as input, the experimental results from the DCB specimen, it has been shown that the cohesive law model can reproduce accurately the R-curve for the DCB and CT specimens.

7.7 Publications

It is envisaged that the contents of this chapter will be submitted for journal publication in the near future.

Chapter 8

Conclusions

8.1 Damage identification using acoustic emission

AE signals were collected from an extensive test programme consisting of standard tensile tests with various layups and orientations, as well as tests for intra- and interlaminar fracture toughness characterisation. The advantage of these toughness tests, over the tensile tests, is that damage evolves in a reasonably controlled and stable way. Furthermore, collecting AE signals from such tests appears more appropriate as in most structures, failure initiate from geometrical discontinuities, such as holes or notches.

Amongst the three pattern recognition algorithms used, the SOM combined with k-means clustering was found to give the best clustering quality and lowest computational effort. When applied to the whole series of tests, the clustering followed patterns found in the peak frequencies distribution.

The detailed study of the frequency content of each test was performed and a classification of the failure modes was proposed in Chapter 3. Some failure modes are clearly identified, e.g. matrix cracking, fibre / matrix splitting and delamination, while others such as fibre pullout or fibre fracture need further study. In particular, some frequency bands above 600 kHz in the tensile $\pm 45^\circ$ tests require more attention.

In summary, characterisation of failure modes in carbon/epoxy systems using

the frequency content of acoustic emissions appears to be a promising method.

8.2 Longitudinal compressive failure: Experiments

The in-situ and post-mortem fractography study of longitudinal compressive failure of carbon epoxy composites has revealed that shear-driven fibre compressive failure and kink-band formation can both occur. Those two types of failure were found in unidirectional and cross-ply notched laminates. The typical sequence of events is: (i) initiation of the shear-driven fibre compressive failure at the notch tip (promoted by large compressive stresses and small fibre rotations) and (ii) sliding of the crack faces which induces bending of the fibres ahead of the crack tip and promotes kink-band formation.

The 90° plies in the cross-ply specimen were found to inhibit splitting and to constrain fibre rotation, hence postponing the transition to kink-band formation.

The role of matrix microcracking during kink-band formation was also highlighted. Microcracks form in-between fibres and their cusp-like shapes indicate shear failure of the matrix. The edges of the kink-band are defined by bending failure of the fibres, first on the side of maximum compressive stress, then by crack initiation on the other side (the opening of this crack indicates it is driven by tensile stresses).

8.3 Longitudinal compressive failure: Micromechanical modelling

Failure envelope predictions for a case of in-plane shear/longitudinal compression have been obtained using a micro-mechanical FE model.

It was found that the failure envelope is defined by two regions. A first region where the strength is related to the compressive failure of the fibres and a second region which can be related to kink-band formation and splitting.

The effects of mechanical properties such as the fibre compressive strength, the constitutive response of the matrix, and the misalignment in the composite were

quantified.

The FE model was calibrated to reproduce two typical experimental failure envelopes found in the literature, and the difference between the two trends was explained.

When compared to the failure criteria available in the literature, models based on kinking theory ([22, 30]) are in general only able to capture the linear trend seen in the kinking/splitting region, when the response of the composite in shear is linear, and the concave-shaped trend (LaRC05), when the response is nonlinear.

8.4 Longitudinal compression: Analytical modelling

An analytical model to predict the strength associated with fibre kinking and splitting under combined longitudinal compression and in-plane shear has been developed. The model is based on a fracture mechanics study of the microcracks and splits created between the fibres, and results in a failure criterion which can be readily used for failure predictions. The criterion requires only standard properties and the formulation ensures that the predictions are not affected by the details of the microcracking process. A sensitivity analysis has shown that the effects of important parameters such as the nonlinear response in shear of the resin and the initial misalignment in the composite are well captured. The predictions of the model have been found to be in good agreement with experimental data [22, 37] and numerical results presented in Chapter 5.

8.5 Modelling the R-curve effect and its specimen-dependence

Mathematical relationships between crack extension and crack opening displacements for CT and DCB specimens have been derived and were used to define a tri-linear cohesive law from measured R-curves, $G_R(\Delta a)$. These relationships are

based on the assumptions that the arms of the CT specimen remain straight outside the short process zone; and the arms of the DCB deform in pure bending outside the short process zone. These assumptions have been verified numerically.

Experimental tests for intralaminar fracture of CFRP have been carried out and analysed. The R-curve in the DCB tests has been found to rise from an initiation value of $G_{init} = 0.256 \pm 0.034$ kJ/m^2 to a steady state value of $G_{prop} = 1.626 \pm 0.213$ kJ/m^2. A rising R-curve has also been measured in the CT tests, but because of the short width of the specimens, the steady-state has not been reached.

The tri-linear cohesive model has been implemented in FE, and, using as input the experimental results from the DCB specimen, it has been shown that this cohesive law model can reproduce accurately the R-curve for the DCB and CT specimens.

Chapter 9

Future work

9.1 Experimental

9.1.1 Damage identification using acoustic emission

A satisfactory classification of failure modes with the peak frequency of AE signals was achieved in Chapter 3. Some further work could be done using a method similar to the FFT: the Discrete Wavelet Transform (DWT). The DWT is a signal processing method in which a signal is decomposed into shifted and scaled versions of an original wavelet ([52] and Chapter 2). This transform is more suitable to AE signals than the FFT as AE signals are non-stationary and non-periodic. An attempt at classification using the DWT is presented in Appendix A; each AE signal is decomposed in nine wavelet levels and is associated with the level with the highest energy. Unfortunately there was no consistent correspondence of level between tests which had a shared failure mode for the work carried out so far. The potential of this technique should be explored further.

Further work should also aim at collecting signals from other types of specimen configuration, preferably in which stable damage propagation can be achieved. The effect of scaling the size of the specimens should also be studied as, for example, low frequencies could be damped in a larger specimen/structure.

9.1.2 Longitudinal compressive failure

The polishing rig developed in Chapter 4 is already being used to study other types of composites: woven and recycled composites. It could also be used to study the effect of other types of lay-up on compressive failure; in particular, further attention could focus on the role of delamination. The rig itself could be modified and improved; for example, it could be equipped with a load cell which would permit quantitative information to be collected and used for comparison with numerical/analytical models.

A possibility explored during this work is the use of synchrotron tomography to observe failure in 3D and through the material. It was not realised due to too severe constraints on the size of the specimen (1mm^3) for a sufficient resolution of less than 1μm. Further developments in synchrotron tomography could however open further avenues of research in fibre compressive failure.

Finally, the analytical model presented in Chapter 6 revealed that a good understanding of the shear response of the composite is important. Further experimental work could be done to gain information on the development of the shear cusps using test setups similar to the one presented in [119] or using in-situ SEM.

9.2 Analytical

The analytical model presented in Chapter 6 can be extended to a 3D formulation; the effect of the transverse and through the thickness stresses (σ_2, σ_3) can for instance be integrated through the response of the matrix. As mentioned in the review, a 3D formulation is important for predictions under a general stress state and is also mandatory for an implementation in FE.

With more experimental evidence on the accumulation of the microcracks in shear, a more detailed fracture mechanics study can be done to determine the reduction in elastic modulus due to damage in shear.

The findings in Chapter 7 revealed that the shape of the cohesive law used in damage models is important for accurate predictions. Simplified tri-linear cohesive

laws are appropriate for tensile translaminar fracture [87] and intralaminar fracture (Chapter 7). However, the case of compressive translaminar fracture has received little attention. As mentioned throughout this work, collecting information on failure initiation in compression is a challenging task and the same is true for propagation, which makes it difficult to propose a physically sound definition of a softening law for this case.

9.3 Numerical

In Chapter 5, a limit between splitting and kinking was defined using an FE micromechanical model. Further investigation for different types of carbon-epoxy systems could be done and could eventually lead to a criterion to discriminate between these two failure modes.

The accumulation of matrix microcracks could also be studied using the FE model, for instance, by replacing the elasto-plastic response of the matrix by a brittle response using XFEM. However, this would require a very detailed mesh in the matrix layer and could be computationally expensive (especially as the model is already nonlinear).

A criterion to represent the shear-driven fibre compressive observed in Chapter 4 could be developed and integrated with the damage model based on the LaRC05. A first exploration was carried out and some preliminary results are presented in Appendix B.

Appendix A

Damage identification using Acoustic Emission: Discrete Wavelet Transform

A.1 Discrete Wavelet Transform

As a classification of AE signals was achieved using frequency analysis in Chapter 3, this appendix investigates the use of a similar method: the Discrete Wavelet Transform (DWT). The DWT is a signal processing method in which a signal is decomposed into shifted and scaled versions of an original wavelet [52]. This transform is more suitable to AE signals than the Fast Fourier Transform (FFT) as AE signals are non-stationary and non-periodic. During one level of decomposition, the original signal passes through high- and low-pass filters so that approximation and detail coefficients are extracted from each filter, respectively. The approximations correspond to the high scale, low frequency components of the signal while the details correspond to the low scale, high frequency components.

The most suitable wavelet family for asymmetrical signals is the Daubechies wavelets $'db\,20'$ family [53, 54]. After applying the decomposition on several examples, it was found that 9 levels of decomposition gave a satisfactory decomposition without being to computationally demanding.

The wavelet decompositions are done using the wavelet toolbox implemented in MATLAB [52].

A.1.1 Level analysis

The approach taken in the following is: (i) the signal is decomposed into nine levels, (ii) each signal is labeled according to its most energetic level as shown in Fig. A.1 with the wavelet decomposition of a typical AE signal (the decomposition is limited to 6 for clarity purpose only). The top graph shows the original signal and the six levels of decomposition, the bottom graph shows the FFT of the same signals. From the top graph, the signal in level 4 has the greater amplitude and it can be verified that it is also the most energetic. From the power spectrum, it can be seen how the different levels (or scales) correspond to different frequency ranges. Fig. A.1 shows also that while the original signal has a peak frequency of approximately 100 kHz, the most energetic / highest amplitude signal in level 4 has power spectrum centered around 400 kHz.

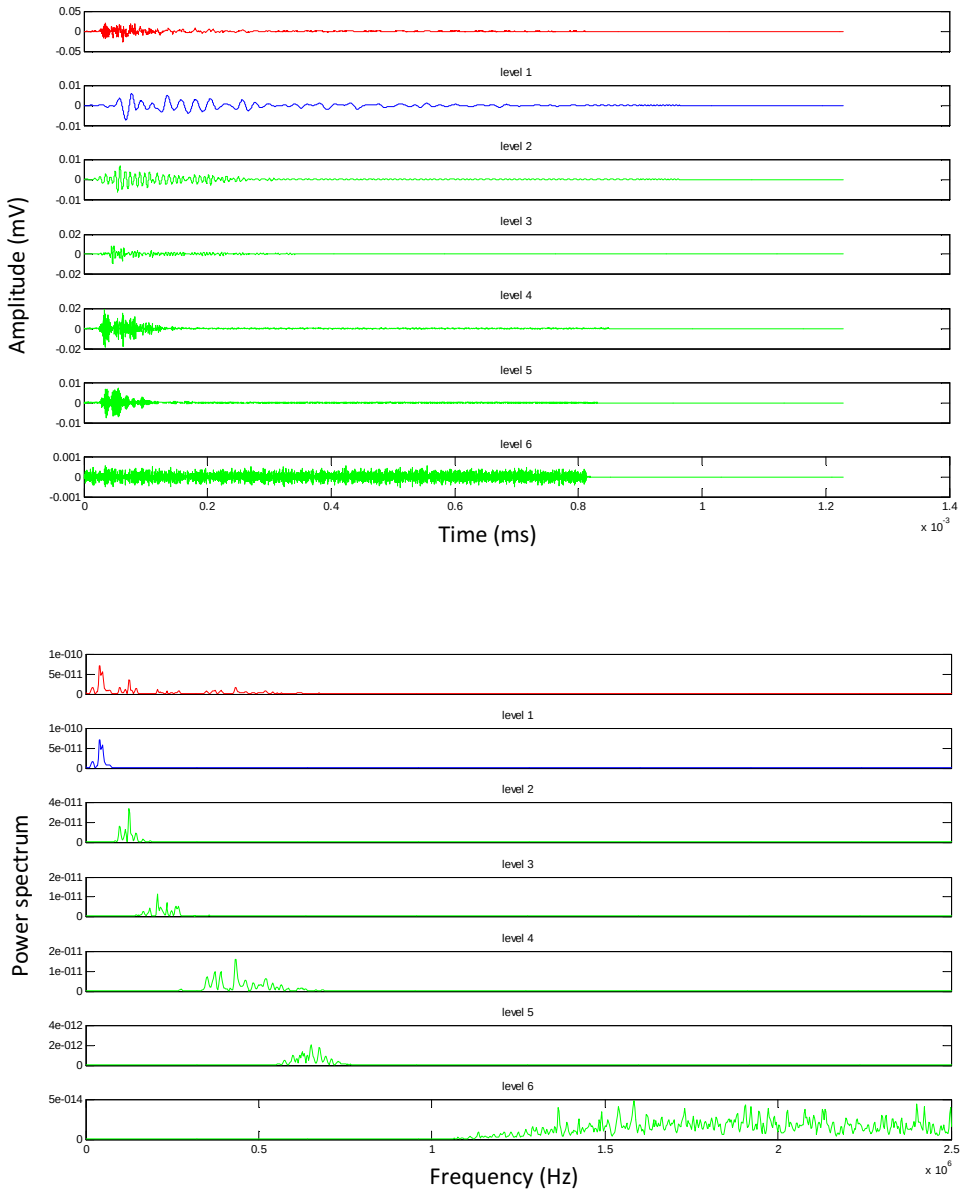


Figure A.1: (a) Wavelet decomposition of a typical AE signal; (b) Power spectrum of each decomposition level.

A.1.2 Results and discussion

Fig. A.2 (Left) shows how the events are distributed by wavelet level during the tests and (Right) the cumulative distribution of events per level for each test.

The wavelet decomposition for the signals generated during the T90 test spread over five levels (5 to 9). From the cumulative plot, levels 7 and 8 account for 80% of all signals. In the level versus displacement plot, events in level 8 are generated throughout the test, while events in level 7 appear towards the end of the test. Because of this, it is thought that level 7 could correspond to debonding and level 8 to matrix microcracking. This is supported by the fact that level 8 accounts also for 56% of the signals in the T0 test, 68% in the T45 and 62% of the signals in the T090 test (in this latter case, the events in this level are being generated from the onset of non-linearity). However, some caution should be taken on the characterisation of level 8 as it accounts for few events in the UDCT, CPCT and CPCC tests, where matrix microcracking plays an important role.

Looking at the CPCT test, 97% of the signals are decomposed in level 7. The quality of the decomposition in this case is questionable as the failure processes are complex and of different natures and should results in a larger spectrum of level.

In the DCB and 4ENF, levels 5 and 6 account for most of the signals (97% and 72% respectively). These levels could be related to delamination, even though this seems unlikely as few signals belong to them in the other tests.

A.2 Conclusion

Signal classification using discrete wavelet transform was also attempted as such decomposition is more appropriate to non-stationary, non-periodic signals than the Fourier transform. Each signals was decomposed into nine levels and labeled according to their most energetic level. Signals mostly fall into one or two levels for each test. Unfortunately those levels do not correspond from one test to another. No conclusive classification was therefore achieved using this method.

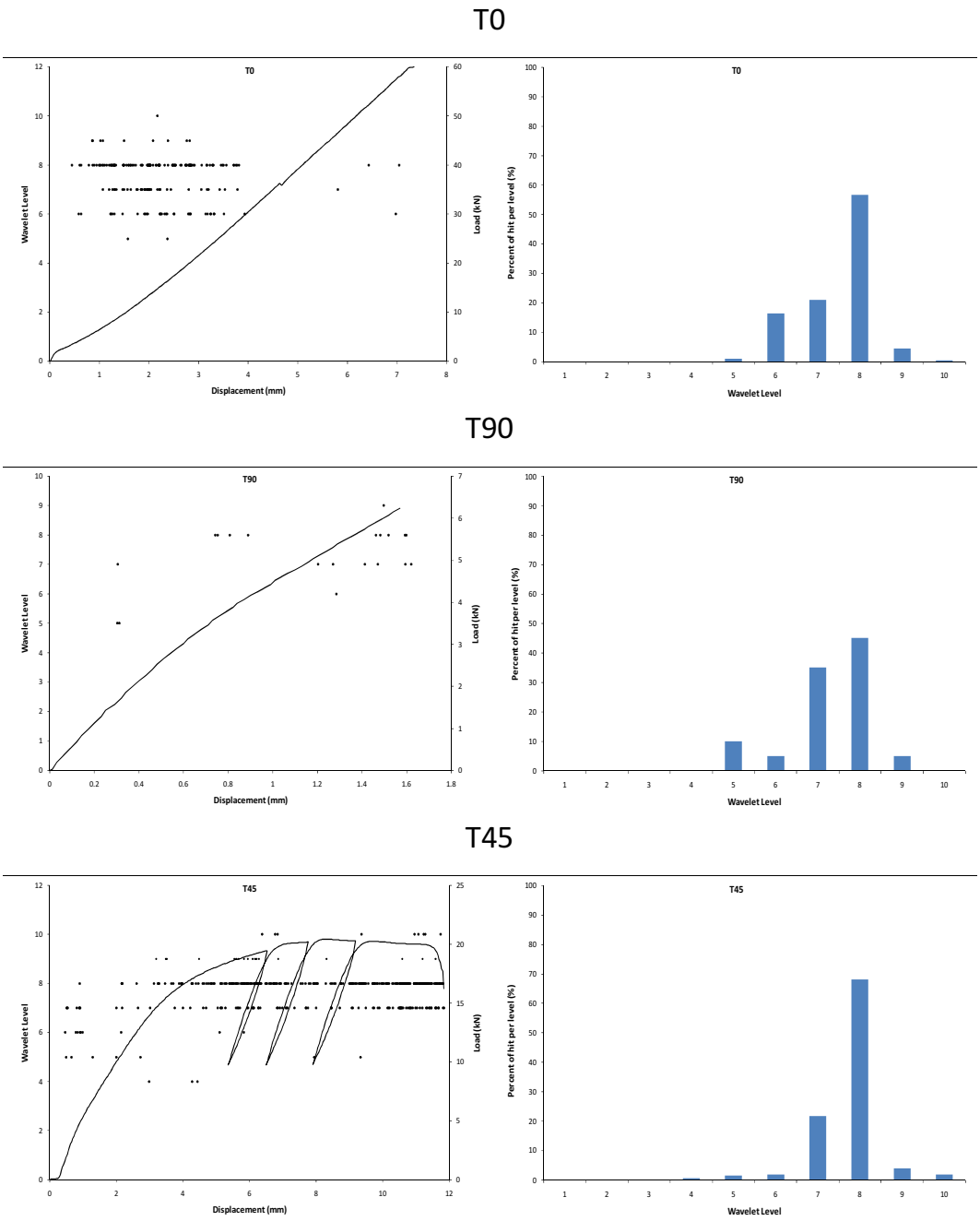


Figure A.2: (Left) Wavelet levels and load versus displacement curves, (Right) Cumulative distribution of events per level for the T0, T90, T45 tests.

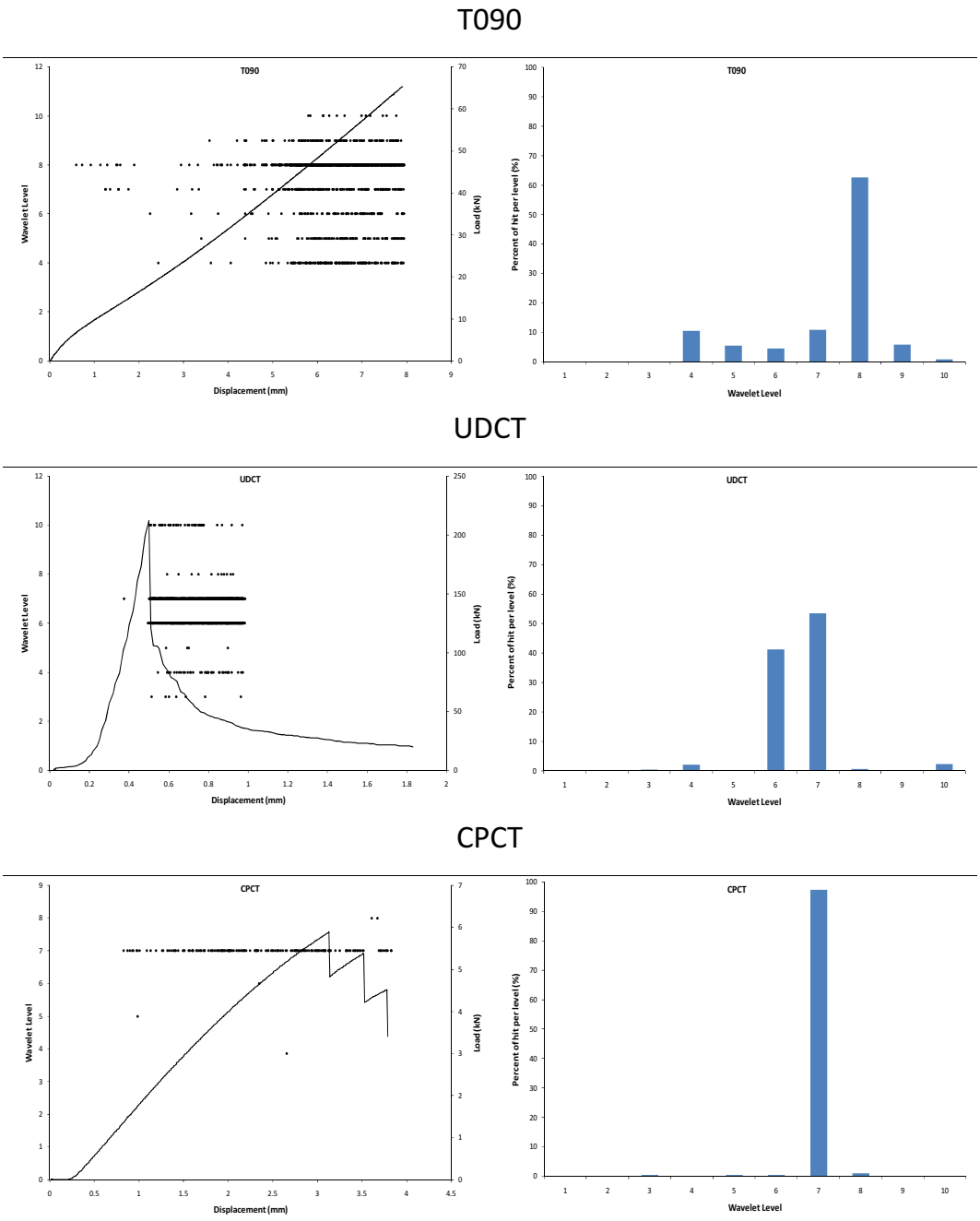


Figure A.2 (cont.): (Left) Wavelet levels and load versus displacement curves, (Right) Cumulative distribution of events per level for the T090, UDCT, CPCT tests.

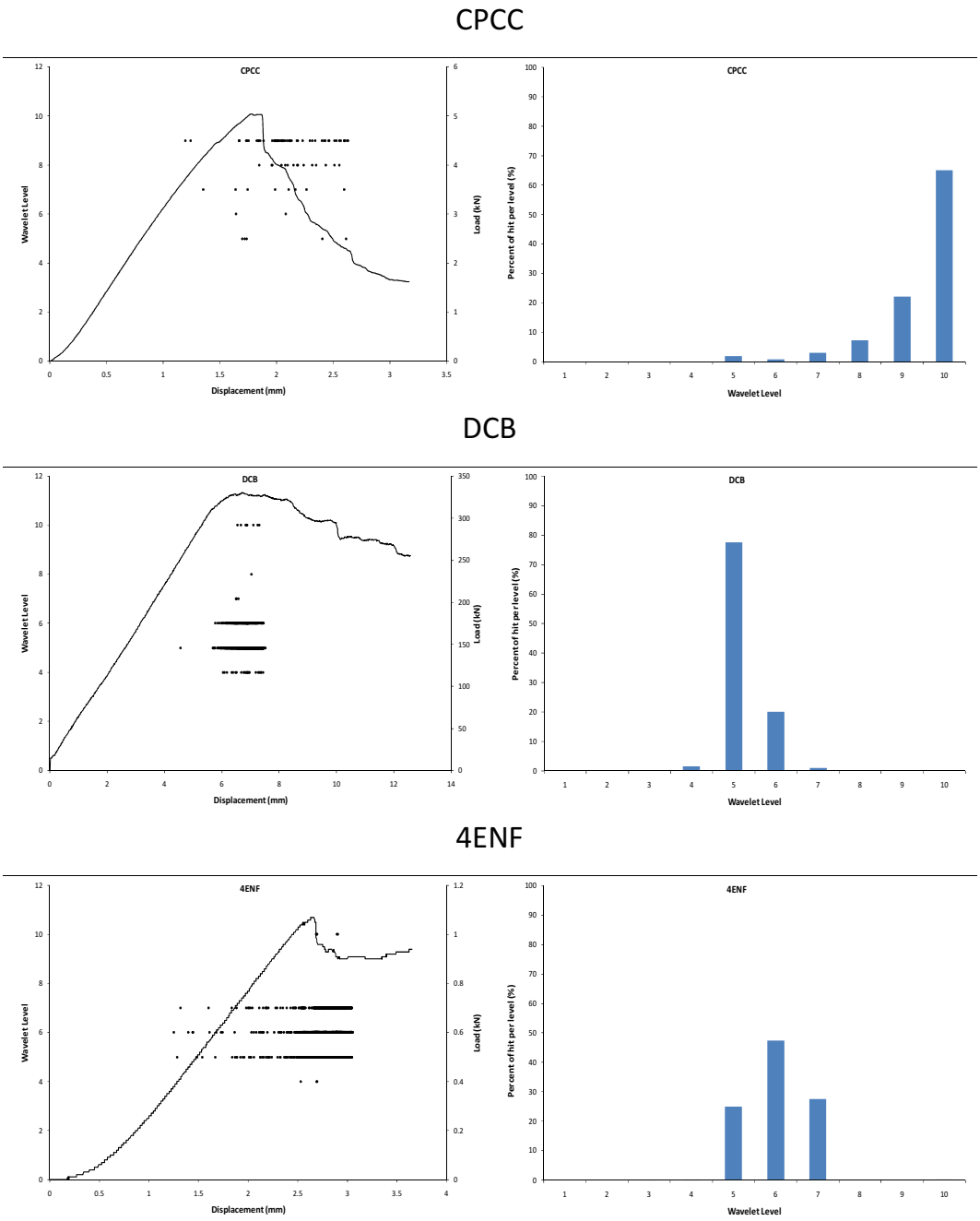


Figure A.2 (cont.): (Left) Wavelet levels and load versus displacement curves, (Right) Cumulative distribution of events per level for the CPCC, DCB, 4ENF tests.

Appendix B

A failure criterion for shear-driven fibre compressive failure

B.1 Introduction

From the experimental and numerical evidences presented in Chapters 4 and 5, failure in longitudinal compression initiates as shear-driven fibre compressive failure. Currently, the failure criteria implemented in an FE framework are either limit criteria (maximum stress in [83]) or based on fibre kinking [30]. Using this type of criterion when shear-driven fibre compressive takes place can result, in the one hand, in predictions of failure initiation at incorrect stress levels and, in the other hand, in the prediction of incorrect fracture plane.

The experimental observations in Chapter 4 show that failure takes consistently place in a fracture plane oriented at 45° to the compressive loading and indicate the compressive shear nature of the failure. This type of failure is often found in metals and well described by the Tresca criterion, which predicts failure initiation when the maximum shear stress in the principal axes reaches the shear strength. In this appendix, a Tresca criterion, is implemented in an FE code and used to predict failure envelopes.

B.2 Failure criterion

The criterion is based on the hypothesis that failure takes place when the maximum shear traction acting on the fracture plane, shown in Fig. B.1, reaches the compressive shear strength of the composite. The tractions on the fracture plane are decomposed as shown in Fig. B.2 and so that the criterion reads

$$f_{fcs} = \frac{\tau_n}{S_c} = 1. \tag{B.1}$$

S_c is the compressive shear strength of the composite which reads

$$S_c = v_f S^f + (1 - v_f) S^m, \tag{B.2}$$

with S^f and S^m the compressive shear strength of the fibres and matrix respectively. Eq B.2 can also be written

$$S_c = \frac{1}{2} \left[v_f X_c^f + (1 - v_f) X_c^m \right] \tag{B.3}$$

with X_c^f and X_c^m the compressive strength of the fibres and matrix, respectively.

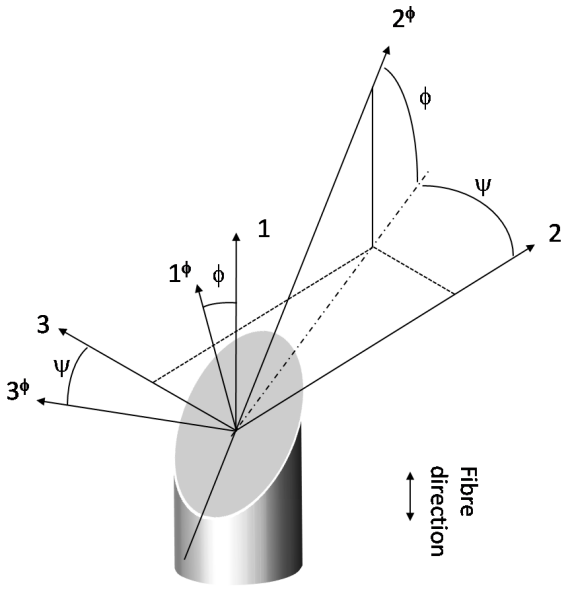


Figure B.1: Orientaton of the fracture plane in a 3D space.

The shear traction is evaluated by rotating the applied stresses to the coordinate system associated with the fracture plane

$$\tau_n = -\frac{\sigma_{2^\psi} - \sigma_{1^\psi}}{2}\sin(2\phi) - \tau_{12^\psi}\cos(2\phi), \tag{B.4}$$

where

$$\begin{cases} \sigma_{1^\psi} & = \sigma_1 \\ \sigma_{2^\psi} & = \frac{\sigma_2+\sigma_3}{2} + \frac{\sigma_2-\sigma_3}{2}\cos(2\psi) + \tau_{23}\sin(2\psi) \\ \tau_{12^\psi} & = \tau_{12}\cos(\psi) + \tau_{13}\sin(\psi) \end{cases}. \tag{B.5}$$

From the experimental observations detailed in Chapter 3, it is observed that the fracture plane is consistently orientated at 45 ° to the 1-2 plane, therefore, it is assumed that $\phi = 45\,^\circ$ under any load combination. The choice between $+45\,^\circ$ and $-45\,^\circ$ is made so that the failure index f_{fcs} is maximised. The axes 2^ψ and 3^ψ are principal directions, therefore ψ is given by

$$\tan(2\psi) = \frac{2\tau_{23}}{\sigma_2 - \sigma_3}. \tag{B.6}$$

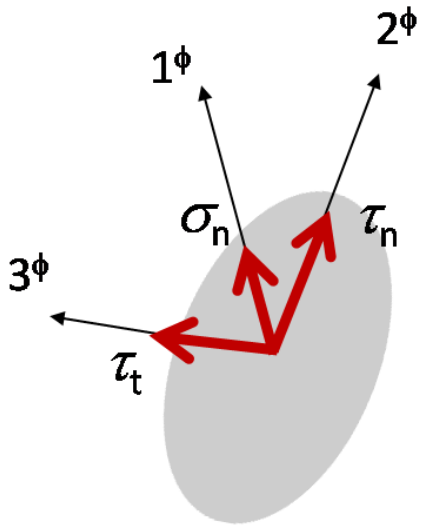


Figure B.2: Traction components on the fracture plane.

B.3 Applications

B.3.1 Failure envelope

Using a single element, the failure envelope for longitudinal compression and in-plane shear can be predicted and compared to the ones found using the micromechanical FE model presented in Chapter 5 and to experimental data [37]. The failure criterion used to predict fibre kinking is the LaRC05 fibre kinking criterion [30]. The single element is shown in Fig. B.3; the nodes at the bottom are restricted in the 1 direction (with the exception of one node which is fully fixed) and a multi-points constraint is applied to the nodes on the top face so that the face remains parallel to the 2-3 plane. A shear force in the 2-direction is applied to all the nodes (with the exception of the fully fixed node) and a compressive displacement in the 1-direction is applied to the nodes on the top face.

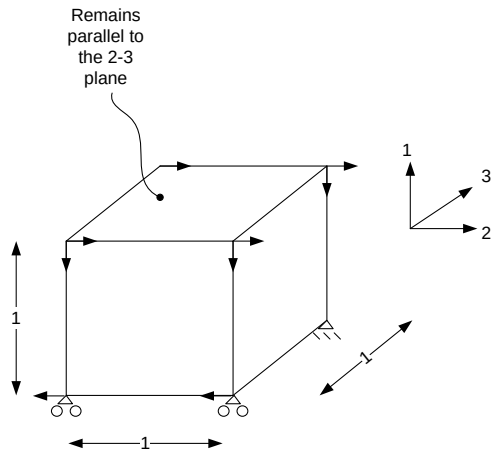


Figure B.3: Single Element for failure envelope generation (dimensions in mm).

The relevant mechanical properties used are given in Table B.1.

Table B.1: Mechanical properties used in the FE model.

E_1 (GPa)	G_{12} (GPa)	θ_0 (°)	S_L (MPa)	X_c^f (GPa)	X_c^m (MPa)	v_f (%)
176	5500	2.3	90	1300	105	0.6

A typical failure envelope predicted by the model is shown in Fig. B.4. The failure envelope is similar to the ones presented in Chapter 5. When the compressive strength of the fibres X_c^f is increased, the region corresponding to shear-driven fibre compressive failure decreases and eventually disappears. The agreement with experimental data is also good.

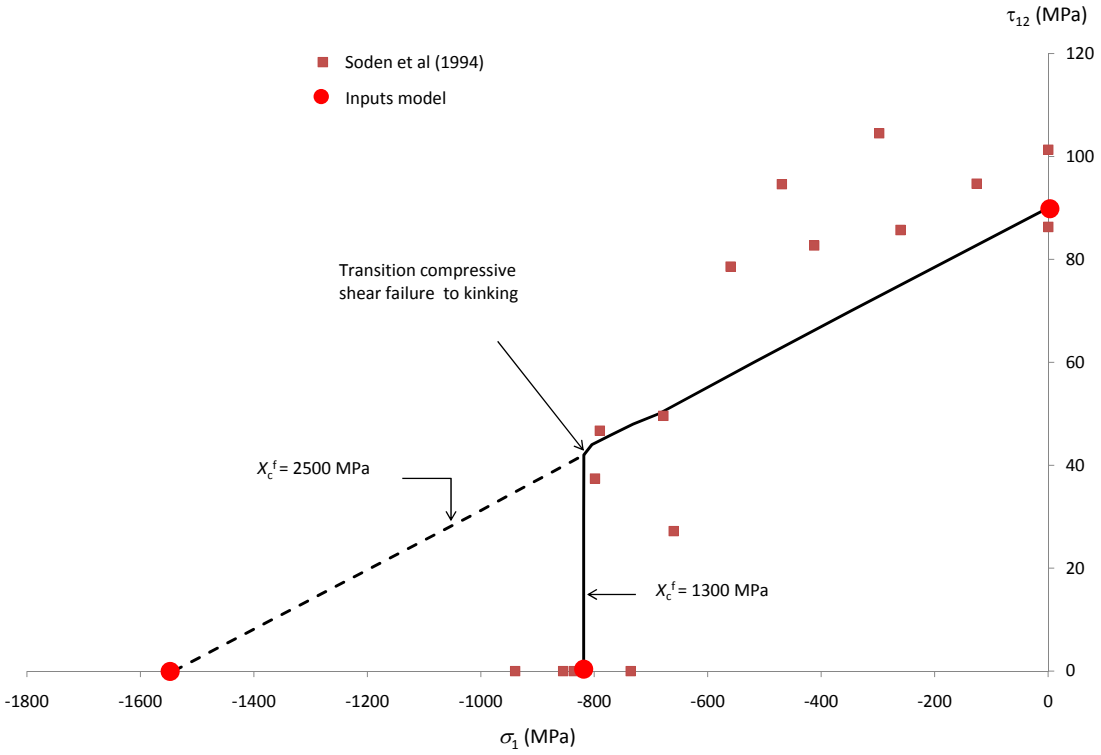


Figure B.4: Failure envelope for combined longitudinal compression and in-plane shear.

B.4 Discussion

The failure envelopes predicted by the current model are in good agreement with the ones presented in Chapter 5 and show the same parametric characteristics. The agreement with the experimental data is also good, the differences coming from the average input values given to the model. Currently, the angle of the fracture plane ϕ is fixed to 45 ° for any load combination to simplify the numerical implementation, but further work would be to calculate ϕ as the angle of the principle axes for a given load combination.

B.5 Conclusions

A failure criterion, based on a Tresca criterion, for shear-driven fibre compressive failure has been implemented in an explicit FE code. The model is able to predict failure envelopes for combined longitudinal compression and in-plane similar to the ones detailed in Chapter 5.

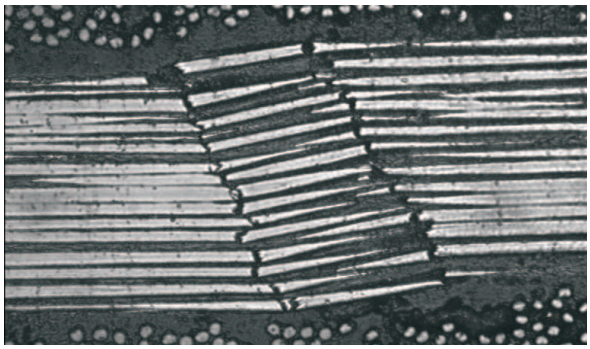
Appendix C

A micromechanical model for kink–band formation: Part I — experimental study and numerical modelling

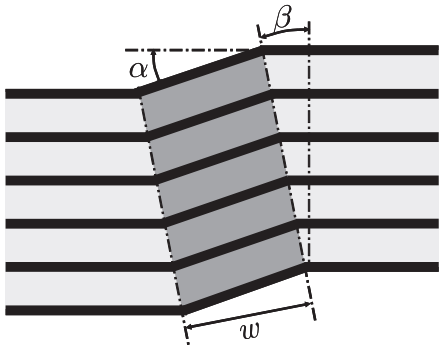
C.1 Abstract

The work in this Appendix was undertaken in collaboration with Ms. Soraia Pimenta, during her Msc project, and is published somewhere else [110].

The initiation and propagation of kink–bands are investigated through an experimental study and numerical modelling. Based on the results achieved, the sequence of events and key features for kink–band formation are identified; particularly, matrix yielding is found to play a crucial role in the process, and fibres are found to fail in the compressive side first. The findings from both the experimental and numerical programmes show a remarkable agreement, and are further applied to the development of an analytical model (*Part II* of this paper) for kink–band formation.



(a) Micrograph from experiments in CFRP [91].



(b) Schematics and definition of the kink–band geometric parameters: fibre angle α, band angle β, and band width w.

Figure C.1: Kink–band.

C.2 Introduction

Kink–band formation (figure D.1.a) is the most common failure mode of fibre reinforced polymer (FRP) composites under longitudinal compression [24]. This paper presents experimental and numerical investigations that were conducted to improve the knowledge on the sequence of events and the key features leading to fibre kinking. The outcome of these studies is used in *Part II* of this paper [105] to develop an analytical model for kink–band formation.

Although there is a large diversity of analytical models aiming to explain and reproduce kink–band formation, no single model has achieved an universal acceptance among researchers and designers [24]. There is therefore the need for a better understanding of the physics and mechanics of fibre kinking, which can be achieved by experimental studies and numerical modelling at the micromechanical scale.

Much information obtained from experimental results on kink–band formation is already available [28, 29, 31, 120]. However, kinking is often studied in post-mortem specimens or with low resolution systems, so there is barely no data on the material behaviour at the micromechanical level. The observation of stable and in-plane kink–bands, in loaded specimens and using in-situ microscopy, is therefore required.

Soutis and Fleck [120] tested carbon–epoxy UD composites under uniaxial compression, using both unnotched and open–hole specimens. The main failure mode observed was fibre microbuckling in the 0 plies.

Kyriakydes [31] studied kink–bands through several experimental procedures.

Regarding fibre imperfections in a UD composite, the researcher found regularly–spaced bands of fibres with high waviness; the bands were around 1 mm wide, spaced by 1 – 1.5 mm. Inside each band, the fibres (diameter $\phi_f = 7\,\mu$m) were randomly misaligned, with half–wavelength and half–amplitude ranging respectively $L \in [1050; 2800]$ μm and $\overline{y_0} \in [21; 70]$ μm; no correlation between wavelength and amplitude was found. Kyriakydes suggested these bands to be caused by tow superposition during ply manufacture.

Moran [28] has observed almost in-plane kink–bands by compressing thick (6 mm) UD notched specimens. The author then proposed the following sequence of events for the phenomenon: (i) initially linear–elastic behaviour; (ii) matrix yielding around the notch; (iii) peak load and sudden kink–band propagation across the entire specimen width; (iv) slow increase of fibre rotation α within the band; (v) unstable increase of fibre rotation α and band angle β until lock-up by matrix response in shear; (vi) band broadening.

Vogler and Kyriakydes [29] achieved a stable and almost in-plane propagation of kink–bands in UD CFRP, using compression combined with shear. Unloaded micrographs showed almost no fibre failure, due to a relatively small fibre angle α. Their results suggest that shear stresses play a significant role in fibre kinking, even leading to the formation of kink–bands without fibre failure. In addition, and despite the effort to produce totally in-plane kink–bands, an out-of-plane component was observed in loaded specimens.

Several micromechanical FE models were also developed to simulate the composite behaviour during kink–band formation, considering matrix yielding and initial imperfections [31, 121, 122]. However, there are no studies reported on kinking in initially perfect fibres and using a failing formulation for the matrix.

Kyriakides et al [31] performed an extended study on the influence of several parameters on the composite response and kink–band geometry. The FE models used a 2D layered — fibres interposed with matrix — approximation. The matrix was formulated as elasto–plastic; the fibres were considered isotropic, and their material non-linearity had only a reduced influence on the results. All the models assumed a sinusoidal initial imperfection. In the overall, the simulations showed

(i) an initial linear–elastic domain, (ii) a peak load, (iii) a sudden softening with unstable kink–band formation, and (iv) a stable band broadening. It was also found that the addition of more fibres to the model would increase the peak remote stress.

Morais [121] used a unit-cell numerical approach. In his 3D models this author found that, if a hexagonal arrangement for the fibres is considered, kinking is isotropic. For this reason, this type of fibre arrangement will be assumed in the models presented in this paper.

Vogler et al. [122] modelled kink–band propagation in FE analyses, using both global and local imperfections and a plastic formulation for the matrix. The numerical simulations reproduced the behaviour previously observed in the experiments [29]; it was shown that a much more stable numerical response was achieved if direct shear loading was introduced.

The experimental and numerical programmes presented in this paper aim to study the formation of kink–bands at the micro–scale. The final goal is to provide useful information on the physics and micromechanics of the process, so a phenomenological analytical model can be developed in *Part II* of this paper [105]. This paper is organised as follows: sections C.3 and C.4 present respectively the experimental and numerical procedures carried out; based on the results obtained, the sequence of events leading to kink–band formation is proposed in section C.5, and key features for kinking are identified in section C.6; section D.6 summarizes the main conclusions.

C.3 Experimental study

The material used in the experiments is a T800/924 carbon–epoxy unidirectional (UD) pre-preg. Small and thick UD specimens [28] (figure C.2) were machined from plates manufactured using pre-preg technology by the standard procedures. A long notch was made with a band saw and sharpened with a modelling blade to assist kink–band initiation. The off-axis scheme shown in figure C.2, with angles φ_f or φ_L under 5°, was used to induce shear and in-plane kink–band propagation [29, 122].

Kink–band initiation was achieved by compressing each specimen in a vice, after

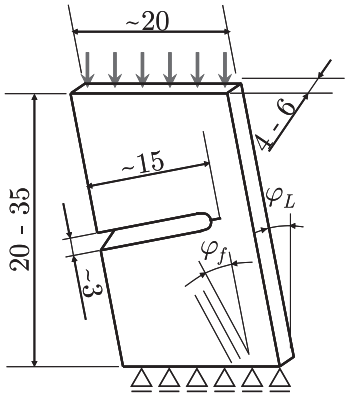
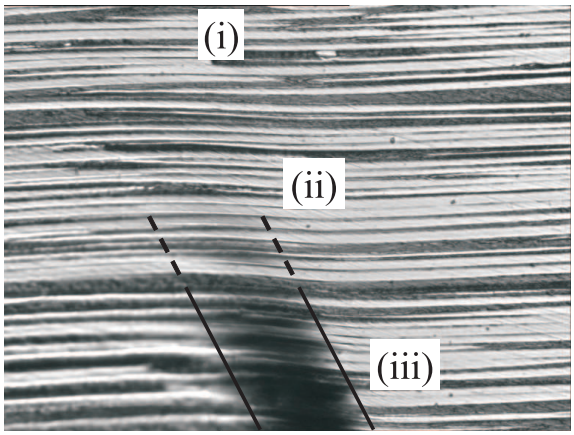


Figure C.2: Specimen used in the experimental study and imposed displacements. All dimensions in mm.



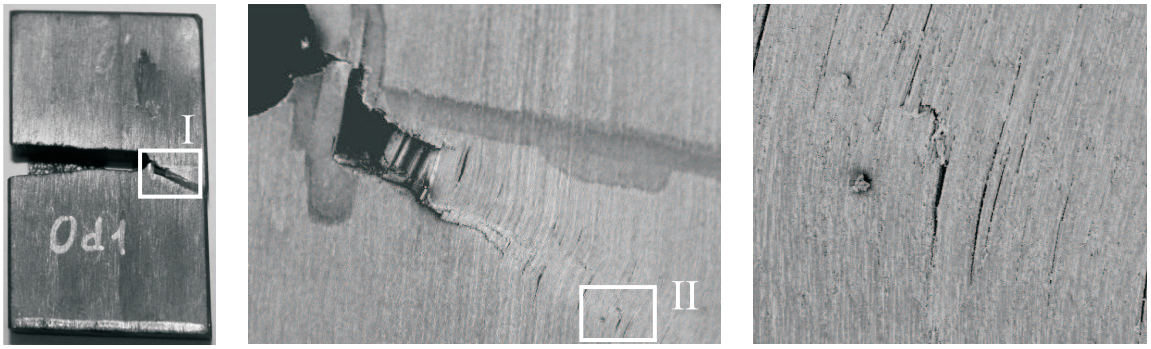
(i) *elastic domain*; (ii) *softening domain*; (iii) *fibre failure domain.*

Figure C.3: Stages of fibre kinking (loaded).

which the specimen was reloaded in a small portable clamp; propagation was observed while loaded and unloaded under optical and scanning electron microscopes. Sample micrographs — taken at a considerable distance from the notch, so stress concentration can be neglected — are shown in figures C.3, C.4 and C.5.

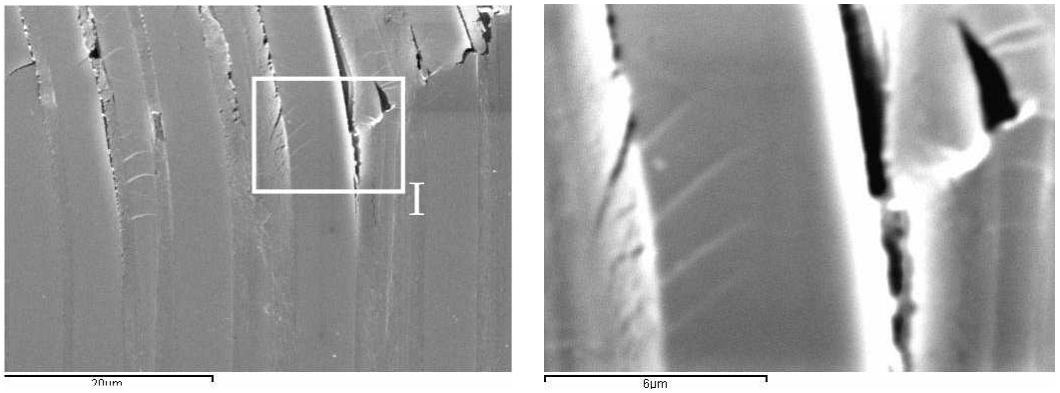
C.4 Numerical modelling

Kink–band formation was simulated using several 2D equivalent [31, 121, 122] micromechanical FE models of the composite. The overall approach consisted of compressing a large number of fibres with free longitudinal boundaries, as performed by Kyriakydes and Vogler [31, 122]; this allows the kink–band angle β to be different from 0, keeping at the same time a considerable number of inner fibres sufficiently



(a) Overview. (b) Zoom-in of zone I. (c) Zoom-in of zone II.

Figure C.4: Kink–band with matrix yielding and no fibre failure (unloaded).



(a) Overview of kink–band edge. (b) Zoom-in of zone I.

Figure C.5: Detail of kink–band edge and fibre failure in compression (loaded) [123].

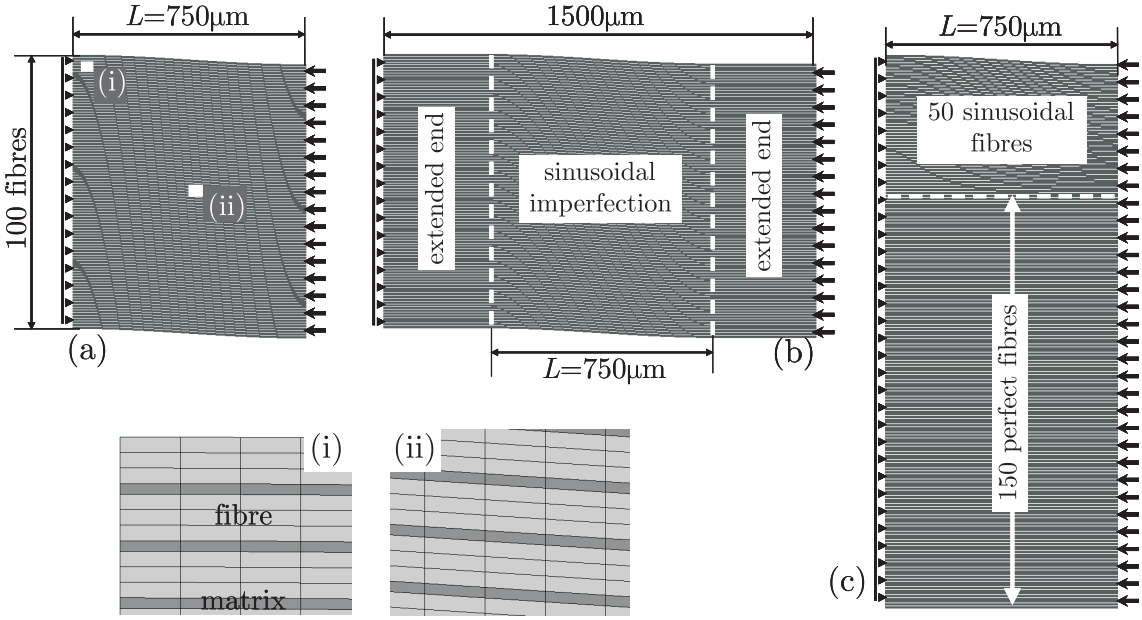
distant from free–edge effects. The thicknesses of the fibre and matrix layers were derived using the approach suggested by Morais, considering a symmetry plane in an hexagonal fibre arrangement [121]. The main parameters that were analysed with the numerical simulations include:

- matrix failure: models with matrix yielding (plasticity model) and with matrix failure (cohesive model) were investigated;
- the length of the fibres in the model;
- the initial shape of the fibres (sinusoidal and straight);
- fibre failure: models with purely elastic fibres and with fibres which are allowed to fail (using a continuum damage mechanics (CDM) model) were investigated.

The main conclusions from the study can be drawn by analysing the results corresponding to three different models (see also figure C.6):

- *Cohesive* model, with elastic fibres, cohesive matrix (failing bi-linear constitutive law, modelled with cohesive elements) and global imperfection (figure C.6.a);
- CDM_f model, with failing (bi-linear constitutive law) fibres, elasto–plastic matrix and global imperfection (figure C.6.b). This model has extended ends, so the kink–band can be studied at later stages — when considerable fibre failure is verified — without being affect by edge effects;
- *Propagation* model, with elastic fibres, cohesive matrix and both initially misaligned and straight fibres (figure C.6.c).

The analysis were run in the finite element code ABAQUS [83], by the static solver and using geometric non-linearity. Numerical stabilization was added to the models here presented, by specifying a constant damping factor (5000 for the *cohesive* and *propagation* models, 500 for the CDM_f model). The artificial energy dissipated by damping was monitored throughout the analyses, and always found to



(a) model containing fibres with initial geometrical imperfection; magnified details of the mesh are shown in (a.i) and (a.ii);
(b) model with fibres with extended straight segments;
(c) model containing both sinusoidal (with the amplitude decreasing linearly with the fibre index) and straight (perfect) fibres.

Figure C.6: Geometries, meshes and boundary conditions of the numerical models.

be less than 10% of the total energy; in addition, models run with no stabilization showed a very similar response (apart from increased convergence problems).

Plane–strain elements with reduced integration were used for the fibres (all models) and for the matrix with elasto–plastic formulation (CDM_f model). Cohesive (failing) matrix (*cohesive* and *propagation* models) was modelled using ABAQUS' cohesive elements [83], and fibre failure (CDM_f model) using the Continuous Damage Mechanics (CDM) model for FRP (with transverse modes deactivated); bi-linear laws were used in both cases, but to avoid convergence problems matrix failure and fibre failure were studied in independent models. An experimental [124] shear curve was used for the elasto–plastic matrix (CDM_f model) up to a shear strain of 5.1% (limit of experimental data), with a perfect-plastic response for larger deformations (figure C.7).

Kink–band formation was triggered by a sinusoidal imperfection. The amplitude of this imperfection was constant for all the fibres in the *cohesive* and CDM_f models (figure C.6.a–b); in the *propagation* model, the nominal (for the first fibre) ampli-

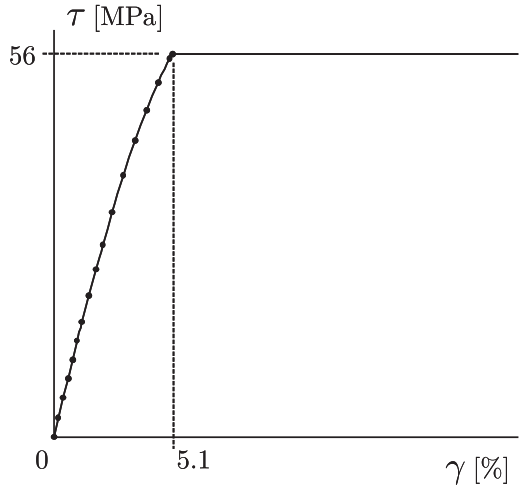


Figure C.7: Non-linear elastic–plastic constitutive law for the matrix (CDM_f model).

Table C.1: Constituents elastic properties used in the numerical models (typical values for IM7/8551-7 from [124]).

Fibre Young's Modulus E_f [MPa]	Fibre Poisson's ratio ν_f [ ]	Matrix Shear Modulus G_m [MPa]	Matrix Poisson's ratio ν_m [ ]
276	0.20	1.478	0.38

tude was linearly reduced to zero along the following 50 fibres (figure C.6.c). For the three models presented, the nominal imperfection (table C.4) was 30% proportionally smaller than the range measured by Kyriakydes [31]; no significant qualitative difference was found in models with different amplitude parameters.

The models were loaded in longitudinal compression with displacement control. The geometry, mesh and boundary conditions are shown in figure C.6. Tables C.1 to C.4 present the input parameters used in the model [91, 124]. Results are shown in figures C.8, C.9, C.10 and C.11.

Table C.2: Constituents strength properties used in the numerical models (typical values for IM7/8551-7 from [124]).

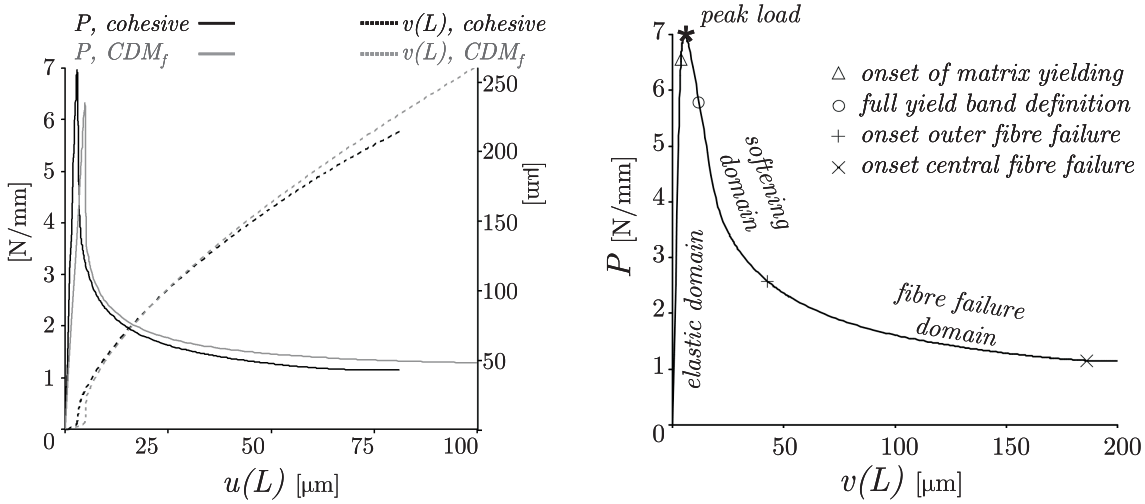
Fibre Compression X_C^f [MPa]	Fibre Tension X_T^f [MPa]	Matrix Mode I Y_m [MPa]	Matrix Shear S_m [MPa]
3200	5180	73	56

Table C.3: Constituents fracture toughness used in the numerical models (values based on [91]).

Fibre Compression $\mathcal{G}_C^f$ [kJ/m^2]	Fibre Tension $\mathcal{G}_T^f$ [kJ/m^2]	Matrix Mode I $\mathcal{G}_{IC}^m$ [kJ/m^2]	Matrix Mode II $\mathcal{G}_{IIC}^m$ [kJ/m^2]
100	100	0.21	0.80

Table C.4: Geometrical and numerical composite parameters used in the numerical models.

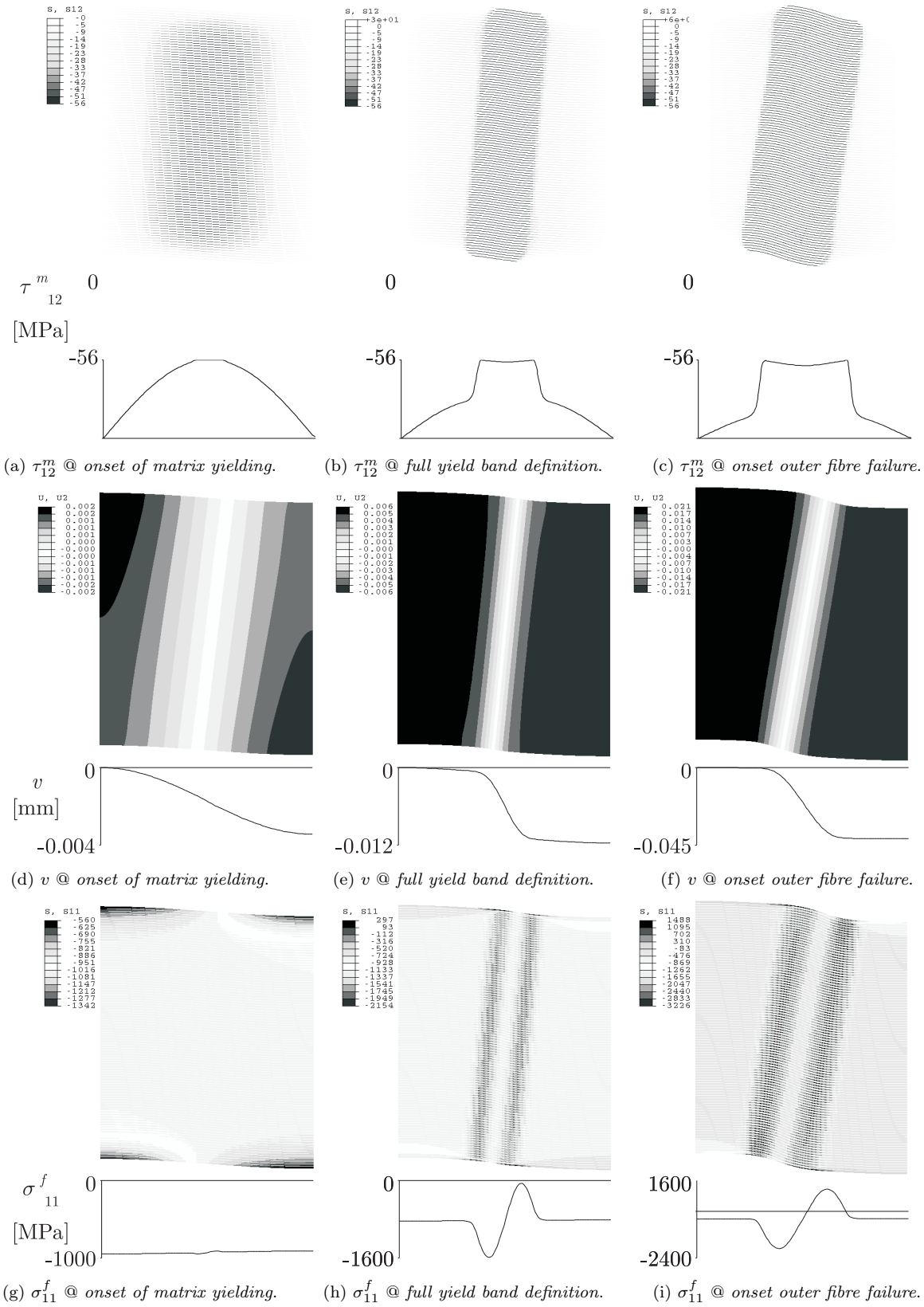
Imperfection 1/2 wavelength L [μm]	Imperfection 1/2 amplitude $\overline{y_0}$ [μm]	Fibre volume fraction V_f [%]	Fibre diameter ϕ_f [μm]	Mixed–mode BK exponent η [ ]
750	15	60	7	1.5



(a) Load P and transverse displacement v vs. compressive displacement u.

(b) Load P vs. transverse deflection $v(L)$ (*cohesive* model).

Figure C.8: Load vs. displacement curves from numerical models.

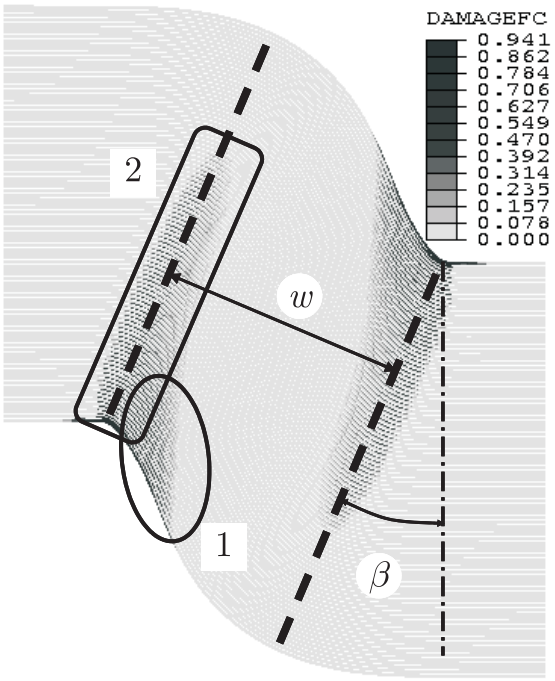


(a) τ^m_{12} @ *onset of matrix yielding.* (b) τ^m_{12} @ *full yield band definition.* (c) τ^m_{12} @ *onset outer fibre failure.*

(d) v @ *onset of matrix yielding.* (e) v @ *full yield band definition.* (f) v @ *onset outer fibre failure.*

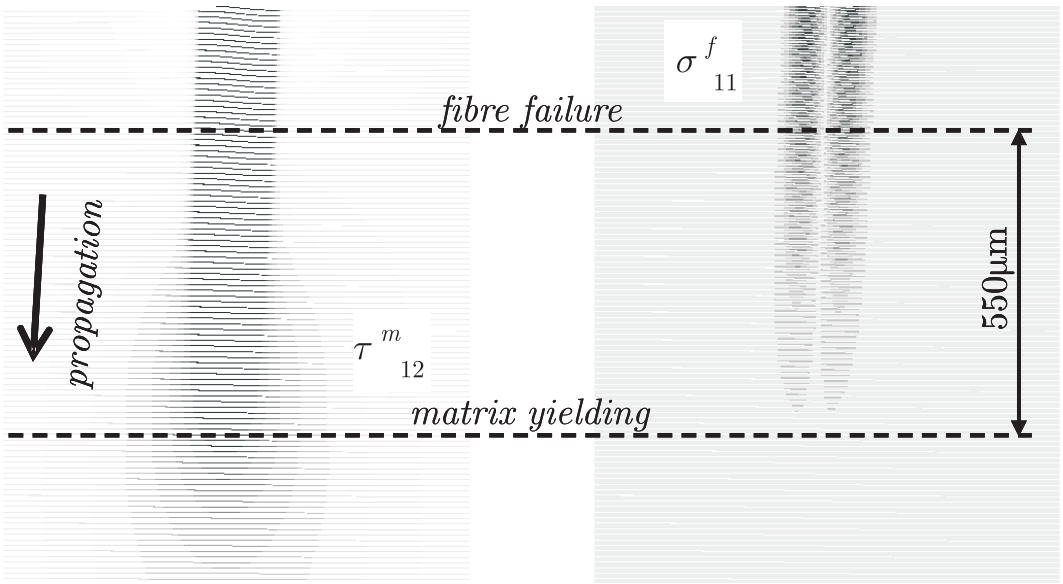
(g) σ^f_{11} @ *onset of matrix yielding.* (h) σ^f_{11} @ *full yield band definition.* (i) σ^f_{11} @ *onset outer fibre failure.*

Figure C.9: Fields from numerical analysis (curves for the central fibre and adjoining interface), at the points highlighted in figure C.8.b.



1: Damage propagation along the edge; 2: Damage propagation across the width.

Figure C.10: Fibre failure in compression (index `DAMAGEFC`) and damage propagation during kink–band formation.



(a) Shear stresses in the matrix.

(b) Axial stresses in the fibres.

Figure C.11: Kink–band *propagation* in initially straight fibres.

C.5 Sequence of events

Figure C.3 suggests the existence of three domains in kink–band formation. In the *elastic domain* — region (i), way from the kink–band tip — the fibres show a waviness with small amplitude and high wavelength. In the *softening domain* — region (ii), just ahead the kink–band tip — the waviness is more pronounced and more localised (higher amplitude and lower wavelength). In the *fibre failure domain* — region (iii) — a shaded kink–band is observable; the fibres at the band edges are broken, which (together with the free–surface effect) allows the kink–band to acquire a considerable out-of-plane component, which is responsible for the shading in that region.

In figure C.8.b, these three domains can also be distinguished: in the *softening domain* the matrix is progressively degraded; in the *fibre failure domain*, the strength of the fibres is reached, starting from the outer fibres and progressing towards the central ones (although, in the *cohesive* model, no fibre–stiffness degradation results from overcompression). Regarding the sequence in which all these events take place, a macroscopic kink–band where matrix yielding can be observed prior to fibre failure is shown in figure C.4.c.

Combining all these results with the fields obtained from the numerical analysis (figure C.9), the following sequence of events for kink–band formation is proposed:

1. *Elastic domain*: fibres and matrix deform elastically; the imperfection induces slight bending of the fibres and shears the matrix, amplifying moderately the misalignment in a positive feedback process (figure C.9.a, d, g).

2. Beginning of the *softening domain* and *peak load*: as compression continues, the matrix yields in shear within an inclined band developed across all the layers along the full model width (*full yield band definition*, figure C.9.b). The limited support given there to the fibres promotes deflection in a kinked (not sinusoidal) shape (figure C.9.e), with highly curved and stressed regions near the *yield band* boundaries (in the *maximum bending* bands, figure C.9.h). The overall stiffness drops suddenly, so the load P decreases and the transverse displacement

v increases abruptly (figure C.8.a). In the FE results, due to use of numerical stabilization and to the edge effect (finite number of fibres), the peak load is artificially increased and the transition between the *elastic* and *softening domains* is smoothed (figure C.8.b).

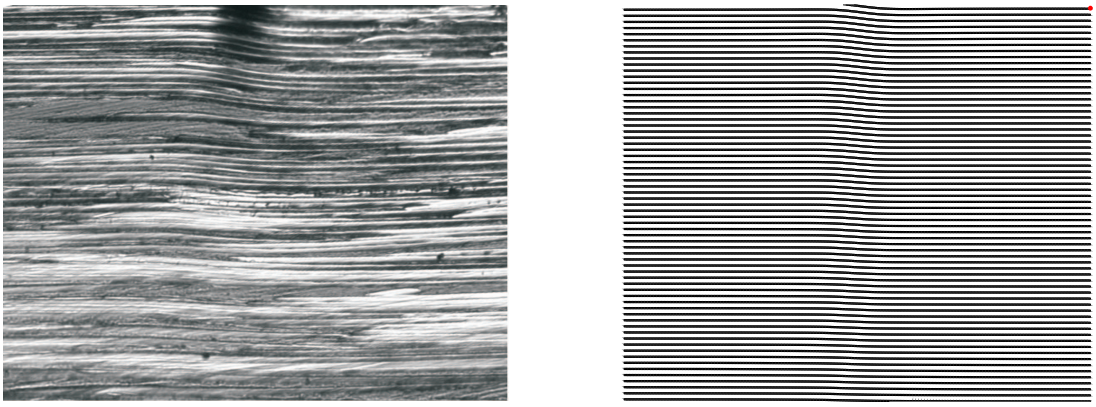
3. *Softening domain* (post–peak): after the peak load is reached, fibre rotation increases locally within a widening *yield band*; at its boundaries, axial bending stresses increase within the *maximum bending* bands (figure C.9.c, f, i).

4. *Fibre failure domain*: as fibre curvature increases in the *maximum bending* bands, their strength is reached and failure starts at the outer fibres (figures C.9.i and C.10–feature 1); as the damage propagates inwards (away from edge–effects), the location and orientation (β) of the *yield* and *maximum bending* bands stabilizes (and so does w, figure C.10–feature 2), and only fibre rotation (α) increases until final fibre failure occurs and the kink–band geometry is fully defined.

The failure sequence described above is based on the experimental results and on numerical models with global imperfection; in addition, it is also observed in numerical kink–band propagation across initially straight fibres. Figure C.11.a shows the matrix shear stresses in a portion of the *propagation* model with perfect fibres; an inclined *yield* band propagating downwards is clearly defined in the centre of the model. Figure C.11.b shows the axial stresses in the fibres in the same location; the fibres are bent very locally within the *yield* band, forming two *maximum bending* bands; the axial stresses in these bands progressively increase, so the compressive fibre strength is reached (no stiffness–reduction due to fibre–overcompression was considered in this model).

It can also be confirmed in figure C.11 that, during kink–band propagation, the *yield* band runs ahead of the *maximum bending* bands; in the *propagation* model, matrix yielding occurred over a length approximately 550 μm longer than that of failing fibres. This supports that matrix yielding (i) is the responsible for the kinked shape of the fibres, and (ii) takes place prior to onset of fibre failure.

Finally, figure C.12.a shows a micrograph from the experimental study of a loaded kink–band propagating, while figure C.12.b represents a set of the initially–perfect



(a) Experimental (loaded) result.

(b) Numerical (*propagation*) result.

Figure C.12: Kink–band propagation: experimental and numerical results (same scale).

fibres in the numerical *propagation* model. Both figures are at the same scale, and the agreement between experimental and numerical results is remarkable.

C.6 Key features

The numerical and experimental results suggest the following features:

- Two different domains — *elastic domain* and *softening domain* — must be considered in kink–band formation (figure C.3, features i–ii); matrix yielding is the feature distinguishing them (figures C.8 and C.9);
- Fibres deform in bending and compression, and are laterally supported by the matrix in shear (figures C.3, C.4 and C.9);
- For small strains, the fibres deform approximately in-phase (figure C.9.a, d, g); however, inside the *yield band* the out-of-phase angle is not negligible (figure C.9 c, f, i);
- The similarity between the results from the *cohesive* and CDM_f models (figure C.8.a) shows that matrix non-linearity for small strains is not essential, and neither is the choice of modelling the matrix non-linear behaviour for larger strains as plasticity or cohesive failure. This agrees with published

work according to which kink–band formation is matrix–strength (and not matrix–toughness) dominated [123];

- Each fibre is deflected over a small length (figures C.3 and C.12.a);
- Fibres are damaged first in compression; this is supported both by experimental micrographs (figure C.5) and by numerical results (figure C.10). This finding contrasts with a conclusion attributed to Soutis and Fleck [120] by several other publications [21, 75], but not explicited in the original work in reference [120]. This finding (initiation of fibre failure in the compressive side) is however in agreement with other published work [99];
- Matrix yielding in shear is a key feature for kink–band formation (figure C.4); fibre failure is simply a consequence of the displacement field after a kink–band (due to matrix failure) is observable (figure C.9.d–i).

C.7 Conclusions

Kink–band formation was studied at the micromechanical level in experimental and numerical programmes, and the phenomenological basis for the development of an analytical micromechanical model was established.

The experimental observations were performed with UD CFRP, using notched specimens and off-axis compression. Stable and almost in-plane kink-bands were observed, both while loaded and unloaded, using optical and scanning-electron microscopy. It was shown that kink-band formation does not rely on fibre failure, but on matrix yielding; when fibres do fail, damage starts in compression first.

Kinking was simulated with several numerical FE models. The influence of the matrix behaviour — plastic vs. failing — was studied, and a linear–elastic — perfectly–plastic constitutive law proved to be sufficient for an accurate modelling. Fibre failure was simulated, and it was suggested that the kink–band width and orientation are locked after the onset of fibre failure. Propagation of kinking was observed in fibres with no initial imperfection, and it was found that considering a small initial sinusoidal imperfection does not affect the mechanics of the process. In

addition, and although no quantitative comparison was performed, the numerical results proved to have a remarkable qualitative agreement with the experimental ones.

A sequence of events leading to fibre kinking was proposed. According to this, the composite begins deforming globally in an *elastic domain*, until matrix yielding initiates and the *peak load* is reached; then, within the *softening domain*, the deformation localizes within a narrow band, and the composite softens due to further matrix yielding; finally, in the *fibre failure domain*, fibres are gradually damaged — starting in the compressive side — until ultimate failure occurs.

Some key features for kink–band formation were also identified; above all, the important role of matrix yielding was confirmed at the micromechanical level. As the matrix yields, the composite softens locally, the deflection increases within a narrow band and, consequently, the fibres may fail near its boundaries. It is matrix yielding — and not any type of local instability or fibre failure — that leads to the definition of the peak load and promotes all the post–peak events — including fibre failure (when occurring) and the definition of kink–band geometry. Another important numerical finding is that the matrix provides lateral support to the fibres until the onset of fibre failure.

The outputs from the experimental and numerical programmes, namely the sequence of events and the key features, are applied to the development of an analytical micromechanical model for kink–band formation, presented in *Part II* of this paper [105].

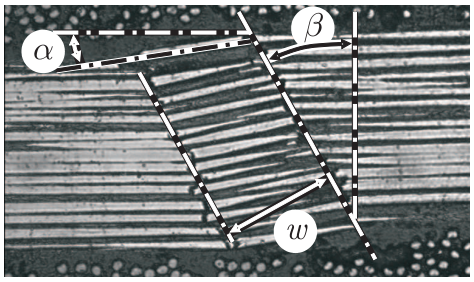
Appendix D

A micromechanical model for kink–band formation: Part II — analytical modelling

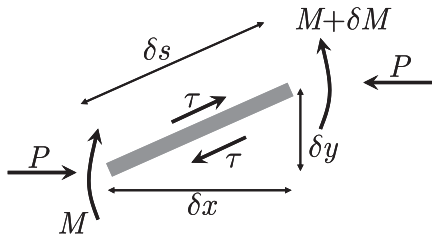
D.1 Abstract

The work in this Appendix was undertaken in collaboration with Ms. Soraia Pimenta, during her Msc project, and is published somewhere else [105].

An analytical micromechanical model for kink–band formation in an unidirectional fibre-reinforced composite is developed. This is supported by the conclusions of experimental and numerical programmes (presented in *Part I* of this paper) and is based on the equilibrium of an imperfect fibre laterally supported by an elasto–plastic matrix. The model predicts the longitudinal compressive strength of the composite (in closed form), the deflection and main stress fields in fibres and matrix at different stages of kink–band formation, the kink–band width, and the orientation of the fibres at the onset of fibre failure.



(a) Micrograph from experiments in CFRP [91] and kink–band geometric parameters: fibre angle α, band angle β, and band width w.



(b) Equilibrium of an infinitesimal part of the fibre.

Figure D.1: Kink–band.

D.2 Introduction

Kink–band formation (figure D.1.a) is the most common failure mode of fibre reinforced polymer (FRP) composites under longitudinal compression [24]. In this paper, an analytical micromechanical model for fibre kinking, based on the results of previous experimental and numerical investigations (*Part I* of this paper [105]), is derived.

Composite materials are preferred for advanced structural applications due to their high specific mechanical properties. To fully exploit these advantageous properties, it is necessary to accurately model the structural response of these materials. However, despite the large amount of work published on fibre kinking, there is no universal agreement among researchers on the micromechanics of this process and the appropriate modelling approach [24]. More recently, the results from the first World-Wide Failure Exercise [125] — where 19 failure theories for fibre reinforced polymer composites were applied to 14 different problems — showed that even the 5 top ranked theories have significant weaknesses; many of these are related to load cases where fibre kinking is likely to occur (longitudinal compression and shear).

Two approaches — microbuckling and kinking — are found in the literature to explain kink–band formation in FRPs [24]. It is generally accepted that they differ in the sense that the kinking approaches are not based on an instability at the micro–scale, but rather on matrix yielding or cracking due to initial fibre misalignments and further phase–shifted ($\beta \neq 0$) rotation due to loading.

Rosen1972 [73] proposed the first model for FRP failure under longitudinal com-

pression; his analysis is based on the in-phase microbuckling of a 2D layered (fibres and matrix) medium, elastic and with no initial imperfection. The composite longitudinal compressive strength X_C^C is predicted as

$$X_C^C = \frac{G_m}{1 - V_f} \,, \tag{D.1}$$

where G_m is the matrix shear modulus and V_f the fibre volume fraction in the composite. This model, and many of its later refinements, overestimate considerably the experimental values found for the composite compressive strength.

It was only with Argon1972 [33] that the quantitative agreement of the predictions started improving significantly. His analysis was the first one considering kinking to be independent from microbuckling. He proposed that, during compression, an initial local fibre misalignment (θ_0) would induce fibre bending and matrix shearing, forcing the material to rotate further in a positive feedback process, and leading subsequently to ultimate failure. The longitudinal compressive strength was then found to be defined at the moment when the shear stresses in a coordinate system aligned with the initially misaligned fibres reach the matrix shear yield strength (S_m):

$$X_C^C = \frac{S_m}{\theta_0} \,. \tag{D.2}$$

Argon1972's model does not take into account the additional (to the initial misalignment) fibre rotation that occurs during longitudinal compression.

After Argon1972, several other researchers proposed models for kinking under similar principles, taking into account the effect of initial fibre misalignments and matrix yielding in shear. Hahn and Williams [78], Steif1990a [77], Fleck et al [21, 75] and Morais and Marques [112] presented different models for the process, all having in common the analysis of a geometrically imperfect (sinusoidal) fibre or smeared composite in bending (figure D.1.b), under the action of an eccentric compressive load and shear stresses transmitted by the surrounding material with a non-linear constitutive response.

Hahn and Williams' model [78] predicts the composite compressive strength as

$$X_C^C = V_f \cdot G_C \cdot \frac{\gamma_{critical}}{\gamma_{critical} + \pi \cdot \frac{\overline{y_0}}{L}} , \tag{D.3}$$

where $\gamma_{critical}$ is the average shear strain in the composite that maximizes the function $X_C^C(\gamma_{critical})$, $G_C(\gamma) = {}^{G_m}/_{1-V_f}$ is the composite shear tangent modulus for that strain, and $\overline{y_0}$ and L are respectively the initial imperfection amplitude and wave length. The correlation between Hahn's model and his experimental data is good, especially for composites with stiff matrix, but his analysis is concerned with the composite longitudinal strength only and not with the softening process that takes place after the peak load is reached.

Steif1990a [77] considers that fibre failure occurs when the maximum tensile strain (combining the effect of compression and bending) reaches the fibre tensile fracture strain. Steif1990a's model is able to reproduce the load versus displacement response during kinking, predicting the composite compressive strength and fibre failure. However, the kink–band width is an input parameter to the model, as the two points of maximum curvature in the fibre (at which failure occurs) are kept at a distance equal to the initial fibre half–wavelength L.

Fleck et al [75] proposed a *bending theory* for fibre kinking, which is (together with its further developments [21]) widely recognized. The authors assume an initial sinusoidal fibre imperfection, forming an initial misaligned band inclined at an angle β; fibres and matrix are smeared in a homogeneous anisotropic solid. The material is in equilibrium under compressive stresses, bending moments, and shear stresses; the corresponding differential equilibrium equation is solved numerically, giving as outputs the deformed shape of the material. The kink–band width (computed in the longitudinal direction only) is defined at the onset of fibre *tensile* failure due to local bending and remote compression. The composite compressive strength is found to be highly dependent of the amplitude of the imperfection, while the kink–band width is fairly insensitive to that parameter.

Morais and Marques [112] model the behaviour of a fibre during kinking by solving the governing differential equation using load incrementation, until the com-

posite strength is reached. Their study is focused on the sensitivity analysis of the effect of material properties and geometric parameters on the composite strength. The model imposes directly a sinusoidal and in-phase deformed shape with constant wavelength, and requires an iterative process to compute the composite strength.

The model proposed in this paper is based on the equilibrium of an imperfect fibre loaded in compression and bending, and supported in shear by an yielding matrix. The model does not involve microbuckling, it imposes no constrains to the fibre deformed shape and it is able to reproduce the composite response from the beginning of compression until the onset of fibre failure. The paper is organised as follows: section D.3 details the development of the analytical model; the results of a numerical application are presented and compared with the outputs from previous FE analyses in section D.4; finally, in section D.5 several implications of the model are discussed, and in section D.6 the main conclusions summarized.

D.3 Development of the analytical micromechanical model

D.3.1 Strategy

The analytical model is formulated through the bending equilibrium of a fibre; it is based on an initial fibre misalignment and on matrix yielding in shear, which (according to the outputs from the experimental and numerical programmes presented in *Part I* of this paper [105]) plays an important role in the formation of a kink–band.

It is assumed that the fibres behave according to simple beam theory combined with compression. The matrix resists only to shear stresses; these are considered constant within each matrix layer across the radial direction, as the composite fibre content is typically high and thus the matrix layers thin [77, 78, 112]. The model requires mechanical continuity between matrix and fibres, as shear stresses are transferred through their interface. Geometrically, a 2D approximation of the real composite is used. A localized imperfection is assumed in the initially unloaded

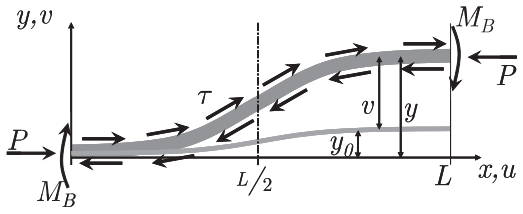


Figure D.2: Schematics of the fibre considered in the model: geometry and loads.

fibres; away from this, the fibres are kept straight throughout the analysis. Constitutively, a linear–elastic – perfect–plastic matrix behaviour in shear is assumed, so two domains — the *elastic domain* and the *softening domain* — are defined in the process. The initial imperfection amplitude, deflections and rotations are assumed to be small.

The composite behaviour is modelled from the beginning of compression until the onset of fibre failure; no further assumptions — notably on the deformed shape of the fibres and on the kink–band width — are introduced.

D.3.2 Fibre geometry and loading

The governing equations of this analytical model are deduced from the equilibrium of one single fibre within the composite, represented in figure D.2. The fibre is loaded by the compressive force P, the bending moments M_B applied at its boundaries and the shear stresses transmitted by the matrix $\tau(x)$ acting on its surface [77, 78, 112]. The fibre initial misalignment is

$$y_0(x) = \overline{y_0} \cdot \left(1 - \cos\left(\pi \cdot \frac{x}{L}\right)\right) , \tag{D.4}$$

and the corresponding slope is denoted $\theta_0(x)$. The fibre undergoes a deflection $v(x)$, with associated slope $\theta(x)$. Its final position is $y(x)$, with slope $\theta_f(x)$.

D.3.3 2D equivalent model

For the sake of simplicity, an 2D layered representation of the composite with unit thickness (in the z-direction) is used. The fibres (perfect cylinders with diameter

ϕ_f) are assumed to be arranged in a hexagonal pattern, being V_f the composite fibre volume fraction; a 2D equivalent model (figure D.3.a) is taken from one of the symmetry planes, resulting in the width of the matrix layers between fibres

$$t_m = \phi_f \left(\sqrt{\frac{\pi}{2 \cdot \sqrt{3} \cdot V_f}} - 1 \right) . \tag{D.5}$$

D.3.4 Equilibrium of the fibre

The equilibrium of moments of an infinitesimal part of the fibre length (figure D.1.b) results in:

$$\delta M + P \cdot \delta y - \tau \cdot \phi_f \cdot \delta s = 0 . \tag{D.6}$$

In equation D.6, the bending moment M per unit thickness is given by the bending theory for thin and straight fibres and small deflections,

$$M = E_f \cdot I_f \cdot \frac{d^2 v}{dx^2} , \tag{D.7}$$

where E_f and I_f are respectively the fibre Young's modulus and second moment of area per unit thickness.

The term corresponding to the compressive load P per unit thickness can be expressed as

$$P \cdot \delta y(x) = P \cdot \delta y_0(x) + P \cdot \delta v(x) . \tag{D.8}$$

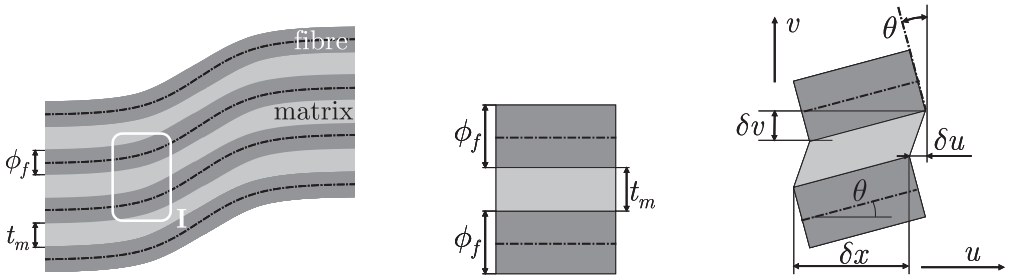
D.3.5 Shear stresses acting on the fibres

According to the hypothesis of thin layers of matrix, the shear traction acting on the fibre surfaces $\tau(x)$ can be obtained from the average shear stresses developed within the matrix.

Shear stresses in the matrix $\tau_{12}^m(x)$ are defined by its deformed geometry and constitutive law:

(i) In the elastic domain,

$$\tau_{12}^m(x) = G_m \cdot \gamma_{12}^m(x) , \tag{D.9}$$



(a) 2D layered equivalent.

(b) Zoom-in of zone I, in the underformed configuration.

(c) Zoom-in of zone I, in the derformed configuration.

Figure D.3: 2D equivalent and matrix deformation.

where G_m is the shear modulus of the matrix. The fibres rotation here is very small, so the deformed shapes of adjacent fibres are approximately in-phase, as indicated in figure D.3.b (as suggested by Morais and Marques [112]); the shear deformation of each matrix layer is then defined as

$$\gamma_{12}^m = \frac{\delta v^m}{\delta x} + \frac{\delta u^m}{\delta y} = \frac{\delta x \cdot \tan\theta}{\delta x} + \frac{\phi_f \cdot \tan\theta}{\delta y} \,. \tag{D.10}$$

As the fibre rotation $\theta(x)$ is small and the layer of matrix is thin (such as $\delta y \approx t_m$), then equation D.10 results in

$$\gamma_{12}^m(x) = \left(1 + \frac{\phi_f}{t_m}\right) \theta(x) \,. \tag{D.11}$$

For a 2D layered composite, the fibre volume fraction is given by equation D.12.a, and an equivalent shear modulus can be defined by equation D.12.b.

$$V_f^{2D} = \frac{\phi_f}{\phi_f + t_m} \quad \text{(a)} \qquad\qquad G_m^{2D} = \frac{G_m}{1 - V_f^{2D}} \quad \text{(b)} \tag{D.12}$$

Using equation D.12.a to eliminate ϕ_f/t_m in equation D.11 gives

$$\gamma_{12}^m(x) = \frac{1}{1 - V_f^{2D}} \cdot \theta(x) \,, \tag{D.13}$$

and using equations D.12.b and D.13 in equation D.9 then the shear stresses in the matrix in the elastic domain can be expressed (as suggested by Steif1990a [77])

as

$$\tau_{12}^{m,\,elastic}(x) = G_m^{2D} \cdot \theta(x)\,. \tag{D.14}$$

(ii) In the plastic domain, $\tau_{12}^{m,\,plastic}(x) = S_m$, where S_m is the yield strength of the matrix in shear.

Summarizing, the shear tractions acting on the fibre surfaces are

$$\tau(x) = \begin{cases} G_m^{2D} \cdot \theta(x) & \text{, if } \theta(x) \leq \frac{S_m}{G_m^{2D}} \\ S_m & \text{, if } \theta(x) > \frac{S_m}{G_m^{2D}} \end{cases}. \tag{D.15}$$

D.3.6 Governing differential equations

Substituting equations D.7, D.8 and D.15 in the equilibrium equation D.6, considering θ to be small (so $\delta s \approx \delta x$), and using $\theta(x) = {}^{\delta v(x)}/_{\delta x}$, then the governing differential equations of the problem become:

(i) Before matrix yielding (*pre-yielding*):

$$E_f \cdot I_f \cdot \frac{d^2\theta^{pre}(x)}{dx^2} - \left[G_m^{2D} \cdot \phi_f - P\right] \cdot \theta^{pre}(x) = -P \cdot \frac{dy_0(x)}{dx}\,, \tag{D.16}$$
$$\text{where } \theta^{pre}(x) = \theta(x) \leq \frac{S_m}{G_m^{2D}}\,;$$

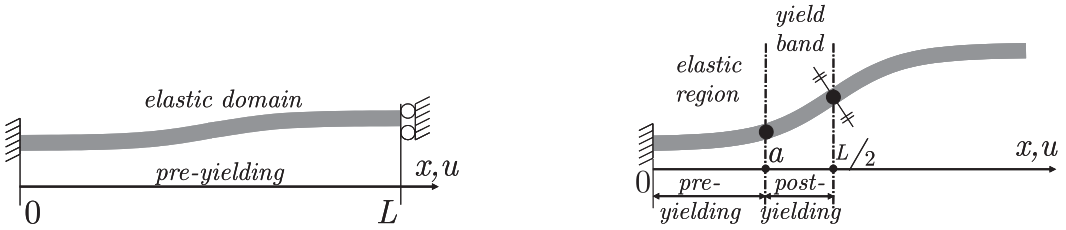
(ii) Where the matrix has yielded (*post-yielding*):

$$E_f \cdot I_f \cdot \frac{d^2\theta^{post}(x)}{dx^2} + P \cdot \theta^{post}(x) = -P \cdot \frac{dy_0(x)}{dx} + \phi_f \cdot S_m\,, \tag{D.17}$$
$$\text{where } \theta^{post}(x) = \theta(x) > \frac{S_m}{G_m^{2D}}\,.$$

D.3.7 Continuity and boundary conditions

The continuity and boundary conditions for equations D.16 and D.17 are defined differently for the two domains of compression:

(I) In the *elastic domain* (figure D.4.a), the matrix follows a linear–elastic behaviour within the entire length L; the equation for *pre-yielding* (equation



(a) *Elastic domain.* (b) *Softening domain.*

Figure D.4: Boundary and continuity conditions.

D.16) applies to the whole domain in $0 \leq x \leq L$, under the following boundary conditions:

- $\theta^{pre}(0) = \theta^{pre}(L) = 0$, to avoid rotation at the boundaries;
- $v^{pre}(0) = 0$, to avoid rigid body movement.

(II) In the *softening domain* (figure D.4.b), the fibre rotations $\theta(x)$ in the *yield band* ($a \leq x \leq L - a$) are large enough to promote matrix yielding, so the equation for *post-yielding* (equation D.17) applies; in the *elastic regions* ($0 \leq x \leq a$ or $L - a \leq x \leq L$), the equation for *pre-yielding* (equation D.16) is still valid. The boundary conditions are:

- $\theta^{pre}(0) = 0$, to avoid rotation at the boundary;
- $v^{pre}(0) = 0$, to avoid rigid body movement;
- $\theta^{post'}(L/2) = 0$, to impose an anti-symmetric shape on the deflection.

Continuity between the *elastic regions* and *yield band* is ensured at $x = a$ by:

- $v^{pre}(a) = v^{post}(a)$, continuity of fibre deflection;
- $\theta^{pre}(a) = \theta^{post}(a) = S_m/G_m^{2D}$, continuity of fibre slope and matrix shearing;
- $\theta^{pre'}(a) = \theta^{post'}(a)$, continuity of curvature and bending moments in the fibre (additional condition, used to locate $x = a$).

D.3.8 Composite compressive strength

The (2D) composite compressive strength X_C^C is defined by the peak load per unit thickness P^{peak} as

$$X_C^C = P^{peak} \cdot \frac{V_f^{2D}}{A_f} \,, \tag{D.18}$$

where A_f is the area of the fibre cross section per unit thickness. It was found, from the numerical simulations previously performed, that the peak load occurs closely after the onset of matrix yielding (see the *Sequence of events* in *Part I* of this paper [105]), and is therefore estimated from:

$$\max\left\{\tau_{12}^m(x)\right\} = S_m. \tag{D.19}$$

Equations D.16 (see resulting $\theta(x)$ in equation D.29) and D.15 give, for the *elastic domain*, a maximum shear stress of

$$\max\left\{\tau_{12}^{m\,,elastic}(x)\right\} = \tau_{12}^{m,elastic}\left(x = {}^{L}/_{2}\right) = G_m^{2D} \cdot \frac{\pi \cdot \frac{\overline{y_0}}{L} \cdot P}{G_m^{2D} \cdot \phi_f + \frac{\pi^2}{L^2} \cdot E_f \cdot I_f - P} \,. \tag{D.20}$$

Introducing equation D.20 into equation D.19, and then the resulting peak load (as given in equation D.31) into equation D.18, the composite compressive strength comes as

$$X_C^C = S_m \cdot \frac{G_m^{2D} \cdot \phi_f + \frac{\pi^2}{L^2} \cdot E_f \cdot I_f}{S_m + \pi \cdot \frac{\overline{y_0}}{L} \cdot G_m^{2D}} \cdot \frac{V_f^{2D}}{A_f} \,. \tag{D.21}$$

D.3.9 Axial stresses and fibre failure

The axial stresses in the fibre $\sigma_{11}^f(x)$ result from the combination of the compressive load P and the bending moment $M(x)$:

(a) Compressive load P. Assuming an uniform stress distribution over the fibre's cross section A_f and small slopes of the deformed shape (so $P \cdot cos(\theta_0 + \theta) \approx P$), this stress is given by:

$$\sigma_{11}^{f,P} = \frac{P}{A_f} \,; \tag{D.22}$$

note that $\sigma_{11}^{f,P}$ is defined as being positive for compression.

(b) Bending moment $M(x)$. From beam theory, the maximum axial stress within the fibre cross section is

$$\sigma_{11}^{f,M}(x) = \frac{M(x) \cdot \phi_f}{2 \cdot I_f} \,, \tag{D.23}$$

where $M(x)$ is given by equation D.7; the value of x which maximizes $\sigma_{11}^{f,M}(x)$ is designated b, with $b \in [0, L/2]$.

Then, for a given load P and location $x \in [0, L/2]$, it comes (positive for compression):

$$\sigma_{11}^{f}(x, P) = \frac{P}{A_f} + \frac{\phi_f \cdot E_f}{2} \cdot \frac{d\theta(x)}{dx} \,. \tag{D.24}$$

Due to $\sigma_{11}^{f,P}$ being compressive and $\sigma_{11}^{f}(x, P)$ being symmetrical, the magnitude of the compressive axial stress in the fibre is always greater than that of the tensile one. In addition, experimental results presented in *Part I* of this paper [105] show that fibres are damaged first in compression. For these reasons, fibre failure (ff) initiates when the stress $\sigma_{11}^{f}(x, P)$ in equation D.24 equals the fibre strength in compression X_C^f, for a load $P = P^{ff}$ and at a location $x = b^{ff}$. The condition is then

$$\frac{d\theta}{dx}(b^{ff}) = 2 \cdot \frac{X_C^f - \frac{P^{ff}}{A_f}}{\phi_f \cdot E_f} \,. \tag{D.25}$$

Considering damage propagation within the fibre cross section to be sudden, then the kink–band width can be roughly estimated by the location of onset of fibre failure $\left(b^{ff},\, y(b^{ff})\right)$ as

$$w \approx 2 \cdot \sqrt{\left[L/2 - b^{ff}\right]^2 + \left[y\left(L/2\right) - y\left(b^{ff}\right)\right]^2} \,. \tag{D.26}$$

D.4 Results

The analytical model previously presented was solved and evaluated for successive loads P and using the input data from tables D.1 and D.2. Figures D.5 and D.6 show the analytical curves obtained, plotted together outputs of a previous

Table D.1: Geometrical and composite parameters used in the analytical model.

L [μm]	$\overline{y_0}$ [μm]	V_f [%]	ϕ_f [μm]
750	15	60	7

Table D.2: Constituents mechanical properties used in the analytical model.

E_f [GPa]	X_C^f [MPa]	G_m [GPa]	S_m [MPa]
276	3200	1.478	56

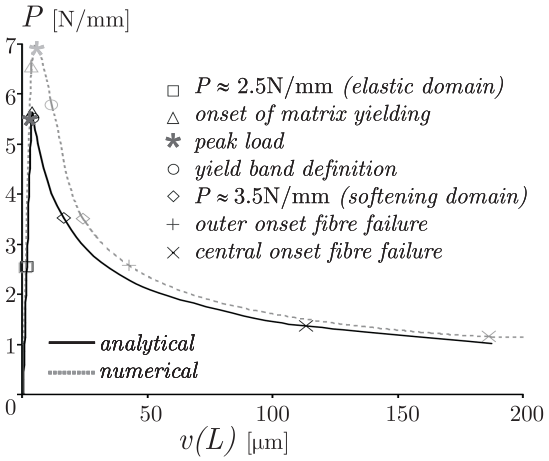
numerical FE simulation (*Part I* of this paper [105]). The main quantitative results are provided in tables D.3 and D.4.

In the overall, the following results were obtained:

- The *load vs. displacement curve* (figure D.5.a) shows an almost linear and stiff response in the *elastic domain* and, after the *peak load*, a progressively reducing load in the *softening domain*;
- The *resulting fields* for $v(x)$, $\theta(x)$, $\tau_{12}^m(x)$ and $\sigma_{11}^f(x)$ are, in the *elastic domain*, sinusoidal (see figures D.5.b–d and D.6.b–d, and corresponding equations in appendix D.A.1). In the *softening domain*, these fields are much more complex (see figures D.5.b–d and D.6.b–d, and corresponding equations in appendix D.A.3) and with distinct shapes within the *elastic regions* and the *yield band*;
- The *shear stresses* in the matrix $\tau_{12}^m(x)$ (figures D.5.b and D.6.b) follow, in the *elastic domain*, a sinusoid with maximum at $x = L/2$. In the *softening domain*, a central *yield band* with constant stresses $\tau_{12}^m(x) = S_m$ is defined, outside which the shear stresses drop abruptly;
- The fibre *transverse displacements* $v(x)$ (figures D.5.c and D.6.c) in the *elastic domain* are a magnification of the sinusoidal imperfection. In the *softening domain*, the deformed shape changes completely: the points of maximum cur-

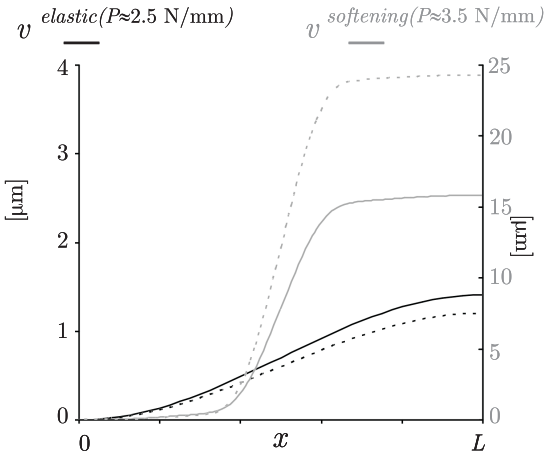
Table D.3: Quantitative results from the analytical model at the peak load.

P^{peak} [N/mm]	$v^{peak}(L)$ [μm]	$\theta_f^{peak,average}$ [°]	X_C^C [MPa]
5.62	3.37	2.51	654

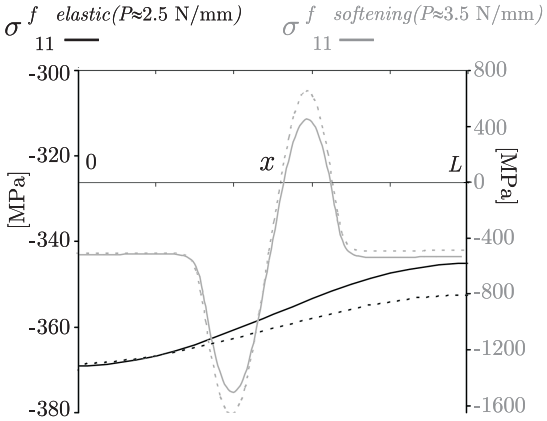


(a) Load vs. transverse displacement curve.

(b) Shear stresses in the matrix.



(c) Fibre deflection.

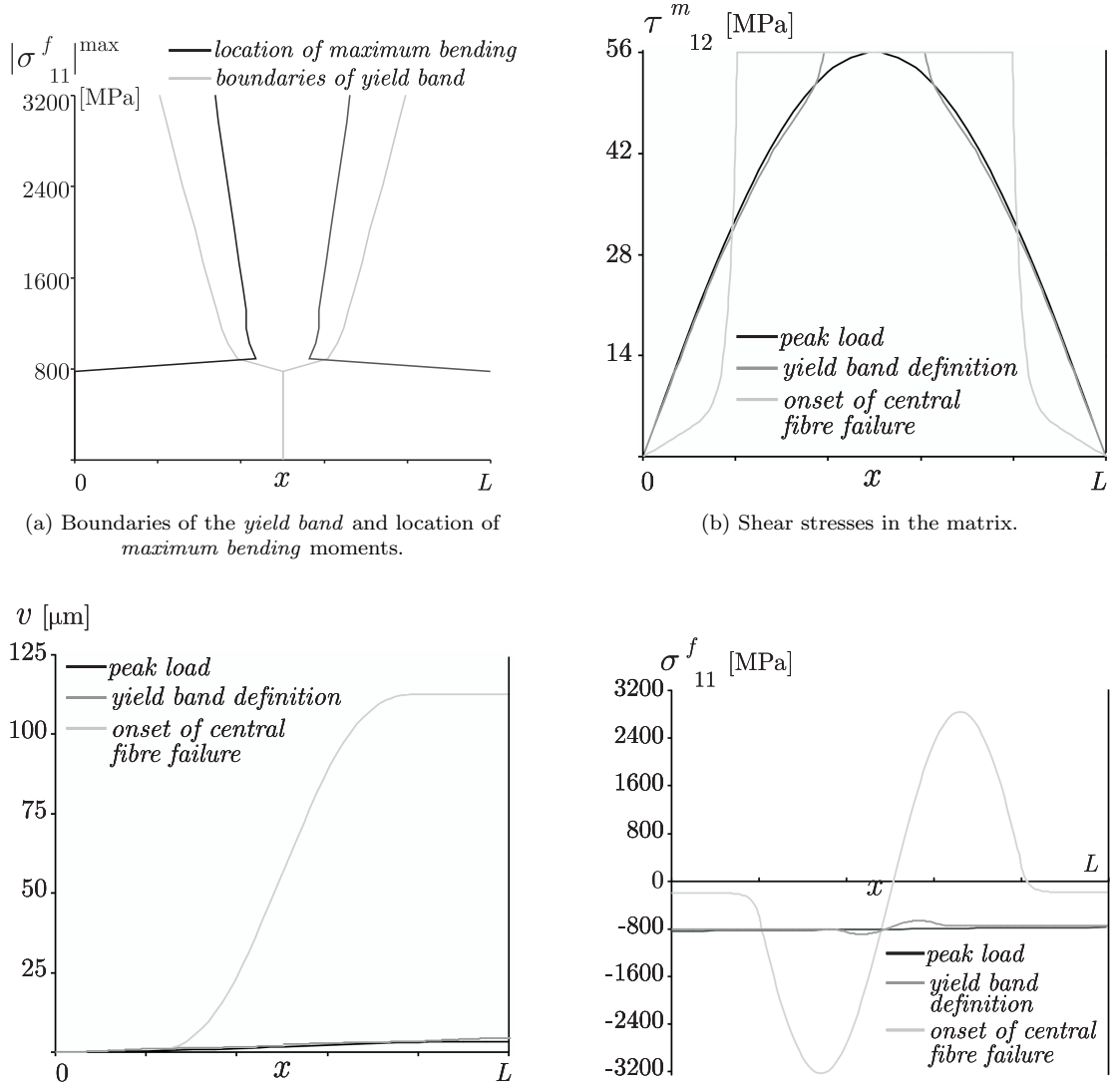


(d) Axial stresses in the fibre (top surface).

Figure D.5: Results of the analytical model (compared to those of the *cohesive* model (detailed in *Part I* of this paper [105]), for a similar compressive load P).

Table D.4: Quantitative results from the analytical model at the onset of fibre failure.

P^{ff} [N/mm]	$v^{ff}(L)$ [μm]	$\theta_f^{ff}(L/2)$ [°]	w [μm]
1.35	112.8	16.3	249



(a) Boundaries of the *yield band* and location of *maximum bending* moments.

(b) Shear stresses in the matrix.

(c) Fibre deflection.

(d) Axial stresses in the fibre (top surface).

Figure D.6: Results of the analytical model (evolution of fields).

vature move suddenly inwards, away from the fixed ends of the model. As the compression progresses, the fibre ends become flatter relatively to the centre; the central inclined region (between the points of maximum curvature) rotates further and extends smoothly towards the fibre boundaries;

- The magnitude of the *axial stresses* in the fibre $\sigma_{11}^{f}(x)$ (figures D.5.d and D.6.d) in the *elastic domain* are maximum at the fibre boundaries and dominated by the compressive component $\sigma_{11}^{f,P}$. In the *softening domain*, the bending component $\sigma_{11}^{f,M}$ increases considerably inside the *yield band* (tensile stresses develop as well) and $\sigma_{11}^{f,P}$ is reduced;

- A matrix *yield band* forms almost instantaneously as the composite goes into the *softening domain*, and widens smoothly as compression progresses (figure D.6.a). Also immediately after the peak load, the *maximum bending* points move from the fibre boundaries towards its centre, inside the *yield band*, and are kept at approximately half of the *yield band* width during further compression.

D.5 Discussion

D.5.1 Qualitative analysis of fields

The $P\,[v(x)]$ curve obtained with the analytical model (figure D.5.a) represents the common behaviour documented for kink–band formation [28].

When it comes to the $v(x)$, $\theta(x)$, $\tau_{12}^{m}(x)$ and $\sigma_{11}^{f}(x)$ fields (equations in Appendix D.A and figure D.5.b–d), in the *elastic domain* the response merely amplifies the initial imperfection; however, as soon as the matrix starts yielding, deformation localizes within the *yield band* and the shapes (and not only the amplitude) of the deflection and stress fields change completely, reflecting the typical response of kink–band formation [29].

In the elastic domain, the contribution of the matrix to the overall stiffness is very important (see for instance equation D.27 in Appendix D.A, where $G_{m}^{2D} \cdot \phi_{f} =$

55.6N/mm, against $\pi^2/L^2 \cdot E_f \cdot I_f = 0.14$N/mm from fibres). When the *yield band* forms, the shear stress in the matrix is limited and therefore the material becomes softer there (figure D.5.b). For this reason, fibre deflection increases significantly and locally, deforming into a kinked shape (figure D.5.c). This type of deflection has an almost-zero curvature within the *elastic regions* and in the centre of the *yield band*; near the *yield band* boundaries, the fibre is highly curved, which reflects on the $\sigma^f_{11}(x)$ field (figure D.5.d).

D.5.2 Agreement between analytical and FE results

The analytical model previously developed is based on the outputs from the numerical simulations performed in *Part I* of this paper [105]; the analytical results are compared to the FE ones in figure D.5. It is found that all the qualitative features present in the numerical curves are shown in the analytical ones, and the quantitative agreement is also remarkable. This proves that the numerical models were correctly interpreted, and that the main assumptions of the analytical model — regarding matrix deformation & constitutive law (section D.3.5) and, consequently, the prescription of periodic boundary conditions in the *elastic regions* and plastic foundation in the *yield band* — accurately represent the behaviour during kink–band formation.

The $P\,[v(x)]$ analytical curve has a peak load below the numerical one (figure D.5.a); this is due to the use of numerical damping in the FE routine and (as also noted by Kyriakides et al [31]) to the high number of matrix layers (through which the *yield band* must propagate transversely) in the numerical simulation. This effect is slowly reduced as compression proceeds, but has nevertheless a quantitative repercussion in the displacement $v(x)$ field (figure D.5.c).

The onset of fibre failure in the numerical simulation starts in the outer fibres and progresses transversely (see FE results in *Part I* of this paper [105]). As the analytical model has no edge effect, it predicts fibre failure to start after the numerical onset of outer fibre failure. On the other hand, the curvature of the central fibre in the numerical model is reduced due to the transverse stiffness of the composite as a

whole, delaying its failure. For these reasons, analytical onset of fibre failure occurs between the numerical onset of failure in outer and central fibres (figure D.5.a).

D.5.3 Model outputs

The primary outputs of the analytical model are the deflection and stress fields (Appendix D.A); through them, the process of kink–band formation can be fully tracked until the onset of fibre failure. As no deformed shape for the compressed fibre is imposed a priori, the shape — and not only the magnitude — of these fields are outputs of the model, and reproduce the expected behaviour of kink–band formation.

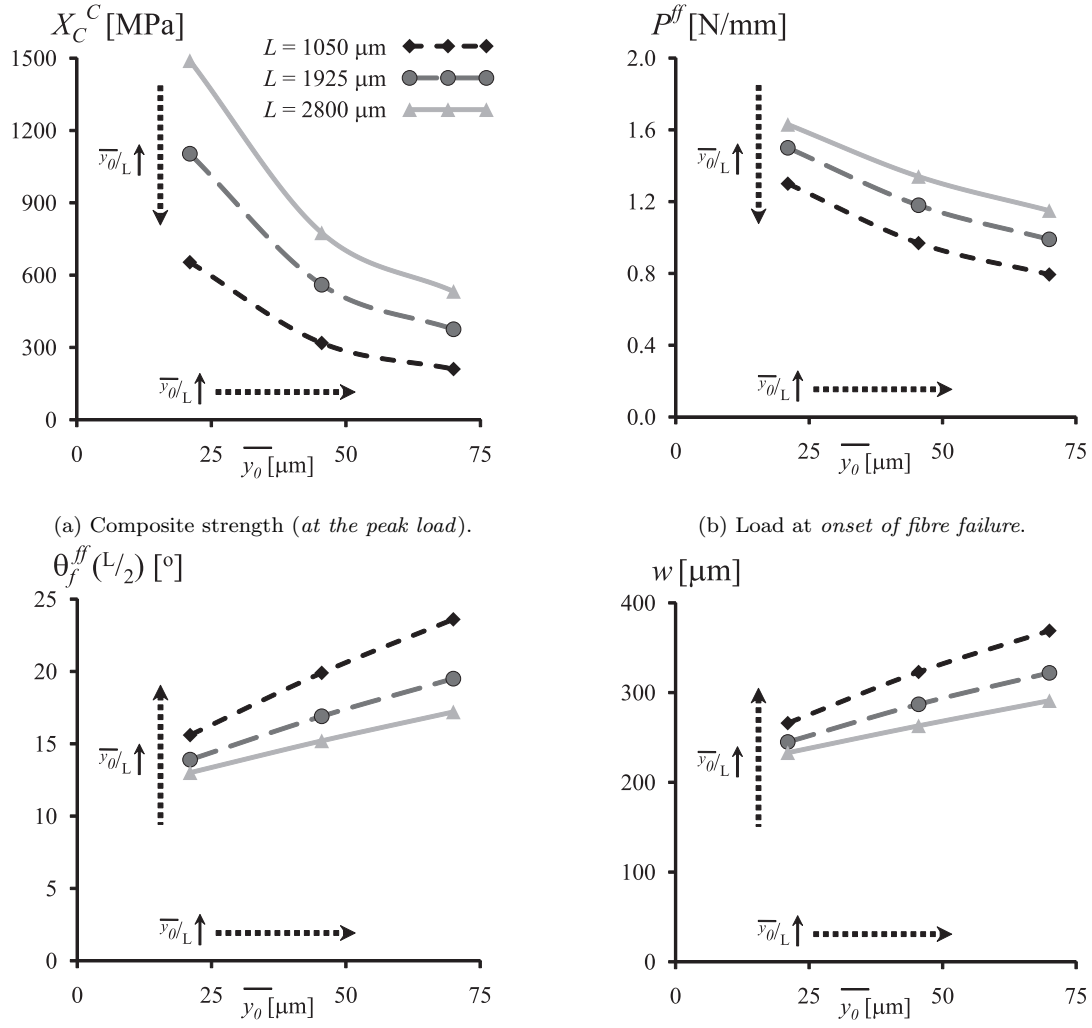
In addition, this model predicts the composite longitudinal compressive strength X_C^C (in closed form, equation D.21), the kink–band width w and the orientation $\theta_f(x)$ of fibres at the onset of failure (which can be further related to the band angle β and fibre angle α). However, the behaviour after the onset of fibre failure needs to be studied further, to confirm the assumption of no effect of damage propagation in the kink–band width and orientation.

D.5.4 Sensitivity study

A sensitivity study was carried out, regarding the influence of the initial imperfection on the model outputs. The range of imperfections analysed was measured by Kyriakydes [31], who found regularly–spaced bands of highly–misaligned fibres with half–wavelength and half–amplitude of respectively $L \in [1050; 2800]$ μm and $\overline{y_0} \in [21; 70]$ μm. This range of imperfections is considerably large, with variations of nearly 50% relatively to the central values for both amplitude and wavelength; imperfection misalignments (measured by $\overline{y_0}/L$) ranged from 0.8 to 6.7%. The results from the sensitivity study are presented in figure D.7.

For the whole range tested, the shape of stress & field curves and the sequence of events for kink–band formation are independent of the initial imperfection parameters.

The compressive strengths (figure D.7.a) show a considerable dependency on the



(a) Composite strength (*at the peak load*).

(b) Load at *onset of fibre failure*.

(c) Fibre angle at *onset of fibre failure*.

(d) Kink–band width at *onset of fibre failure*.

Figure D.7: Sensitivity study for the initial imperfection.

initial imperfection, with higher strengths verified for the less–pronounced misalignments (smaller amplitudes and larger wavelengths). This agrees with the well-known fact that the longitudinal compressive strength of UD CFRP is highly dependent on the manufacturing process and material defects.

Regarding the onset of fibre failure, the main parameters for kink–band formation — load, fibre–angle and kink–band width (figure D.7.b–d) — evidence a reduced sensitivity to the imperfection parameters; for instance, the kink–band width is kept within $w \in [233; 369]$ μm, which represents a variation of $\pm 22\%$ for misalignments varying almost 80% around the central value. Both the kink–band width and fibre angle increase for more severe imperfections, specially in terms of larger amplitudes (the effect of smaller wavelengths is slightly less pronounced).

Overall, the kink–band width and the fibre–angle at fibre fibre are kept within a reasonable range of values ($\theta_f^{ff}(L/2) \in [13; 24]^\circ$, i.e. $\pm 29\%$), comparable with the ones commonly observed experimentally [24, 29]. In addition, these results show that the model here proposed is applicable to a wide range of imperfections, giving outputs and trends consistent with those obtained analytically by other researchers [75].

D.6 Conclusions

An analytical model has been developed for kink–band formation in compressively loaded unidirectional composites. This was based on the conclusions of experimental and numerical programmes (detailed in *Part I* of this paper [105]).

The model considers the equilibrium of a single imperfect fibre under compression and supported in shear by the matrix. Matrix yielding is found to be a key feature for kink–band formation.

As global outputs, the model is able to provide load vs. displacement curves and fields for the deflection, axial stresses in fibres and shear stresses in matrix, from the beginning of compression to the onset of fibre failure. It also predicts the composite compressive strength (in closed form), the kink–band width and the orientation of the fibres at the onset of their failure. A sensitivity study for the imperfection parameters showed the composite strength to be severely degraded

by more pronounced imperfections; by opposition, the geometric parameters at the onset of fibre failure — kink–band width and fibre angle — were found to be kept within a narrow band of values, with good agreement with experimental data.

Unlike other analytical models for kink–band formation [77, 112], no deformed shape is imposed a priori in the one here developed; all the features captured — namely the location of the *maximum bending* points inside the *yield band* and the deflection in a kinked (and not sinusoidal) shape — are also outputs of the model. The model is able to predict kink–band formation without fibre failure (width given in this case by the *yield band*), can be adapted (by modification of equations D.14 and D.15) to layered materials with frictional interface (like rocks), and can be extended to composites under hydrostatic pressure (by making the yield strength of the matrix a function of the hydrostatic pressure).

The results of the analytical model were compared against results from an FE model; a good agreement was found, both quantitatively and qualitatively.

D.A Analytical expressions for displacement and stress fields

D.A.1 Elastic domain

- Transverse displacements

$$v^{pre}(x,P) = \frac{\overline{y_0}\cdot P}{G_m^{2D}\cdot\phi_f + \frac{\pi^2}{L^2}\cdot E_f\cdot I_f - P}\cdot\left(1-\cos\left(\pi\frac{x}{L}\right)\right) \tag{D.27}$$

- Slope

$$\theta^{pre}(x) = \frac{\pi\cdot\frac{\overline{y_0}}{L}\cdot P}{G_m^{2D}\cdot\phi_f + \frac{\pi^2}{L^2}\cdot E_f\cdot I_f - P}\cdot\sin\left(\pi\frac{x}{L}\right) \tag{D.28}$$

- Shear stresses

$$\tau_{12}^{m}(x,P) = G_m^{2D}\cdot\frac{\pi\cdot\frac{\overline{y_0}}{L}\cdot P}{G_m^{2D}\cdot\phi_f + \frac{\pi^2}{L^2}\cdot E_f\cdot I_f - P}\cdot\sin\left(\pi\frac{x}{L}\right) \tag{D.29}$$

- Axial stresses

$$\sigma_{11}^{f}(x,P) = \frac{P}{A_f} + \\ + G_m^{2D} \cdot \frac{\phi_f \cdot E_f}{2} \cdot \frac{\overline{y_0} \cdot \frac{\pi^2}{L^2} \cdot P}{G_m^{2D} \cdot \phi_f + \frac{\pi^2}{L^2} \cdot E_f \cdot I_f - P} \cdot \cos\left(\pi \frac{x}{L}\right) \tag{D.30}$$

D.A.2 Peak load

- Peak load

$$P^{peak} = S_m \cdot \frac{G_m^{2D} \cdot \phi_f + \frac{\pi^2}{L^2} \cdot E_f \cdot I_f}{S_m + \pi \cdot \frac{\overline{y_0}}{L} \cdot G_m^{2D}} \tag{D.31}$$

- Transverse displacements

$$v(x, P^{peak}) = \frac{L \cdot S_m}{\pi \cdot G_m^{2D}} \cdot \left(1 - \cos\left(\pi \frac{x}{L}\right)\right) \tag{D.32}$$

D.A.3 Softening domain

- Slope in the elastic region

$$\theta^{pre}(x) = C^{pre} \cdot \left(e^{\sqrt{\frac{G_m^{2D} \cdot \phi_f - P}{E_f \cdot I_f}} \cdot x} - e^{-\sqrt{\frac{G_m^{2D} \cdot \phi_f - P}{E_f \cdot I_f}} \cdot x} \right) + \\ + \frac{P}{G_m^{2D} \cdot \phi_f + \frac{\pi^2}{L^2} \cdot E_f \cdot I_f - P} \cdot \frac{\pi \cdot \overline{y_0}}{L} \cdot \sin\left(\pi \frac{x}{L}\right) \ , \ x \leq a \tag{D.33}$$

with

$$C^{pre} = \frac{1}{e^{\sqrt{\frac{G_m^{2D} \cdot \phi_f - P}{E_f \cdot I_f}} \cdot a} - e^{-\sqrt{\frac{G_m^{2D} \cdot \phi_f - P}{E_f \cdot I_f}} \cdot a}} \cdot \\ \cdot \left(\frac{S_m}{G_m^{2D}} - \frac{P}{\left(G_m^{2D} \cdot \phi_f + \frac{\pi^2}{L^2} \cdot E_f \cdot I_f - P\right)} \cdot \frac{\pi \cdot \overline{y_0}}{L} \cdot \sin\left(\pi \frac{a}{L}\right) \right)$$

- Slope in the yield band

$$\theta^{post}(x) = C_1^{post} \cdot \sin\left(\sqrt{\frac{P}{E_f \cdot I_f}} \cdot x\right) + C_2^{post} \cdot \cos\left(\sqrt{\frac{P}{E_f \cdot I_f}} \cdot x\right) + \frac{S_m \cdot \phi_f}{P} - \frac{P}{P - \frac{\pi^2}{L^2} \cdot E_f \cdot I_f} \cdot \frac{\pi \cdot \overline{y_0}}{L} \cdot \sin\left(\pi \frac{x}{L}\right),\ a < x \leq \frac{L}{2} \tag{D.34}$$

with

$$C_1^{post} = \frac{1}{\cot\left(\sqrt{\frac{P}{E_f \cdot I_f}} \cdot \frac{L}{2}\right) \cdot \cos\left(\sqrt{\frac{P}{E_f \cdot I_f}} \cdot a\right) + \sin\left(\sqrt{\frac{P}{E_f \cdot I_f}} \cdot a\right)} \cdot \cdot \left(\frac{P \cdot \frac{\pi \cdot \overline{y_0}}{L} \cdot \sin\left(\pi \frac{a}{L}\right)}{P - \frac{\pi^2}{L^2} \cdot E_f \cdot I_f} - S_m \cdot \left(\frac{\phi_f}{P} + \frac{1}{G_m}\right)\right)$$

$$C_2^{post} = \frac{1}{\cos\left(\sqrt{\frac{P}{E_f \cdot I_f}} \cdot a\right) + \tan\left(\sqrt{\frac{P}{E_f \cdot I_f}} \cdot \frac{L}{2}\right) \cdot \sin\left(\sqrt{\frac{P}{E_f \cdot I_f}} \cdot a\right)} \cdot \cdot \left(\frac{P \cdot \frac{\pi \cdot \overline{y_0}}{L} \cdot \sin\left(\pi \frac{a}{L}\right)}{P - \frac{\pi^2}{L^2} \cdot E_f \cdot I_f} - S_m \cdot \left(\frac{\phi_f}{P} + \frac{1}{G_m}\right)\right)$$

Bibliography

[1] M. Hinton, A. Kaddour, P. Soden, Failure criteria in fibre reinforced polymer composites: The world-wide failure exercise, M.J. Hinton, A.S. Kaddour, P.D. Soden, Elsevier, Ch. Predictive capabiities of ninenteen failure theories and design methodologies for polymer composite laminates. Part B: comparison with experiments, pp. 1073–1221.

[2] D. Purslow, Some fundamental aspects of composites fractography, Composites 12 (1981) 241–247.

[3] C. Ramirez-Jimenez, N. Papadakis, N. Reynolds, T. Gan, P. Purnell, M. Pharaoh, Identification of failure modes in glass/polypropylene composites by means of the primary frequency content of the acoustic emission event, Composites Science and Technology 64 (2004) 1819–1827.

[4] B. F. Sørensen, T. K. Jacobsen, Determination of cohesive laws by the J integral approach, Engineering Fracture Mechanics 70 (2003) 1841–1858.

[5] B. F. Sørensen, T. K. Jacobsen, Large-scale bridging in composites: R-curves and bridging laws, Composites Part A 29A (1998) 1443–1451.

[6] S. T. Pinho, C. G. Dávila, P. P. Camanho, L. Iannucci, P. Robinson, Failure models and criteria for FRP under in-plane or three-dimensional stress states including shear non-linearity, Tech. rep., NASA (2005).

[7] Standard test method for in-plane shear properties of polymer matrix composite materials by the rail shear method (D 4255/D 4255-01).

[8] Standard test method for shear properties of composite materials by the V-notched beam method (D 5379/D 5379M-98).

[9] Standard test method for in-plane shear response of polymer matrix composite materials by tensile test of a $\pm 45^\circ$ laminate (D 3518/D 3518M-94).

[10] Standard test method for tensile properties of fiber-resin composite (D 3039-76).

[11] P. P. Camanho, C. G. Dávila, S. T. Pinho, L. Iannucci, P. Robinson, Prediction of in situ strengths and matrix cracking in composites under transverse tension and in-plane shear, Composites, Part A: applied science and manufacturing 37 (2006) 165–176.

[12] A. Puck, J. Kopp, M. Knops, Guidelines for the determination of the parameters in Puck's action plane strength criterion, Composites Science and Technology 62 (2002) 371–378.

[13] D. Purslow, Matrix fractography of fibre-reinforced epoxy composites, Composites 17 (1986) 289–303.

[14] A. Parvizi, K. Garrett, J. Bailey, Constrained cracking in glass fibre-reinforced epoxy cross-ply laminates, Journal of Materials Science 13 (1978) 195–201.

[15] J. E. Bailey, P. T. Curtis, A. Parvizi, On the transverse cracking and longitudinal splitting behaviour of glass and carbon fibre reinforced epoxy cross ply laminates and the effect of poisson and thermally generated strain, Proceedings of the Royal Society of London. Series A, Mathematical and Physical Sciences 366 (1979) 599–623.

[16] K. W. Garrett, J. E. Bailey, Multiple transverse fracture in 90° cross-ply laminates of a glass fibre-reinforced polyester, Journal of Material Sciemnce 12 (1977) 157–168.

[17] P. D. Ewins, R. T. Potter, S. M. Bishop, P. J. Worthington, Some observations on the nature of fibre reinforced plastics and the implications for structural

design [and discussion], Philosophical Transactions of the Royal Society of London. Series A, Mathematical and Physical Sciences 294 (1980) 507–517.

[18] S. Behzadi, P. T. Curtis, F. R. Jones, Improving the prediction of tensile failure in unidirectional fibre composites by introducing matrix shear yielding, Composites Science and Technology 69 (2009) 2421–2427.

[19] M. Laffan, S. Pinho, P. Robinson, L. Iannucci, Measurement of the in situ ply fracture toughness associated with mode I fibre tensile failure in FRP. Part II: Size and lay-up effects, Composites Science and Technology 70 (2010) 614–621.

[20] R. K. A.S. Crasto, Compression strengths of advanced composites from a novel mini-sandwich beam, Sampe Quarterly 22 (1991) 29–39.

[21] N. Fleck, Compressive failure of fiber composites, Advances in applied mechanics 33 (1997) 43–117.

[22] P. M. Jelf, N. A. Fleck, The failure of composite tubes due to combined compression and torsion, Journal of materials science 29 (1994) 3080–3084.

[23] M. Mannigel, Influence of shear stresses on the fibre failure behaviour in carbon fibre reinforced plastics (CFRP), Ph.D. thesis, Technical University of Aachen (2007).

[24] C. R. Schultheisz, A. M. Waas, Compressive failure of composites, Part I: Testing and micromechanical theories, Progress In Aerospace Science 32 (1996) 1–42.

[25] F. Edgren, L. E. Asp, R. Joffe, Failure of NCF composites subjected to combined compression and shear loading, Composites Science and Technology 66 (2006) 2865–2877.

[26] L. Benabou, Predictions of compressive strength and kink band orientation for wood species, Mechanics of Materials 42 (2010) 335–343.

[27] M. A. Wadee, G. W. Hunt, M. A. Peletier, Kink band instability in layered structures, Journal of the mechanics and physics of solids 52 (2004) 1071–1091.

[28] P. Moran, X. Liu, C. Shih, Kink band formation and band broadening in fiber composites under compressive loading, Acta metallugirca materialla 43 (1995) 2943–2958.

[29] T. Vogler, S. Kyriakides, On the initiation and growth of kink bands in fiber composites. Part I: experiments, International journal of solids and structures 38 (2001) 2639–2651.

[30] S. T. Pinho, R. Darvizeh, P. Robinson, C. Schuecker, P. P. Camanho, Material and structural response of polymer-matrix fibre-reinforced composites, Composites Science and Technology 2008; accepted for publication. (Special issue on Second World Wide Failure Exercise).

[31] S. Kyriakides, R. Arseculeratne, E. J. Perry, K. Liechti, On the compressive failure of fiber reinforced composites, International Journal of solids and structures 32 (1995) 689–738.

[32] E. G. Guynn, O. O. Ochoa, W. L. Bradley, A parametric study of variables that affect fiber microbuckling initiation in composite laminates: Part I-Analysis, Journal of composite materials 26 (1992) 1594–1616.

[33] A. Argon, Treatise on Material Science and Technology, volume1, Academic press, 1972, Ch. Fracture of Composites, pp. 79–114.

[34] P. Berbinau, C. Soutis, I. Guz, Compressive failure of 0 ° unidirectional carbon-fibre-reinforced plastic (CFRP) laminates by fibre microbuckling, Composites Science and Technology 59 (1999) 1451–1455.

[35] K. Oguni, C. Y. Tan, G. Ravichandran, Failure mode transition in unidirectional E-glass/Vinylester composites under multiaxial compression, Journal of Composite Materials 34 (2000) 2081–2097.

[36] T. V. Parry, A. S. Wronsky, Kinking and compressive failure in uniaxially aligned carbon fibre composite tested under superposed hydrostatic pressure, Journal of materials Science 17 (1982) 893–900.

[37] P. Soden, M. Hinton, A. Kaddour, Biaxial test results for strength and deformation of a range of E-glass and carbon fibre reinforced composite laminates: failure exercise benchmark data, Composites science and technology 62 (2002) 1489–1514.

[38] C. S. Yerramalli, A. M. Waas, A failure criterion for fiber reinforced polymer composites under combined compression torsion loading, International Journal of Solids and Structures 40 (2003) 1139–1164.

[39] R. Finlayson, M. Friesel, M. Carlos, P. Cole, J. Lenain, Health monitoring of aerospace structures with acoustic emission and acousto-ultrasonics, Insight 43.

[40] M. R. Gorman, Plate wave acoustic emission, Journal of the Acoustical Society of America 90 (1991) 358–364.

[41] M. Surgeon, M. Wevers, Modal analysis of acoustic emission signals from CFRP laminates, NDT&E International 32 (1999) 311–322.

[42] M. Arrington, Non-Destructive Testing of Fibre-Reinforced Plastics Composites, vol. 1, Elsevier, 1987, Ch. Acoustic Emission, pp. 25–63.

[43] D. Valentin, P. Bonniau, A. Bunsell, Failure mechanism discrimination in carbon fibre-reinforced epoxy composites, Composites 14 (1983) 345–351.

[44] J. M. Berthelot, J. Rhazi, Acoustic emission in carbon fibre composites, Composites Science and Technology 37 (1990) 411–428.

[45] N. Godin, S. Huguet, R. Gaertner, L. Salmon, Clustering of acoustic emission signals collected during tensile tests on unidirectional glass/polyester composite using supervised and unsupervised classifiers, NDT&E International 37 (2004) 253–264.

[46] L. Bounouas, S. Benmedakhene, A. Laksimi, F. Neumann, A. Imad, Z. Azarid, Experimental analysis of the influence of structural parameters on the behaviour of glass-fiber reinforced polypropylene composites, Strength of Materials, Vol. 33, No. 1, 2001 33 (2001) 42–51.

[47] C. Rowland, L. Butler, M. Preston, Acoustic emission technique to assist the formula one designer in structural design lecture 34, NDT.net DGZfP-Proceedings BB 90-CD 26th European Conference on Acoustic Emission Testing 10 (2005) 349–359.

[48] S. Huguet, Application de classificateur aux donnees d'emission acoustique: identification de la signature acoustique des mecanismes d'endommagement dans les composites a matrice polymere, Ph.D. thesis, Institut National des Sciences Appliquees de Lyon (2002).

[49] Q. Q. Ni, M. Iwamoto, Wavelet transform of acoustic emission signals in failure of model composites, Engineering Fracture Mechanics 69 (2002) 717–728.

[50] P. J. de Groot, P. A. M. Wijnen, R. B. F. Janssen, Real-time frequency determination of acoustic emission for different fracture mechanisms in carbon/epoxy composites, Composites Science and Technology 55 (1995) 405–412.

[51] G. Qi, Wavelet-based AE characterization of composite materials, NDT&E International 33 (2000) 133–144.

[52] Matlab, The Mathworks Inc, Matlab R2009b user's manual.

[53] T. Loutas, V. Kostopoulos, C. Ramirez-Jimenez, M. Pharaoh, Damage evolution in center-holed glass-polyester composites under quasi-static loading using time-frequency analysis of acoustic emission monitored waveforms, Composites Science and Technology 66 (2006) 1366–1375.

[54] A. Marec, J.-H. Thomas, R. E. Guerjouma, Damage characterization of polymer-based composite materials: Multivariable analysis and wavelet trans-

form for clustering acoustic emission data, Mechanical Systems and Signal Processing 22 (2008) 1441–1464.

[55] T. Kohonen, The self-organizing map, Proceedings of the IEEE 78 (1990) 1464–1480.

[56] J. Vesanto, J. Himberg, E. Alhoniemi, J. Parhankangas, SOM toolbox for Matlab 5, Tech. rep., Helsinki University of Technology: http://www.cis.hut.fi/projects/somtoolbox (2000).

[57] N. Godin, S. Huguet, R. Gaertner, Integration of the Kohonen self-organising map and k-means algorithm for the segmentation of the AE data collected during tensile tests on cross-ply composites, NDT&E International 38 (2005) 299–309.

[58] R. de Oliveira, A. Marques, Health monitoring of frp using acoustic emission and artificial neural networks, Computers and Structures 86 (2008) 367–373.

[59] J. Vesanto, E. Alhoniemi, Clustering of the self-organizing map, IEEE transactions on neural networks 11 (2000) 586–600.

[60] M. Johnson, Waveform based clustering and classification of AE transients in composite laminates using principal component analysis, NDT&E International 35 (2002) 367–376.

[61] M. Johnson, P. Gudmundson, Broad-band transient recording and characterization of acoustic emission events in composite laminates, Composites Science and Technology 60 (2000) 2803–2818.

[62] Z. Hashin, A. Rotem, A fatigue failure criterion for fibre reinforced materials, Journal of Composite Materials 7 (1973) 448–464.

[63] I. M. Daniel, O. Ishai, Engineering mechanics of composite materials, Oxford University Press, 1994.

[64] S. W. Tsai, E. M. Wu, A general theory of strength for anisotropic materials, Journal of Composite Materials. 5 (1971) 58–80.

[65] V. D. Azzi, S. Tsai, Anisotropic strength of composites, Experimental Mechanics 9 (1995) 283–288.

[66] S. Yamada, C. Sun, Analysis of laminate strength and its distribution, Journal of composite materials 12 (1978) 275–284.

[67] S. Pinho, L. Iannucci, P. Robinson, Physically-based failure models and criteria for laminated fibre-reinforced composites with emphasis on fibre kinking: Part I: Development, Composites, PartA: applied science and manufacturing 37 (2006) 63–73.

[68] A. Puck, H. Schurmann, Failure analysis of FRP laminates by means of physically based phenomenological models, Composites Science and Technology 58 (1998) 1045–1067.

[69] Z. Hashin, Failure criteria for unidirectional fiber composites, J. Appl. Mech. 31 (1980) 223–232.

[70] F. Paris, A study of failure criteria of fibrous composites materials, Tech. rep., NASA (2001).

[71] J. M. Hodgkinson (Ed.), Mechanical testing of advanced fibre composites, Woodhead Publishing Limited, 2000.

[72] P. D. Ewins, A. C. Ham, The nature of compressive failure in unidirectional carbon fibre reinforced plastics, AIAA/ASME/SAE 15th Structures, Structural Dynamics and Materials Conference. Las Vegas.

[73] B. Rosen, N. Dow, Fracture, An advanced treatise, vol.7, Academic press, New York, London, 1972, Ch. 7-Mechanics of failure of fibrous composites, pp. 612–672.

[74] B. Budiansky, N. Fleck, Compressive failure of fibre composites, Journal of mechanics and physics of solids 41 (1993) 183–211.

[75] N. A. Fleck, L. Deng, B. Budiansky, Prediction of kink width in compressed fiber composites, Journal of Applied Mechanics 62 (1995) 329–336.

[76] B. Budiansky, Micromechanics, Computers & Structures 16 (1983) 3–12.

[77] P. Steif, A model for fibre kinking in fiber composites–I. fiber breakage via micro-buckling, International Journal of Solids and Structures 26 (1990) 549–561.

[78] H. T. Hahn, J. G. Williams, Compression failure mechanisms in unidirectional composites, Composite materials: Testing and Design (7th conference), ASTM STP 893, J. M. Whitney, Ed., American Society for Testing and Materials, Philadelphia (1986) 115–139.

[79] P. P. Camanho, C. G. D. ., Failure criteria for frp laminates in plane stress, nasa/tm-2003-212663, Tech. rep., NASA (2003).

[80] C. G. Dávila, P. P. Camanho, Failure criteria for FRP laminates in plane stress, NASA Technical report TM-2003-212663.

[81] H. T. Hahn, T. Johannesson, Mechanics of Composite Materials, AMD, 1983, Ch. Fracture of unidirectional composites: Theory and applications, pp. 135–142.

[82] A. S. D. Wang, Fracture mechanics of sublaminate cracks in composite materials, Composites Technology Review 6 (1984) 45–62.

[83] K. Hibbit, S. Inc., ABAQUS Users Manual Version 6.6, Hibbit and Karlsson and Sorensen Inc., 6th Edition (2006).

[84] C. Schuecker, H. Pettermann, Fiber reinforced laminates: Progressive damage modeling based on failure mechanisms, Archives of Computational Methods in Engineering 15 (2008) 163–184.

[85] P. Ladeveze, E. L. Dantec, Damage modelling of the elementary ply for laminated composites, Composites science and technology 43 (1992) 257–267.

[86] Z. P. Bazănt, B. H. Oh, Crack band theory for fracture of concrete, Materials and Structures 16 (1983) 155–177.

[87] C. G. Dávila, C. A. Rose, P. P. Camanho, A procedure for superposing linear cohesive laws to represent multiple damage mechanisms in the fracture of composites, International Journal of Fracture 158 (2009) 1573–2673.

[88] S. Pinho, L. Iannucci, P. Robinson, Physically-based failure models and criteria for laminated fibre-reinforced composites with emphasis on fibre kinking: Part II: FE implementation, Composites, PartA: applied science and manufacturing 37 (2006) 766–777.

[89] C. A. Paget, Delamination laocation and size by modified acoustic emission on cross-ply CFRP laminates during compression-compression fatigue loading, in: Proceedings of the 17th International Conference on Composite Materials, Chicago, Illinois, USA, 2009.

[90] Q. Q. Ni, M. Iwamoto, Wavelet transform of acoustic emission signals in failure of model composites, Engineering Fracture Mechanics 69 (2002) 717–728.

[91] S. Pinho, P. Robinson, L. Iannucci, Fracture toughness of the tensile and compressive fibre failure modes in laminated composites, Composites science and technology 66 (2006) 2069–2079.

[92] Standard test method for mode I interlaminar fracture toughness of unidirectional fiber-reinforced polymer matrix composites, ASTM standard D 5528-94a.

[93] Standard test method for tensile properties of polymer matrix composite materials, ASTM D 3039/D 3039M.

[94] Physical Acoustic Corporation, PCI-2 based ae system, user's manual.

[95] R. Gutkin, S. T. Pinho, P. Robinson, P. T. Curtis, On the transition from shear-driven fibre compressive failure to fibre kinking in notched CFRP laminates under longitudinal compression, Composites Science and Technology 70 (2010) 1223–1231.

[96] Y. Z. Pappas, M. Y.P, V. Kostopoulos, Failure mechanisms analysis of 2D carbon/carbon using acoustic emission monitoring, NDT & E International 31 (1998) 157–163.

[97] F. Bação, V. Lobo, M. Painho, Lecture Notes in Computer Science, Springer-Link, 2005, Ch. Self-organizing Maps as Substitutes for K-Means Clustering, pp. 476–483.

[98] P. Perner, Machine Learning and Data Mining in Pattern Recognition: 5th International Conference, MLDM 2007, Leipzig, Germany, July 18-20, 2007, Springer, 2007.

[99] H. T. Hahn, M. Sohi, S. Moon, Compression failure mechanisms of composite structures, Tech. rep., NASA Contractor report 3988 (1986).

[100] C. Soutis, Measurement of the static compressive strength of carbon-fibre epoxy laminates, Composites Science and Technology 42 (1991) 373–392.

[101] E. S. Greenhalgh, M. J. Hiley, Fractography of polymer composites: current status and future issues, In: Proceedings of the 13th European conference on composite materials (ECCM13), Stockholm, Sweden; 2008.

[102] W. Michaeli, M. Mannigel, F. Preller, On the effect of shear stresses on the fibre failure behaviour in CFRP, Composites Science and Technology 69 (2009) 1354–1357.

[103] T. Vogler, S.Kyriakides, On the axial propagation of kink bands in fiber composites: Parti. experiments, International journal of solids and structures 36 (1999) 557–574.

[104] H. Thom, A review of the biaxial strength of fibre-reinforced plastics, Composites PartA 29 (1998) 869–886.

[105] S. Pimenta, R. Gutkin, S. Pinho, P. Robinson, A micromechanical model for kink-band formation: Part I—experimental study and numerical modelling, Composites Science and Technology 69 (2009) 948–955.

[106] S. Ogihara, Y. Imafuku, R. Yamamoto, Y. Kogo, Direct evaluation of fracture toughness in a carbon fiber, In: Proceedings of the 17th International conference on composite materials (ICCM17), Edinburgh, Scotland.

[107] N. Oya, D. Johnson, Longitudinal compressive behaviour and microstructure of PAN based carbon fibres, Carbon 39 (2001) 635–645.

[108] V. V. Kozey, Fibre strength-dominated failure model in unidirectional composites under compression, Journal of materials science letters 12 (1993) 48–52.

[109] R. Effendi, J.-J. Barrau, D. Guedra-Degeorges, Failure mechanism analysis under compression loading of unidirectional carbon/epoxy composites using micromechanical modelling, Composites structures 31 (1995) 87–98.

[110] S. Pimenta, R. Gutkin, S. Pinho, P. Robinson, A micromechanical model for kink-band formation: Part II—analytical modelling, Composites Science and Technology 69 (2009) 956–964.

[111] A. De Morais, A. Marques, A micromechanical model for the prediction of the lamina longitudinal compression strength of composite laminates, Journal of Composite Materials 31 (1997) 1397–1412.

[112] Z. Suo, G. Bao, B. Fan, Delamination R-curve phenomena due to damage, Journal of Mechanics and Physics of Solids 40 (1992) 1–16.

[113] T. K. Jacobsen, B. F. Sørensen, Mode I intra-laminar crack growth in composites — modelling R-curves from measured bridging laws, Composites Part A: Applied Science and Manufacturing 32 (2001) 1–11.

[114] B. F. Sørensen, S. Goutianos, T. K. Jacobsen, Strength scaling of adhesive joints in polymer-matrix composites, International Journal of Solids and Structures 46 (2009) 741–761.

[115] A. Carpinteri, R. Massabó, Bridged versus cohesive crack in the flexural behavior of brittle-matrix composites, International Journal of Fracture 81 (1996) 125–145.

[116] A. L. Hansen, E. Lund, B. F. Sørensen, Simulation of delamination including fiber bridging using cohesive zone models, in: Proceedings of ECCOMAS Thematic conference on mechanical response of composites, 2007.

[117] R. M. L. Foote, Y.-W. Mai, B. Cotterell, Crack growth resistance curves in strain-softening materials, Journal of Mechanics and Physics of Solids 34 (1986) 593–607.

[118] E. S. Greenhalgh, C. Rogers, P. Robinson, Fractographic observations on delamination growth and the subsequent migration through the laminate, Composites Science and Technology 69 (2009) 2345–2351.

[119] C.Soutis, N.A.Fleck, Static compression failure of carbon fibre T800/924C composite plate with a single hole, Journal of Composite Materials 24 (1990) 536–558.

[120] A. B. De Morais, Modelling lamina longitudinal compression strength of carbon fibre composite laminates, Journal of Composite Materials 30 (1996) 1115–1131.

[121] T. Vogler, S. Kyriakides, On the initiation and growth of kink bands in fiber composites. Part II: analysis, International journal of solids and structures 38 (2001) 2653–2682.

[122] R. Gutkin, S. Pinho, P. Robinson, P. Curtis, Physical mechanisms associated with initiation and propagation of kink-bands., In: Proceedings of the 13th European conference on composite materials (ECCM13), Stockholm, Sweden.

[123] M.J.Hinton, P.Soden, A.S.Kaddour, Instructions to contributers of the Second World-Wide Failure Exercise (WWFE-II): Part A., Submitted to Composite Science and Technology.

[124] M.J.Hinton, A.S.Kaddour, P.Soden, Failure criteria in fibre reinforced polymer composites: The World-Wide Failure Exercise, Elsevier Science Ldt, 2004.